

OPTIMIZED FATIGUE AND FRACTURE PERFORMANCE OF FRICTION STIR  
WELDED ALUMINIUM PLATE: A STUDY OF THE INTER-RELATIONSHIP  
BETWEEN PROCESS PARAMETERS, TMAZ, MICROSTRUCTURE, DEFECT  
POPULATION AND PERFORMANCE

By

HANNALIE LOMBARD

A THESIS SUBMITTED TO THE UNIVERSITY OF Plymouth  
In the fulfilment for the degree of

DOCTOR OF PHILOSOPHY

Faculty of Technology  
University of Plymouth  
England

in collaboration with

Nelson Mandela Metropolitan University  
South Africa

June 2007

### Copyright Statement

This copy of the thesis has been supplied on condition that anyone who consults it is understood to recognize that its copyright is with its author and that no quotation from the thesis and no information derived from it may be published without the author's prior consent.

University of Plymouth Library	
Item no.	9007622957
Shelfmark	THESIS 671.52 LOM.

LIBRARY STORE

<b>Contents</b>	<b>Page</b>
Contents	i
List of figures	iv
List of tables	xiii
Glossary of terms	xiv
Nomenclature	xxi
Author's declaration	xxiii
Acknowledgements	xxv
Abstract	1
1. Introduction	4
1.1 History	4
1.2 Industrial advantages and application areas	4
1.2.1 Shipbuilding and marine industries	5
1.2.3 Aerospace industry	5
1.2.4 Railway industry	6
1.2.5 Land transportation	6
1.2.6 Other industry sectors	6
1.3 The work described in this thesis	7
2. Overview of the FSW process	10
2.1 Introduction	10
2.2 Description of the FSW process	12
2.3 FSW parameters	16
2.3.1 Tool feed rate and rotational speed	16
2.3.2 Torque	19
2.3.3 Tool rake (tilt angle)	21
2.3.4 Plunge depth	23
2.3.5 Tool geometry	23
2.3.5.1 Tool pin (probe)	24
2.3.5.2 Tool shoulder	27
2.3.6 Forces on the tool during FSW	29
2.3.7 The polar plot or "force footprint " diagram	34
2.3.8. Tool temperature	36
2.5 Microstructure	41
2.5.1 FS weld microstructures	42
2.5.2 Grain size and hardness variation in the nugget	50

2.6	Mechanical properties	54
2.6.1	Defects	54
2.6.2	Type of defects in FSW	55
2.6.2.1	Voids	55
2.6.2.2	Root defects or kissing bonds	58
2.6.2.3	Planar facets	59
2.6.3	Tensile Investigations	61
2.6.4	Fatigue strength	64
2.6.5	Residual stresses	71
2.7	Heat and power input	80
2.8	Summary of findings of existing research	94
3	Experimental design for identifying critical process parameters	96
3.1	Introduction	96
3.2	Experimental setup for welding	98
3.2.1	Instrumentation	98
3.2.2	The force foot print polar plot	102
3.2.3	Experimental conditions	106
3.2.3.1	Tool geometry	106
3.2.3.2	Input parameters	107
3.3	Experimental results	108
3.4	Interrelationship of input and process parameters	111
3.4.1	Energy input into the welds	112
3.4.2	Regression models of weld parameters	119
3.4.3	Surface plots of process parameters versus rotational speed and feed rate	125
3.4.3.1	Tool torque versus feed rate and rotational speed	126
3.4.3.2	$F_z$ force versus feed rate and rotational speed	127
3.4.3.3	Tool temperature versus feed rate and rotational speed	128
3.4.3.4	$F_x$ and $F_y$ forces versus feed rate and rotational speed	129
3.4.4	The dependence of the coefficient of friction on process parameter	130
3.5	Conclusions	133
4.	Microstructure, defect occurrence, tensile strength and vickers hardness of FSW	136
4.1	Introduction	136
4.2	General properties of Aluminium 5083 – H321	136
4.3	Specimens taken from the weld	137
4.4	Microstructural specimen preparation	138
4.5	FS microstructure	139
4.5.1	Macrostructure variation as a function of process	

	Parameters	139
	4.5.2 Effect of weld parameters on defects	142
4.6	Tensile Results	143
	4.6.1 Variation of UTS and 0.2% proof strength along the weld.	144
	4.6.2 Tensile fracture surfaces	146
	4.6.3 Variation of UTS and 0.2 % proof strength with weld parameters	152
4.7	Micro hardness results	156
	4.7.1 Relationship between rotational speed and hardness	157
	4.7.2 Relationship of Vickers hardness with respect to increasing feed rate and rotational speed at a constant pitch	159
	4.7.3 Comparison of hardness and process parameters	160
4.8	Conclusions	161
5.	Determination of residual stress in FSW using synchrotron radiation	162
	5.1 Introduction	162
	5.2 Residual stress definitions	163
	5.3 Techniques used to measure residual stresses	164
	5.4 Continuum mechanical definition of stress and strain	168
	5.5 The biaxial stress case	170
	5.6 Determination of strain and stress from X-ray diffraction (XRD) data	171
	5.7 The $\sin^2\psi$ method	174
	5.8 Elastic anisotropy	176
	5.9 Strain measurement using synchrotron X-ray diffraction methods	177
	5.9.1 The production and advantages of synchrotron X-ray diffraction	177
	5.9.2 Setup on beam line ID31	179
	5.9.3 The gauge volume and slit system	180
	5.9.4 Determining the position of strain measurement	182
	5.10 Strain-free lattice data	182
	5.11 Longitudinal and transverse strain and stress in FSW	186
	5.12 Variation of residual stress data with respect to process parameters in FSW.	190
	5.13 Regression analyses	193
	5.14 Residual stress and heat input	195
	5.15 Surface plots of transverse and longitudinal residual stresses	195
	5.16 Residual stress and the force footprint	196
	5.17 FWHM results in FSW	200

5.18	Results of residual stress mapping at various weld positions	201
5.18.1	Transverse and longitudinal stress at 10 mm intervals along the weld	201
5.18.2	Transverse and longitudinal stress maps of longitudinal weld sections on the advancing side of the weld	206
5.19	Conclusions	207
6.	Fatigue Life in FSW aluminium 5083-H321 as a function of process conditions	209
6.1	Introduction	209
6.2	Background to Fatigue	209
6.3	Experimental setup	210
6.3.1	Fatigue testing instrument	210
6.3.2	Fatigue specimens	210
6.3.3	Determining the constant stress to apply to all specimens	211
6.4	Fatigue life of FSW	213
6.5	Statistical analyses of fatigue data	214
6.6	Defects in FS welds of Al 5083-H321	216
6.7	Defect population in FSW 5083-H321 aluminium alloys	219
6.8	Residual stress versus fatigue life and the type of defects	226
6.9	Conclusions	227
7.	Summary of results and suggestions for future work	229
	References	236
	Appendix	254

## List of figures

### Chapter 2

Figure 2.1:	Important parameters of FSW.	12
Figure 2.2:	Features of friction stir welding.	13
Figure 2.3:	Variation of input and process parameters with respect to time for welds made with the instrumental FSW at NMMU.	14
Figure 2.4:	The third body region formed around the tool.	18
Figure 2.5:	Variation of torque with rotational speed and feed rate.	20
Figure 2.6:	Surface plot relating spindle speed, feed rate and spindle torque in FSW of 5083-H321 alloy.	21
Figure 2.7:	Definition of tool push, rake and tilt angle. The rake, tilt and push angle are equal in size.	22
Figure 2.8:	Effect of rake angle on flow of material for 1100 and 5005 aluminium alloys.	22

Figure 2.9:	Whorl™, Triflute™, Trivex™ and MX Trivex™ tool designs.	25
Figure 2.10:	Whorl type FSW pins.	25
Figure 2.11:	Triflute family of probe variants for friction stir welding. (a)MX Triflute™ for butt welding (b) Flared-Triflute™ with tip.	26
Figure 2.12:	Some shoulder geometries used by TWI.	27
Figure 2.13:	Side flash obtained during a trial weld at the Nelson Mandela Metropolitan University.	28
Figure 2.14:	Graph showing typical M-type distribution of residual stresses, as a function of tool shoulder diameter in a 6013-T4 aluminum FS weld.	28
Figure 2.15:	Bobbin tool.	29
Figure 2.16:	Forces relevant to FSW.	30
Figure 2.17:	Surface plot relating spindle speed, feed rate and vertical compressive force applied on the tool.	31
Figure 2.18:	Variation of transverse force with (a) rotational speed and (b) feed rate.	31
Figure 2.19:	Surface plot relating spindle speed, feed rate and maximum horizontal force exerted on the tool.	32
Figure 2.20:	Surface plot relating spindle speed, feed rate and maximum vertical force exerted on the tool.	32
Figure: 2.21	Typical 2D polar force plot for a spindle speed of 300 rotational speed and feed rate of 120mm/min in 5083-H321 alloy.	35
Figure 2.22:	Surface plot relating spindle speed, feed rate and tool temperature.	37
Figure 2.23 :	Peak temperature as a function of distance from the weld centre line.	38
Figure 2.24:	The effect of the shoulder on the peak temperature.	39
Figure 2.25:	The variation of peak temperature with respect to tool rotation speed/feed rate ( that is 1/pitch) .	40
Figure 2.26:	Classification of Microstructure in FSW.	42
Figure 2.27:	Effect of feed rate, type of tool, heat input on the HAZ during FSW.	43
Figure 2.28:	Formation of onion rings.	44
Figure 2.29:	Relationship between pitch=(feed rate/rpm) and rotational speed in for 6061 and 7075 alloys.	45
Figure 2.30:	Banded structure in the horizontal plane of the FSW indicating high and low density particles for 2024-T351 aluminium alloy.	46
Figure 2.31:	Macrographs showing the stir zone/TMAZ in dissimilar welds between 6061-T6 and AA 5083 aluminium alloys. 5083 is on the AS (AS = advancing side, RS = retreating side).	48

Figure 2.32: Transverse section of FSW 5083-H131 at zero rake angle made at a rotational speed of 250 rpm and a feed rate 127 mm/min.	48
Figure 2.33: Variation in nugget size with rotational speed and feed rate for 2524-T351 aluminium alloy.	49
Figure 2.34: Variation of nugget area with the parameter $w^2/f$ .	49
Figure 2.35: Variation of grain size through the nugget and as a function of rotational speed.	50
Figure 2.36: Vickers Hardness profiles for most FSW alloys.	51
Figure 2.37: Hardness versus rotational speed for feed rates at (a)59 mm/min and (b) 95 mm/min for 7010-T7651 aluminium alloy.	52
Figure 2.38: Variation of grains size with process parameters.	53
Figure 2.39: Typical defects observed in FSW.	55
Figure 2.40: (a) Wormhole or tunnel defect in Al 5083-H131. (b) Large void defect in the cross section of a FSW in Al 5083-H321.	55
Figure 2.41: (a) void on advancing side of weld (b) surface breaking void i.e. faying surface flaw (c) void beneath the upper surface of the weld	56
Figure 2.42: Elliptical void on the fracture surface of a FSW sample.	56
Figure 2.43: Variation of $F_x$ with rotational speed.	57
Figure 2.44: Lines indicating remnants of the weld line.	58
Figure 2.45: Root flaws indicated by the arrow.	59
Figure 2.46: Planar facets observed on a bend fatigue specimen.	60
Figure 2.47: Summary of defects in welds of 2024-T6,5083(O) and 7075-T6 aluminium alloys.	60
Figure 2.48: Tensile properties of the nugget zone for AA 7010-T7651.	62
Figure 2.49: Effect of pitch on tensile properties of 5083-O.	63
Figure 2.50: Tensile tests fracture locations for three different types of alloys.	64
Figure 2.51 : Surface topography of FSW.	65
Figure 2.52: Stress life fatigue data for FSW 5xxx series butt welds at $R=-1$ compared with Eurocode 9 design curves.	66
Figure 2.53: Influence of welding speed on results on fatigue life of FSW specimens of 6084-T6 + post weld aged.	67
Figure 2.54: Variation of fatigue life with (a) pitch and (b) rotational speed.	68
Figure 2.55: Fatigue limit corresponding to a fatigue life of $10^7$ cycles as a function of travel speed.	70
Figure 2.56: Endurance fatigue results for the flawed specimen tests ( $R = 0.1$ and $0.4$ ) and draft Eurocode 9 fatigue design lines.	70
Figure 2.57: Longitudinal Residual stress distribution in friction stir welded 6013-T4 sheet as a function of process parameters.	74



Figure 2.58: (a) Variation of longitudinal and transverse residual stress in FSW welds 304L stainless steel.	
(b) Variation of transverse stress in FS welds made in 304L stainless steel.	76
Figure 2.59: (a) Longitudinal residual stress in 5083-AA similar material welds as a function of the lateral distance from the weld line.	
(b) Transverse residual stress in 5083-AA similar material welds as a function of the lateral distance from the weld line.	78
Figure 2.60: Residual stress maps of 2024-T3 for two transverse sections at different longitudinal positions as a function of depth(z) below the surface	79
Figure 2.61: Heat processes in the FSW process.	81
Figure 2.62: Heat input from pin and shoulder.	82
Figure 2.63: Heat generated by specific areas underneath the FSW tool.	85
Figure 2.64: Variation of friction with pressure exerted on the tool.	87
Figure 2.65: Heat model developed by Schmidt et al.	91
Figure 2.66: The relationship between 1/pitch and peak welding temperature for Al 5083-O.	92
Figure 2.67: Specific Weld energy (heat input in J/mm) and power (Watts) as a function of welding speed (feed rate mm/min) for 7050-T751 aluminium alloy.	93
 <b>Chapter 3</b>	
Figure 3.1: Complete experimental setup.	99
Figure 3.2: Tool monitoring system.	101
Figure 3.3: Typical polar force plot obtained for FSW using the tool geometry shown in Figure 3.7.	103
Figure 3.4: Directions of forces on the tool and strain gauge measurements.	104
Figure 3.5: Resultant force polar plot of a weld made at a feed rate of 185 mm/min and 870 rpm.	104
Figure 3.6: Comparison of polar plot data with total power input determined from the translational forces.	105
Figure 3.7: Flute tool geometry used to make the FSW.	106
Figure 3.8: (a) Variation of tool torque along the weld.	108
(b) Variation of vertical force ( $F_z$ ) along the weld.	
(c) Variation of tool temperature along the weld.	
(d) Variation of $F_x$ max and $F_x$ min along the weld.	109
Figure 3.9: Functional relationships model for parameters.	111
Figure 3.10: (a) 3D plot of heat input versus tool rotational speed and feed rate.	
(b) Contour plot of heat input versus tool rotational speed and feed rate.	114

Figure 3.11: (a) 3D plot of frictional power input versus rotational speed and feed rate.	
(b) Contour plot of frictional power input versus rotational speed and feed rate.	114
Figure 3.12: (a) 3D plot of the sum of rotational and translational power input versus rotational speed and feed rate.	
(b) Contour plot of the sum of rotational and translational power input versus rotational speed and feed rate.	115
Figure 3.13: The relationship between $\omega^2/f$ and the effective coefficient of friction.	116
Figure 3.14: (a) Normal force versus $\omega^2/f$ .	
(b) Tool temperature versus $w^2/f$	
(c) Tool torque versus $\omega^2/f$ .	117
Figure 3.15: A comparison between the effective coefficient of friction, tool temperature and $\omega^2/f$ .	118
Figure 3.16: The parameter ( $\omega^2/f$ ) versus temperature/coefficient of friction.	118
Figure 3.17 : Frictional power versus tool temperature.	124
Figure 3.18: (a) 3D plot of torque versus rotational speed and feed rate.	126
(b) Contour plot of torque versus rotational speed and feed rate.	126
(c) 3D plots of $F_z$ versus rotational speed and feed rate.	127
(d) Contour plots of $F_z$ versus rotational speed and feed rate.	127
(e) 3D plot of Tool Temperature versus rotational speed and feed rate.	128
(f) Contour plot of tool temperature versus rotational speed and feed rate.	128
(g) 3D plot of $F_y$ max versus rotational speed and feed rate.	129
(h) Contour plot of $F_y$ max versus rotational speed and feed rate.	129
(i) 3D plot of $F_x$ max versus rotational speed and feed rate.	129
(j) Contour plot of $F_x$ max versus rotational speed and feed rate.	129
(k) 3D plot of the resultant polar plot areas versus rotational speed and feed rate.	130
(l) Contour plot of the resultant polar plot areas versus rotational speed and feed rate.	130
Figure 3.19: (a) 3D plot of effective coefficient of friction versus rotational speed and feed rate.	131
(b) Contour plot of effective coefficient of friction versus rotational speed and feed rate.	131
(c) 3D plot of effective coefficient of friction versus normal force and tool temperature.	131
(d) Contour plot of effective coefficient of friction versus normal force and tool temperature.	131

(e) 3D plot of effective coefficient of friction versus tool torque and normal force $F_z$ .	132
(f) Contour plot of effective coefficient of friction versus tool torque and normal force $F_z$ .	132
Figure 3.20: The effective coefficient of friction versus tool temperature and normal force.	133

## Chapter 4

Figure 4.1: Position of specimens taken from the friction stir welds.	138
Figure 4.2: Identification of planes for a rectangular plate.	139
Figure 4.3: Relationship of the occurrence of defects to feed rate and rotational speed.	142
Figure 4.4: Tensile specimen dimensions.	143
Figure 4.5: Instron 8801 general purpose tensile testing machine.	143
Figure 4.6: Tensile results for weld 6.	144
Figure 4.7: Variation of ultimate tensile strength and 0.2% proof strength along the weld length.	146
Figure 4.8: Fractographs illustrating root defects for	
(a) weld 2 at position 221 mm along the weld.	147
(b) weld 4 at position 221 mm along the weld.	147
(c) weld 2 at position 221 mm bottom side of weld.	147
(d) weld 4 at position 221 mm bottom side of weld.	147
Figure 4.9: Tensile fractographs of the shoulder region of the welds as a function of UTS and frictional power.	150
Figure 4.10: (a) 3D plot of UTS versus rotational speed and feed rate.	152
(b) Contour plot of UTS versus rotational speed and feed rate.	152
Figure 4.11: Comparison between frictional power and UTS.	153
Figure 4.12: Tensile strength as a function of tool frictional power.	153
Figure 4.13: (a) 3D plot of UTS versus rotational speed and feed rate.	154
(b) Contour plot of UTS versus rotational speed and feed rate.	154
Figure 4.14: Tensile strength as a function of tool temperature and $F_y$ max.	155
Figure 4.15: Tensile strength as a function of $\omega^2/f$ .	156
Figure 4.16: Buehler Micromet 5103 micro hardness tester at FAME38 in Grenoble, France.	157
Figure 4.17: An example of a micro hardness indentation.	157
Figure 4.18: (a) Hardness versus rotational speed for a feed rate of 185 mm/min.	158
(b) Hardness versus rotational speed for a feed rate of 135 mm/min.	158
(c) Hardness versus rotational speed for a feed rate of 85 mm/min.	158
Figure 4.19: Trends of Vickers hardness versus pitch.	159

Figure 4.20: (a) 3D plot of Vickers hardness values 3 mm below the crown of the weld versus input process parameters.	160
(a) Contour plot of Vickers hardness values 3 mm below the crown of the weld versus input process parameters.	160
Figure 4.21: (c) Contour plot of heat input and as a function of feed rate and rotational speed.	161
(d) Frictional power input as a function of feed rate and rotational speed.	161
<b>Chapter 5</b>	
Figure 5.1: The different types of residual stresses.	164
Figure 5.2: Components of stresses in three dimensions matrix representation.	168
Figure 5.3: Determination of the interplanar spacings.	172
Figure 5.4: Diffracting geometry showing incident ( $k_i$ ), diffracted $k_d$ and the direction of the scattering vector $Q$ .	173
Figure 5.5: Angular arrangement to determine the stress component in the $\varphi$ direction.	174
Figure 5.6: Behaviour of different lattice planes under loading perpendicular to the planes for elastic anisotropic materials such as steel.	176
Figure 5.7: (a) Movement of the beam through bending magnets and undulators.	178
(b) Example of a beam line station.	178
Figure 5.8: Slit system and gauge volume.	181
Figure 5.9: The influence of an incomplete gauge volume on the shift in the diffraction angle.	182
Figure 5.10: Illustration of EDM $d_o$ sample consisting several rows of 32 teeth machined transverse to the weld and extending across the plate thickness.	183
Figure 5.11: Measurements of $2\theta$ as a function of position along teeth for a toothcomb specimen parallel to the weld and cut from the parent plate (weld 4: 185 mm/min, 870 rpm).	185
Figure 5.12: The variation of the unstrained lattice parameter expressed as strain between welds.	185
Figure 5.13: Strain measurements sample for weld 11.	186
Figure 5.14: The residual longitudinal stress profile at the mid section across the weld.	188
Figure 5.15: The residual transverse stress profile at the mid section across the weld.	189
Figure 5.16: Longitudinal stress for a feed rate of 135 mm/min as a function of tool rotational speed.	191
Figure 5.17: Transverse stress for a feed rate of 135 mm/min as a function of tool rotational speed.	191
Figure 5.18: Longitudinal stress for pitch 0.2.	192
Figure 5.19: Transverse stress at a pitch of 0.2.	193

Figure 5.20:	Features of residual stress profile as a function of average heat input.	195
Figure 5.21:	Comparison between maximum tensile residual stresses of (a) longitudinal and (b) transverse directions as a function of tool rotational speed and feed rate.	196
Figure 5.22:	(a) Polar plots of $F_x$ for pitch 0.2. (b) Polar plots of $F_y$ for pitch 0.2. (c) Resultant polar plots for pitch 0.2.	197 197 197
Figure 5.23:	Maximum tensile longitudinal and transverse stress as a function of $F_{xmax}$ .	199
Figure 5.24:	Maximum tensile longitudinal and transverse stress as a function of the resultant force.	199
Figure 5.25:	FWHM for welds 1 and 8.	200
Figure 5.26:	Regression between width of the HAZ and the average heat input.	201
Figure 5.27:	Example of Longitudinal scan on transverse section of weld (LSTS -scans).	202
Figure 5.28:	Longitudinal stress maps of the transverse section for welds made at a single feed rate of 135 mm/min and increasing rotational speeds of (a) 254 rpm (b) 423 rpm and (c) 635 rpm.	203
Figure 5.29:	Transverse stress maps of the transverse section for welds made at a single feed rate of 135 mm/min and increasing rotational speeds of (a) 254 rpm (b) 423 rpm and (c) 635 rpm.	205
<b>Chapter 6</b>		
Figure 6.1:	Typical loading parameters used to characterize cyclic loading.	210
Figure 6.2:	Dimension of fatigue specimen according to ASTM E 466-96.	210
Figure 6.3:	Experimental data obtained for the parent plate cut in the rolling direction.	212
Figure 6.4:	Variation of fatigue life for each sample at different positions along the weld.	214
Figure 6.5:	(a) 3 D map of fatigue life as a function of feed rate and rotational speed. (b) Contour map of fatigue life as a function of feed rate and rotational speed.	215 215
Figure 6.6:	Fatigue compared to (a) frictional power and (b) UTS.	216
Figure 6.7:	(a) Fatigue onion skin defect for weld 5 (135 mm/min, 254 rpm). (b) Fatigue void like feature for weld 5 (135 mm/min, 254 rpm).	217 217
Figure 6.8:	Onion skin defects for weld 8 (85 mm/min, 400 rpm,	

pitch 0.21).	218
Figure 6.9: Optical micrograph indicating planar facets at fatigue initiation site for weld 6 (85 mm/min, 266 rpm, pitch 0.3).	218
Figure 6.10: Planar facets for (a) weld 2 (b) weld 3 and (c) weld 9.	219
Figure 6.11: Histograms relating FSW parameters with defect types.	222
Figure 6.12: Defect population of tensile and fatigue samples versus process parameters and frictional power.	224
Figure 6.13: Fatigue life as a function of defect type and frictional power input.	225
<b>Chapter 7</b>	
Figure 6.12: Defect population of tensile and fatigue samples versus process parameters and frictional power.	232
<b>Appendix</b>	
Figure A.1: (a) Resultant polar plot for pitch 0.3.	257
(b) Resultant polar plot for pitch 0.4.	257
(c) Resultant polar plot for pitch 0.5.	257
Figure A.2: Longitudinal stress maps of transverse sections of weld 5 (135 mm/min, 254 rpm) at intervals of 15 mm.	258
Figure A.3: Transverse stress maps of transverse sections of weld 5 (135 mm/min, 254 rpm) at intervals of 15 mm.	259
Figure A.4: Longitudinal stress maps of transverse sections of weld 11(135 mm/min, 635 rpm) at intervals of 15 mm.	260
Figure A.5: Transverse stress maps of transverse sections of weld 11 (135 mm/min, 635 rpm) at intervals of 15 mm.	261
Figure A.6: Longitudinal stress maps of longitudinal sections on the advancing side of weld 5 (135 mm/min, 254 rpm)	
(a) 35 mm, in parent plate area.	262
(b) 10 mm, close to the edge of the shoulder.	262
(c) 5mm, at edge of the pin.	262
(d) 0 mm, on weld centre-line.	262
Figure A.7: Transverse stress maps of longitudinal sections on the advancing side of weld 5 (135 mm/min, 254 rpm)	
(e) 35 mm, in parent plate area.	263
(f) 10 mm, close to the edge of the shoulder.	263
(g) 5mm, at edge of the pin.	263
(h) 0 mm, on weld centre-line.	263
Figure A.8: Longitudinal stress maps of longitudinal sections on the advancing side of weld 11 (135 mm/min, 635 rpm)	
(a) 0 mm, on weld centre-line.	264
(b) 5mm, at edge of the pin.	264
(c) 10 mm, close to the edge of the shoulder.	264
(d) 35 mm, in parent plate area.	264

(d) 35 mm, in parent plate area.	264
Figure A.9: Transverse stress maps of longitudinal sections on the advancing side of weld 11 (135 mm/min, 635 rpm)	
(a) 0 mm, on weld centre-line.	265
(b) 5mm, at edge of the pin.	265
(c) 10 mm, close to the edge of the shoulder.	265
(d) 35 mm, in parent plate area.	265

## List of Tables

### Chapter 3

Table 3.1: Input parameters of FS welds.	108
Table 3.2: Weld input and process parameters.	110
Table 3.3: Polar plot data.	110
Table 3.4: Percentage deviation in process parameters.	111
Table 3.5: Energy calculations and analyses.	113
Table 3.6: Analyses of variance.	121
Table 3.7: Multiple regression analyses.	123

### Chapter 4

Table 4.1: Nominal wt% of Al 5083-H321.	137
Table 4.2: Photo montages of welds cross sections.	140
Table 4.3: Variation of the nugget zone with respect to $F_z$ .	141
Table 4.4: Defects identified on the macrographs.	142
Table 4.5: Tensile results of the parent plate in MPa.	144
Table 4.6: Tensile results of the welds in MPa.	144
Table 4.7: 0.2 % Proof stress along the weld	145
Table 4.8: Optical fractographs of tensile fractures.	149
Table 4.9: Summary of defects detected in tensile fractured specimens of FSW.	151
Table 4.10: UTS and 0.2% proof strength regression models.	154

### Chapter 5

Table 5.1: Summary of various measurement techniques and their characteristics to determine residual stress.	167
Table 5.2: FSW parameter data for welds at 135 mm/min.	190
Table 5.3: Regression analyses of the longitudinal and transverse residual stresses.	194
Table 5.4: Summary of weld parameters and residual stress data.	198
Table 5.5: Process parameters at 254, 423 and 635 rpm.	204

## Chapter 6

Table 6.1: Initial trials to investigate fatigue life.	213
Table 6.2: Average fatigue data for five samples taken along the weld.	213
Table 6.3: Statistical analyses of fatigue data.	215
Table 6.4: Optical classification of fatigue fracture surfaces.	220
Table 6.5: Ranking order used in this thesis.	220
Table 6.6: Comparison of fatigue lives and residual stress data.	227

## Glossary of terms

### A

**absorption**—the decrease in intensity which radiation undergoes during its passage through matter when the ratio of transmitted or reflected luminous flux to incident is less than 1.

**alloy** — A substance having metallic properties and being composed of two or more chemical elements of which at least one is a metal.

**augering effect** — the gripping movement of the rotating tool in FSW where the tool shape or profile pulls or stirs the plasticized material in a downward direction.

**alloying element**— an element added to and remaining in metal that changes structure and properties.

**anisotropic** —having different values for a property, in different directions.

**annealing** — heating to and holding at a suitable temperature followed by cooling at a suitable rate.

### B

**bending stress** — if a beam is subjected to a bending moment the fibres in the upper part are extended and those in the lower part are compressed. Tensile and compressive stresses are thereby induced which vary from zero at the neutral axis of the beam to a maximum at the outer fibres. These stresses are called bending stresses.

**butt weld** — A welded joint formed between the squared ends of two joining pieces, which do not overlap.



## C

**capillary action** — This when a fluid rises or falls within a narrow tube.

**coefficient of thermal expansion**—change in unit of length (or volume) accompanying a unit change of temperature, at a specified temperature.

**cold worked structure**—a microstructure resulting from plastic deformation of a metal or alloy below its recrystallization temperature.

**Computational Fluid Dynamics (CFD)** — This is the analysis of fluid dynamics and flow dynamics using computational means.

**conventional friction welding** — Is the process where two materials are welded together by the friction generated when they are forced together under load.

**crystallographic cleavage**—the separation of a crystal along a plane of fixed orientation relative to the three-dimensional crystal structure within which the separation process occurs, with the separation process causing the newly formed surfaces to move away from one another in directions containing major components of motion perpendicular to the fixed plane.

**cycle**—*in fatigue*, one complete sequence of values of load (strain) that is repeated under constant amplitude loading (straining).

## D

**deformation** — Is a change in the form of a body due to stress, thermal, or other causes.

**die** - A shaped block of hard material used to form metal with the use of heat and pressure.

**diffraction** — the scattering of electrons, by any crystalline material, through discrete angles depending only on the lattice spacing of the material and the velocity of the electrons.

## E

**elastic region** — a material is said to be stressed within the elastic region when the working stress does not exceed the elastic limit.

**equilibrium**—a state of dynamic balance between the opposing actions, reactions, or velocities of a reversible process.

**etchant** — a chemical solution used to etch a metal to reveal structural details.

**etching** — subjecting the surface of a metal to preferential chemical or electrolytic attack to reveal structural details for metallographic examination.

**Extrusion** — The process where a material is shaped by force or squeezed through die or nozzle.

## **F**

**fatigue** — a phenomenon which results in the sudden fracture of a component after a period of cyclic loading in the elastic regime.

**fatigue life** — the number of load cycles a component can withstand prior to failure.

**face-centered**—having atoms (or groups of atoms) separated by translations of  $\frac{1}{2}$ ,  $\frac{1}{2}$ , 0;  $\frac{1}{2}$ , 0,  $\frac{1}{2}$ ; and 0,  $\frac{1}{2}$ ,  $\frac{1}{2}$  from a similar atom (or group of atoms). The number of atoms in a face-centered cell must be a multiple of four.

**Finite Element Analysis (FEA)** —The analysis of static and dynamical systems using computational methods such as the numerical technique finite difference method. The finite difference method is an approximation to an ordinary and partial differential equation.

**Finite element method (FEM)** is used for finding approximate solutions of partial differential equations as well as of integral equations over complex domains (like cars and oil pipelines), when the domain changes (as during a solid state reaction with a moving boundary), or when the desired precision varies over the entire domain. The finite element method is an approximation to a solution of the finite difference differential equation.

**flow dynamics** — The analysis of the motion of material objects in relation to physical factors affecting them: force, mass, momentum and energy.

**fusion welding** — Is the process where materials are liquefied or melted together by the application of heat to form a bond.

## **G**

**grain growth** — an interface separating two grains at which the orientation of the lattice changes from that of one grain to that of the other. When the orientation change is very small the boundary is sometimes referred to as a sub-boundary structure.

**grain**—an individual crystallite in metals.

**grain boundary**—an interface separating two grains, where the orientation of the lattice changes from that of one grain to that of the other. When the orientation change is very small the boundary is sometimes referred to as a subboundary.

**Guinier-Preston zones**—those regions of a crystal which give rise to Guinier-Preston streaks.

## H

**hardness** — a term used for describing the resistance of a material to plastic deformation under the action of an indenter.

**hardening** — increasing hardness by suitable treatment, usually cold working.

**homogeneous** — a chemical composition and physical state of any physical small portion are the same as those of any other portion.

**hot working** — deformation under conditions that result in re-crystallization.

**intensity (X-rays)**—the energy per unit of time of a beam per unit area perpendicular to the direction of propagation.

## L

**longitudinal plane** — is a plane that is normal to the longitudinal axis.

**longitudinal axis** — that direction parallel to the direction of maximum elongation in a worked material.

## M

**mechanical properties** — The properties of a material that reveal its elastic or inelastic behaviour when force is applied, indicates the suitable mechanical applications.

**macrograph** — a graphic reproduction of a prepared surface of a specimen at a magnification not exceeding 25x.

**macrostructure** — the structure of metals as revealed by macroscopic examination of the etched surface of a polished specimen.

**macrostrain** —the mean strain over any finite gage length of measurement large in comparison with interatomic distances.

**magnification** — the ratio of the length of a line in the image plane to the length of a line on the imaged material.

**Maximum torsional strain** — a cylindrical shaft is said to be subject to pure torsion when the torsion is caused by a couple, applied so that the axis of the couple coincides with the axis of the shaft. The state of stress, at any point in the cross-section of the rod, is one of pure shear, and the strain is such that one cross-section of the shaft moves relative to another.

**microstructure** — the structure of a prepared surface of a metal as revealed by a microscope at a magnification exceeding 25x.

**microstrain**—the strain over a gage length comparable to inter-atomic distances.

**Miller indices (for lattice planes)**—the reciprocals of the fractional intercepts which a plane makes on the three axes. The symbols are  $(hkl)$ .

**monochromator (X-rays)**—a device for producing monochromatic radiation from heterochromatic radiation. It usually consists of a crystal so arranged as to diffract one wavelength of particularly high intensity, such as the characteristic, out of a beam of mixed white and characteristic radiation.

## **N**

**non-fusion** — Is the process where the materials are not liquefied or nor melted, to form a bond, however with heat applied to reduce the energy required to caused plastic deformation.

**Non-metallic inclusions**—particles of impurities (usually oxides, sulfides, silicates and such) that are held mechanically or are formed during solidification or by subsequent reaction within the solid metal

## **O**

**onion-skin flow pattern** — a characteristic weld pattern featuring a cyclic ring or onion skin-like profile.

**oxidation** — the addition of oxygen to a compound. More generally, any reaction involving the loss of electrons from an atom.

## **P**

**plane (crystal)**—an idiomorphic face of a crystal. Any atom containing plane in a crystal.

**plastic deformation** — Is the distortion of material continuously and permanently in any direction. The deformation that remains or will remain permanent after release of the stress that caused it.

**plasticity** — capacity of a metal to deform non-elastically without rupturing.

**polished surface** — a surface that reflects a large proportion of the incident light in a specular manner.

**Poisson's ratio**—the absolute value of the ratio of transverse strain to the corresponding axial strain resulting from uniformly distributed axial stress below the proportional limit of the material.

**principal strains** — the maximum and minimum direct strains in a material, subjected to complex stress are called Principal Strains. These strains act in the directions of the principal stresses.

**principal stresses** — at any point within a stressed material it will be found that there exist three mutually perpendicular planes on each of which the resultant stress is a normal stress (i.e. no shear stresses occur on these planes). These mutually perpendicular planes are called principal planes, and the resultant normal stresses are called Principal Stresses.

**plunge force** — during the plunging stage of the tool pin in FSW, the vertical force in the direction of the Z-axis movement is normally referred to as the plunging force.

**porosity**—holes in a solid, not necessarily connected.

## R

**residual stress**—stress in a body which is at rest and in equilibrium and at uniform temperature in the absence of external and mass forces.

**rolling direction** — refers to the direction in which the billet was rolled during the sheet metal plate manufacture.

## S

**friction** — The force required to cause one body in contact with another to begin to move.

**side-flash** — in FSW, a build-up of weld material, normally on the retreating side of the rotating, which has a 'peal like' effect is termed side-flash.

**solid-phase** — a physically homogeneous and distinct portion of a material system in the solid state.

**spindle speed** — the speed of the work holding device (chuck), measured in revolutions per minute.

**stagnation point** — the point, at or near the nose of a body in motion in a fluid, where the flow divides and where, in a viscous fluid pressure is at a maximum.

**Strain** — strain is a measure of the deformation of a body acted upon by external forces and can be expressed as a change in dimension per unit of original dimension or in the case of shear as a change in angle between two initially perpendicular planes.

**strain amplifier** — the ratio of the voltage supplied to the voltage delivered by the Wheatstone Bridge as a result of the unbalance caused by a change of strain gauge resistance is equivalent to the strain and is amplified into a suitable voltage or current which can be fed into an analogue or digital indicator or graphic recorder.

**stress** — load applied to a piece of material tends to cause deformation which is resisted by internal forces set up within the material which are referred to as stresses. The intensity of the stress is estimated as the force acting on the unit area of the cross-section, namely as Newtons per square meter or Pascals.

**sub-surface** — a location just beneath the surface of a component.

## V

**viscosity** — the resistance of a fluid to shear forces, and hence to flow. Such shear resistance is proportional to the relative velocity between the two surfaces on either side of a layer of fluid, the area in shear, the coefficient of viscosity of the fluid and the reciprocal of the thickness of the layer of fluid.

**void** — the space that exist between particles or grains. Normally in welding voids are associated with defects and incomplete penetration.

## W

**welding** — the process of joining, in which materials are enabled to form metallurgical bonds under the combined action of heat and pressure

**worm holes** — a sub-surface defect in a Friction Stir weld, normally on the advancing side of the rotating tool, due to the lack of mixing and re-bonding of plasticized material.

## Nomenclature

A	- surface area, area of the tool shoulder ( $m^2$ )
D	- the plunge depth over which the load was applied (m)
E	- modulus of Elasticity (MPa)
F	- force (N)
$F_x$	- bending force in the direction of welding (N)
$F_y$	- bending force perpendicular to the direction of welding (N)
$F_z$	- vertical downwards force on the tool (N)
$H_{pin}$	- the tool pin height (m)
L	- length (mm)
$M_{tot}$	- total torque (Nm)
P	- pressure distribution across the interface (Pa)
$P_{av}$	- measured experimentally torque $\times \omega$ (J/s)
Q	- heat (J/mm)
$Q_{total}$	- total heat generation (W)
$R_{probe}$	- tool radius (m)
$R_{shoulder}$	- tool shoulder radius (m)
R	- tool pin radius (m)
T	- torque (Nm)
$T_{solidus}$	- solidus temperature of the substrate (K)
$T_{ambient}$	- room temperature (K)
$T_m$	- melting temperature of the alloy (K)
$T_{max}$	- maximum temperature during welding (K)
$V_{welding}$	- the travel speed (m/s)
X	- distance (m)
c	- specific heat
d	- diameter, plate thickness (m)
f	- feed rate (mm/min)
h	- length of pin (m)
$k_{th}$	- thermal conductivity of the substrate
l	- length (m)
r	- distance from a point on the tool surface to the tool centre (mm)
$r_s$	- radius of the shoulder (mm)
$r_i$	- pin radius (mm)
$r_o$	- shoulder radius (mm)
q	- heat input, heat flux (J/s)
$\dot{q}$	- rate of heat generation (J/s)
$q_0$	- net power ( J/s)
t	- time (s)
v	- velocity, welding speed ( m/s)
$v_{tool}$	- tool velocity that depends on position away from the tool
$v_{material}$	- velocity of the material at the interface (m/s)

$x-X_{\text{tool}}$	- revolutions per minute x coordinate distance from the tool centre (mm)
$x, y, z$	- coordinate, distance (mm)
$y$	- coordinate distance from tool centre (mm)
$\alpha$	- thermal diffusivity
$\eta$	- efficiency factor = 0.9 for Al <sup>1</sup>
$\alpha$	- the tool shoulder cone angle
$\alpha_{\text{yield}}$	- yield strength (Pa)
$\beta$	- empirical constant
$\delta$	- contact state variable
$\epsilon$	- strain
$\xi$	- width of plasticised region
$\theta$	- theta
$\mu$	- coefficient of friction
$\sigma$	- stress (Pa)
$\tau$	- uniform shear stress (Pa)
$\nu$	- Poisson's ratio
$\nu$	- material viscosity
$\omega$	- rotational speed (rad/s)
$\frac{w^2}{f}$	- a pseudo heat index.

## Abbreviations

DF	- defect free
FSW	- friction stir weld
FWHM	- full width at half maximum
HV	- Vickers hardness
LPB	- Low Plasticity Burnishing
OS	- onion-skin defect
PF	- planar facet
rpm	- revolutions per minute
SEM	- Scanning Electron Microscope
SHT	- Severe Heat Treated



## Author's declaration

At no time during the registration for the degree of Doctor of Philosophy has the author been registered for any other University degree..

This study was financed with the financial aid provided by the Faculty of Technology Plymouth University, National Research Foundation of South Africa (NRF) and Nelson Mandela Metropolitan University (South Africa).

Relevant scientific seminars and conferences were regularly attended at which work was often presented; external institutions were visited for consultation purposes and several papers prepared for publication.

### Publications

- (i) N. James, G. R. Bradley, H. Lombard and D. G. Hattingh (2004) The Relationship between Process Mechanisms and Crack Paths in Friction Stir Welded 5083-H321 and 5383-H321 Aluminium Alloys. M. Fatigue & Fracture of Engineering Materials & Structures Volume 28, Issue 1-2, Page 245 - January (2005)
- (ii) MN James, A Steuwer, DG Hattingh, H Lombard (2005) Process and Performance Optimization for Friction Stir Welds Using the Force Footprint and Strain Scanning, ESRF Experimental Report ME 992.
- (iii) H Lombard, PR Brendt, JH Neethling, MN James and DH Hattingh, An investigation of Al-Fe-Mn-Si Precipitates in Al 5083-H321. Electron Microscopy of South Africa conference proceedings (2004)
- (iv) Lombard, H; Hattingh, DG; Steuwer, A and James, MN (2006) Synchrotron Diffraction Residual Strain Scanning in Friction Stir Welds as a Function of Process Conditions, Proceedings of 6<sup>th</sup> International Friction Stir Welding Symposium, Saint-Sauveur Nr Montreal, Canada, 10 - 13 October.
- (iv) Lombard, H; Hattingh, DG; Steuwer, A and James, MN (2006) Relationships among FSW Process Parameters, Defects, Crack Paths and Fatigue Strength in 5083-H321 Aluminium Alloy, Proceedings of International conference of Crack paths, Parma, Italy, 14-16 September.

Presentations and Conferences Attended:

- (i) Optimisation of Friction stir welding using Taguchi as DOE. International Workshop on Friction Stir Welding" 1-3 April (2003)
- (ii) FSW an introduction. Seminar at Nelson Mandela University (2004)
- (iii) Synchrotron Diffraction Residual Strain Scanning in Friction Stir Welds as a Function of Process Conditions EUROMAT 2005, 5-8 September, Prague, Czech Republic
- (iv) Lombard, H; Hattingh, DG; Steuwer, A and James, MN (2006) Relationships among FSW Process Parameters, Defects, Crack Paths and Fatigue Strength in 5083-H321 Aluminium Alloy, International conference of Crack paths, Parma, Italy, 14-16 September.
- (v) Lombard, H; Hattingh, DG; Steuwer, A and James, MN (2006) Synchrotron Diffraction Residual Strain Scanning in Friction Stir Welds as a Function of Process Conditions, Proceedings of 6<sup>th</sup> International Friction Stir Welding Symposium, Saint-Sauveur Nr Montreal, Canada, 10 - 13 October.

External Contacts: Dr A. Steuwer, Dr M. Peel and Dr D. Hughes at the ESRF Grenoble, France

Word count of main body of thesis: 54303

Signed A Lombard

Date 5-06-2007

## Acknowledgements

Completing a thesis is the result of a team effort and not a one man show. I therefore want to acknowledge many people who assisted me in obtaining this qualification.

Firstly, my promoter, Prof Neil M James for giving me multiple opportunities to succeed and enough direction, advice and encouragement to keep me on track. This has been the most exciting, rewarding and interesting project I have ever worked on. I will not forget the discussions we had about engineering.

My greatest thanks also go to my co-promoter, Prof Danie G. Hattingh, for numerous discussions about life and material science. Thank you for the assistance provided in France with obtaining the residual stress data.

Dr Axel Steuwer and Dr Matthew Peel, for peer reviewing my work and the fruitful discussions about synchrotron X-ray radiation. Francois Fauth and Michela Brunelli were the beam-line scientists who assisted in obtaining the synchrotron X-ray data.

Ian Clark, who kindly assisted with sorting out large data files in a format that could be used in a Matlab program.

The following people from the Automotive Components Technology Station (ACTS): A special thanks to Lucinda Lindsay, for organizing all the requirements and bookings for the overseas trips. William Rall, for his systematic approach to CAD and FEA. Zacharias Georgeou, for many enjoyable intense discussions and his ideas about Friction Stir Welding.

The staff at Plymouth University: Terry Richards, for assisting with the metallographic and Vickers hardness measurements. Karen Ley, for always making me feel welcome and at home at Plymouth University.

The staff of the Nelson Mandela Metropolitan University (NMMU), especially Dr Annelize Els-Botes, Gideon Gouws, Tim Tonkin, Mervin Knoesen for all their help and willingness to give that bit extra in the laboratory. Also my colleagues, Gys Kleyn, Zacharias Georgeou, Calvin Blignault, Riekie Slabbert and Waultraud Heitzer who were willing to decrease my workload.

This research was funded by the Faculty of Technology and the National Research Foundation whom I thank for giving me this opportunity.

To my parents, Henry (1937-1999) and Elsa, from whom I was taught the virtues of God, patience, perseverance and respect and most importantly that we have

to make the best of every day and enjoy it to the full. Thank you for the endless support and encouragement that made the road of life easier to follow.  
To my 5 year old daughter, Hannelize, my pride, joy and inspiration.

"I'm just looking to find out more about the world and if it turns out there is a simple law which explain everything, that would be very nice to discover"

Richard P. Feynman

## **Abstract**

### **OPTIMIZED FATIGUE AND FRACTURE PERFORMANCE OF FRICTION STIR WELDED ALUMINIUM PLATE: A STUDY OF THE INTER-RELATIONSHIP BETWEEN PROCESS PARAMETERS, TMAZ, MICROSTRUCTURE, DEFECT POPULATION AND PERFORMANCE**

HANNALIE LOMBARD

Friction stir welding (FSW) is an exciting new solid-state welding process with the potential to advantageously impact many fabrication industries. Current take-up of the process by industry is hindered by lack of knowledge of suitable welding parameters for any particular alloy and sheet thickness. The FSW process parameters are usually chosen empirically and their success is evaluated via simple mechanical property testing. There are severe drawbacks with such methods of determining manufacturing conditions. These include indirect relationships between tensile and fatigue properties, particularly for welds, and a high probability of totally missing real optimized conditions.

This research is therefore undertaken as a first step in providing information that will assist manufacturing industry to make sound decisions with respect to selecting FSW parameters for weldable structural alloys. Some of the key issues driving material selection for manufacturing are weld quality in terms of defects, fatigue strength and crack growth, and fracture toughness. Currently a very limited amount of data exists regarding these mechanical properties of FSW welds, and even less information exists regarding process parameter optimization. This is due to the mechanical microstructural complexity of the process and the relatively large number of process parameters (feed, speed, force and temperature) that could influence weld properties. In order to advance predictive understanding and modeling for FS welds, it is necessary to develop force and energy based models that reflect the underlying nature of the thermo-mechanical processes that the material experiences during welding.

This project aims at determining the influence and effect of Friction Stir Welding process control parameters on the microstructure of the thermo-mechanically affected zone, the defect population in the weld nugget, hardness, residual

stresses, tensile and fatigue performance of 6 mm plate of 5083-H321 aluminium alloy, which is known to be susceptible to planar defect formation<sup>1</sup>. Welds were made with a variety of process parameters (that is feed rate and rotational speed) to create different rates of heat input. Forces on the FSW tool (horizontal and vertical), torque and tool temperature were measured continuously during welding from an instrumented FSW tool.

Detailed information on fatigue performance, residual stress states, microstructure, defect occurrence, energy input and weld process conditions, were investigated using regression models and contour maps which offer a unique opportunity to gain fundamental insight into the process-structure-property relationships for FS welds.

Weld residual strains have been extensively measured using synchrotron X-ray diffraction strain scanning to relate peak residual stresses and the widths of the peak profiles, taken from a single line scan from the mid depth of the FS welds, with the weld process conditions and energy input into the welds. Several residual stress maps were also investigated.

The optical and scanning electron microscope were used to determine the type of intrinsic defects present in the FSW fatigue and tensile specimens. Vickers hardness measurements were taken from the mid depth of the welds and were compared with the weld input parameters.

The main contribution of this thesis is as follow:

- (i) the relationship between input parameters and process parameters;
- (ii) the relationship between input weld parameters (that is feed rate and rotational speed) and process parameters (that is vertical downwards force  $F_z$ , tool temperature, tool torque and the force footprint data), energy input and tensile strength, fatigue life and residual stresses to obtain regions of optimum weld conditions;

---

<sup>1</sup> Dickerson, TL and Przydatek ,J ( 2003)

- (iii) identification of the defects present in FSW, their relationship with process parameters and their effect on tensile strength and fatigue life; and
- (iv) the usefulness of the real time process parameter monitoring automated instrumented FSW tool to predict the mechanical properties of the welds.

# 1. Introduction

## 1.1 History

The process of joining, in which materials are enabled to form metallurgical bonds under the combined action of heat and pressure, is commonly defined as welding<sup>2</sup>. In the never-ending goal of industry to reduce weight and increase performance, different fusion welding techniques have been developed and improved for many years, such as tungsten inert gas, metal inert gas, laser welding, ultrasonic welding, arc welding, plasma welding and friction welding. Most of these techniques require the material to melt and fuse together in order to form the final weld.

The first attempt to use friction heat for solid phase joining was made 100 years ago in the United States of America, followed by a technique developed in Britain referred to as friction surfacing, 50 years later<sup>3,4</sup>. Friction stir welding (FSW), invented by TWI (The Welding Institute in the UK) in 1991, is a solid state joining technique. FSW therefore requires less energy and has better joint quality properties, making it a suitable method for joining aluminum alloys of the 2xxx and 7xxx grades that could not previously be joined by fusion techniques<sup>5</sup> without resulting in cracks, voids, hydrogen embrittlement or distortion. TWI successfully filed for patents in Europe, the USA, Japan and Australia.

## 1.2 Industrial advantages and application areas

Aluminum alloys are used in many structural applications today where their combination of high strength and low weight are attractive. In the past few years significant effort has been applied to putting FSW to use in full-scale production in shipbuilding, the aerospace industry and the automotive sector. However, the limited availability of scientific information; the lack of understanding of the process;

---

<sup>2</sup> Messler, RW (1999)

<sup>3</sup> Bevington, J (1891)

<sup>4</sup> Klopstock, H and Neelands, AR (1941)

<sup>5</sup> Easterling, K (1992)



FSW has been used for the manufacture of different types of weld joint configurations, such as butt welds, overlap welds, T-sections, fillet, and corner welds. Longitudinal butt welds and circumferential lap welds of Al alloy fuel tanks for space flights have been friction stir welded and successfully tested<sup>1</sup>. The FSW process can also be utilized for circumferential, annular, non-linear, and three-dimensional welds.

### 1.2.1 Shipbuilding and marine industries

The shipbuilding and marine industries are two of the first industry sectors that have adopted the process for commercial applications. The process is suitable for joining panels for decks and floors, aluminum extrusions, hulls and superstructures, helicopter platforms, offshore accommodation, marine and transport structures, masts and booms for sailing boats and refrigeration plants.

### 1.2.3 Aerospace industry

In the aerospace industry, Boeing uses FSW to weld the propellant tanks for the Delta II, III and IV launch vehicles, as well as non-structural parts for its civil aircraft<sup>2</sup>. The use of FSW in complex parts requiring curvilinear paths has been successfully demonstrated by Boeing for use in complex landing gear door and FSW sandwich assemblies for a fighter aircraft fairing<sup>3,4</sup>. NASA has successfully welded the external fuel tanks for the Space Shuttle program and Eclipse Aviation has completely constructed the first FSW aircraft by August 2002, using FSW to replace the rivets commonly found in aircraft construction<sup>5</sup>. Mechanical testing performed by Eclipse has shown that FS welding produces joints with more than twice the strength of a single-row riveted joint. Fatigue life of the welds also equals riveted joints for the Eclipse 500 alloys and stress levels. The friction stir welding process can also be considered for wings, fuselages, empennages, cryogenic fuel tanks for space vehicles, aviation fuel tanks, external disposable tanks for military aircraft, military and scientific rockets and the repair of faulty MIG welds<sup>6</sup>.

---

<sup>1</sup> [http://www.twi.co.uk/j32k/unprotected/band\\_1/fswjoint.html](http://www.twi.co.uk/j32k/unprotected/band_1/fswjoint.html)

<sup>2</sup> Nicolas, ED and Kallee, SW (2000)

<sup>3</sup> Technology Transfer Dept (2001)

<sup>4</sup> Heston, T (2002)

<sup>5</sup> Hansen, M (2003)

<sup>6</sup> Threadgill, PL and Nunn, ME (2003)

#### 1.2.4 Railway industry

Details of the commercial production of high speed trains made from aluminum extrusions joined by friction stir welding have been published in open literature<sup>1</sup>. Applications include high speed trains, underground carriages, railway tankers and container bodies.

#### 1.2.5 Land transportation

The friction stir welding process is currently being experimentally assessed by several automotive companies and by suppliers to this industrial sector in terms of its commercial application. Developments in the automotive industry have been made by Mazda, where FSW is used in the new RX-7 model, Ford has also begun production of FSW to join panels<sup>1</sup>. In Sweden, car seat frames are being welded using dual FSW weld heads<sup>2</sup>. The use of aluminium is on the increase in the automotive industry, especially in engines, drive trains, heat exchangers, wheels and bumper reinforcements. This has led to investigations into FSW techniques to replace the conventional welding processes for joining aluminium alloys.

A Group Sponsored Project by the Edison Welding Institute (EWI) and TWI is investigating joint designs for lightweight automotive structures. Other potential applications include engine and chassis cradles, wheel rims, attachments to hydroformed tubes, tailored blanks, truck bodies, tail lifts for trucks, mobile cranes, armour plate vehicles, fuel tankers, caravans, buses, airfield transportation vehicles, frames and personnel bridges.

#### 1.2.6 Other industry sectors

The use of portable FSW equipment is now possible for fabricating aluminium bridges; facade panels made from aluminum, copper or titanium; window frames; aluminum pipelines; aluminum reactors for power plants and the chemical industry; heat exchangers; air conditioners; and pipe fabrication. The electrical industry shows increasing interest in the application of friction stir welding for electric motor housings, busbars, electrical connectors, and encapsulation of electronics. Friction stir welding can also be considered suitable for refrigeration panels, cooking

---

<sup>1</sup> Mortimer, J (2005)

<sup>2</sup> Kohstall, P(1999)

equipment, white goods, gas tanks and gas cylinders, joining aluminum or copper coils in rolling mills and various items of furniture.

### 1.3. The work described in this thesis

The motivation for the research outlined in this thesis is the need to understand the interrelationship between the process parameters and mechanical properties of FS welds. Knowledge of these interrelations is required to develop process maps that could be used to predict optimized weld conditions to produce high fatigue strength. Semi-empirical predictive models could hence eliminate the empiricism in the techniques usually implemented by industry to determine the manufacturing conditions required to give sound welds. Currently, FSW process parameters are chosen empirically and their success is evaluated via simple mechanical property testing. There are severe drawbacks with such methods of determining appropriate manufacturing conditions. These include the existence of indirect relationships between tensile and fatigue properties, particularly for welds, and a high probability of totally missing peak optimized welding conditions.

In relation to FSW, Record et al<sup>1</sup> were the first to attempt a statistical approach to characterizing and model the FSW process. 7075-T7351 aluminium alloy FS welds with a thickness of 9.53 mm were made in this investigation. Their investigations indicated that feed rate, rotational speed and plunge depth are the most important process parameters. The distance between the welds and the side of the plate influenced the vertical force on the tool. No work was done on relating the mechanical properties to the process or input parameters. Most researchers have related the mechanical properties to input parameters such as feed rate, rotational speed and the ratio of feed rate/rotational speed (referred to as pitch) and not to process parameters, such as tool temperature and forces acting on the tool.

This project has several linked aims. The first aim is to evaluate the interrelationship of process parameters and their correlation with several energy models. Secondly it aims to determine the influence and effect of friction stir welding (FSW) process-control parameters on the microstructure of the thermo-

---

<sup>1</sup> Record et al (2004)

mechanically affected zone and on the defect population in the weld nugget. Thirdly, it seeks to clarify the residual stress state in friction stir butt welds in 5083 alloy as a function of varying process parameters. This information is essential to advance our ability in predicting optimized process conditions for FSW joints, through the other aims of linking the residual stress state with the characteristic 'force footprint' obtained during welding and of correlating these aspects with process parameters and the dynamic fatigue performance of the welded joints.

The work described in this thesis used butt welds in 5083-H321 Al plate, which is known to be susceptible to intrinsic FSW defects<sup>1</sup>. The relationships between welding conditions, such as rotational tool speed and feed rate for a specific set of pitch values (defined as the ratio of feed rate / tool rotational speed) are related to static and dynamic mechanical properties, i.e. tensile, fatigue performance, hardness, heat input and residual stress. In order to examine the effects of process parameters on weld properties, metallographic macrographs and fractographs are compared with tensile strength and with fatigue performance. The force footprint is also investigated in detail, to assess its influence on residual stress, fatigue and tensile strength.

The techniques and data discussed in this thesis allow prediction of weld conditions for optimum joint performance. This represents a significant improvement in understanding and modeling of the process-structure-performance relationships of FSW butt joints in 5083-H321 aluminium alloy plate.

This dissertation is divided as follows:

Chapter two contains a literature review of FSW. Emphasis is placed on the influence of FSW process parameters on the mechanical properties. Reference is also made to the specific microstructures and energy input to the welds.

Chapter three introduces general aspects of experimental design. It also presents the specific experimental setup, instrumentation and experimental matrix used in

---

<sup>1</sup> James, MN and Hattingh, DG (2002)

Chapter two contains a literature review of FSW. Emphasis is placed on the influence of FSW process parameters on the mechanical properties. Reference is also made to the specific microstructures and energy input to the welds.

Chapter three introduces general aspects of experimental design. It also presents the specific experimental setup, instrumentation and experimental matrix used in the investigation. These have been chosen to elucidate the interrelationship between the parameters, as well as the relationship between energy models and process parameters. The force foot print is also introduced, described in detail, and its output compared with energy models.

The first section of Chapter 4 presents the general properties of Al 5083-H321, while the second part of this chapter illustrates the macroscopic metallographic aspects of the welds, such as nugget features and defects. Their relationship with feed rate, rotational speed and pitch is also discussed. Mechanical properties such as tensile strength, 0.2% proof stress, Vickers hardness and defect population are also investigated and related to these process parameters.

Chapter five contains an explanation of synchrotron X-ray diffraction strain scanning as well as the experimental setup for the synchrotron X-ray diffraction measurements. The distribution of the residual strain and stresses in a number of welds made with different process parameters are reported and their trends examined as a function of feed rate, rotational speed and pitch. The force footprint data is also related to residual stress in FSW.

The fatigue investigations are presented in Chapter 6. Information regarding fatigue testing is presented and this is followed by an analysis of the relationship between fatigue life, discussed intrinsic defects at fatigue initiation sites, and process parameters. The process maps of tensile strength and residual stress are also related to fatigue performance.

In the last chapter of this thesis, Chapter 7, recommendations for further study are proposed.

## 2. Overview of the FSW process

### 2.1 Introduction

Friction stir welding (FSW), patented in December 1991 by The Welding Institute TWI at Cambridge in the United Kingdom<sup>1</sup>, is the most remarkable welding technology developed in the last decade. Friction stir welding (FSW) is a multiple input-output process and can be regarded as a continuous thermo-mechanical-fluid-solid-state, forging and extrusion joining technique<sup>2,3,4,5</sup>. Several advantages can be mentioned: the risk of producing porosity, hot cracks, inclusions, high residual stresses<sup>6</sup>, low fatigue strength<sup>7</sup>, and distortions are minimized, due to the low welding temperature relative to the alloy melting point<sup>8</sup>. The crushing, stirring and forging action of the FSW tool produces a weld with a finer microstructure than the parent material, providing butt and lap joints with excellent mechanical properties<sup>9,10</sup>. FSW is well adapted to making high quality welds in wrought aluminum alloys in the 2xxx, 5xxx, 6xxx and 7xxx series, Mg and Ti alloys, Fe alloys and thermo plastics. It can also join dissimilar metals, such as Al6013-Al2024<sup>11</sup>, Al 6061-Cu<sup>12</sup>, Al-steel<sup>13</sup>, Cu-steel, Al-Be and Al-Mg<sup>14</sup> for thicknesses from 0.6 to 40 mm for single sided welds and 75 mm for double sided welds<sup>15,16</sup>. Good weld quality and repeatability can be obtained because the welding procedure is automated<sup>1</sup>. Less distortion or shrinkage occurs in FSW compared to conventional fusion weld technology<sup>17</sup>. The power used to perform FSW is approximately in the range of 3 – 7 kW and is less than metal inert-gas (MIG) or laser welding. The fatigue strength at  $10^7$  cycles is reported to be higher than that found with either laser, MIG or tungsten inert-gas (TIG) welds<sup>18</sup>.

---

<sup>1</sup> Thomas, WM et al (1991)

<sup>2</sup> Thomas, WM (1999)

<sup>3</sup> Chao, YJ and Qi, X (1999)

<sup>4</sup> Reynolds, AP et al (1999)

<sup>5</sup> Chen, C and Kovacevic, R (2003)

<sup>6</sup> James, MN et al (2005)

<sup>7</sup> Lomolino, S et al (2004)

<sup>8</sup> Thomas, WM and Andrews, RE (1991)

<sup>9</sup> Stewart, WW (2001)

<sup>10</sup> Midling, OT et al (1998)

<sup>11</sup> Dalle Donne, C and Raimbeaux, G(2001)

<sup>12</sup> Dalle Donne, C and Raimbeaux, G(2001)

<sup>13</sup> Uzun, H et al (2005)

<sup>14</sup> Sato, YS et al (2004)

<sup>15</sup> Shinoda, T et al (2001)

<sup>16</sup> Nicholas, ED and Kallee, SW (2000)

<sup>17</sup> Thomas, WM et al (1999)

<sup>18</sup> Hori, H et al (1999)

The process is also environmentally friendly, as hazards such as welding fumes, radiation, high voltage, liquid metals, arc glare and spatter are not generated. No pre-weld dressing, filler metal or gas shielding are required, except to protect the tool from high temperature oxidation when welding high melting point materials such as titanium and steel<sup>19</sup>. This innovative new welding method has captured the attention of all industries in Europe as a solid-phase joining technique capable of producing good quality single sided and double sided butt, 'T', and lap joints. Use of FSW enables cost savings, lighter structures and increased fatigue strength from welded joints<sup>20</sup>. The first industrial application of FSW was reportedly to join hollow aluminium panels for deep freezing fish on fishing boats<sup>21</sup>. The combination of advantageous features found in FSW means that it is now widely used in welding long lengths of material in the aircraft, aerospace, marine shipbuilding (Al-5083) and railway industries. In the automotive industry FSW is increasingly replacing fusion welding in the production of light alloy wheels, tailored blanks and suspension parts<sup>22</sup>. Complex curved shapes can now also be welded<sup>23</sup>. A few potential disadvantages of the FSW process can, however, be mentioned:

- (i) Welding speeds are slower than some fusion techniques, particularly for thinner materials.
- (ii) A well designed clamping mechanism is necessary to ensure that the tool does not cause separation of the two plates during welding.
- (iii) A backing bar is required to oppose the downward force of approximately 20 – 25 kN.
- (iv) A keyhole is left after tool removal from the weld, but this can be post-weld mended by using a retractable tool pin where the pin can slowly be retracted up into the shoulder while re-welding at lesser depths until the keyhole is closed<sup>24</sup>.
- (v) Tools with different pin lengths are required when welding materials with different thicknesses in order to avoid root defects.
- (vi) FSW shows some asymmetry in the weld, due to tool rotation which could lead to defects such as intrinsic voids, worm holes or surface breaking grooves that usually run along the region of the weld where the direction of

---

<sup>19</sup> <http://www.twi.co.uk>

<sup>20</sup> Pedwell, R et al (1999)

<sup>21</sup> Benson, PG and Backland, J (2000)

<sup>22</sup> Nicholas, ED and Kallee, SW (2000)

<sup>23</sup> Arbegast, WJ and Allen, CD (2004)

<sup>24</sup> Threadgill, PL and Nunn, ME (2003)

welding and tool rotation is the same<sup>1</sup>. This process asymmetry causes a differential pressure around the pin such that the rotating tool tries to veer away from the retreating side of the weld towards the advancing side<sup>2</sup>.

As friction stir welding becomes better established, it may replace plasma arc welding and electron beam welding in some applications using Al and Ti alloys respectively<sup>3</sup>. This chapter discusses the basic principles of FSW and describe the main process parameters that can be monitored on the FSW machine built at the Nelson Mandela Metropolitan University. A literature review of the effects of the process parameters on weld mechanical properties will then be presented.

## 2.2 Description of the FSW process

A factor characterization diagram, illustrating the main parameters that need to be considered during friction stir welding, can be seen in Figure 2.1.

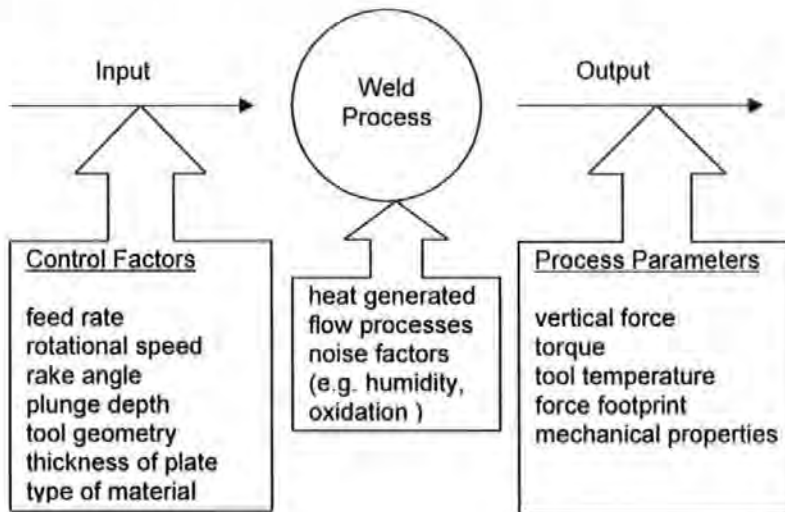


Figure 2.1: Important parameters of FSW.

Since FSW is by its nature asymmetrical, two different conditions can be distinguished in friction stir welds, namely the advancing side of the weld, where the rotational velocity of the tool has the same direction as the welding velocity

<sup>1</sup> Johnson, R (2001)

<sup>2</sup> Thomas, WM et al (1999)

<sup>3</sup> Mendez, PF(2000)



and the retreating side, where the reverse occurs<sup>1</sup>. Figure 2.2 illustrates the terminology used in this welding method.

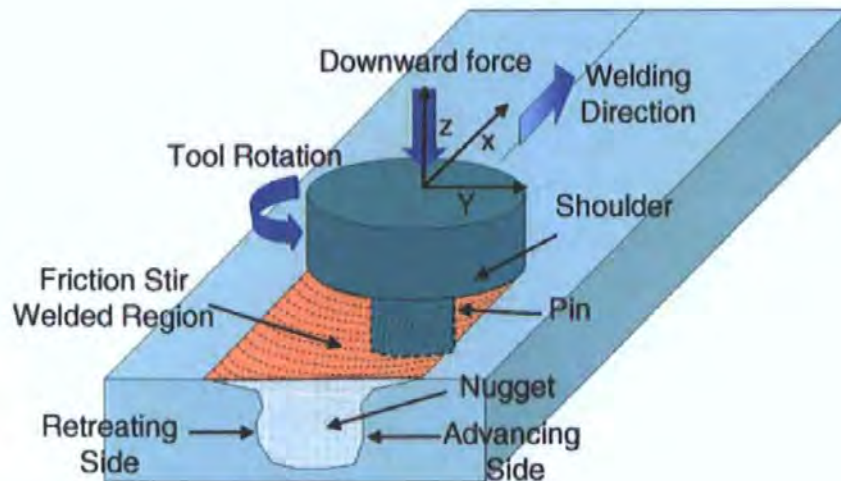


Figure 2.2: Features of friction stir welding<sup>2</sup>.

The weld track produced by the shoulder of the tool displays a characteristic onion skin pattern. Typically the surface appearance of FSW is a regular series of part circular ripples, which convexes towards the start of the weld<sup>1</sup>.

The FSW process consists of six main steps:

- (i) moving the tool to just contact the surface of the plate (A);
- (ii) plunging the tool pin into the joint line (B);
- (iii) shoulder makes full contact with the plate (C);
- (iv) a dwell period (D);
- (v) then tool traverse along the weld (E); and
- (vi) finally, extraction of the tool (F).

Figure 2.3 demonstrates the variation observed in several weld parameters with respect to time. The five different stages (A, B, C, D, E and F) are separated by vertical lines drawn on the graphs.

During the first stage (A)<sup>3</sup> the FSW machine bed moves vertically towards the tool to enable the pin to come into contact with the top surface of the base material.

<sup>1</sup> Thomas, WM (1999)

<sup>2</sup> Mishra, RA and Ma, ZY (2005)

<sup>3</sup> Hattingh, DG et al (2004)

The machine use vertical force feedback to detect the surface of the alloy in order to obtain a reference point for the plunge depth. The tool temperature, normal force ( $F_z$ ) and tool torque are all low during this stage as there is little contact between the tool and the alloy.

Stage two (B)<sup>1</sup> represents the plunging period during which the tool pin is inserted into the alloy until the shoulder just makes intimate contact with the surface of the plate. A pre-set small vertical force is applied to the tool which leads to an increase in spindle torque and tool temperature. As the temperature of the alloy increases, the flow stress of the material decreases and the vertical force and pressure exerted consequently decrease slightly.

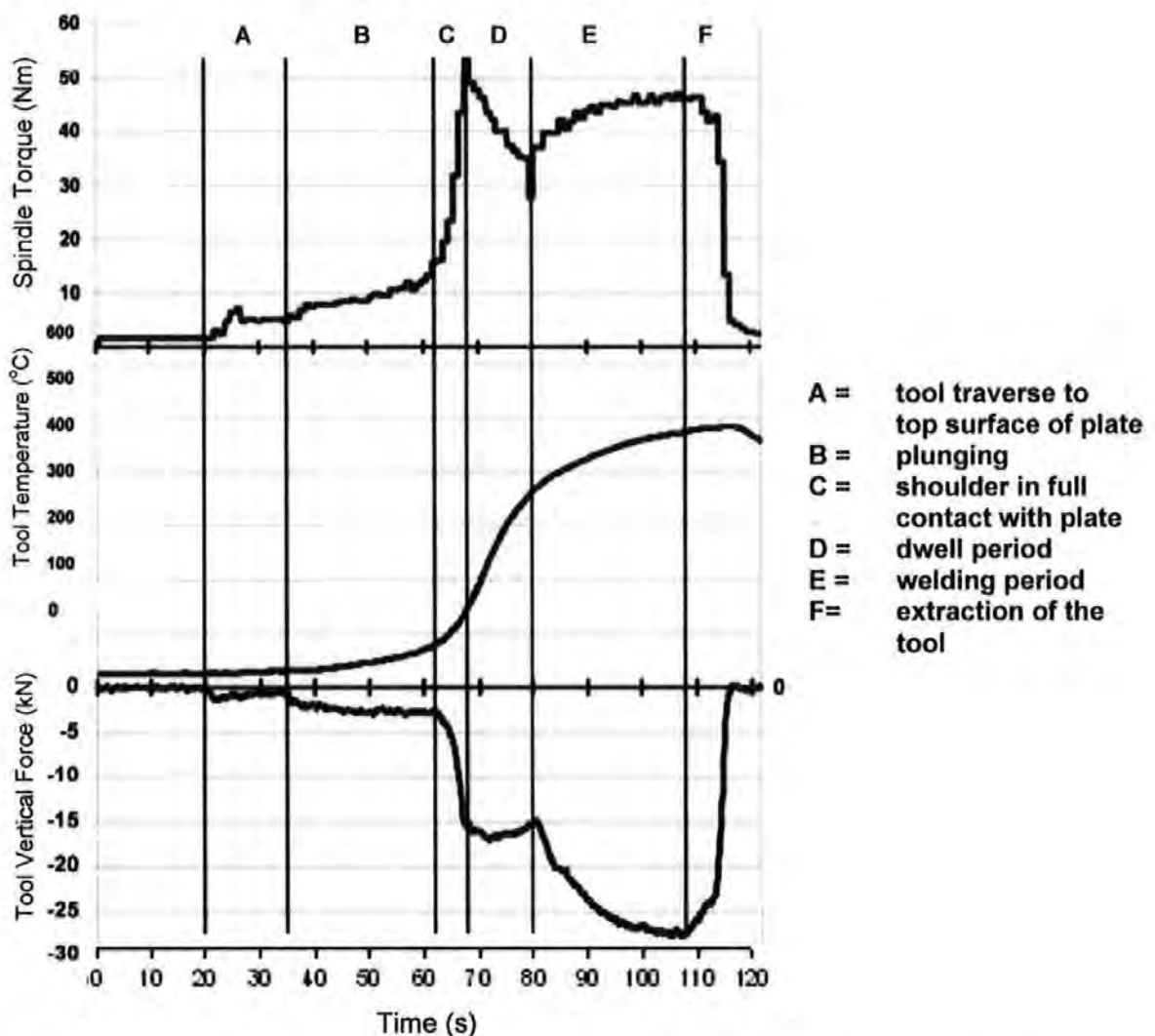


Figure 2.3: Variation of input and process parameters with respect to time for welds made with the instrumental FSW at NMMU<sup>1</sup>.

<sup>1</sup> Hattingh, DG et al (2004)

Stage three (C)<sup>1</sup> is the period in which the tool shoulder makes full contact with the alloy to a pre-determined depth (around 0.2 mm) and hence supplies the frictional heat necessary to plasticize the material. The tool temperature, downwards force and spindle torque increase sharply during this stage.

Dwell time is allowed at the start of the weld to allow the material around the FSW tool to become sufficiently plasticized, to allow welding to commence, with the duration usually determined from empirical experience. This dwell time period represents stage four (D) of the process. The temperature of the metal rises rapidly while the spindle torque decreases as the flow stress of the alloy decreases. If the dwell time is too short the plasticized state is insufficient and welding could lead to tool seizure or fracture due to large forces exerted on the tool<sup>1</sup>.

The fifth stage (E)<sup>1</sup> represents the period during which the weld is made. All the process parameters tend to a pseudo-steady state. This plastic deformation process implies that there is a minimum required contact time for good weld formation. Heat is generated by friction between the translating-rotating tool shoulder and pin and the metal. The softened metal is extruded from the advancing side of the tool to the retreating side and comes into contact with metal swept from the retreating side; both layers having different thermal histories implying that strain partitioning could occur during fatigue testing<sup>2</sup>.

A characteristic onion skin structure is often formed in the weld nugget as a consequence of the way that the profiled pin moves extruded material from the leading to trailing edge of the tool during each revolution. A downward flow of the metal is also induced if there are helical threads on the rotating pin<sup>3</sup>. The trailing edge of the shoulder forges and consolidates the extruded material.

The final stage of the weld process reflects the time during which the tool is being withdrawn from the base material to leave a keyhole at the end of the weld. FSW is an autogenous solid-state process which enables the retention of parent plate chemistry and gives a uniform distribution of hardening particles in the matrix<sup>4,5</sup>.

---

<sup>1</sup> Hattingh, DG et al (2004)

<sup>2</sup> James, MN et al (2003)

<sup>3</sup> Ulliyse, P (2002)

<sup>4</sup> Sato, YS et al (2001a)

<sup>5</sup> Hayashi, M and Oyama, K(2001)

Monitoring of this type of data during welding may assist in understanding and predicting suitable weld conditions as a function of alloy, plate thickness and property requirements of the joint. This will reduce the current empiricism in the choice of FSW process parameters. A limited amount of research has been conducted to determine the influence of input parameters, such as tool rotational speed and feed rate, on process parameters and weld performance. This thesis investigates whether the resultant force of the polar plot obtained<sup>1</sup>, from the bending forces acting on the tool, can be used to define an indicator of optimum weld conditions. Further investigations will also be done to determine the influence of process parameters on microstructure, hardness, tensile properties, residual stresses and fatigue strength. In the rest of this chapter an overview of the nomenclature and parameters used to describe FSW is presented. It also discusses the microstructure and mechanical properties of the welds, with specific reference to the influence of input and process parameters on FSW properties. The intention is to illustrate the importance of process parameters and their interrelationship to achieve a sound weld with high performance.

## 2.3 FSW parameters

### 2.3.1 Tool feed rate and rotational speed

In principle the optimization of FSW is non-complex as described by Thomas:

*" For a given tool shape and tool inclination, the process only involves, rotational speed and travel rate, which enables the FSW process to be easily optimized" <sup>2</sup>.*

The feed rate and rotational speed can easily be controlled and vary only slightly during the pseudo-steady state region in FSW<sup>3</sup>. The choice of feed rate and rotational speed should be tailored to the thickness of plate to be welded and will alter the forces, plasticized width (or width of the thermo-mechanically affected zone TMAZ), heat input and the banded structure of the onion rings<sup>2,4</sup>. The choice of the feed rate and rotational speed is crucial to provide enough generation of heat in order to create good flow of the material around the tool while minimizing the forces on the tool. The ratio of feed rate to rotational speed is usually reduced

---

<sup>1</sup> Hattingh, DG (2004)

<sup>2</sup> Thomas, WM (1999)

<sup>3</sup> Loftus, Z et al (1999)

<sup>4</sup> North, TH et al (2000)

to a single parameter referred to as pitch. The properties of the welds are usually related to pitch, which is believed to be an important parameter in FSW<sup>1,2</sup>. Studies by Seidel and Reynolds<sup>2</sup> on AA 5454-H32 plates revealed that the amount of vertical flow of material in the weld on the retreating side is inversely proportional to the pitch and also to the peak temperature at which the welds are made. The problem with optimizing the FSW process for any particular tool geometry, alloy and plate thickness lies with the empirical nature of optimizing the tool feed rate and rotational speed. These are chosen through observation of the weld quality and after mechanical property testing of sample welds. It is therefore difficult to extrapolate data to different situations or to know *a priori* which tool parameters should be altered to give optimum geometry and process conditions. For example, TWI has compiled an empirical relationship shown in equation 2.1 that may be used as an indication of the feed rate to apply to a particular thickness of material for certain tool geometry on a specific material type<sup>3</sup>.

$$\text{Feed rate} = \text{material factor} (\text{Tool factor} / \text{thickness}) \quad \dots(2.1)$$

Typical material factors for various alloys are:

- (i) Lead = 3700;
- (ii) Magnesium = 400;
- (iii) Copper = 300;
- (iv) Titanium = 100;
- (v) Aluminum 6xxx = 1200;
- (vi) Aluminum 5xxx = 700; and
- (vii) Aluminum 7xxx and 2xxx = 600.

Tool designs with no special pin and shoulder profiles have tool factors equal to one, while for tool designs containing flutes or other more complicated profiles, a tool factor of two is used. Equation 2.1 was derived for specific tool designs and should actually only be applied to the tools designed by TWI. Calculations based on equation 2.1 reveal that for 6 mm thick Al 5083-H321 the possible feed rates that could be used for the two types of tools lie in the range of 117 to 233 mm/min. For this study a profiled tool design containing a scalloped pin is used. Applying equation 2.1 indicates that a feed rate of 233 mm/min should be used.

<sup>1</sup> Hashimoto, T et al (1999)

<sup>2</sup> Seidel, TU and Reynolds, AP (2001)

<sup>3</sup> Kallee, SW et al (1998)

Unfortunately the FSW machine was limited to a maximum feed rate of 200 mm/min at the time of this investigation.

This illustrates another problem of such an empirical approach, where the nominal parameters are unattainable in practice. In order to advance predictive understanding and modeling for FS welds, it is necessary to develop force and energy based models which reflect the underlying nature of the thermo-mechanical processes that the material experiences during welding. This describes the fundamental intent of this thesis, which seeks to link force and energy data acquired from an instrumented FSW tool to the metallurgical processes occurring in the weld and the consequent mechanical properties and fatigue performance.

As the pin rotates, friction heats the surrounding material and rapidly produces a softened 'plasticized' region around the pin, defined as the third body region, illustrated in Figure 2.4.

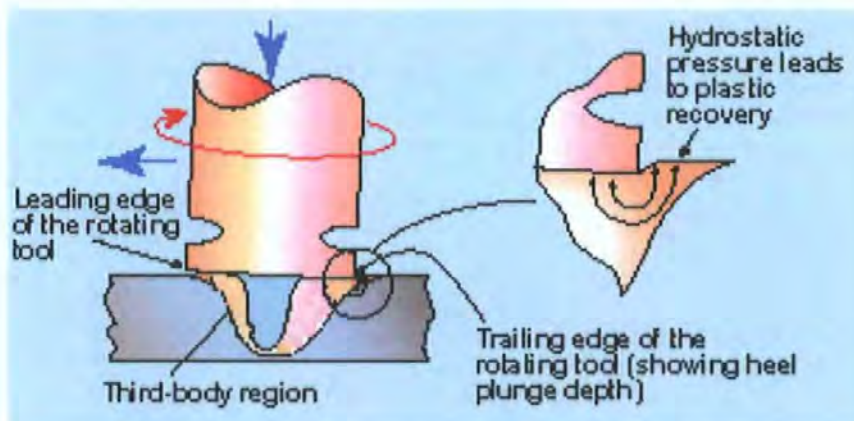


Figure 2.4: The third body region formed around the tool<sup>1</sup>.

Properties of the plasticized third body region that comprises side flash, onion ring flow pattern and plasticized material flow can be controlled by adjusting mainly feed rate and rotational speed<sup>2</sup>. In order to increase weld quality and reduce defects in the welds the relationship between viscosity and process parameters is important. The width of the plasticized region ( $\xi$ ), formed ahead of the moving pin, can be determined from the following relation<sup>2</sup>:

<sup>1</sup> Thomas, WM (1999)  
<sup>2</sup> North, TH et al (2000)

$$\xi = u\beta\alpha\omega \left( \frac{R\omega}{V_{\text{welding}}} \right) \left( \frac{R}{k_{\text{th}}(T_{\text{solidus}} - T_{\text{ambient}})} \right) \quad \dots(2.2)$$

where

R = tool radius

u = material viscosity

$\alpha$  = thermal diffusivity

$\omega$  = angular velocity of the tool

$V_{\text{welding}}$  = the travel speed

$T_{\text{solidus}}$  = solidus temperature of the substrate

$T_{\text{ambient}}$  = room temperature

$k_{\text{th}}$  = thermal conductivity of the substrate

$\beta$  = empirical constant

Equation 2.2 shows that the width of the plasticized region formed ahead of the traversing tool is inversely proportional to the travel speed and is also dependent on the amount of preheat available prior to the FSW. This width also depends on the ratio of the square of the tool rotational speed as well as the thermal conductivity of the aluminum alloy base material. The plasticized width is therefore related to energy input. Thus the parameters that govern the plasticized width should also correlate with energy input and mechanical properties of the welds. These relationships will be investigated in this thesis as described in Chapter 3. The flow dynamics around the tool should also be affected by the width of the plasticized region. It is, however, very difficult to accurately quantify the flow dynamics around the tool and this will not be part of this thesis.

### 2.3.2 Torque

Results by Johnson<sup>1</sup> showed that torque is governed more by the diameter of the tool shoulder than the pin diameter. The torque on the tool is dependent upon the rotational speed of the tool and is almost constant at a particular feed rate, as shown in Figure 2.5. Figure 2.5 indicates that torque decreases with increasing rotational speed but shows a weak correlation with feed rate. Torque values differ when welding different materials<sup>1</sup>.

---

<sup>1</sup>Johnson, R (2001)

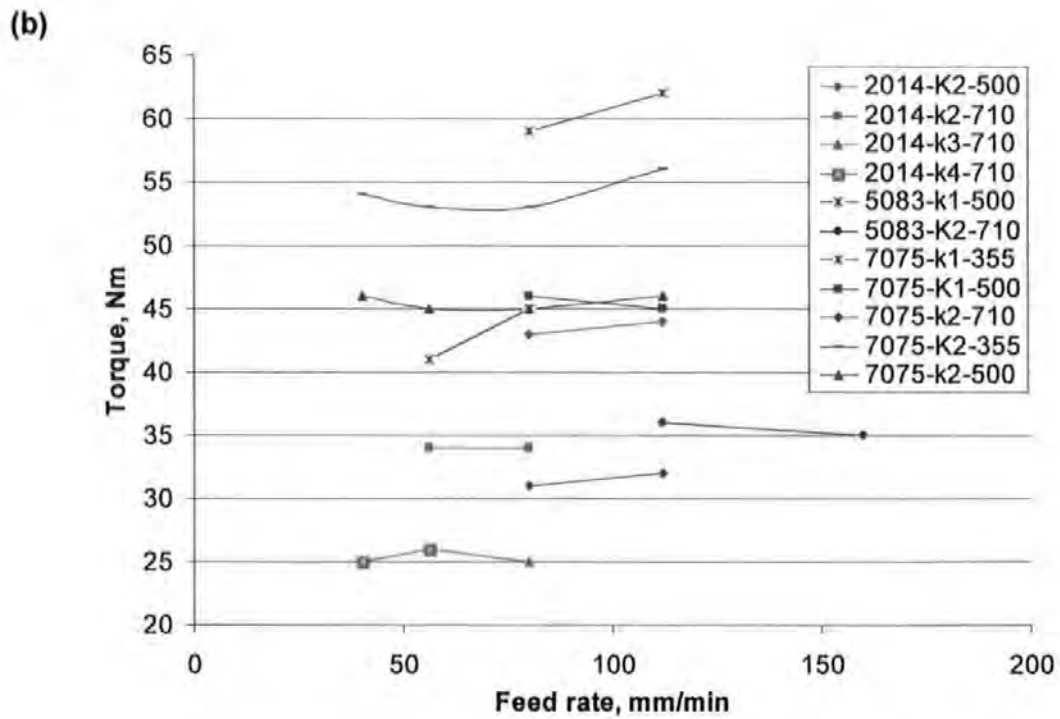
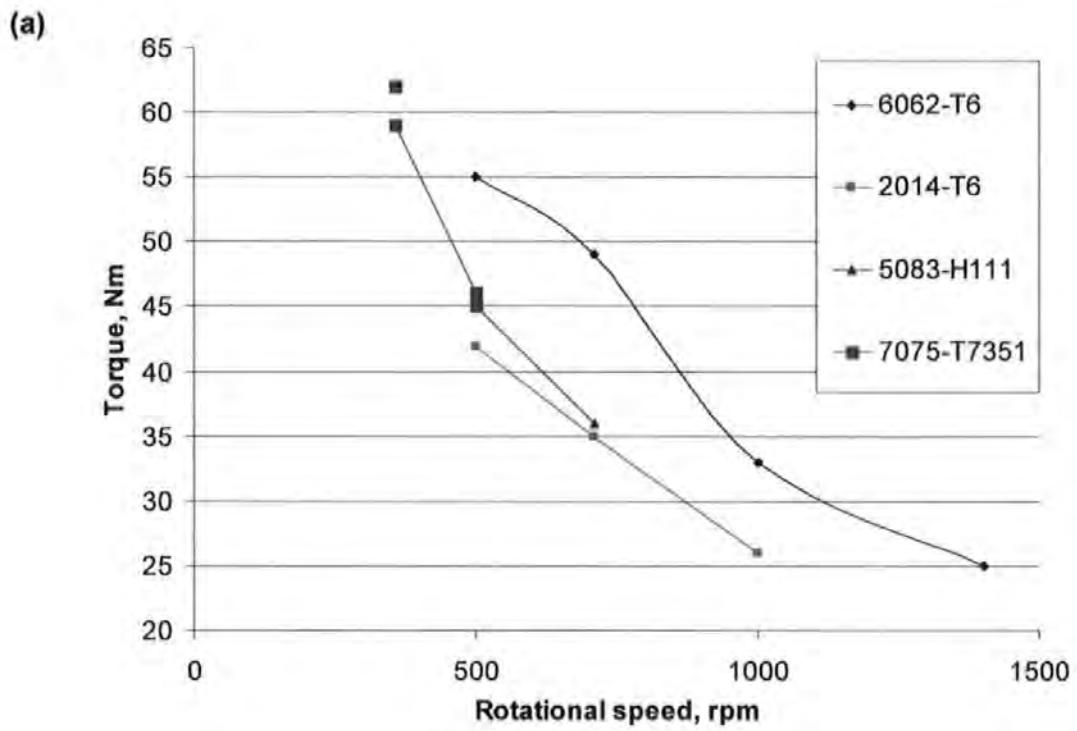


Figure 2.5: Variation of torque with (a) rotational speed (b) feed rate<sup>1</sup>.

<sup>1</sup> Johnson, R (2001)



The only results available for Al 5083-H321 under position controlled FS welding are given by Blignault<sup>1</sup> and indicate that the highest spindle torques are obtained at high feed rates and low tool rotational speeds. At increased tool speeds increasing feed rate has less of an influence on spindle torque, as illustrated in Figure 2.6.

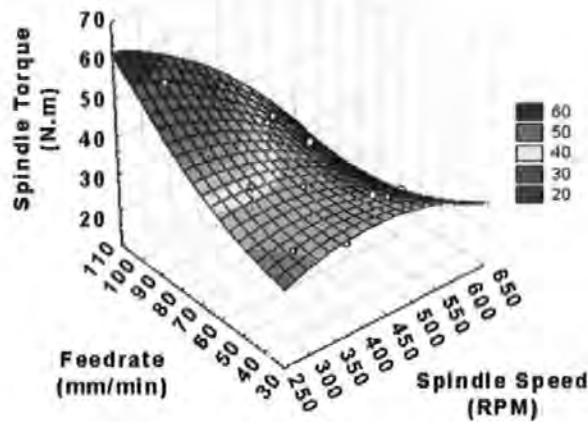


Figure 2.6: Surface plot relating spindle speed, feed rate and spindle torque in FSW of 5083-H321 alloy<sup>1</sup>.

For this thesis the torque per revolution of the tool was monitored and used to determine the heat input into the weld as discussed in Chapter 3. The spindle motor torque measurements are not included in this investigation, since the parameters on the tool were measured during welding. The interrelationships among tool torque, rotational speed and feed rate will also be investigated over a wider range of values, for example between 250 - 900 rpm and 85 - 185 mm/min.

### 2.3.3 Tool rake (tilt angle)

The forwards rake angle of the tool pin (illustrated in Figure 2.7) affects the two material flow patterns present in a weld, namely the flow around the pin and the flow under the shoulder. Research by Shinoda<sup>2</sup> indicated that the rake angle affected the intersection of these two flows, and resulted in stagnant material flow at the bottom of the weld when using a 0° tool tilt, which could lead to weld defects. Increasing the rake angle moved the stagnant point upwards, thereby tending to remove defects as shown in Figure 2.8.

<sup>1</sup>Blignault, C (2002)

<sup>2</sup>Shinoda, T (2001)

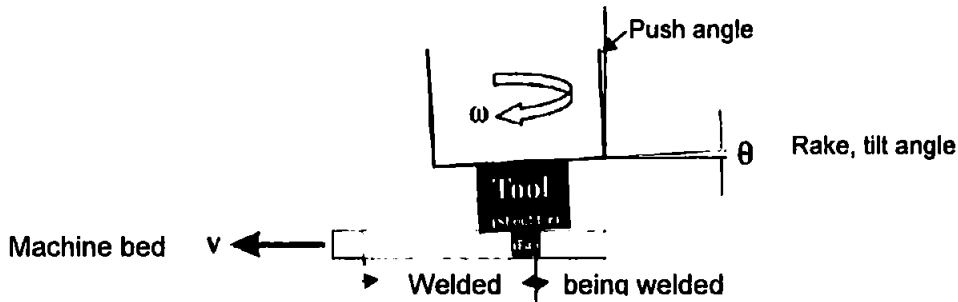
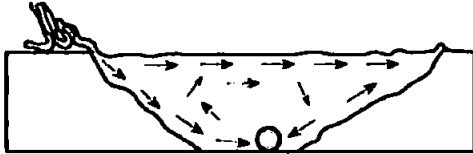


Figure 2.7: Definition of tool push, rake and tilt angle. The rake, tilt and push angle are equal in size<sup>1,4</sup>.

a) Push angle of stir rod :  $0^{\circ}$



b) Push angle :  $1.5^{\circ}$

Stagnant point of metal flow



c) Push angle :  $3.0^{\circ}$

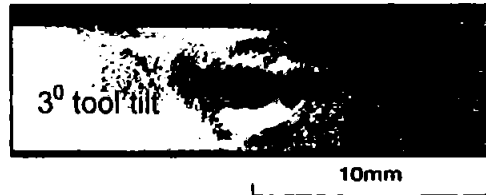


Figure 2.8: Effect of rake angle on flow of material for 1100 and 5005 aluminium alloys<sup>1</sup>.

The rake angle has an effect on flow patterns and on the formation of the onion ring structure in the weld nugget. Tilting the tool head by 1-5 degrees establishes sufficient downwards pressure and moves the stagnant point upwards enough to create a weld without defects. As tool tilt angle increases, however, the contact area between the shoulder and the alloy decreases, thus lowering the efficiency of the process since less heat will be generated by friction between the tool shoulder and the material being welded. A tilted tool also limits the feed rate that can be used because the tool may lift out of the material at high feed rates<sup>2</sup>. Large tilt angles increase back flash and vertical force on the tool<sup>3</sup>. Results by Chen and Maginess<sup>4</sup> indicate that an increase in tilt angle from  $0^{\circ}$  to  $4^{\circ}$  increases the depth at which the rear of the shoulder presses downward into the alloy. This then pushes more material forwards, producing a larger forging force and a larger

<sup>1</sup> Shinoda, T (2001)

<sup>2</sup> Dawes, CJ and Thomas, WM (1991)

<sup>3</sup> Smith, CB (2000)

<sup>4</sup> Chen, ZW and Maginess, R (2004)

volume of material to fill the tool "channel", resulting in a more oval shaped nugget and an increase in the width of the nugget from 7.6 mm to 8.9 mm. For the purpose of this thesis and to obtain repeatable weld microstructures the tilt angle was kept constant at  $2.5^{\circ}$  for each weld made. This angle was experimentally shown to produce sound welds in the 5083-H321 alloy.

#### 2.3.4 Plunge depth

The plunge depth is usually defined as the vertical depth of the lowest point of the shoulder that is pushed into the material<sup>1</sup>. The plunge depth is a critical parameter during FSW, as it is meant to avoid root defects by ensuring that the pin completely penetrates the weld. Plunging the tool into the material assists in the forging process. As plunge depth increases, so  $F_z$  increases significantly<sup>2</sup>. The plunge depth is difficult to control. TWI has developed a roller system to ensure that a constant plunge depth will be maintained<sup>3</sup>. Experience at NMMU has shown that setting the plunge depth at 0.2 mm from the surface of the plate prior to welding reduces the probability of formation of root defects.

#### 2.3.5 Tool geometry

Three criteria need to be considered when designing a FSW tool i.e. the type of material used, and the size and shape of both the tool shoulder and pin. Choosing the correct tool geometry is critical to achieving acceptable welds with good mechanical properties. Dawes<sup>4</sup> has shown that the tensile strength of a FSW weld in 7075-T7531 aluminum alloy can be increased from about 60% to 90% of the parent plate by altering the tool design. Investigations by Yan-hau et al<sup>5</sup> on FSW aluminium alloy 2014 showed that welds made with an unthreaded taper or columnar tool pins contained voids, in contrast to welds made with 1 mm pitch threads. The FSW containing voids resulted in a decrease of approximately 41% in UTS.

The tool should ideally have the following characteristics<sup>6</sup>:

- (i) good tool wear and creep resistance to extend tool life;

<sup>1</sup> Leonard, AJ and Lockyear, SA (2003)

<sup>2</sup> Johnson, R (2001)

<sup>3</sup> Kallee, SW et al (2001)

<sup>4</sup> Dawes, CJ et al (2000)

<sup>5</sup> Yan-hau, Z et al (2005)

<sup>6</sup> Threadgill, PL and Nunn, ME (2003)

- (ii) good fracture toughness to withstand shocks due to high force loading;
- (iii) thermal and environmental stability and must be inert to the chemical elements in the material being welded; and
- (iv) diffusivity and conductivity values that are less than the alloy being welded. This ensures that heat flows to the alloy and not to the tool, which would cause damage to the spindle and telemetry system.

The tool should be designed to achieve a suitable ratio between the volumes of alloy swept by the pin during rotation and the volume of the pin itself to create a "sufficient" flow path<sup>1</sup>. This ratio is usually 1.1:1 for conventional tool pins, and 2.6:1 for the MX Triflute™ pin shown in Figure 2.9<sup>2</sup>. The section between the shoulder and the pin is well radiused in order to reduce stress concentration. The tool shoulder diameter should be designed to minimize horizontal traverse forces. This will reduce the amount of energy required to produce sound welds, will allow faster weld traverse rates to be used and result in lower thermal cycles<sup>3</sup>. This is very important when welding strain-hardened material such as Al 5083-H321, as heat input will cause softening and therefore loss of alloy strength<sup>4</sup>.

Altering tool geometries and welding parameters transforms the material flow patterns obtained in FSW and thus general conclusions about flow mechanisms are difficult to make<sup>5</sup>. In the work described in this thesis, the same tool geometry will therefore be used for every weld made. Tool design will be discussed in Chapter 3.

#### 2.3.5.1 Tool pin (probe)

The functions of the pin are to sufficiently break up and disperse the oxide material at the weld line, control the flow of the material around the tool, and facilitate an augering effect encompassed by the profile of a right handed thread on the pin turning counter-clockwise. If the pin is too short root defects will be introduced, which are difficult to detect without destructive testing<sup>6,7,8</sup>. Different pin diameters have virtually no effect on spindle torque values<sup>7</sup>. Pin geometries have included a

<sup>1</sup> Thomas, WM (1999)

<sup>2</sup> <http://www.twi.co.uk> (1999)

<sup>3</sup> Johnson, R (2001)

<sup>4</sup> Thomas, WM (1999)

<sup>5</sup> Seidel, TU and Reynolds, AP(2001)

<sup>6</sup> Thomas, WM and Gittos, MF (1999)

<sup>7</sup> Thomas, WM (1998)

<sup>8</sup> Kallee, SW (2001)

cylindrical shaped pin, non-parallel sided pin such as a frustum shape, truncated cones, non-round cross sections, conical spirals or whisks<sup>1</sup>.

TWI has designed a number of widely used tool geometries referred to as the Whorl<sup>TM</sup>, Triflute<sup>TM</sup>, Trivex<sup>TM</sup>, and MX-Trivex<sup>TM</sup> which are shown in Figure 2.9<sup>2</sup>.



Figure 2.9: Whorl<sup>TM</sup>, Triflute<sup>TM</sup>, Trivex<sup>TM</sup> and MX Trivex<sup>TM</sup> tool designs.

Whorl<sup>TM</sup> tools have been used to weld plates from 6 to 50 mm thick<sup>3</sup>. For butt welding the pin is shaped as a frustum which displaces less material than a cylindrical tool of the same maximum diameter. The frustum also is more uniformly stressed and the shape ensures that the lower surface of the helical ridge provides a clear downward augering force, with less interference from the next ridge below. To enable more effective flow of the plasticized material, it is preferable that the distance between each ridge is greater than the thickness of the ridge itself. Some typical pin profiles for the Whorl<sup>TM</sup> tool design are shown in Figure 2.10. The Whorl<sup>TM</sup> reduces the displaced volume by about 60%.



(a) Oval shape (b) paddle shape (c) Re-entrant (d) Changing spiral form

Figure 2.10: Whorl type FSW pins<sup>4</sup>.

The Triflute<sup>TM</sup> tools are also frustum shaped. Together with flutes that act as re-entrant features, the Triflute<sup>TM</sup> pin displaces substantially less material during welding (approximately 70%) than a cylindrical pin. It provides a more uniformly stressed tool and allows for a more efficient flow path. It also incorporates a coarse helical ridge around the triflute lands. This is used to reduce the tool volume further, (and therefore aid material flow), and help break up and disperse

<sup>1</sup> Nicholas, ED and Kalllee, SW (2000)

<sup>2</sup> Kalllee, SW (2001)

<sup>3</sup> Thomas, WM and Gittos, MF (1999)

<sup>4</sup> Thomas, WM et al (1998)

surface oxides. Moreover, the re-entrant helical flutes and thread features used on these pins increase the surface area of the pin. This means that the interface between the pin and the plasticized material is also increased. It is believed that the major factor determining the high performance and the superiority of the Triflute™ pin over the conventional cylindrical pin type tools, (especially for thick plate welding), is the ratio of the volume of the pin swept during rotation to the volume of the pin itself. Typically, this ratio for similar root diameter and length pins was 1.1:1 for conventional pins and is 2.6:1 for Triflute™ pins.

The Trivex™ tool reduces the traverse force between 18% and 25% and the vertical downwards force by 12% compared to the MX Triflute™<sup>1</sup>. Results by Colegrove et al<sup>1</sup> showed that a cylindrical shaped pin had lower torque values than the Trivex tools because they had no threads on the pin to impede flow of material around the tool.

Typically, the pin designs that give sound butt welding incorporate flats or flutes, as shown in Figure 2.11, and a coarse helical ridge (usually a coarse thread) around the pin<sup>2</sup>. These flat or re-entrant features reduce the pin volume and provide a suitable swept-to-static volume ratio. The greater this ratio, the greater the efficiency of material flow around the pin. In addition, these re-entrant features help break up and disperse the surface oxides, within the joint region. Welds without defects in 6082 and 7075 aluminium alloys could be obtained in 25 mm thick material at a feed rate of 60 mm/min when using a frustum shaped Trivex™ tool with three helical flutes<sup>3</sup>.

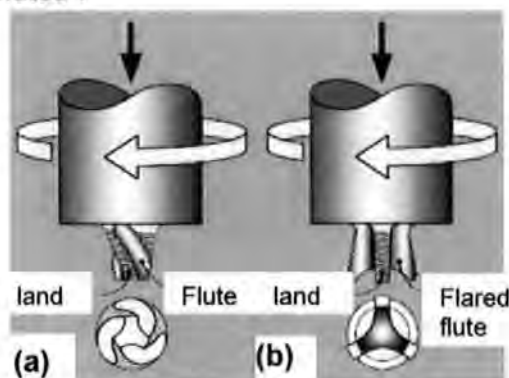


Figure 2.11: Triflute family of pin variants for friction stir welding. (a) MX Triflute™ for butt welding (b) Flared-Triflute™ with tip<sup>4</sup>.

<sup>1</sup> Colegrove, PA et al (2003)

<sup>2</sup> Thomas, WM and Dolby, RE (2002)

<sup>3</sup> Thomas, WM and Gittos, MF (1999)

<sup>4</sup> Thomas, WM et al (2001)

### 2.3.5.2 Tool shoulder

The function of the shoulder is to compress the surface of the work piece, which contains the plasticized weld region, to generate sufficient frictional heat in order to produce good welds and to consolidate material to form the weld joint<sup>1,2</sup>. The contact area of the shoulder is determined by the tool tilt angle. A scrolled shoulder profile has the advantages of enabling welds to be made at increased feed rates, allowing the use of smaller shoulders to produce similar heat inputs, eliminating side flash on the advancing side of the tool and reducing tool surface undercutting<sup>3</sup>. A larger heat input can be achieved if the scrolled tool is positioned perpendicular to the plate since a larger surface area will be in contact with the plate<sup>3</sup>. Welding at a tilt angle of 0° is advantageous for making non-linear welds<sup>4</sup>. The disadvantage of using the scrolled shoulder is that special care need to be taken to ensure that the tool just touches the weld surface, otherwise joint thicknesses slightly greater than the parent material will be achieved which risks the formation of voids in the welds<sup>3</sup>.

Various shoulder profiles are used to improve coupling between the tool shoulder and the work piece by means of trapping plasticized material within special re-entrant features, as shown in Figure 2.12. This improves the formation of the weld, by preventing plasticized material expulsion<sup>5</sup>. Figure 2.12 shows some examples of shoulder geometries that have been used by TWI.

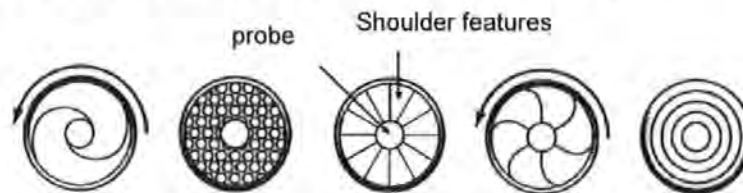


Figure 2.12: Some shoulder geometries used by TWI<sup>6</sup>.

A smaller tool diameter also enables higher feed rates to be achieved, which decreases the vertical force and spindle torque on the tool at higher temperatures and leads to greater efficiency of the process<sup>7</sup>. The diameter of the tool shoulder is proportional to the torque at a constant rotational speed. Increasing the diameter

<sup>1</sup> Threadgill, PL and Nunn, ME (2003)

<sup>2</sup> Bhadeshia, HKDH (2003)

<sup>3</sup> Dawes, CJ and Thomas, MN (1999)

<sup>4</sup> Dawes, CJ et al (1999a)

<sup>5</sup> Thomas, WM et al (2000)

<sup>6</sup> Thomas, WM et al (2001)

<sup>7</sup> Ericsson, M and Sandström, R (2003)

of the shoulder has practical limitations and tends to produce side flash on the weld surface, as can be seen in Figure 2.13<sup>1</sup>.

Side flash



Figure 2.13: Side flash obtained during a trial weld at the Nelson Mandela Metropolitan University<sup>1</sup>.

The shape of the shoulder also affects the residual stress distribution in the welds. The residual stress distribution widens and becomes more positive as the diameter of the shoulder increases from 15 to 22 mm, as shown in Figure 2.14<sup>2</sup>.

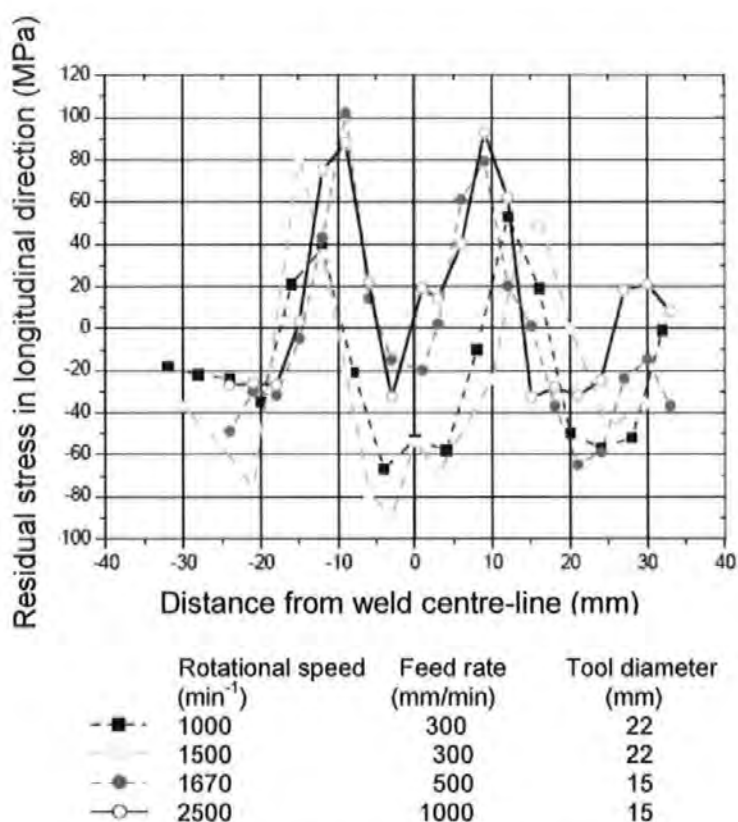


Figure 2.14: Graph showing typical M-type distribution of residual stresses, as a function of tool shoulder diameter in a 6013-T4 aluminum FS weld<sup>2</sup>.

<sup>1</sup> Blignault, C (2004)

<sup>2</sup> Dalle Donne, C (2001)



The latest tool development is a bobbin or self-reacting tool which was designed by Marie et al<sup>1</sup>. Compared with a conventional FSW tool it reduces vertical forces by between 12.5% - 25%. This enables a lighter fixture and clamping mechanism for FSW welding<sup>1</sup>. The tool consists of an upper and lower shoulder and a sliding pin, as shown in Figure 2.15. Force, rotational speed and position can be controlled independently for each shoulder. Welds without root flaws can be obtained. Pin failure occurs more often, however, and these tools are suitable for welding plates in the range of 8-15 mm for 6056-T4 and 2219-T87. FS welds made from 4mm thick 2024-T3 aluminium alloy plates are more difficult to weld. The bobbin tool does not seem to be suitable for welding at high feed rates.

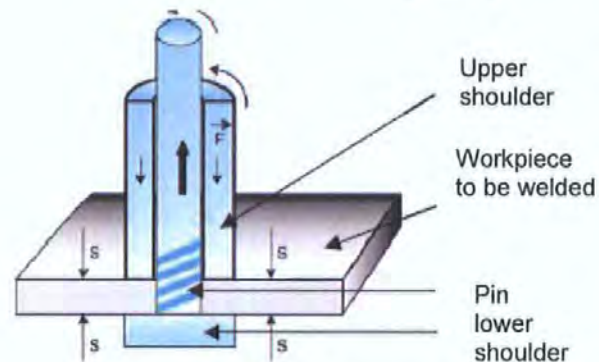


Figure 2.15: Bobbin tool<sup>1</sup>.

Material flow and the resultant microstructure of welds varies with each tool geometry and the generalized conclusions regarding microstructural development and the influence of processing parameters are therefore difficult to determine.

### 2.3.6 Forces on the tool during FSW

Movement of the tool along the joint line produces translational forces ( $F_x$ ), along the weld and transverse forces ( $F_y$ ) perpendicular to the weld direction. The magnitude of these forces depends on the material flow viscosity as well as the rotational speed and feed rate of the process. The force perpendicular to the direction of travel,  $F_z$ , is greater in magnitude than the translational forces<sup>2</sup>. Figure 2.16 identifies the force directions considered in FSW.

<sup>1</sup> Marie, F et al (2004)

<sup>2</sup> Johnson, R (2000)

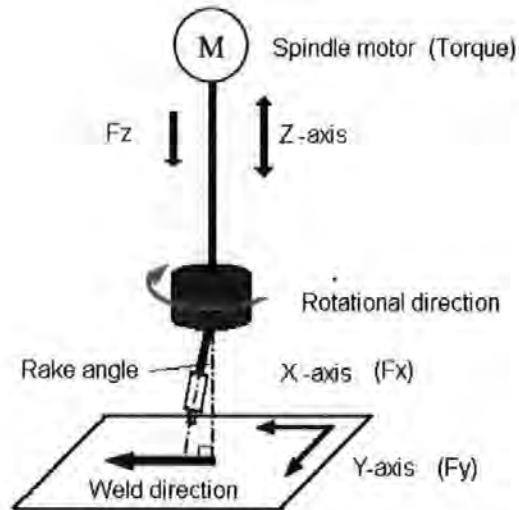


Figure 2.16: Forces relevant to FSW <sup>1</sup>.

Minimizing tool forces implies improved process efficiency and reduced heat input into the material being welded. Johnson<sup>2</sup> found that the force on the tool ( $F_y$ ) perpendicular to the welding direction was 5-10% lower than the force ( $F_x$ ) resisting the forward motion. Forces and torques measured in welding for 5083-O were higher than for 6082-T6 Al material despite the high room temperature proof stress for the 6082-T6 alloy. Downward forces ( $F_z$ ) are much larger than horizontal forces. Variation in  $F_z$  usually indicates an uneven surface under the tool shoulder which also increases heat generation<sup>3</sup>. Variation in the force in the welding direction ( $F_x$ ) also indicates overheating. Results by Reynolds et al<sup>4</sup> showed that if the rotational speed was varied between 90 and 900 rpm, at a constant feed rate,  $F_x$  attained a minimum value at intermediate rotational speeds. This minimum value of  $F_x$  was an indicator of good weld quality with no tunnel or wormhole defects. If higher values of  $F_x$  are consistently generated, a running void may be detected<sup>4</sup>. The dependence of  $F_x$ ,  $F_y$  and  $F_z$  on feed rate and rotational speed is illustrated in Figures 2.17 - 2.22<sup>2,5</sup>. By welding with high or low rotational speeds in conjunction with high feed rates, the compressive force can be minimized, thereby reducing the power requirement of the machine and minimizing the weld time as seen in Figure 2.17<sup>5</sup>. It is apparent from the graph that high rotational speeds between 600 and 650 rpm will produce the lowest compressive forces ( $\approx$ -24kN).

<sup>1</sup> Hirano, S et al (2001)

<sup>2</sup> Johnson, R (2001)

<sup>3</sup> Stewart, MB et al (1998)

<sup>4</sup> Reynolds, AP (2003)

<sup>5</sup> Blignault, C (2004)

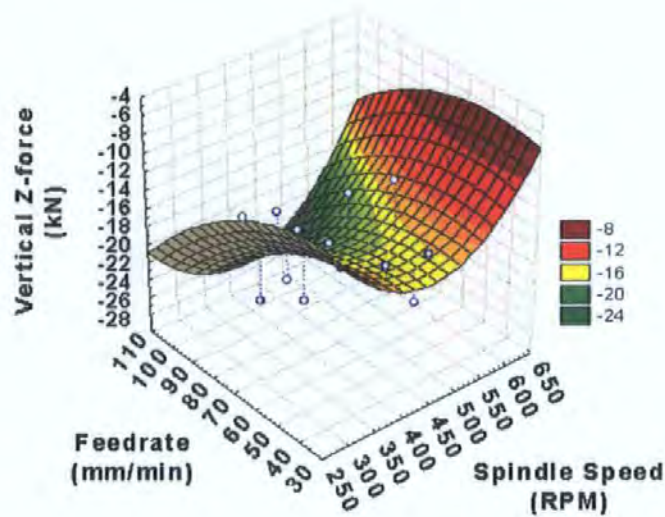


Figure 2.17: Surface plot relating spindle speed, feed rate and vertical compressive force applied on the tool<sup>1</sup>.

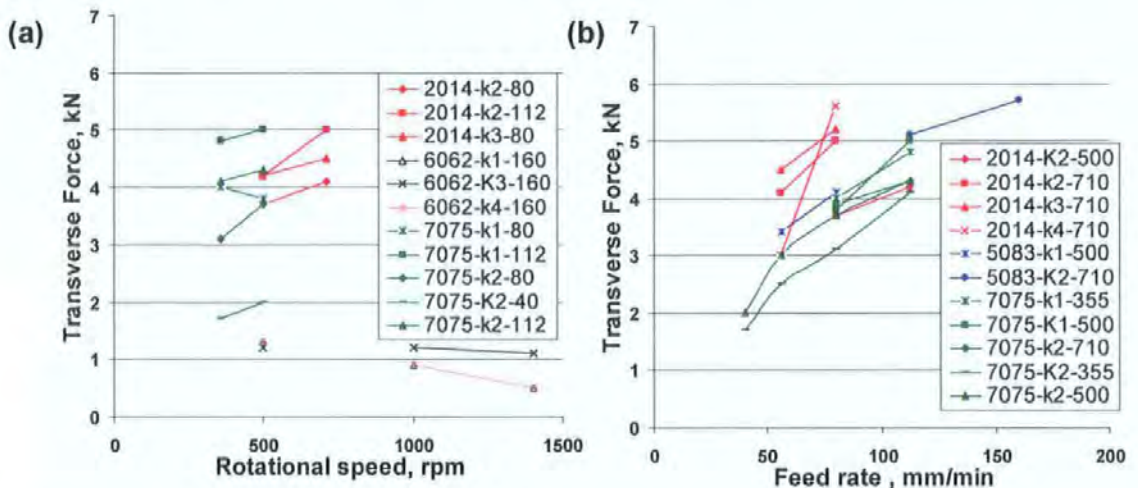


Figure 2.18: Variation of transverse force with (a) rotational speed and (b) feed rate<sup>2</sup>.

Data obtained by Johnson<sup>2</sup> indicates that  $F_x$  increases with feed rate but for a variety of materials can either increase or decrease with an increase in rotational speed, as shown in Figure 2.18. Fig 2.18 (b) shows there is a strong increase in transverse force with increase in feed rate, while Fig 2.18 (a) indicates that increasing rotational speed corresponds with a weaker change in transverse force. The investigation by Johnson<sup>1</sup> however did not use systematic parameter variation and makes it difficult to interpret the data.

<sup>1</sup> Blignault, C (2004)

<sup>2</sup> Johnson, R (2001)

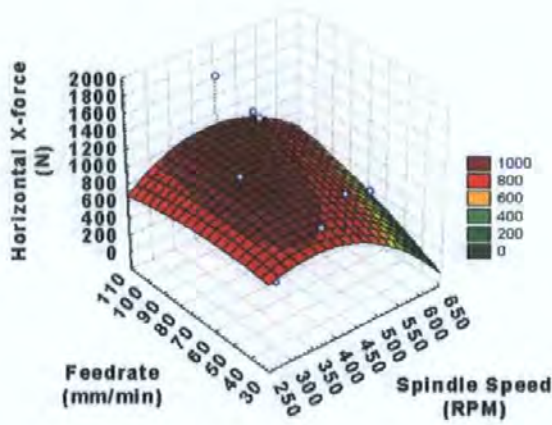


Figure 2.19: Surface plot relating spindle speed, feed rate and maximum horizontal force exerted on the tool<sup>1</sup>.

Results by Blignault<sup>1</sup> on welding 5083-H321, shown in Figure 2.19, show spindle speed and feed rate in the form of a surface plot of the force perpendicular to the welding direction. Note that the sign convention used by Blignault is opposite to that used in this thesis, that is  $F_x$  is  $F_y$  in this thesis. It demonstrates that feed rate has a secondary effect on  $F_y$  at any particular tool speed except at rotational speeds  $\geq 550$  rpm where a steep decline in  $F_y$  occurs. This type of information is not, in itself, sufficient to guide users to optimum welding conditions, as it gives no information on weld properties or performance.

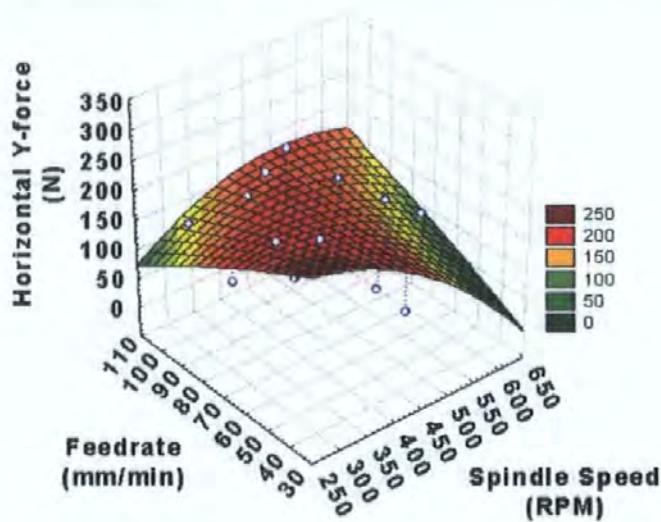


Figure 2.20: Surface plot relating spindle speed, feed rate and maximum vertical force exerted on the tool<sup>1</sup>.

Figure 2.20 shows the force measured perpendicular to the welding direction on the FSW tool. It demonstrates similar trends in those observed for  $F_y$ , and

<sup>1</sup> Blignault, C (2004)

indicates that high spindle speed and low feed rate lead to lower tool forces. Force analysis can assist in developing optimized tools as well as helping to explain the flow behaviour around the tool, since the material flow behaviour is the cause of the forces acting on the tool<sup>1</sup>.

Forces acting on the tool pin can be used to predict whether a tool will fail or not<sup>2</sup>. As the plunge depth increases all forces increase, for example  $F_z$  (downward force),  $F_x$  (transverse or side force) and torque<sup>3</sup>. Ulysse<sup>4</sup> used a 3D FEM viscoplastic model to predict the effect of rotational speed and feed rate on plate temperature and tool forces in order to avoid tool breakage. The heat contribution of the pin was included in the model. He also validated the model with experimental investigations. It was found that the pin forces increased with feed rate and decrease with rotational speed. In this model the rotation of the pin surface was simulated by a constant tangential velocity. A small plate size of 60 x 100 mm and a smooth pin surface were considered in the model, in order to save computational time. The measured temperature was consistently less than the temperature predicted by the FEM model. The temperature decreased with increasing feed rate and increased with rotational speed.

The forces on the tool have been modeled by Shi et al<sup>5</sup> assuming that a constant shear stress acts on the tool. The torque under the tool surface was resolved in  $F_x$  and  $F_y$  components and is given by

$$F_x = \frac{1.5T}{\pi D r_s^3} \frac{(y)}{(r)}, \quad F_y = \frac{1.5T}{\pi D r_s^3} \frac{(x - X_{tool})}{r} \quad \dots(2.3)$$

where

T = torque (Nm)

r = distance from a point on the tool surface to the tool centre (mm)

$x - X_{tool}$  = x coordinate distance from the tool centre

y = coordinate distance from tool centre

$r_s$  = radius of the shoulder

D = the plunge depth over which the load was applied

---

<sup>1</sup> Ouyang, JH et al (2002)

<sup>2</sup> Ulysse, P (2002)

<sup>3</sup> Johnson, R (2001)

<sup>4</sup> Ulysse, P (2002)

<sup>5</sup> Shi, Q et al (2003)

This mechanical tool loading was combined with a thermal model by Shi et al<sup>1</sup> to determine the residual stresses in the welds.

According to Chen and Kovacevic<sup>2</sup> Finite Element Models revealed that increasing rotational speed decreases  $F_z$  and no significant effect was seen in the  $F_y$  or  $F_x$  directions.  $F_x$  and  $F_y$  increased with feed rate, with an associated slight increase in  $F_z$ .

Results by Colligan et al<sup>3</sup> show that introducing flats on the tool pins influences the forces generated on the tool. A new parameter was introduced, by these authors namely, travel per flat per revolution = (feed rate/(spindle speed\*number of flats)). They found that an increase in this parameter from 0.127 to 0.254 increased  $F_y$  from 9 to 16 kN, while results for  $F_x$  did not show any clear trends. These authors proposed that the number of flats influence the amount of material captured by the tool as it rotates. The tool that had no flats exhibited a very large transverse force,  $F_y$ . Colligan et al<sup>3</sup> attributed this to the fact that the plastic material was now being extruded around the pin instead of being captured during a revolution by the flats on the pin.

It is clear from this literature review that past research has not focused on any dependencies between forces on the tool and mechanical properties of the welds for 5083-H321 alloy. In the investigation described in this thesis the tool forces were measured during welding and their influence on the tensile, residual stress and fatigue characteristics of the FS welds was examined. The underlying hypothesis was that there is a correlation between energy input and the forces on the tool and hence with mechanical properties of the welds.

### 2.3.7 The polar plot or "force footprint" diagram

The 'force footprint' is a graphical representation of the resultant force vector experienced by the tool during a single revolution, which can be resolved into x and y components<sup>4</sup>. The force footprint data are obtained via strain gauges that rotate with the tool and measure its deflections under load. These strain values can be converted to forces from conventional strain gauge theory. The analogue

---

<sup>1</sup> Shi, Q et al (2003)

<sup>2</sup> Chen, C and Kovacevic, R (2003)

<sup>3</sup> Colligan, K.J et al (2003)

<sup>4</sup> Hattingh, DG et al (2004)

signals from the strain gauges are converted into digital signals and are transferred to the interface units that link the telemetry system with a computer. Once the raw data has been processed a mean value of the horizontal tool force at specified angles can be obtained. These force-angle data are then plotted to create a polar plot or sinusoidal diagram, as shown in Figure 2.21.

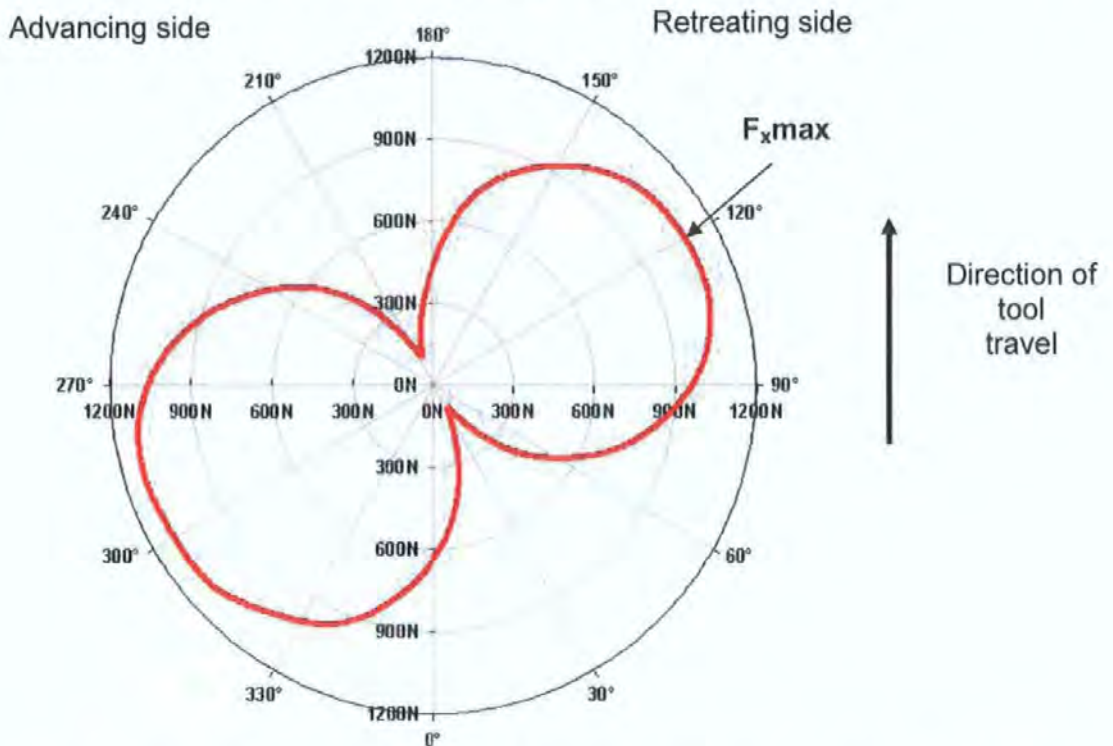


Figure 2.21: Typical 2D polar force plot for a spindle speed of 300 rpm and feed rate of 120mm/min in 5083-H321 alloy<sup>1</sup>.

As the tool rotates in the nominally frictionless bearing, the force readings would be expected to be approximately symmetric through a revolution and to approach zero force at 90° and 270°. The observed rotation of the direction of maximum force in this bi-lobed plot changes from its reference angle (180°), during welding as a result of the tool/material interaction and the rotational plastic flow zone in the weld nugget and thermo-mechanically affected zone (TMAZ). Polar plots can be obtained at any point along the weld run. The measured force vector is an indicator of the flow properties in the weld zone, and hence may be related to the degree of plasticity in the deformed region. Additionally, the area of the polar plot should be proportional to the energy input per revolution. In principle, both the defect population and the mechanical properties of the weld zone will reflect the energy and the amount of plastic deformation put into the weld<sup>1,2</sup>. The force

<sup>1</sup> Hattingh, DG et al (2004)

<sup>2</sup> Bradley, G R et al (2003)

footprint should therefore provide useful insight into routes to optimise these critical aspects of the welded joint. The anticipated result should be a substantial improvement in our ability to predict appropriate welding conditions for various combinations of alloy, plate thickness, tool design, and production rates. Results by Hattingh et al<sup>1</sup> indicated that the areas of the polar plots while welding 6 mm thick Al 5083-H321 plates increased when the rotational speed was increased from 300 to 600 rpm. This supports the theory that the areas of these diagrams should be related to energy input into the welds. It was also found that a decrease in tool pitch of 0.18 mm/rev caused a 30° counter-clockwise rotation of the peak force position in the polar plots. It was speculated that this shift is related to the plastic flow processes in FSW<sup>1</sup>.

Information on forces could be coupled with single-point machining models<sup>2</sup> to extend model predictions to different alloys and weld conditions, and to determine optimum tool form. The polar 'force' footprint associated with FS welding may therefore provide fundamental insights linking process parameters with weld properties and performance.

Polar plots were obtained and analyzed for all the welds made in this research. The maximum force per revolution was used to determine the work input per revolution as the tool moves along the weld from the relationship  $Work = Force \times distance$ . The resultant force is calculated to determine an interrelationship between the process parameters and energy input. To the knowledge of the author this is the first time that this avenue of research has been undertaken in FS welding.

### 2.3.8 Tool temperature

The optimum temperature to ensure adequate plasticity of the material to be friction stir welded is usually 0.6 to 0.8 of the material melting point<sup>3</sup>. As the temperature rises the yield strength of the material falls below the applied shear stress so that a region of highly deformed plasticized material forms around the immersed and contacting regions of the tool. The plasticized material provides some hydrostatic effect that enables the material from the front of the tool to be

---

<sup>1</sup> Hattingh, DG et al (2004)

<sup>2</sup> Allintas, Y (2000)

<sup>3</sup> Li, Y et al (1999)



swept around the plasticized annulus to the back of the tool, thus forming the solid state weld on consolidation<sup>1</sup>.

Since the temperature distribution within and around the stirred zone directly influences the microstructure of the welds, such as grain size, grain boundary character, coarsening and dissolution of precipitates, and resultant mechanical properties of the welds, it is important to obtain information about temperature distribution during FSW<sup>2</sup>. However, taking temperature measurements within the stirred zone is very difficult due to the intense plastic deformation produced by the rotation and translation effects of the tool. Therefore, in previous work the maximum temperatures within the stirred zone during FSW have been either estimated from the microstructure of the weld<sup>3,4</sup> or recorded by embedding a thermocouple in the regions adjacent to the rotating pin<sup>5,6</sup>.

Figure 2.22 plots measurements of tool temperature, taken at NMMU, for a range of spindle speeds and feed rates while welding 6 mm plate of 5083-H321 alloy.

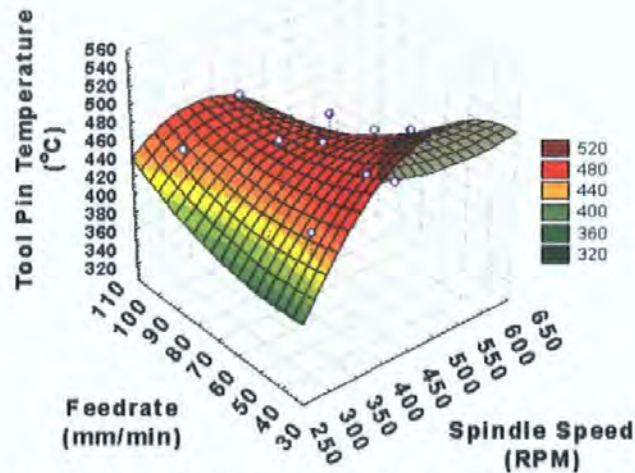


Figure 2.22: Surface plot relating spindle speed, feed rate and tool temperature<sup>7</sup>.

If the melting temperature ( $T_m$ ) for this material lies in the range of 590-640 °C, then  $0.6 T_m$  is equivalent to 355-383 °C and  $0.8 T_m$  is equivalent to 473-510 °C. Clearly, these temperatures can be attained over the complete range of feed rates and spindle speeds used in the present research. The question to be answered

<sup>1</sup> Bhadeshia, HKDH (2003)  
<sup>2</sup> Mishra, RA and Ma, ZY (2005)  
<sup>3</sup> Rhodes, CG et al (1997)  
<sup>4</sup> Liu, G et al (1997)  
<sup>5</sup> Mahoney, MW et al (1998)  
<sup>6</sup> Sato, YS et al (1999a)  
<sup>7</sup> Bignaut, C (2004)

relates the effect of temperature and the various possible combinations of speed and feed on the weld properties and performance. This needs to be clarified before an informed trade-off can be made between weld properties, defects, performance, and the industrial requirement for high production rates (high feed and optimum spindle speed). The work described in this thesis seeks to clarify these aspects of FS welding.

Results by Tang et al<sup>1</sup> show that with a tool rotation speed of 400 rpm and a feed rate of 122 mm/min, a peak temperature of 450 °C was observed at the weld center one quarter from the top surface. These authors observed a nearly isothermal region  $\pm 4$  mm from the weld centre-line. The gradient in the peak weld temperature in the thickness direction of the welded joint is very small within the stirred zone and only 25 °C to 40 °C in the region away from the stirred zone<sup>1</sup>. This indicates that the temperature distribution within the stirred zone is relatively uniform. Tang et al<sup>1</sup> further investigated the effect of weld pressure and tool rotation rate on the temperature field of the weld zone. It was reported that increasing both tool rotation rate and weld pressure resulted in an increase in the weld temperature. Figure 2.23 shows the effect of tool rotation speed on the peak temperature achieved as a function of distance from the weld centre-line. Clearly, within the weld zone the peak temperature increased by almost 40 °C as the tool rotation speed increased from 300 to 650 rpm, whereas it only increased by 20 °C when the rotational speed increased from 650 to 1000 rpm, that is, the rate of temperature increase is lower at higher tool rotation rates. This reverses 10 mm from the weld centre-line.

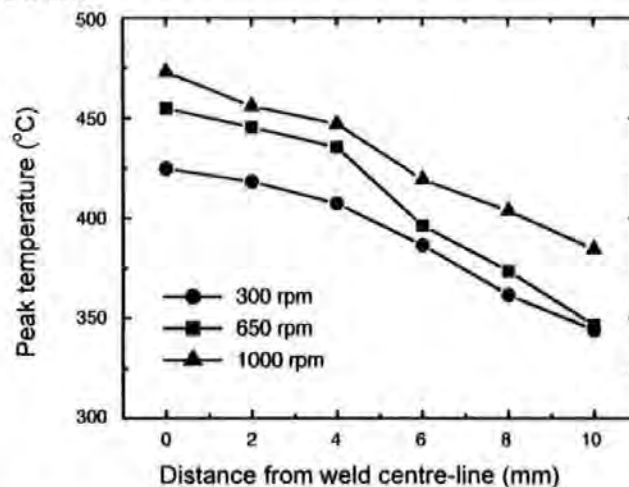


Figure 2.23: Peak temperature as a function of distance from the weld centre-line<sup>1</sup>.

<sup>1</sup> Tang, W et al (1998)

Tang et al<sup>1</sup> also studied the effect of shoulder contact on the temperature field by using two tools, one with a pin and one without a pin. Shoulder contact dominated the heat generation during FSW, as shown in Figure 2.24.

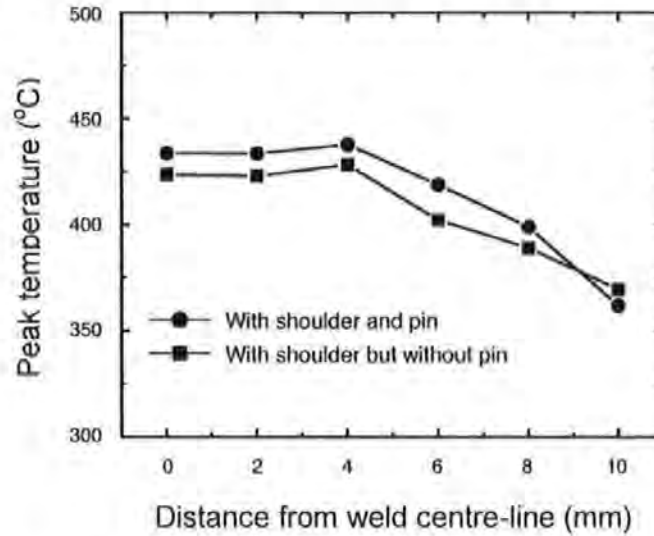


Figure 2.24: The effect of the shoulder on the peak temperature<sup>1</sup>.

This was attributed by the authors to the fact that the contact area and vertical pressure between the shoulder and workpiece is much larger than those between the pin and workpiece, and the shoulder has higher linear velocity than the pin with its smaller radius<sup>1</sup>. Additionally, Tang et al<sup>1</sup> showed that thermocouples placed at equal distances from the weld seam but on opposite sides of the weld showed no significant differences in the temperature. Similarly, Kwon et al<sup>2</sup>, Sato et al<sup>3</sup>, and Hashimoto et al<sup>4</sup> also measured the temperature rise in the weld zone by embedding thermocouples in the regions adjacent to the rotating pin. Kwon et al<sup>1</sup> reported that in FSW of 1050 aluminium alloy, the peak temperature in the FS process zone increased linearly from 190 to 310 °C with increasing tool rotation speed from 560 rpm to 1840 rpm at a constant tool feed rate of 155 mm/min. An investigation by Sato et al<sup>3</sup> similarly indicated that in FSW of 6063 aluminium alloy the peak temperature of the thermal cycle increased sharply, with increasing tool rotation speed from 800 rpm to 2000 rpm at a constant tool feed rate of 360 mm/min. Above 2000 rpm, however, peak temperature rose gradually up to 3600 rpm. Peak temperatures > 500 °C were recorded at a tool rotation speed of 3600 rpm. Hashimoto et al<sup>4</sup> reported that the peak temperature in the weld zone

<sup>1</sup>Tang, W et al (1998)

<sup>2</sup>Kwon, YJ et al (2002)

<sup>3</sup>Sato, YS et al (1999a)

<sup>4</sup>Hashimoto, T et al (1999)

increases with increase in the ratio of tool rotation speed/feed rate in FSW of 2024-T6, 5083-O and 7075-T6 aluminium alloys (Fig.2.25).

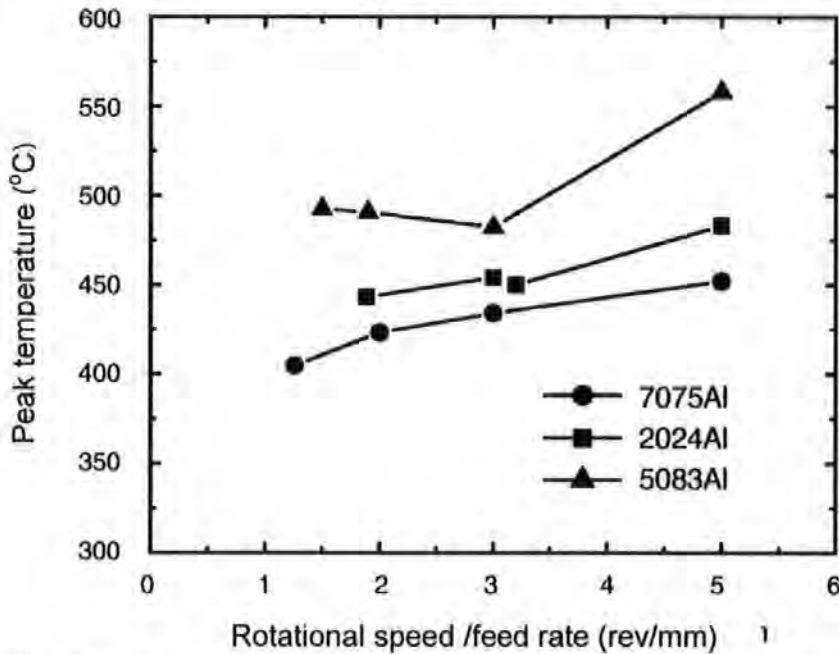


Figure 2.25: The variation of peak temperature with respect to tool rotation speed/feed rate ( that is 1/pitch)<sup>1</sup>.

Tang et al<sup>2</sup> found that the maximum temperature was less than 80% of the melting temperature for 6061-T6 aluminium alloy and that the temperature distribution perpendicular to the weld was nearly isothermal beneath the tool shoulder, and symmetrical about the weld centre-line. They also observed that increasing the weld pressure and rotational speed of the tool increased the peak weld temperature. The grains in the weld centre seemed to be fine and equiaxed because of the large induced deformation that facilitates dynamic recrystallisation.

Arbegast and Hartley<sup>3</sup> measured the average maximum temperature during welding and determined a general empirical relationship given by

$$\frac{T_{max}}{T_m} = k \left( \frac{w^2}{fx10^4} \right)^a \quad (2.4)$$

where

<sup>1</sup> Hashimoto, T et al (1999)

<sup>2</sup> Tang, W et al (1998)

<sup>3</sup> Arbegast and Hartley (1998)

$$\alpha = 0.04-0.06$$

$$k = 0.65-0.75$$

w = rotational speed

f = feed rate

$T_m$  = melting temperature of the alloy

$T_{max}$  = maximum temperature during welding

$$\frac{w^2}{f} = \text{a pseudo heat index}$$

They noted that a slightly higher temperature was found on the advancing side of the weld.

In summary, it is clear that the temperature in the weld can be altered by changes in feed rate, rotational speed and type of material welded. Previous research has proven that the maximum temperature in the stirred zone of the welds is below the melting point of the material; that the maximum temperature during welding increases with an increase in rotational speed at a constant feed rate; that the maximum temperature decreases with increasing feed rate at a constant rotational speed; and that the maximum temperature increases with 1/pitch. No studies have yet been made that relate tool temperature to other process parameters or to mechanical properties of welds. These aspects are investigated in this research study.

## 2.5 Microstructure

Weld microstructures are determined by the thermal welding cycle, by the plastic deformation and by the properties of the base metal. The small recrystallised grain structure within FSW nuggets would generally be considered beneficial for the mechanical properties. The types of grain structure found within FSW depend on the welding parameters, energy input and feed rate of welding. An understanding of micro-structural evolution during FSW and the effect of microstructure on mechanical and physical properties, such as fatigue crack growth and toughness, is critical to weld process optimization. Such an understanding will bring broader acceptance in industry and, inevitably, new applications for this innovative technology. A good understanding of the heat transfer process in the work piece would be helpful in predicting weld thermal

cycles and determining the subsequent hardness in the weld zone<sup>1</sup>. The following sections include a discussion of the classification of FS weld microstructures as well as the influence of various process parameters on the microstructure, grain size and hardness of the welds.

### 2.5.1 FS weld microstructures

TWI has developed a system of classification for FSW microstructures in aluminium alloys<sup>2</sup>. The action of the tool can produce up to five distinct microstructural zones as follows:

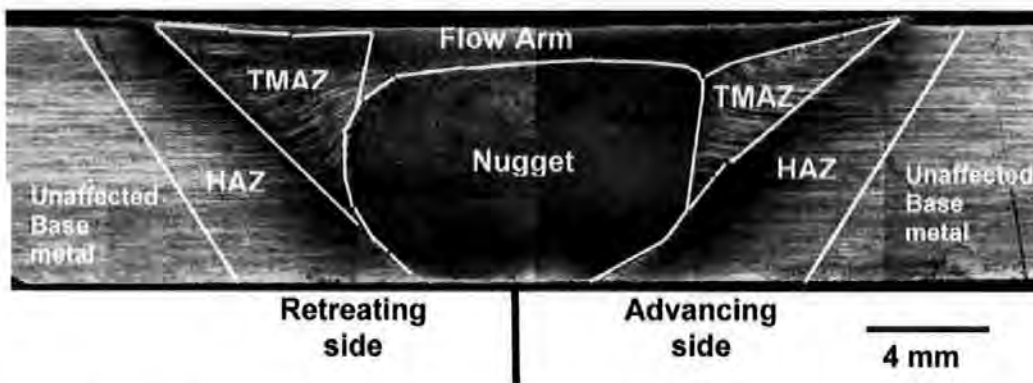


Figure 2.26: Classification of Microstructure in FSW<sup>3</sup>.

The unaffected base metal is remote from the weld and although it may have experienced a thermal cycle during welding, this will not have altered its microstructure or mechanical properties.

The heat affected zone (HAZ) lies closer to the weld centre and shows a typically trapezoidal shape, reflecting the influence of the tool taper and the shoulder. The microstructure and mechanical properties in this region are changed by the thermal cycle without any contribution from plastic deformation. The increase in the width of the HAZ with increasing heat input, as a function of feed rate can be seen in Figure 2.27<sup>4</sup>. The feed rate and downward force were kept constant during these tests.

<sup>1</sup> Song, M and Kovacevic, R (2002)

<sup>2</sup> <http://www.twi.co.uk/j32k/protected/band8/spwmf99.html>

<sup>3</sup> Reynolds, AP (2003)

<sup>4</sup> Midling, OT and Rørwick, G (1999)

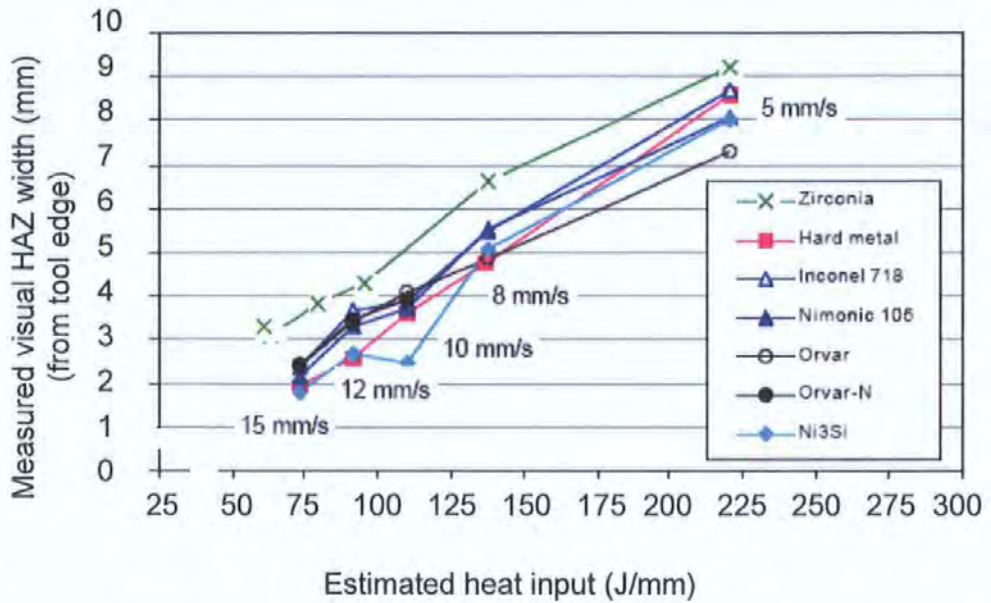


Figure 2.27: Effect of feed rate, type of tool and heat input on the width of the HAZ during FSW<sup>1</sup>.

In the thermo-mechanically affected zone (TMAZ), the material was both plastically deformed and experienced a thermal cycle. Aluminium materials can undergo extensive plastic strain at high temperatures without recrystallisation, and there is generally a distinct boundary between the dynamically recrystallised region (nugget) and the unrecrystallised region of the TMAZ<sup>2</sup>. The unrecrystallised region of the TMAZ consists of grains of a similar size to the base material. Strangwood et al<sup>3</sup> have suggested that the grains may however, have been rotated by up to 90<sup>0</sup>.

It has also been suggested<sup>4</sup> that the area immediately below the tool shoulder (which is clearly part of the TMAZ) should be given a separate category, as the grain structure is often different here. It is suggested that this area is treated as a separate sub-zone of the TMAZ, which is referred to as the flow-arm zone (Figure 2.26.).

The nugget is centred around the pin path and has experienced the most severe plastic deformation. Various authors have reported that dynamic recrystallisation is the most likely mechanism to account for the fine equiaxed grains seen in the

<sup>1</sup> Midling, OT and Rørwick G (1999)

<sup>2</sup> TWI (1999)

<sup>3</sup> Strangwood, M et al (1999)

<sup>4</sup> TWI (1999)

nugget<sup>1,2,3,4,5</sup>. The grain size of this region generally lies between 1 and 20  $\mu\text{m}$ <sup>6,7,8,9</sup>. Yang et al<sup>10</sup>, however, has suggested that dynamic recovery is the mechanism involved. The transverse nugget cross-section often shows macroscopic concentric rings known as onion rings. Series of concentric rings occurring in a section along the weld have also been reported by Magnusson and Källman<sup>11</sup>, who claim that these rings are linked to the tool thread and represent a sign of good weld quality. In this thesis transverse optical macrographs were used to examine how the shape of the nugget changes with changes in the process parameters.

Dalle Donne and Biallas<sup>12</sup> describe the onion rings as being concentric tube shaped interfaces that are extruded around the tool during welding. The tubes form a helical structure of decreasing radii, which appear as a series of concentric rings when the surface is observed, is explained in Figure 2.28. The authors<sup>12</sup> also state that the rings disappear as the rotational speed is increased and that non-threaded tools did not produce the rings.

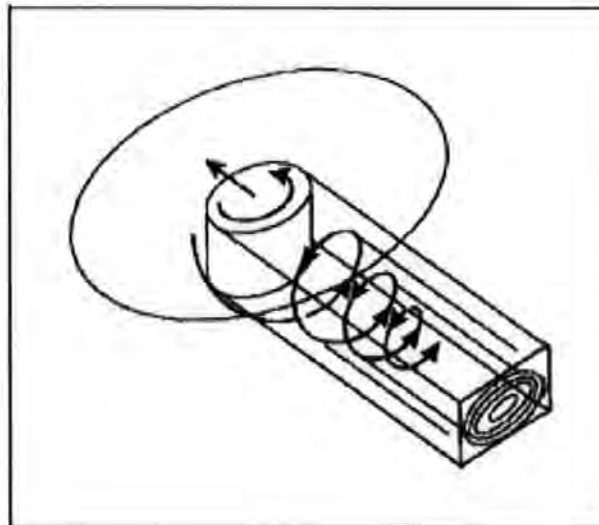


Figure 2.28: Formation of onion rings<sup>12</sup>.

<sup>1</sup> Karlsson, J et al (1998)

<sup>2</sup> Murr, LE et al (1997)

<sup>3</sup> Murr, LE et al (1998)

<sup>4</sup> Strangwood, M et al (1999)

<sup>5</sup> Nelson, TW et al (1999)

<sup>6</sup> Mahoney, MW et al (1998)

<sup>7</sup> Sato, YS et al (1999a)

<sup>8</sup> Svensson, L and Karlson, L (2000)

<sup>9</sup> Jata, KV and Semiatin, SL (2000)

<sup>10</sup> Yang, HS (2000)

<sup>11</sup> Magnusson, L and Källman, L (2000)

<sup>12</sup> Biallas, G et al (1999)



Guerra et al<sup>1</sup> described the formation of the onion skin layers as occurring by means of two main processes:

- (i) Material is moved from the advancing front side of the pin via a zone of metal that advances with the pin. The material undergoes a helical motion within the rotational zone. After a few rotations the zone of metal is sloughed off in the wake of the pin, primarily on the advancing side.
- (ii) Entrainment of material from the front retreating side of the pin that fills in between these sloughed-off layers from the advancing side.

In contrast, Larsson et al<sup>2</sup> have suggested that the concentric rings in Al 5083 and Al 6082 are the result of periodic variations in crystallographic orientation of the grains or in relative orientation of adjacent grains.

Distinctive ripples/bands/rings are produced on the top surface/crown of the FSW and are essentially cycloidal. They are produced by the final sweep of the trailing circumferential edge of the shoulder, during forwards tool motion. The combined relative motion is by definition a superior trochoid, that is a cycloid with a high degree of overlap in successive revolutions<sup>3</sup>. The distance between the bands is determined by the ratio of feed rate to rotational speed and is referred to as pitch. Research by Krishnan<sup>4</sup> illustrated a relationship between the band distances on the crown of the weld and rotational speed, as shown in Figure 2.29.

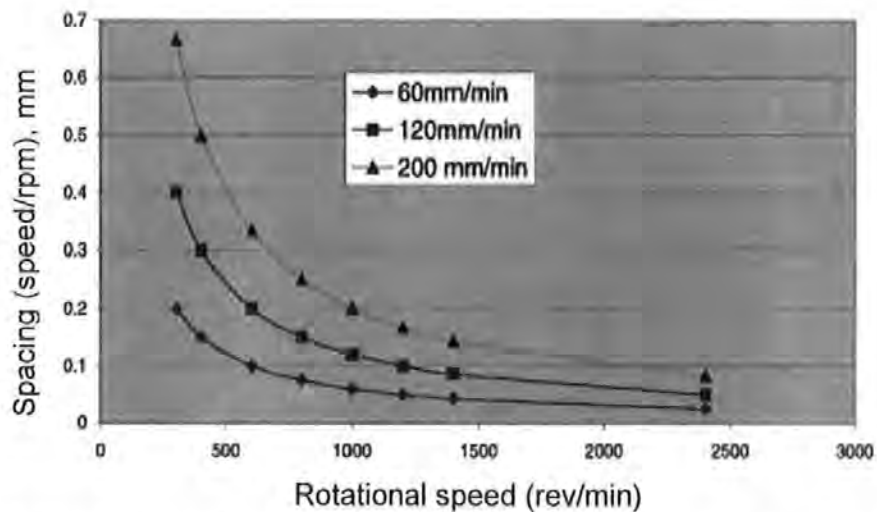


Figure 2.29: Relationship between pitch = (feed rate/rpm) and rotational speed in for 6061 and 7075 alloys<sup>4</sup>.

<sup>1</sup> Guerra, M et al (2003)

<sup>2</sup> Larsson, H et al (1998)

<sup>3</sup> TWI (1999)

<sup>4</sup> Krishnan, N (2001)

The onion ring/skin banded structure in the transverse section of the nugget suggests the existence of a corresponding banded configuration in sections along the weld, either horizontal to the surface of the weld or through the thickness. Sutton et al<sup>1</sup> performed micro-tensile testing using digital image correlation to quantify the local stress-strain variations in the banded region. Their Fourier analysis indicated that strain modulation had the same wavelength as the microstructural bands formed in the welds, thus with intervals equal to the pitch ratio<sup>1</sup>. The bands therefore appear to be associated with the flow of the material at a frequency correlated with the welding parameters<sup>1</sup>. The microstructural bands on the crown of the weld may be characterized through their varying grain size and/or particle content across longitudinal and transverse sections of the weld, as shown in Figure 2.30<sup>2</sup>. These bands have been shown to have different densities of second-phase particles with the redistribution of particles attributed to differing mechanical and thermal conditions associated with band formation. Bands with high numbers of particles exhibit reduced fracture strain in 2024-T351 aluminium alloy and are the crack initiation sites. It was suggested by Sutton et al<sup>1</sup> that a smaller band spacing should result in a more homogeneous structure in the weld. This is likely to occur in conjunction with a hotter weld temperature, leading to lower strength welds.

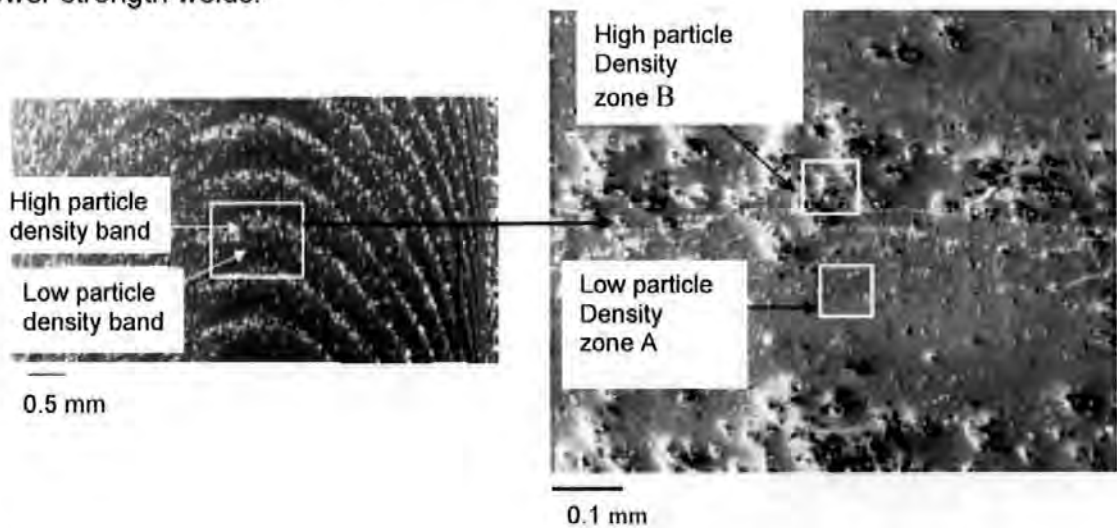


Figure 2.30: Banded structure in the horizontal plane of the FSW indicating high and low density particles for 2024-T351 aluminium alloy<sup>1,2</sup>.

The layers in the onion skin structure therefore consist of streams of material with different thermo-mechanical histories and mechanical properties<sup>3</sup>. The layers therefore etch differently as the different thermo-mechanical histories lead to

<sup>1</sup> Sutton, MA et al (2002b)

<sup>2</sup> Reynolds, AP (2003)

<sup>3</sup> James, MN et al (2004)

different dislocation densities and distributions. Adjacent layers should show different strain hardening exponents and hardness which could lead to strain partitioning between different layers when the weld is loaded. Work by Reynolds has indicated that strain partitioning occurred between the adjacent layers in the TMAZ<sup>1</sup>. Strain partitioning is often associated with the occurrence of ductility-related cracking problems i.e. strain-age embrittlement and reheat cracking. It was proposed by James et al<sup>2</sup> that large planar defects observed on the fracture surfaces of 5083-H321 welds were formed due to strain partitioning-induced ductility drop at layer interfaces, possibly coupled with partial forging occurring during welding. The activation of such mechanisms would be influenced by crack orientation, strain rate and the relative differences in strain hardening exponents of adjacent layers in the onion skin structure. These defects were observed to reduce the fatigue strength by up to 20%<sup>2</sup>.

The shape of the nugget also varies with process conditions and with the type of tool used. Dalle Donne and Biallas<sup>3</sup> concluded that the concentric rings in the nugget seemed to become less evident with increasing weld feed rate and rotational speed for oval shaped tools, and that the V-shaped non-threaded tools did not produce an onion skin structure. Studies by Hassan et al<sup>4</sup> on 7010-T7651 aluminium alloy indicated that the nugget zone became wider and flatter as the spindle speed was increased at a fixed feed rate as heat input increased. The spacing of the rings could be related to the feed rate, and an increase in rotational speed increased the spacing.

Work by Peel et al<sup>5</sup> (Figure 2.31) has demonstrated how the nugget zone varies with changes in feed rate and rotational speed for dissimilar welds made from AA 5083 and 6061-T6 aluminium alloys. These nuggets were obtained using a tool with a standard M5 threaded pin and the rake angle was 2 degrees. The advancing side of the welds is on the right hand side of each macrograph. The 6082 aluminium alloy is on the advancing side. There is a distinct difference in the appearance of the stir zone as the rotational speed increases.

---

<sup>1</sup> Reynolds, AP (2003)

<sup>2</sup> James et al, MN (2003)

<sup>3</sup> Dalle Donne, C and Biallas, G (1998)

<sup>4</sup> Hassan, Kh A.A et al (2003)

<sup>5</sup> Peel, M et al (2003)

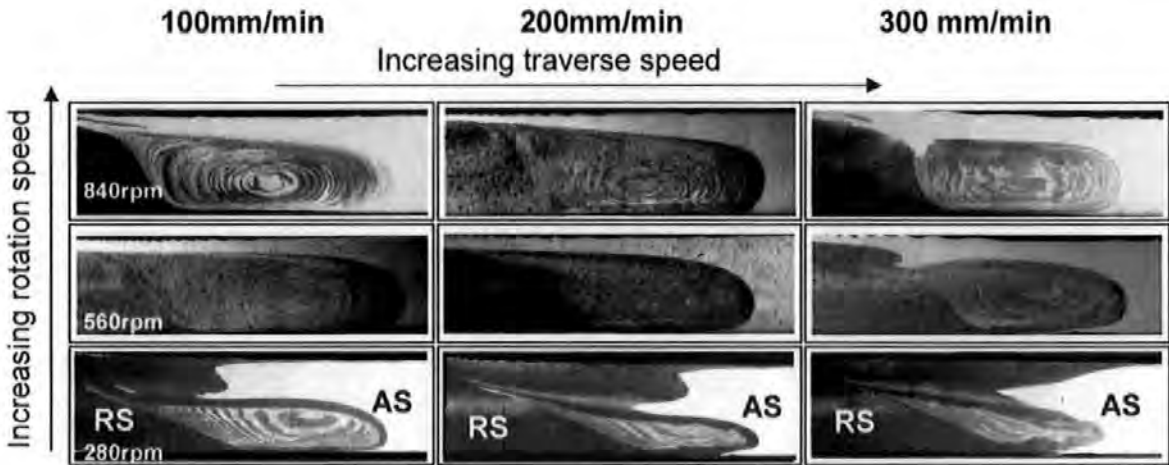


Figure 2.31: Macrographs showing the stir zone/TMAZ in dissimilar welds between 6061-T6 and AA 5083 aluminium alloys. 5083 is on the AS<sup>1</sup> (AS = advancing side, RS = retreating side).

Studies by Colligan et al<sup>2</sup> used a tool consisting of three flats machined into the pin rather than a conventional cylindrical tool. The shape of the nugget can be seen in Figure 2.32, which indicates a typical cross section of a weld made with a rake angle of zero degrees<sup>2</sup>. This is another example of how the tool geometry changes the appearance of the nugget.

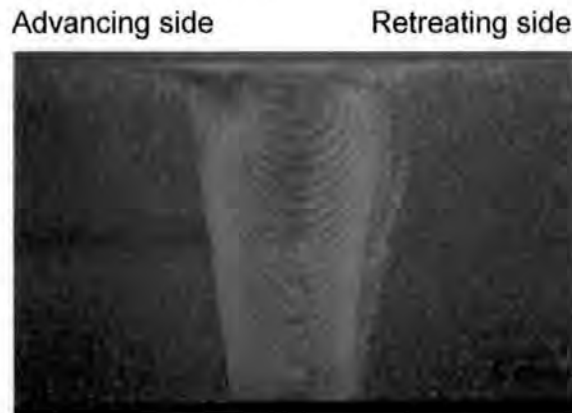


Figure 2.32: Transverse section of FSW 5083-H131 at zero rake angle made at a rotational speed of 250 rpm and a feed rate 127 mm/min<sup>2</sup>.

Studies by Yan et al<sup>3</sup>, shown in Figure 2.33, indicate that the nugget became wider as the rotational speed was increased at a constant feed rate, and the nugget decreased in width as the feed rate increased in welding where the vertical force was controlled.

<sup>1</sup> Peel, M et al (2003)

<sup>2</sup> Colligan et al (2001)

<sup>3</sup> Yan, J et al (2004)

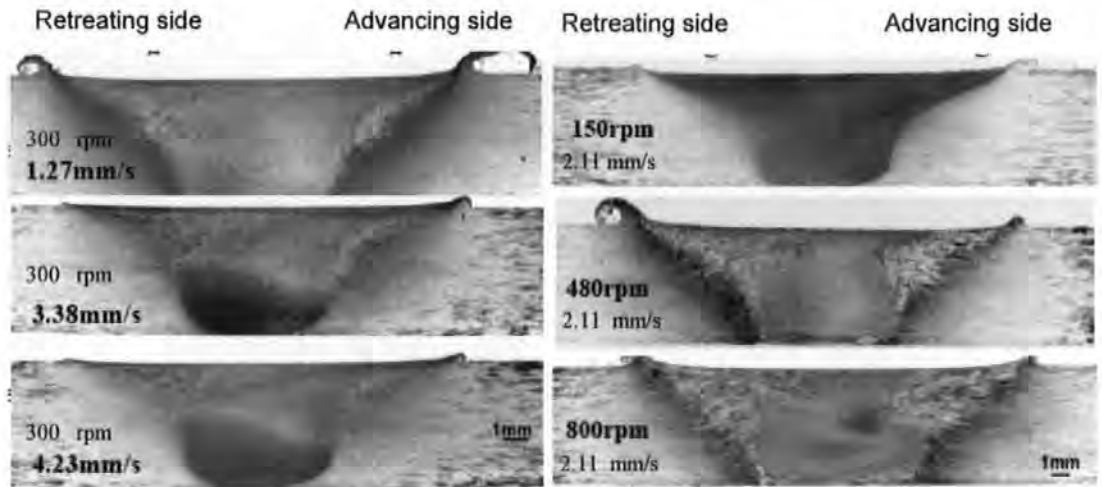


Figure 2.33: Variation in nugget size with rotational speed and feed rate for 2524-T351 aluminium alloy<sup>1</sup>.

The microstructure in the nugget is thus strongly dependent on local position along the weld, on rotational speed and on feed rate. The heat input per unit length (J/mm) becomes greater for low feed rates and high rotational speeds, leading to more uniform temperature distribution in a weld. Higher feed rates result in shorter thermal cycles and greater cooling rates that affect the strain rate experienced in the nugget zone. Strain rate is affected by feed rate and the size of the plastic zone.

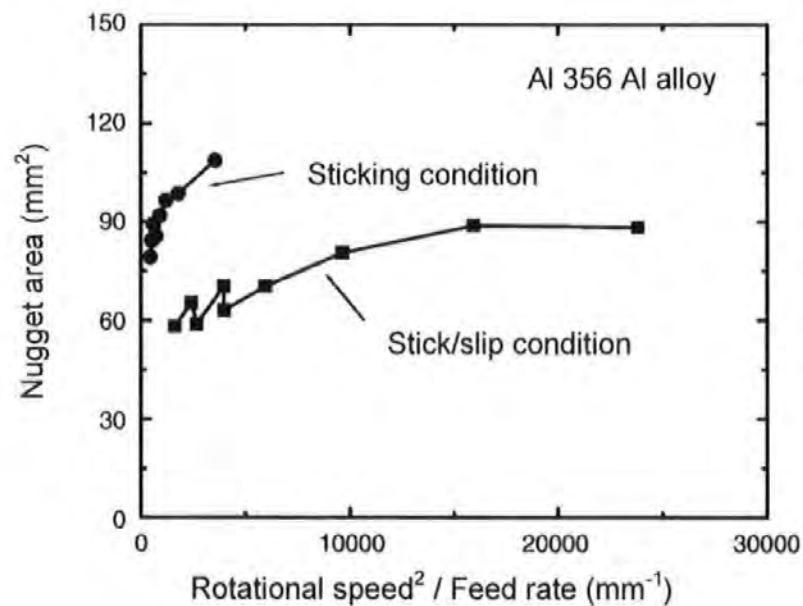


Figure 2.34: Variation of nugget area with the parameter  $w^2/f^2$ .

<sup>1</sup> Yan, J et al (2004)

<sup>2</sup> Sharma, SR and Mishra, RS (2005)

Sharma and Mishra<sup>1</sup> have observed that the nugget area changes with pseudo-heat index ( $w^2/f$ ). The results indicate that the frictional condition change from 'stick' at lower tool rotation rates to 'stick/slip' at higher tool rotation rates. The parameter  $w^2/f$  therefore seems to be an important welding parameter.

### 2.5.2 Grain size and hardness variation in the nugget

Grains in the weld nugget are usually equiaxed, much smaller than the base material and vary in size from 1-10  $\mu\text{m}$ <sup>2,3</sup>. Grain size variations are attributed to changes in strain, strain rate and temperature in the metal under the tool shoulder and between the tool centre-line and the edge of the weld nugget<sup>2</sup>. The average grain size have been shown to increase at both the top and bottom of a weld zone for 7010-T7651 with increasing rotational speed and at a fixed feed rate of 95 mm/min for 7101-T7651, as shown in Figure 2.35. Differences in grain size and hardness between the top and bottom surface of the weld arise from non-uniform thermal transients through the thickness, which therefore give different precipitate dissolution in the nugget region and during subsequent post-weld room temperature aging.

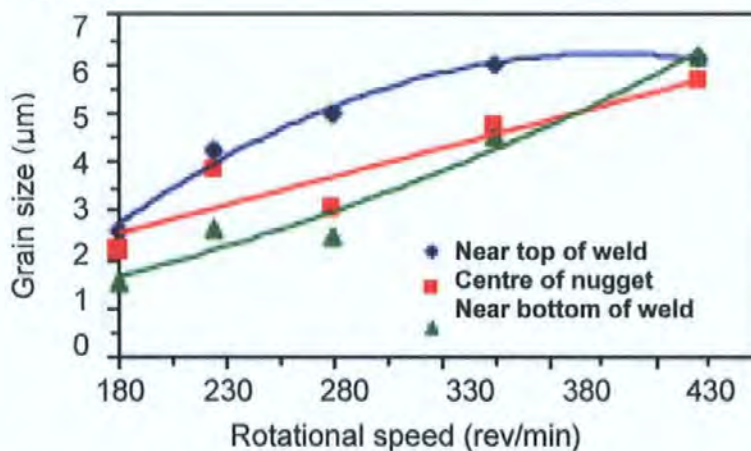


Figure 2.35: Variation of grain size through the nugget and as a function of rotational speed<sup>3</sup>.

Dislocation density is reported to be significantly lower in the weld nugget which supports the operation of a recrystallisation mechanism<sup>4</sup>. Other studies have shown that some grains in the nugget had higher dislocation densities than the

<sup>1</sup> Sharma, SR and Mishra, RS (2005)

<sup>2</sup> Threadgill, PL (1999)

<sup>3</sup> Hassan, Kh AA et al (2001)

<sup>4</sup> Flores, OV et al (1998), Liu, G et al (1997), Murr, LE et al (1998)

bulk of the nugget due to different thermal histories<sup>1,2</sup>. The typical variation in hardness throughout the cross section of FSW for most alloys is illustrated in Figure 2.36<sup>3</sup>. Maximum hardness values are obtained at the centre of the weld and minimum hardness values at the edge of the tool. Moving away from the nugget towards the advancing and retreating side, the hardness gradually increases until it attains the magnitude of the base material.

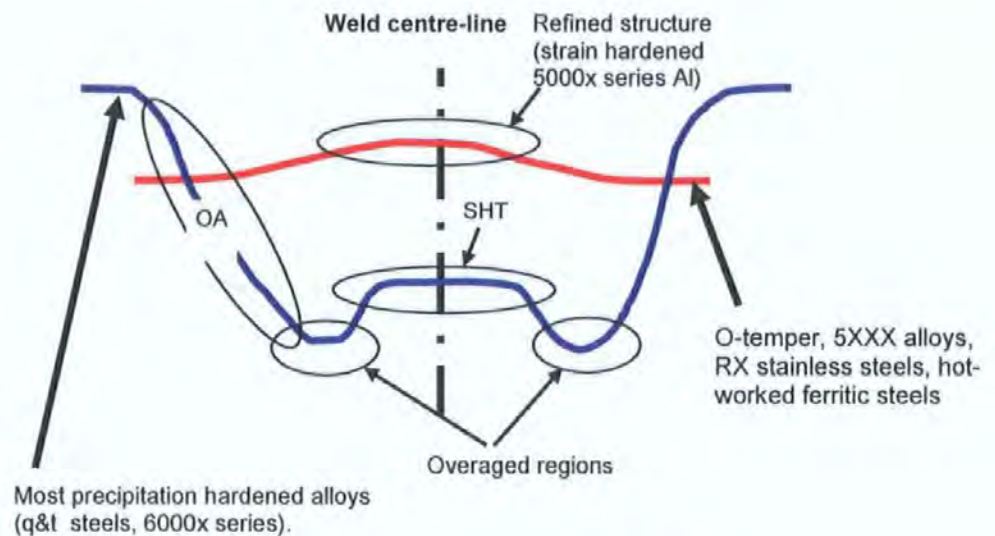


Figure 2.36: Vickers Hardness profiles for most FSW alloys<sup>3</sup>.

The variation in hardness shown in Figure 2.36 therefore indicates that maximum hardness in the TMAZ is related to smaller grain sizes. The effect of peak temperature on hardness during welding has been reported by Sato et al<sup>4</sup> for Al 6063. Their results indicated that increasing the peak temperature during welding from 400 °C to the solvus temperature of MgSi<sub>2</sub> of 518 °C produced an increase in grain size (70 – 40 HV) and hence a large decrease in hardness.

The shape of the hardness profile also changes significantly with rotational speed and depth within the weld. At the centre and root of the weld the width of the plateau (thus the width between the peaks in the HV plots) increases with rotational speed. At the top of the weld the plateau width is not affected by rotational speed. There are therefore optimum combinations of rotational speed

<sup>1</sup> Jata, KV et al (2000)

<sup>2</sup> Jata, KV and Semiatin, SL (2000)

<sup>3</sup> Reynolds, AP (2003)

<sup>4</sup> Sato, YS et al (1999a)

and feed that gives the best nugget zone properties. Figure 2.37 demonstrates this variation<sup>1</sup>.

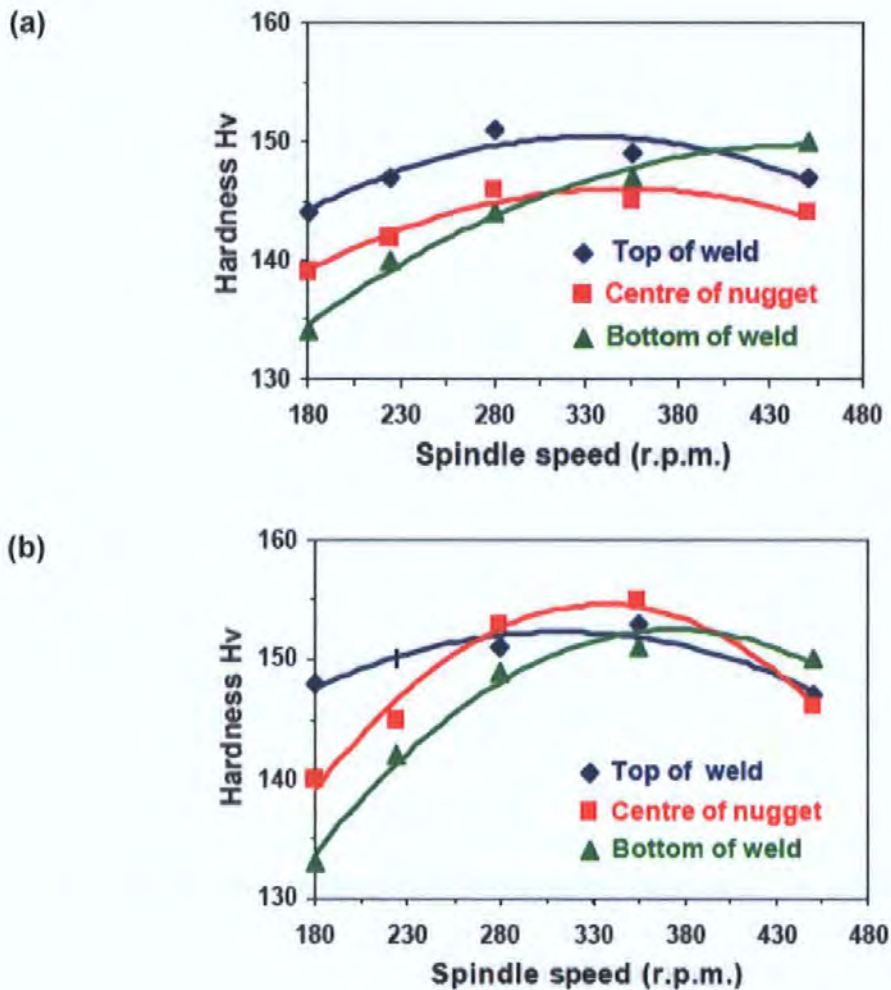


Figure 2.37: Hardness versus rotational speed for feed rates at (a) 59 mm/min and (b) 95 mm/min for 7010-T7651 aluminium alloy<sup>2</sup>.

Recent results by Yan et al<sup>3</sup> show that for FS welds made in precipitation-hardenable AA2524-T351 the tool rotational speed has the dominant effect on nugget properties. This occurs because the rotational speed is the primary determinant of peak temperature during welding. In this alloy increasing tool rotation speed to attain a peak temperature just below the incipient local melting temperature resulted in optimum tensile properties in the nugget. Excessive tool rotation speeds resulted in low ductility in the welds, due to localized grain boundary melting near the weld crown.

<sup>1</sup> Hassan, Kh AA et al (2001)

<sup>2</sup> Hassan, Kh AA et al (2001)

<sup>3</sup> Yan, J et al (2004)



The variation in grain size with various process parameters in 2524-T351 aluminium alloy is illustrated in Figure 2.38. The welding torque appears to be strongly related to the peak weld temperature and has a strong, inverse, linear relationship with grain size, and some nugget properties. Yan et al<sup>1</sup> suggest that the simple relationship between the nugget grain size (hence temperature) and the welding torque could be useful for indicating the onset of overheating. The welding pitch appears to be closely related to peak temperature for this set of welds, and may therefore be useful as a guide to weld temperature modification.

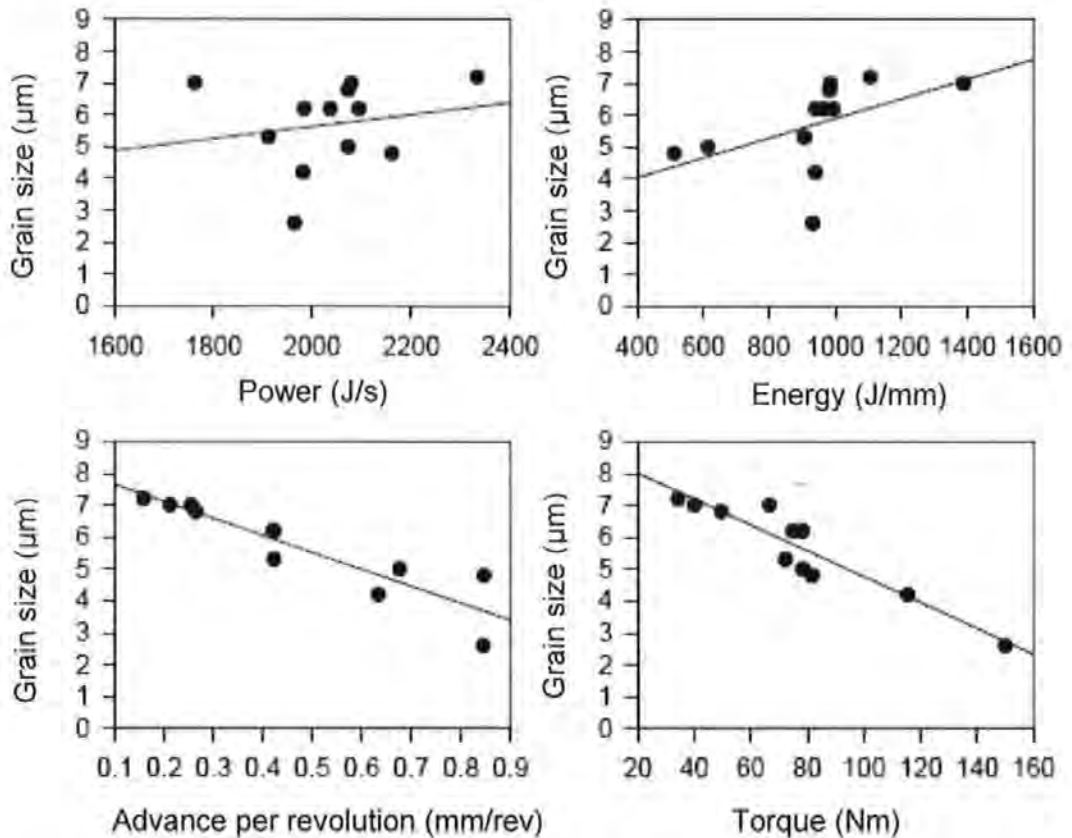


Figure 2.38: Variation of grains size with process parameters<sup>1</sup>.

Thermal finite difference, micro structural and tensile models have been applied to the FSW of Al-6056 by Gallais et al<sup>2</sup>. These results revealed that the peak temperature has a large influence on the hardness evolution through the weld. An increase of pitch resulted in a decrease in peak temperature, due to an increase in the heating and cooling rates. An increase in pitch also shifted the minimum hardness from the HAZ to the TMAZ region. Plastic deformation is localized in the region of lowest hardness values with sharp strain gradients around the softest regions resulting in low strain partitioning.

<sup>1</sup> Yan, J et al (2004)

<sup>2</sup> Gallais, C et al (2004)

Fracture location in tensile tests has been observed as occurring in the positions of largest strain and hardness minima for FS welds 7075-T651 aluminium<sup>1</sup>.

It is clear that feed rate, tool speed, pitch and the thermal cycle produced during welding, influence the magnitude and shape of the hardness profile in FS welds. For a given spindle speed grain size reduces with higher feed rate, while an increase in grain size is observed with higher levels of heat input per unit length.

In this thesis these concepts are examined for each weld. The aim is to link process input parameters with alloy related parameters and thus with property and performance parameters.

## 2.6 Mechanical properties

### 2.6.1 Defects

The defects occurring in FSW are now briefly discussed, with reference to their origin and effect on mechanical properties, since weld defects are often highly detrimental to the mechanical properties. Intrinsic weld-related defects occurring in fatigue samples are also investigated in this work. Defect levels are usually low in FSW since the weld zone produces a fine grained structure in the stirred region and the low heat input limits residual stresses to a low fraction of the proof strength of the weld metal<sup>2</sup>. FSW also overcomes problems with porosity and hot cracking associated with fusion welds. The quality of joints is affected by choice of tool profile, rotational speed, feed rate, tilt angle, plunge depth, welding gap tolerance, thickness mismatch and variation in plate thickness<sup>3</sup>. Good quality welds can only be produced within specific process windows<sup>4</sup>.

Large planar defects have also been observed on the fracture surfaces of fatigue specimens which apparently reflect the onion skin structure and are proposed to result from strain-partitioning at layer boundaries<sup>5</sup>. These are discussed in more

---

<sup>1</sup> Mahoney, MW et al (1998)

<sup>2</sup> James, MN et al (2004)

<sup>3</sup> Leonard, AJ and Lockyer, SA (2003)

<sup>4</sup> Midling, OT (2003)

<sup>5</sup> James, MN and Hattingh, DG (2002)

detail later in this thesis. Figure 2.39 indicates some of the discontinuities observed using phased array ultrasound and eddy current technologies<sup>1</sup>.

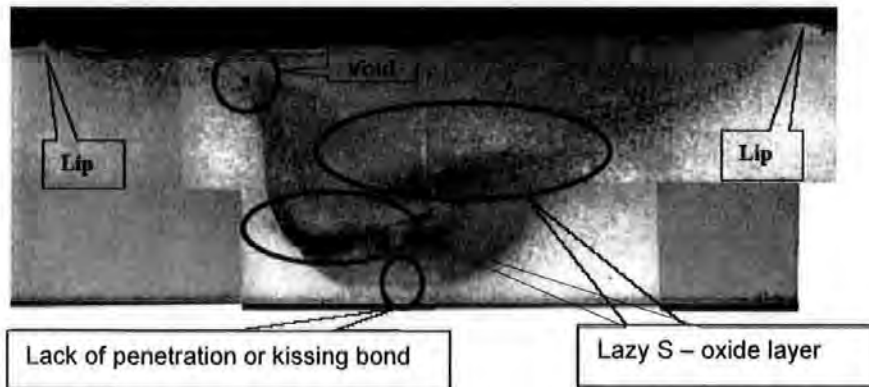


Figure 2.39: Typical defects observed in FSW<sup>1</sup>.

## 2.6.2 Type of defects in FSW

### 2.6.2.1 Voids

Voids are subsurface, volumetric flaws, which may be aligned with the welding direction<sup>2</sup>. Tunnel or wormhole defects are voids which are aligned in the welding direction and are usually found on the advancing side of the nugget<sup>3</sup>. Usually, once they are created, they continue until the end of the weld. An example is shown in Figure 2.40 (a). The formation of voids is likely to be due to fluid dynamics associated with the chaotic plastic flow in the weld zone, on the advancing side, in which the flow is in opposite directions above and below this zone, creating a flow singularity or a vortex<sup>3,5</sup> that can create voids of significant magnitudes, as shown in Figure 2.40(b).

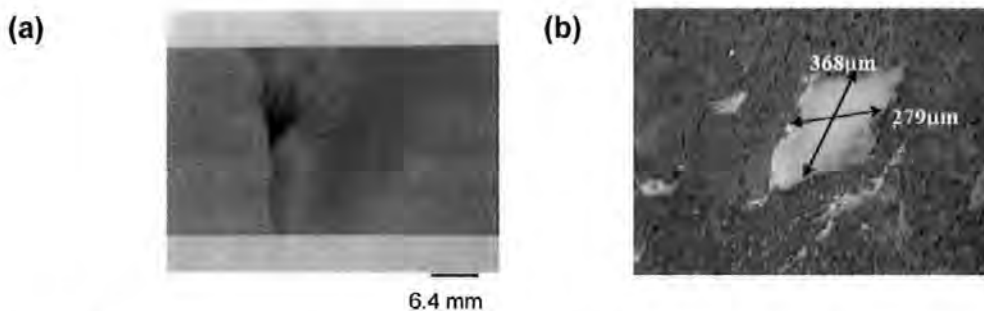


Figure 2.40: (a) Wormhole or tunnel defect in Al 5083-H1314<sup>4</sup>.  
(b) Large void defect in the cross section of a FSW in Al 5083-H321<sup>5</sup>.

<sup>1</sup> Camassa, A and Capitani, V (2001)

<sup>2</sup> Bird, C (2003)

<sup>3</sup> Reynolds, AP et al (2003b)

<sup>4</sup> Colligan, KJ et al (2003)

<sup>5</sup> James, MN et al (2004)

These flow singularities will be affected by feed rate, rotational speed and tool geometry<sup>1</sup>, a vertical force that is too low, or by gaps between the faying surfaces. Voids breaking through to the surface of the welds are referred to as faying surface flaws<sup>1</sup> and are caused by entrapped oxide<sup>2</sup>. If the welding pressure  $F_z$  varies along the weld line, then internal voids can be created that are not visible on the surface. Large increases in the feed rate (e.g. four times the 'normal rate' for aluminium alloy 2014) has also been shown to generate these voids<sup>3</sup>. Leonard and Lockyer<sup>1</sup> proposed that the material receives less heat input into the plasticized material which is therefore less easily forged by the shoulder, resulting in unconsolidated voids. These voids occur on the advancing side, supporting the hypothesis proposed by Bendzack<sup>4</sup>. Results by Leonard and Lockyer also showed that voids occurred at the top advancing side of welds, as demonstrated in Figure 2.41<sup>1</sup>.

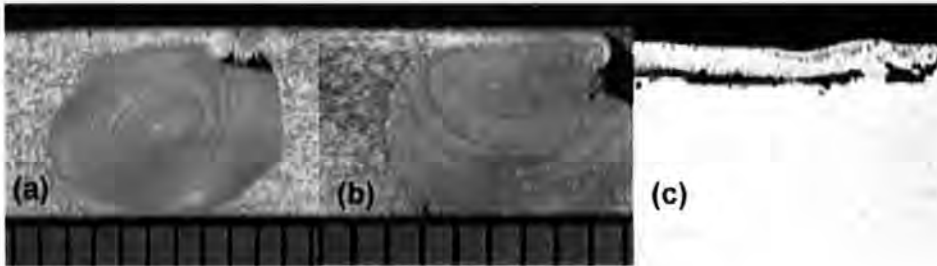


Figure 2.41: (a) void on advancing side of weld  
 (b) surface breaking void i.e. faying surface flaw  
 (c) void beneath the upper surface of the weld<sup>1</sup>.

Large circular or elliptical voids (Figure 2.42) have also been observed on fatigue fracture surfaces and could be associated with the vortex shedding proposed by Bendzack<sup>4</sup>, while the polygonally shaped voids seen in Fig. 2.40(b) could be created by dynamic recrystallisation rather than vortex shedding<sup>5</sup>.

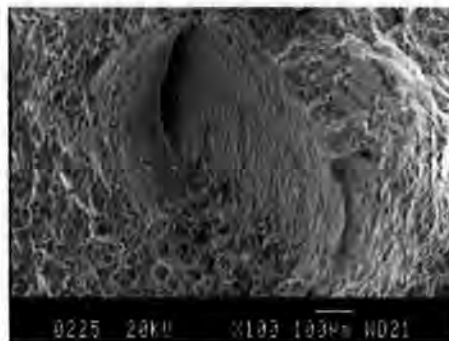


Figure 2.42: Elliptical void on the fracture surface of a FSW sample<sup>5</sup>.

<sup>1</sup> Leonard, AJ and Lockyer, SA (2003)

<sup>2</sup> Bird, CR (2004)

<sup>3</sup> Colligan, KJ et al (2003)

<sup>4</sup> Bendzsak, GJ et al (2000)

<sup>5</sup> James, MN et al (2003)

The voids described above have been seen to reduce the fatigue strength of FSW specimens by 15-20%<sup>1</sup>. In that work, crack path defect behaviors appeared to be triggered by crack plasticity effects and were proposed to reflect the mechanism of thermo-mechanical deformation that underlies the onion skin structure<sup>1</sup>.

The wormholes or tunnel defects shown in Fig 2.41(a) occur at the advancing sides of welds and have also been studied by Reynolds et al<sup>2</sup>. In that work, a weld was made in 9 mm thick plate AA2219-T8, at a feed rate of 75 mm/min. High forces in the welding direction (shown as  $F_x$  in Figure 2.43) correlated with welds containing defects and the minima region shown in Figure 2.43 corresponded with good weld quality. Online measurement of  $F_x$  may therefore be used as an indicator of the quality of welds. The wormhole phenomenon was explained by Reynolds et al<sup>2</sup> as follows: Material flows around the advancing side of the tool and recombines behind the tool. Once the material is pushed from the retreating side to the advancing side there is no driving force which will promote its movement back behind the tool, hence the volume of material moving behind the tool to replace the volume displaced by the tool will be insufficient to fill the gap and a volumetric defect occurs. As tool rotational speed increases more flow occurs around the advancing side until bifurcation of the flow around the pin on the advancing side is achieved. Flow bifurcation is associated with an increase in the predicted x-axis force.

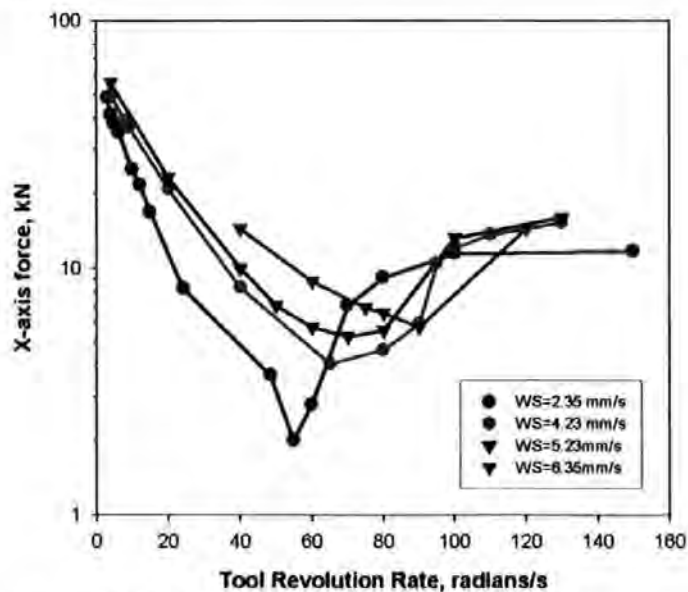


Figure 2.43: Variation of  $F_x$  with rotational speed<sup>2</sup>.

<sup>1</sup> James, MN et al (2003)

<sup>2</sup> Reynolds, AP et al (2003)

### 2.6.2.2 Root defects or kissing bonds

So called "kissing bonds", or entrapped oxide defects, occur when single pass welds achieve only partial bonding because the tool is not plunged deep enough and/or the plate thickness varies along the plate<sup>1</sup>. The oxide interface between the weld plates must be adequately disrupted to form a good bond<sup>1</sup>. If the pin is too short for the material thickness being welded, part of the joint is forged together without sufficient stirring of the surface oxide layers<sup>1</sup>. The severity of this defect depends on the planar extent and proximity of the adjacent oxide particles. Kissing bonds are the most difficult to detect with non-destructive testing techniques, since a very small attenuation in sound or electricity occurs across the flaw<sup>2</sup>.

Such flaws can occur as root defects and can then be detected during U-bend testing. Investigations by Dickerson and Przydatek<sup>1</sup> indicated that flaw-free and flawed welds had similar yield strengths, but that the flawed welds showed lower ductility in tensile tests. They had to choose parameters significantly outside of the usual process parameter tolerance range to obtain root defects. Some of the FSW cross sections in their work showed a thin line that ran from the weld root at the point where the original plates were butted together, up to the retreating side of the nugget; this appears to be a remnant of the joint-line which has occasionally been termed a 'Lazy-S' structure<sup>3</sup>. This feature could be seen in both flaw-free and flawed welds, which failed along these remnants of the joint-line.

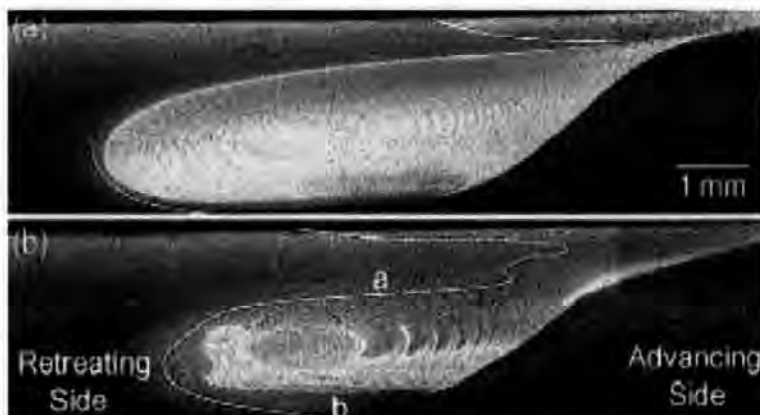


Figure 2.44: Lines indicating remnants of the weld line<sup>4</sup>.

<sup>1</sup> Dickerson, TL and Przydatek, J (2003)

<sup>2</sup> Bird, CR (2004)

<sup>3</sup> Peel, M (2005)

<sup>4</sup> Peel, M et al (2003)



Figure 2.45: Root flaws indicated by the arrow<sup>1</sup>.

To avoid root flaws a tolerance on nominal plate thickness of  $\pm 0.2$  mm is generally required in FSW<sup>2</sup>. The occurrence of these so called kissing bonds also seems to be alloy specific. Al 5083-H321 has been shown to be more susceptible to these defects than 5083-O or 6082-T6<sup>2</sup>. Root flaws of size 1 mm had a significant effect on the fatigue life of 5083-H321<sup>3</sup>. Root flaws are extremely difficult to detect using non-destructive techniques especially the kissing bond oxide entrapped defects<sup>4</sup>.

### 2.6.2.3 Planar facets

Large planar facets, 0.1-1.5 mm, have been observed in fast fracture regions on fatigue samples of 5083-H321 aluminium alloy and are associated with the characteristic 'onion skin' pattern often observed both transverse to, and longitudinally along, the macrostructure of the weld nugget region of the TMAZ<sup>2</sup>. They can occur in sequences, reflecting the weld pitch which have been proposed to be associated with onion skin layer interfaces. The mechanism of their formation is still not fully clear. They could be influenced by the chaotic plastic flow involved in generating the onion skin layers in which pressure and temperature conditions may vary in parts of the FS weld that lead to partial bonds between deposited layers<sup>5</sup>. However, it has been proposed that it is more likely that these defects arise because the peculiar thermo-mechanical history in the FS

<sup>1</sup> Leonard, AJ and Lockyear, SA (2003)

<sup>2</sup> Przydatek, J (2000)

<sup>3</sup> Dickerson, TL and Przydatek, J (2003)

<sup>4</sup> Leonard, AJ and Lockyear, SA (2003)

<sup>5</sup> James, MN et al (2005)

weld region can lead to strain partitioning in the onion skin structure during loading (e.g. during fatigue crack growth or fast fracture)<sup>1</sup>. In turn, this is proposed to trigger layer interface ductility-drop cracking, causing the large planar facets observed<sup>1</sup>. If this proposed mechanism is correct, then analysis of force footprint during welding becomes important to understanding and optimising the flow process/tool geometry interaction that underlies the onion skin structure.



Figure 2.46: Planar facets observed on a bend fatigue specimen<sup>1</sup>.

Hashimoto et al<sup>2</sup> have presented a summary of the effects of tool speed and feed rate on defects in 5083-O, 2024-T6 and 7075-T6 aluminium alloys. This is presented in Figure 2.47 as a function of tool revolutions/mm of feed (thus some sort of energy parameter/unit weld length). Their results indicate that welds with subsurface defects were obtained at lower values for example higher pitch values Al 5083-O exhibited a wider range of optimum conditions for sound welds than 2024-T6 and 7075-T6.

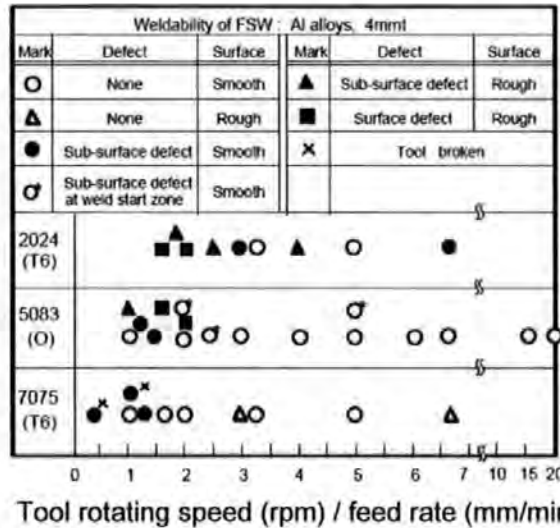


Figure 2.47: Summary of defects in welds for 2024-T6, 5083(O) and 7075-T6 aluminium alloys<sup>2</sup>.

<sup>1</sup> James, MN et al (2003)  
<sup>2</sup> Hashimoto, T et al (1999)



FSW do contain defects as discussed in this section. Some attempts have been made to relate defect formation with FSW parameters. This research study investigates the defects observed from optical macrographs as well as defects at the initiation site on fatigue specimens to determine whether the type of defect formed could be related to input and/or process parameters. The tensile and fatigue strengths are also compared to the type of defects formed in the FS welds.

### 2.6.3 Tensile Investigations

The tensile properties of FS welds, as a function of process parameters, have been studied by several researchers<sup>1,2</sup>. Figure 2.48 illustrates the effects of tool rotational speed and feed on the tensile properties of the nugget zone for AA 7010-T7651 alloy<sup>1</sup>. The base metal values are shown as a dashed line. The 0.2% proof stress shows relatively minor changes ( $\approx 10\%$ ) with spindle speed and feed rate. However, the UTS and ductility values varied sharply as a function of spindle speed, but were less strongly affected by feed rate (about 10%, the same as proof stress). From Figure 2.48 it is evident that higher UTS and proof strength values occur at higher feed rates for all spindle speeds examined. In the case of UTS and ductility maximum values are observed at higher spindle speeds, with increasing feed rates leading to the maximum value occurring at higher spindle speeds. The proof stress shows a variation of up to 10% with rotational speed and feed rate. The tensile strength shown in Figure 2.48 (b) varies up to 25% with tool speed and 10% with feed rate. Figure 2.48 (c) shows that the ductility varies up to 100% to 700% with the variation of rotational speed and from 60% to 100% with feed rate. The ductility of the welds is probably highly dependent on the local micro-strain variations that are dominated by heat input or plastic flow. The ductility is therefore very strongly affected by both feed rate and rotational speed. The tensile and proof strength are macro-level (gross) properties and are less affected by these local variations in microstructure.

---

<sup>1</sup> Hassan, Kh AA et al (2001)

<sup>2</sup> Lee, WB et al (2003)

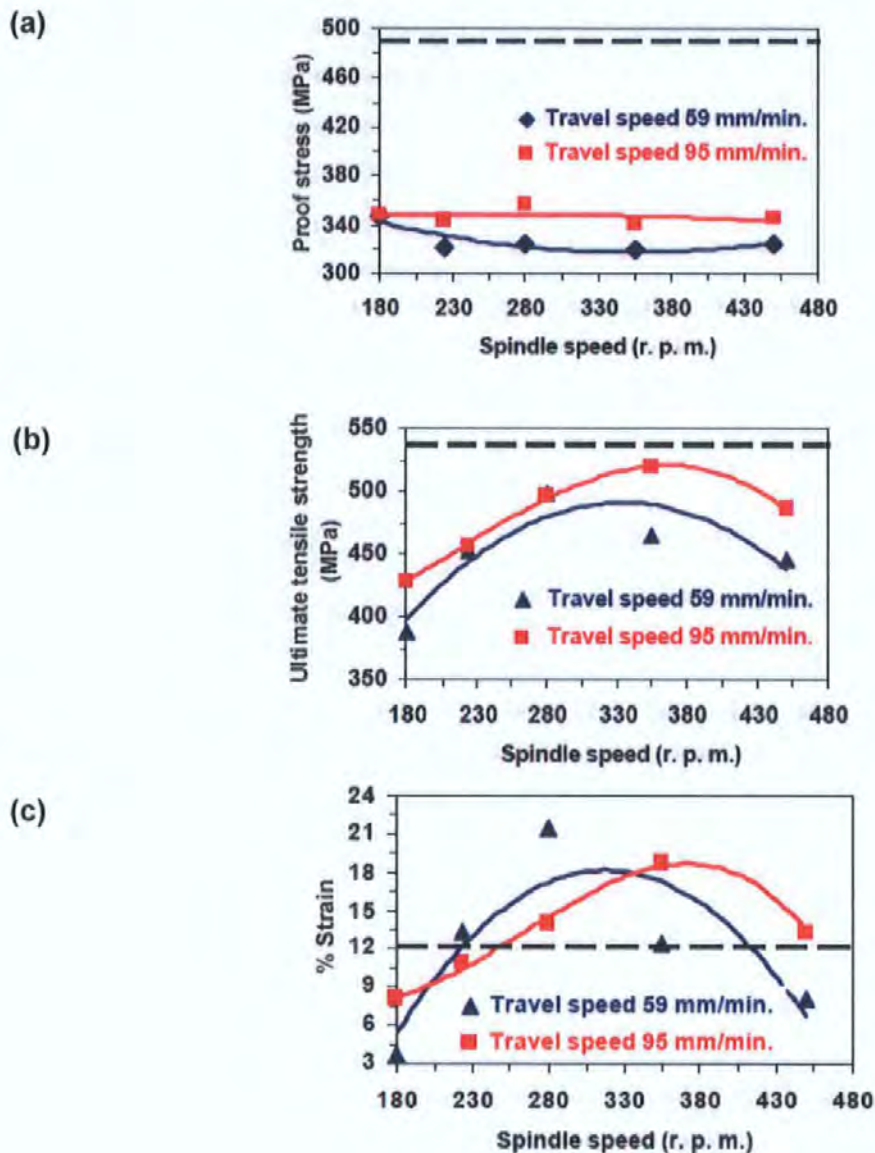


Figure 2.48: Tensile properties of the nugget zone for AA 7010-T7651. The properties of the parent plate are shown as a dashed line<sup>1</sup>.

In contrast to the results of Hassan et al<sup>1</sup>, investigations by Lee et al<sup>2</sup> showed that the UTS and yield strength for FS welds in A 356 cast aluminium alloy were virtually constant over a feed rate range of 100-200 mm/min. A reduction in yield strength and UTS in the nugget zone occurred for welds in Al 7075-T651 alloy while elongation remained unchanged due to a reduction in the number of dislocations and hardening precipitates in the HAZ<sup>3</sup>. Contrary to all the results previously published Lee et al showed that the tensile properties of the welds were 20% greater than the parent metal on A356 aluminium alloy. This was attributed to the fact that the eutectic Si particles are more homogeneously distributed and the

<sup>1</sup> Hassan, Kh AA et al (2001)

<sup>2</sup> Lee, WB et al (2003)

<sup>3</sup> Mahoney, MW et al (1998)

voids and shrinkage defects in the as cast-materials disappeared after mixing of the material during welding.

Studies by Peel et al<sup>1</sup> have revealed that tensile strength was dominated more by heat input than by mechanical deformation in 3 mm plates of alloy AA5083. Increasing the heat input made the weld nugget wider, flatter and more homogeneous. The ultimate tensile strength decreased by 61% when the feed rate was increased by 50%. This is opposite to the trends observed by Hassan et al<sup>2</sup>.

Equally, results from Kwon et al<sup>3</sup> indicated that hardness and tensile strength of aluminium 1050 increased by 33%, while decreasing rotational speed by 58% due to grain refinement, when using a special sub-conical head pin designed tool.

For the case of 5083-O aluminium, as shown in Figure 2.49<sup>4</sup>, ultimate tensile strength has been observed to increase with increasing values of the parameter (1/tool pitch) because the heat input decreases. It was also found for low (1/pitch) values (thus low energy input) and sub surface defects were introduced. The work of Hasimoto et al<sup>4</sup> cannot be compared with the other work discussed in this section, since specific feed rates and rotational speeds cannot be extracted from the given pitch values.

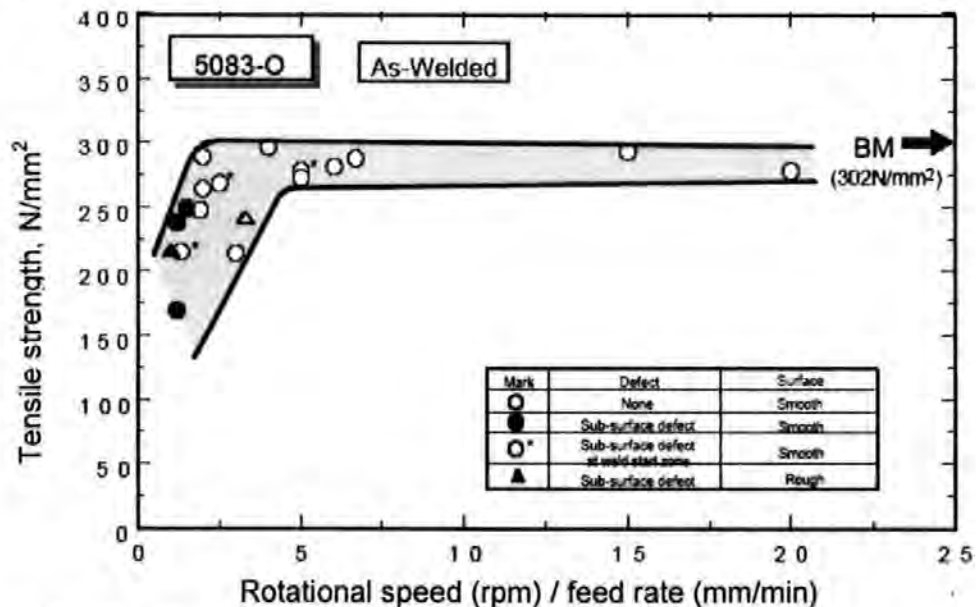


Figure 2.49: Effect of pitch on tensile properties of 5083-O<sup>4</sup>.

<sup>1</sup> Peel, M et al (2003)

<sup>2</sup> Hassan, Kh AA et al (2001)

<sup>3</sup> Kwon, YJ et al (2003)

<sup>4</sup> Hasimoto, T et al (1999)

The locations of fracture in tensile tests are affected by the FS process parameters and are different for different materials, as summarized in Figure 2.50<sup>1</sup>. The fracture position is determined as the distance from the centre of the weld to the fracture initiation site and is given as a negative value when the fracture initiation occurs on the retreating side. As the pitch increases, fracture initiation moves towards the centre of the weld for 6061-T6 but not for 1050-H24. This phenomenon was explained by the authors as being related to the position of the hardness minima. These moved closer to the centre of the weld as pitch increased and hence caused the fracture initiation sites to move towards the centre of the weld.

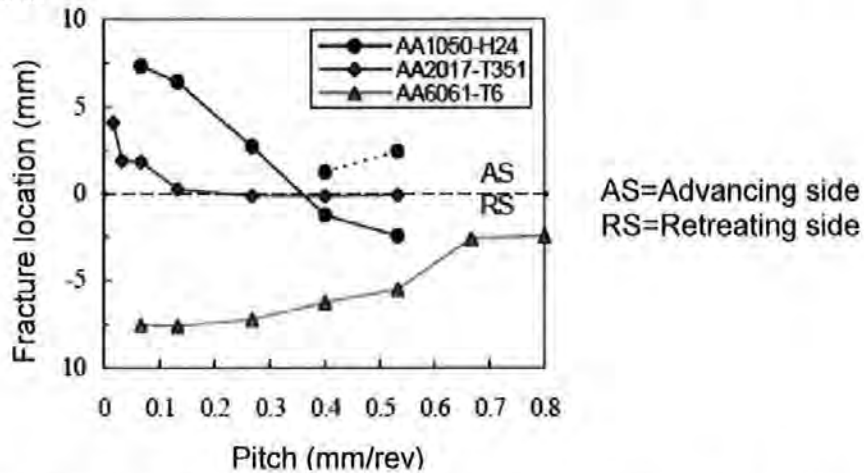


Figure 2.50: Tensile test fracture locations for three different types of alloys<sup>1</sup>.

In summary, the tensile strength, ductility and fracture locations can be affected by feed rate, rotational speed and pitch values. The effect is also strongly related to heat input into the weld. No information was found in the research literature that relates tensile properties or fracture locations with process parameters. The tensile strength is correlated to process parameters in this thesis.

#### 2.6.4 Fatigue strength

This section provides a summary of research performed by other authors on the dynamic performance of FS welds. It is important to understand the fatigue characteristics of FSW welds because of the potentially wide range of engineering applications of the FSW technique. It is well known that material properties, residual stresses, specimen geometry and stress concentrators have an influence on fatigue life<sup>2</sup>. Fatigue failures in fusion welds are usually at the weld site, either

<sup>1</sup> Liu, HJ et al (2003)

<sup>2</sup> Dieter, GE (1976)

along or adjacent to the weld toe. The reduction in thickness and scored surface topography<sup>1</sup> of FSW provides stress concentrators, creating a notched effect, and will hence influence crack initiation and accelerate crack growth.

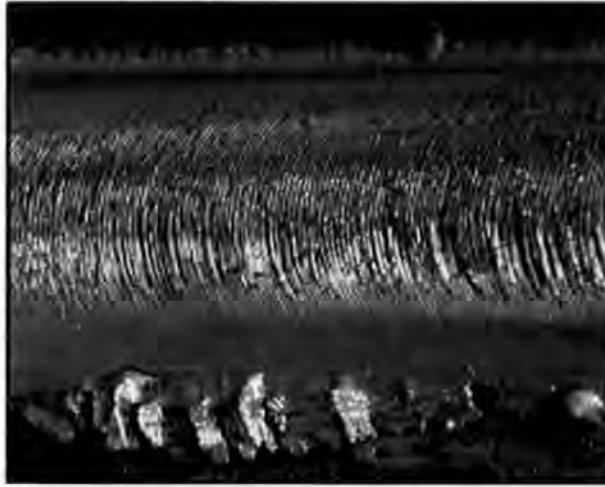


Figure 2.51: Surface topography of FSW<sup>1</sup>.

Fatigue cracks usually occur within the scored region and at the edge of the tool shoulder, that is at the side flash or at points of minimum hardness<sup>2,3</sup>, as well as at typical FSW defects such as 'lack of penetration' due to oxide inclusions under the lip of the weld toe<sup>3,4</sup>. Generally speaking these defects result from incorrect tool geometry and process parameter selection. For instance, lack of bonding in the weld root occurs mostly if the pin length is too short for the plate thickness being welded. It may also occur due to low heat input or incorrect tool tilt angle.

Lomolino et al<sup>1</sup> investigated the available fatigue data on FSW of 2024-T3, 5083-H 321, 6013-T6, 6056-T4 and 7475-T76 aluminium alloys and statistically analyzed the data to obtain a set of reference fatigue curves. Their results indicated that the fatigue strength of the FS welds was 3% lower compared to the parent plate at  $2 \times 10^6$  cycles in naturally aged polished aluminium samples tested at lower R ratios. Fatigue strength curves obtained from statistic analysis of the available data, at the lower 95% confidence limit, were compared with fatigue design curves given in Eurocode 9<sup>1</sup>. The legends in the graph are explained as follows: The solid lines represent FSW natural aged 5xxx parent plate, 5xxx base material and artificial aged 5xxx. The dashed lines represent E9 higher base material class, E9 butt

<sup>1</sup> Lomolino, S et al (2004)

<sup>2</sup> Bradley, GR (2000)

<sup>3</sup> Bussu, G and Irving, PE (1999)

<sup>4</sup> James, MN and Hattingh, DG (2002)

joints mechanically machined and E9 welded butt joints, respectively. These indicate that the fatigue behaviour of friction stir welded joints approaches base material values, supporting results previously reported in the research literature<sup>1</sup>.

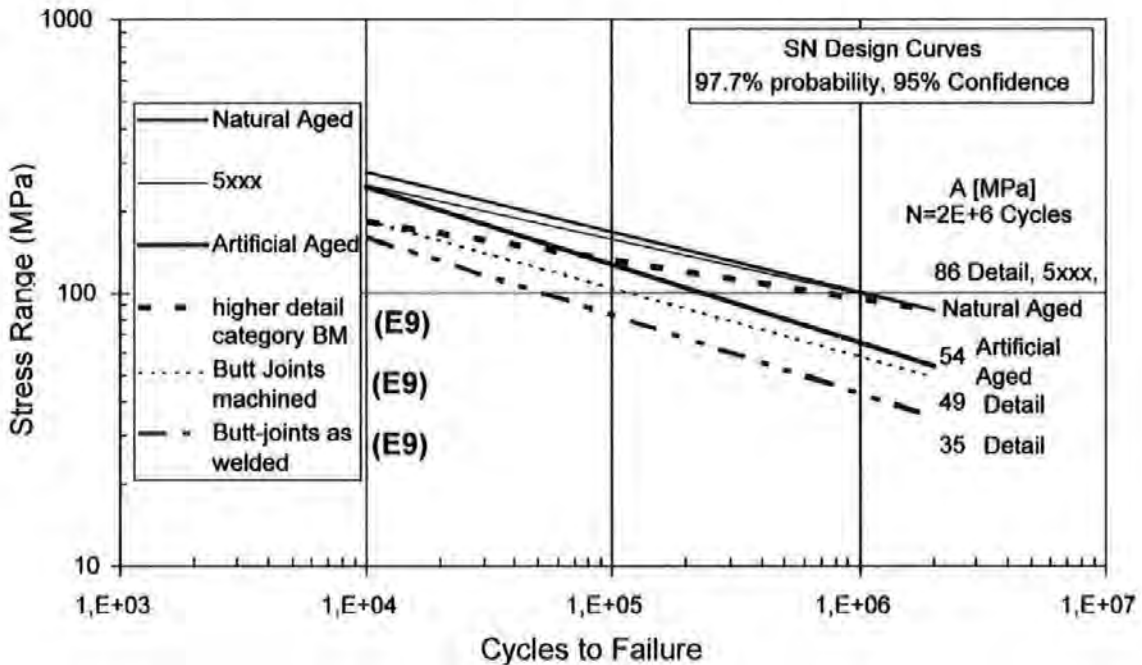


Figure 2.52: Stress life fatigue data for FSW 5xxx series butt welds at R=-1 compared with Eurocode 9 design curves<sup>1</sup>.

Figure 2.52 shows that FSW joints exhibit higher fatigue strengths than indicated by Eurocode 9 recommendations.

High fatigue strength can only be achieved if the root of butt welds is fully bonded. Work by Booth and Sinclair<sup>2</sup> showed that initiation sites for fatigue failures associated with the nugget were linked to discontinuities in the flow pattern, which showed no effect of hardness. Bussu and Irving<sup>3</sup>, however, indicated that the initiation of fatigue cracks in specimens transverse to the weld run could be correlated with the hardness minima and with oxide particles of 10-50  $\mu\text{m}$  near the surface of the weld. There was also a correlation between tensile properties and fatigue data in 2024-T351 aluminium plates, as expected, with higher tensile strength giving higher fatigue strength values. Their results also indicated that samples cut longitudinally to the weld had fatigue lives shorter by between 3.2 - 3.5 times than transverse samples over the stress range of 225 - 260 MPa. There was a difference of less than 25% in the stress region of 90 MPa at  $10^7$  cycles.

<sup>1</sup> Lomolino, S et al (2004)

<sup>2</sup> Booth, D and Sinclair, I (2001)

<sup>3</sup> Busu, G and Irving, PE (1999)

Results by Ericsson and Sandström<sup>1</sup> (Figure 2.53) indicated that feed rate had no significant influence on the tensile strength and fatigue properties of 4mm thick 6082-T6 and 6082-T4, over a range of feed rates between 700-1400 mm/min and tool speeds between 2500 rpm and 2200 rpm. Lowering the feed rate, thus increasing heat input, seemed to increase the fatigue performance by approximately 20% at a low stress level of 70 MPa<sup>2</sup>. An increase in ductility apparently makes the material less sensitive to stress concentration. The average fatigue strength was about 140 MPa at  $5 \times 10^5$  cycles<sup>1</sup>. This is 57% of the average UTS strength of the FS welds.

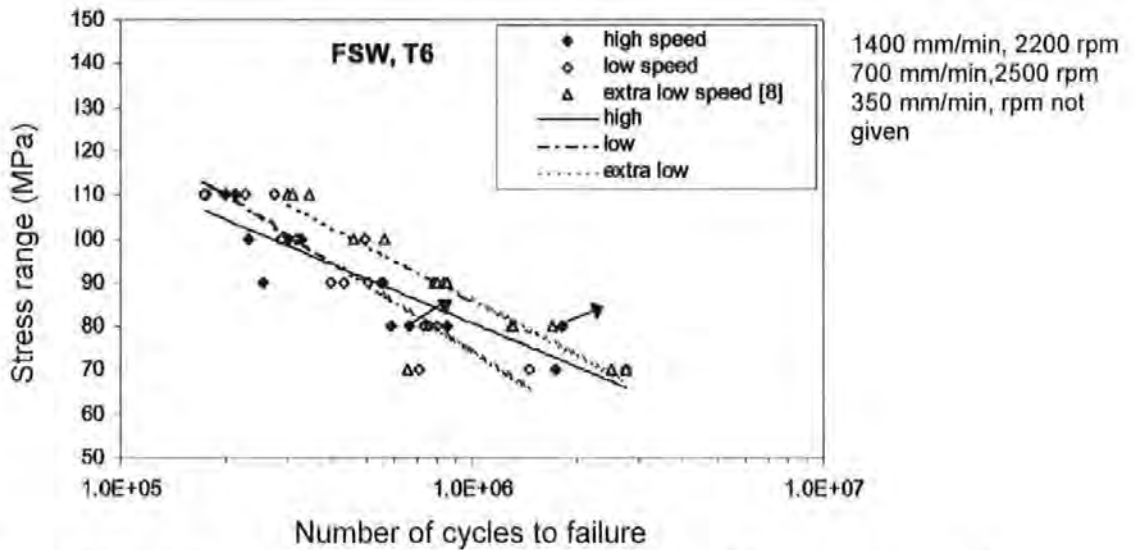


Figure 2.53: Influence of welding speed on fatigue life of FSW specimens of 6082-T6 + post weld aged<sup>1</sup>.

Hori et al<sup>3</sup> found that the fatigue life of FSW extruded flat bar of JIS6N01-T5 aluminium alloy decreased from  $10^7$  to  $5.5 \times 10^5$  cycles at a stress level of 50 MPa when pitch was increased from 0.14 mm/rev to 0.42 mm/rev but remained unchanged for changes in feed rate at the same pitch when tested under a stress ratio of -1, as shown in Figure 2.54 (a) and (b)<sup>3</sup>. This occurred due to the increase of un-welded groove on the root side of the weld. However, when the un-welded groove was skimmed, the fatigue strength of the FSW weld was unchanged by changes in the feed rate/rpm ratio.

<sup>1</sup> Ericsson, M and Sandström, R (2003)

<sup>2</sup> www.southampton.ac.uk/ses/docs/pgconf2001/diccon\_pgc.pdf

<sup>3</sup> Hori, H et al (1999)

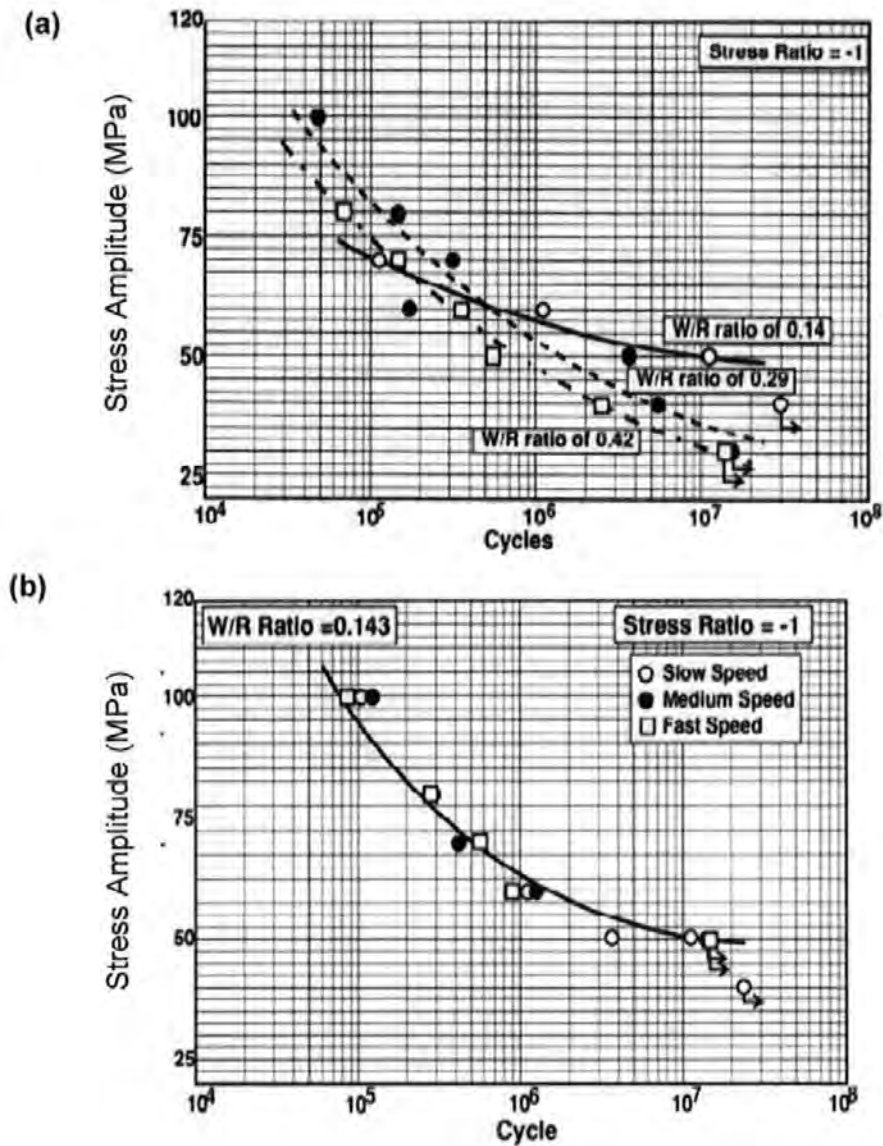


Figure 2:54: Variation of fatigue life with  
 (a) pitch  
 (b) rotational speed<sup>1</sup>.

Bussu and Irving<sup>2</sup> reported that skimming a 0.5 mm thick layer from both root and top sides removed all the profile irregularities and resulted in fatigue strengths, of both transverse and longitudinal 2025-T351 FSW aluminium specimens, comparable to that of the base metal. Similarly, Magnusson and Källman<sup>3</sup> reported that the removal of a 0.1–0.15 mm thick layer from the top side by milling can result in a significant improvement of 25% in the fatigue strength of FS welds. These observations suggest that the observed fatigue life is generally limited by surface crack nucleation and that inherent defects or internal flaws generally play a secondary role in successful FS welds. The effect of FSW parameters on the

<sup>1</sup> Hori, H et al (1999)

<sup>2</sup> Bussu, G and Irving, PE (1999)

<sup>3</sup> Magnusson, L and Källman, L (2000)



fatigue strength is complicated and no consistent trend has been obtained to date. Hori et al<sup>1</sup> reported that for a specific mm/rev ratio, the fatigue strength of the FS weld was not affected by the tool traverse speed. However, Biallas et al<sup>2</sup> observed that for a constant rev/mm ratio = 10, the fatigue strength of 2024-T3 aluminium alloy in plates 1.6 mm and 4 mm thick was increased from 100050 to 100150 cycles while simultaneously increasing tool rotation and traverse speed. S–N data for 1.6 mm thick FS welds made at a high tool rotation rate of 2400 rpm and a traverse speed of 240 mm/min were even within the scatter band of the base metal.

Low plasticity burnishing (LPB) after FSW can enhance the fatigue life of the FSW joints. Jayaraman et al<sup>3</sup> reported that LPB processing increased the high cycle fatigue endurance of FSW aluminum alloy 2219-T8751 by 80% due to the introduction of a deep surface layer of compressive residual stress, coupled with surface polishing. Compressive residual stresses at near-surface and high-quality surface finish are generally desirable for good fatigue properties. While the fatigue resistance of FSW specimens in air is inferior to that of the base metal, Pao et al<sup>4</sup> reported that FSW and parent metal specimens of 2519-T87 aluminium alloy have similar fatigue lives.

Investigations by James and Hattingh<sup>5</sup> were the first to report fairly detailed results relating fatigue strength with feed rate and rotational speed in FSW. A maximum decrease of 19% in endurance limit stress at 10<sup>7</sup> cycles was observed in 5083-H321 aluminium alloy in the as welded state. This reduced to 11% for polished specimens as, travel speed increased from 80 to 200 mm/min, as illustrated in Figure 2.55. It seems that the lowest speed provided the best performance in terms of both absolute endurance limit value, and in terms of the smallest reduction in strength between the as-welded and polished conditions. The surface condition may vary between specimens and thus could also contribute to scatter observed in the data.

---

<sup>1</sup> Hori, H et al (1999)

<sup>2</sup> Biallas, G et al (1999)

<sup>3</sup> Jayaraman, N et al (2003)

<sup>4</sup> Pao, PS et al (2003)

<sup>5</sup> James, MN and Hattingh, DG (2002)

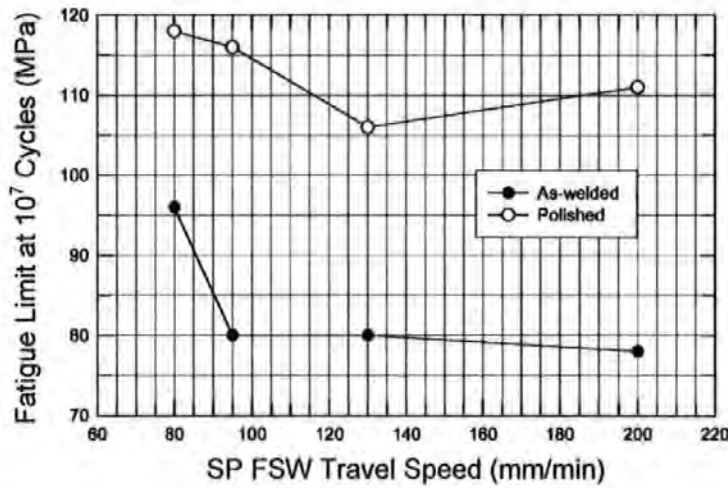


Figure 2.55: Fatigue limit corresponding to a fatigue life of 10<sup>7</sup> cycles as a function of travel speed<sup>1</sup>.

The fatigue strength of welds containing flaws is needed to enhance confidence in the design and application of friction stir welded joints, since it is not always possible to assume that welds are flawless. Research by Dickerson and Przydatek<sup>2</sup> showed that root flaws up to 0.35 mm deep in welds made in 5083-O and 6082-T6 aluminium alloys exceed the two lower Eurocode design life curves as illustrated in Figure 2.56. The design categories 14-3.2 and 18-3.2 relate respectively to partial penetration and full-penetration welds made from one side. The design category 35-4 relates to double-sided (full-penetration) fusion welds.

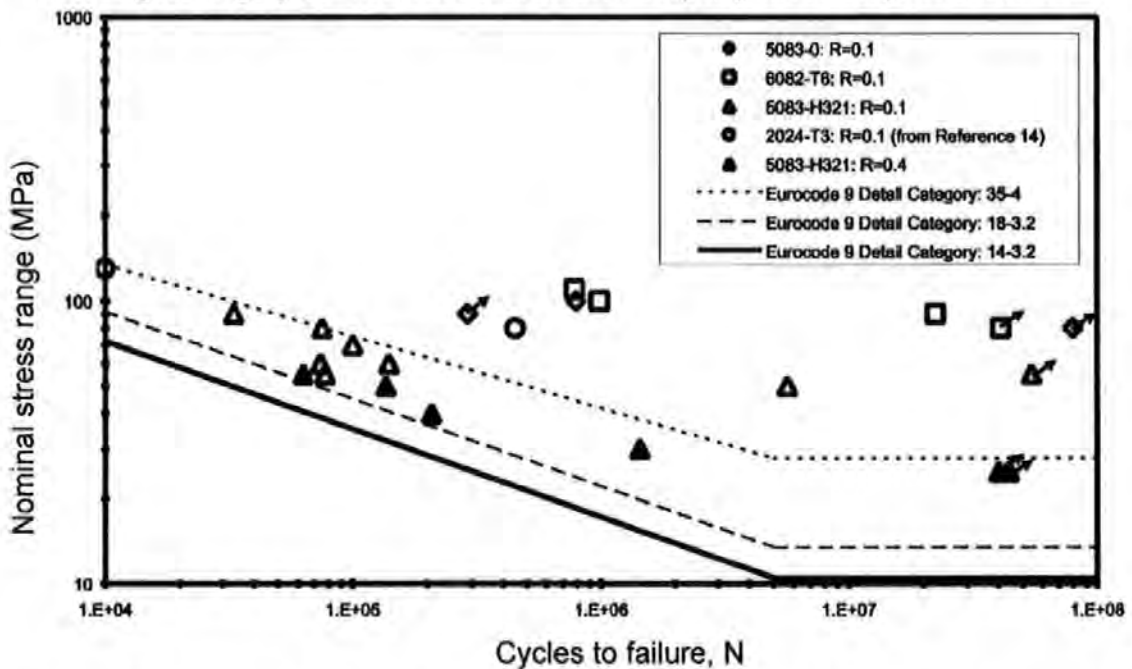


Figure 2.56: Endurance fatigue results for the flawed specimen tests ( $R = 0.1$  and  $0.4$ ) and draft Eurocode 9 fatigue design lines<sup>2</sup>.

<sup>1</sup> James, MN et al (2003)

<sup>2</sup> Dickerson, TL and Przydatek, J (2003)

It is clear from the above literature review that polished specimens yield higher fatigue strength and were therefore used in this investigation. No previous work has reported a comprehensive comparison of fatigue strength as a function of feed rate, rotational speed and pitch. All the previous investigations compared only 3 to 5 test runs. This thesis considers 11 different input parameter settings. Equally, little work has been reported on the relationship between process parameters and energy related functions, such as the force footprint, and the resulting fatigue strength.

#### 2.6.5 Residual stresses

Residual stresses exist within a body in the absence of any externally applied load. Residual stress distribution and distortion in welded plate are strongly affected by structural features, material properties and weld process parameters and their interaction. Restraint, arising from thermal gradients and plate clamping, produces residual stresses in the welding direction  $F_x$  (longitudinal), as well as perpendicular to the welding direction  $F_y$  (transverse), and also normal to the weld direction ( $F_z$ ). Residual stress in welding is primarily caused by the transient thermal exposure in the vicinity of the weld<sup>1</sup>. The intense local heating generates expansion, which is constrained by the surrounding cooler material, and the metal yields easily due to its reduced strength<sup>2</sup>. On cooling, the misfit in strain between the yielded and unyielded regions leads to a self-equilibrating residual stress field around the weld zone<sup>2</sup>.

Since the welding temperature for FSW is approximately 0.6-0.8  $T_m$ , lower residual stresses are expected than those occurring in fusion welding. Nonetheless, as a consequence of the large plastic deformation and non-uniform temperature distribution, material close to the weld is subject to different rates of expansion and contraction and therefore may develop a complex three dimensional residual state. The magnitude of residual stresses and strains and their distribution depends on the type of welding, material properties and degree of constraint during welding. High restraint in FSW limits the formation of angular distortion. Despite significant advances in the application of FSW for welding aluminum alloys, fundamental knowledge of the magnitude and causes of residual stress fields are still not completely understood. It is, however, well known that residual stress associated

---

<sup>1</sup> Norman, AF et al (2000)

<sup>2</sup> Preston, RV et al (2004)

with the weld negatively affects its fatigue performance and its anticorrosion performance<sup>1</sup>.

The influence of residual stresses on fatigue crack initiation and growth arises from their effect on mean stress in a fatigue cycle. It is generally believed that tensile residual stress tends to decrease the sustainable stress range on a component and hence reduces fatigue life under equivalent service stress states. Mean stress has a strong influence on crack initiation and on crack growth, with higher levels of mean stress generally equating to higher crack growth rates and to faster crack initiation. In welded structures, points of high residual stress also tend to coincide with points of local stress concentration, which generally leads to local yield and plastic flow. Fatigue is governed by local stress conditions, implying that the combination of residual and applied stress, influenced by local stress concentrations, leads to variable mean stress levels that may change fatigue life through either plastic relaxation or cyclic hardening. This stress redistribution under fatigue cycling could combine with local microstructural variation to shift favoured crack initiation sites in a complex manner. Understanding of these patterns underlying crack initiation seems likely to assist in designing optimized weld processes. Hence there is significant interest in determining residual stresses and in understanding their modification during applied fatigue cycling.

The importance of residual stresses, and their modification during service, to fatigue performance is somewhat unresolved, partly because of scarcity of detailed data, and partly because reported results can be contradictory. For instance, measured values of residual stresses in aluminium alloys, and the associated scatter, may vary significantly from one study to another. Several investigations of the residual stress distribution in FS welds have been conducted and their results are now presented.

James and Mahoney<sup>2</sup> measured residual stress in FSW 7050-T7451 aluminium alloy, C458 Al-Li alloy, and 2219 aluminium alloy by means of X-ray diffraction using the  $\sin^2\psi$  method. This investigation revealed the following findings:

- (i) The residual stresses in all the FSW welds were quite low, falling in the ranges of -9 to -90 MPa (compressive stress) and 6 to 45 MPa (tensile stresses) compared to those generated during fusion welding.

---

<sup>1</sup> Dalle Donne, C et al (2000)

<sup>2</sup> James, M and Mahoney, M (1999)

- (ii) At the transition between the fully recrystallised and partially recrystallised regions of the TMAZ, the residual stress was about 30-80 MPa higher than that observed in other regions of the weld.
- (iii) Generally, peak longitudinal (parallel to welding direction) residual stresses were tensile and transverse (normal to welding direction) residual stresses were compressive.

The low residual stress observed in the FS welds was attributed to the lower heat input during FSW and recrystallisation in the weld nugget.

Webster<sup>1</sup> reported measurements of residual stress in FSW Al 7108-T79, using the synchrotron X-ray technique, which showed that the longitudinal residual stress varied in the range from -60 MPa to 140 MPa within the tool shoulder region, and also showed a correlation between the detailed residual stress features and the heat flow in the weld.

Residual stress investigations by Dalle Donne et al<sup>2</sup> using laboratory X-ray, synchrotron X-ray and neutron diffraction methods revealed that the longitudinal stresses were always higher than the transverse residual stresses, independent of tool design, rotational speed or feed rate. The stresses had an "M" shaped distribution, with small compressive residual stresses in the weld seam and high tensile residual stresses in the heat affected zone, as shown for the longitudinal stress case in Figure 2.57. Larger tool shoulder diameters widen the M-shape of the residual stress distribution, while decreasing the feed rate tends to decrease the magnitude of the tensile residual stresses in the HAZ. Decreasing rotational speed of the tool produces a similar effect. The unstrained lattice parameter ( $d_0$ ) was determined by stress balancing across the plate, which can lead to errors if  $d_0$  varies across the plate.

---

<sup>1</sup> Webster, PJ (2001)

<sup>2</sup> Dalle Donne, CD et al (2001)

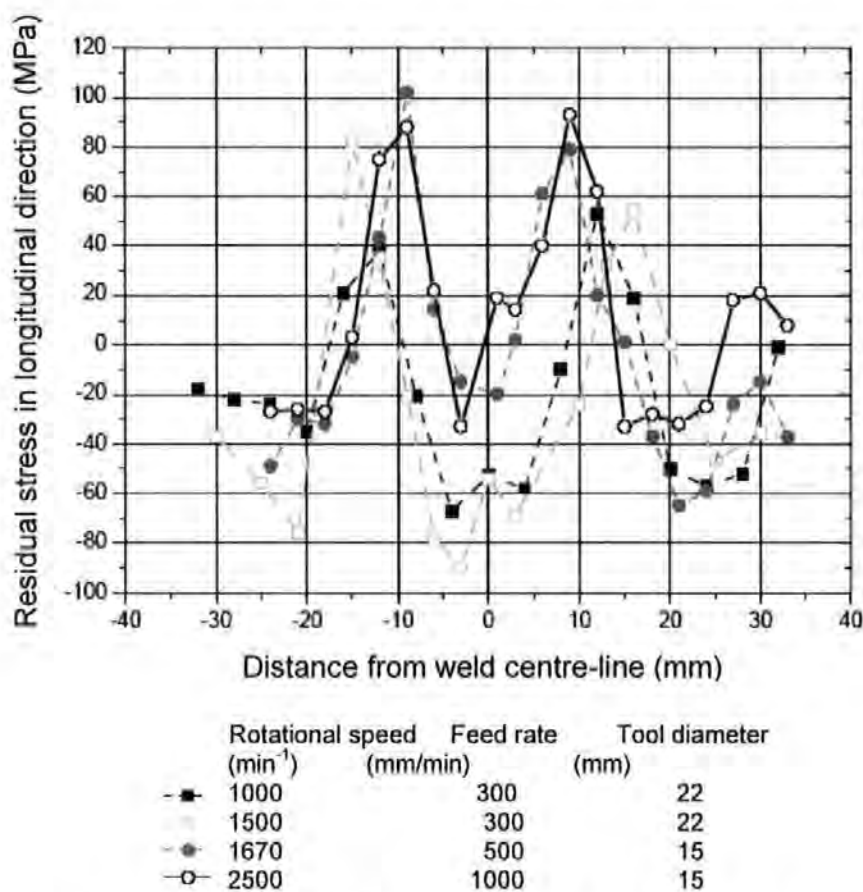


Figure 2.57: Longitudinal Residual stress distribution in friction stir welded 6013-T4 sheet as a function of process parameters<sup>1</sup>.

Results by Wang et al<sup>2</sup>, however, show that higher welding feed rates decrease the width of the HAZ and longitudinal peak residual stress increase from 160 to 200 MPa for 6061-T6 as feed rates increase from 113 mm/min to 195 mm/min. The rotational speed was kept constant but was not given. Strain free lattice measurements ( $d_0$ ) were made on coupons removed from the welded plate. This may cause errors in the data if the coupons are too big to relieve all stresses.

The formation of residual stresses in FSW was explained by Sutton et al<sup>3</sup> as follow:

*"A FSW is obtained by rotational extrusion of material around the tool and pin within a transverse region that is approximately bounded by the shoulder diameter at the crown and pin diameter at the bottom, forming the extrusion zone.*

<sup>1</sup> Dalle Donne, CD et al (2001)

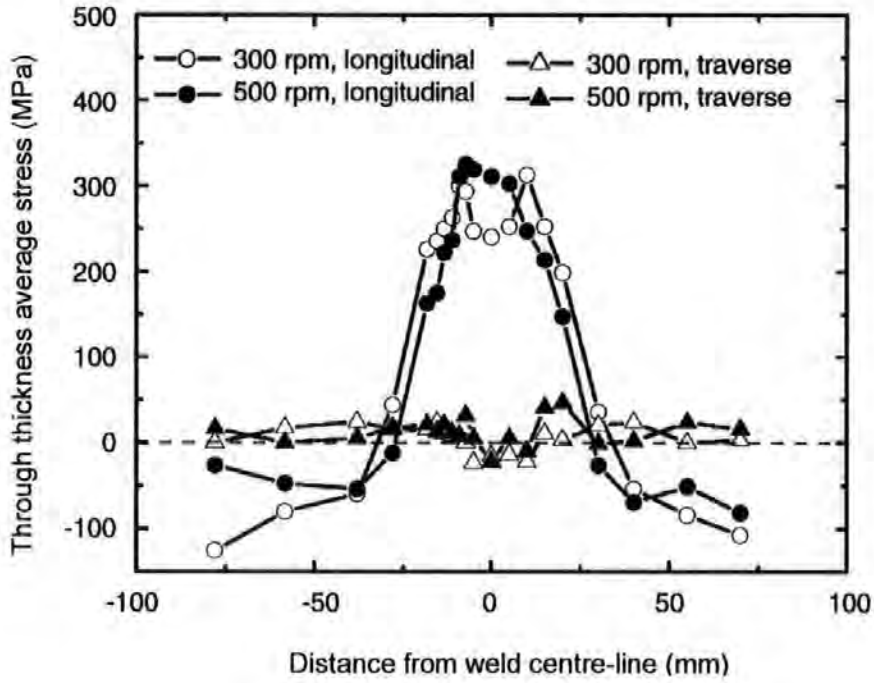
<sup>2</sup> Wang, YD et al (2000)

<sup>3</sup> Sutton, MA et al (2002a)

*Consolidation of the FSW is achieved in the extrusion zone through downward forces exerted by the tool shoulder. Due to the deformation constraint provided by the cold material along each side of the extrusion zone, heating of the extruded material results in thermal expansion that cannot be accommodated by the cold metal. The extruded material therefore experiences compressive plastic strains in transverse and longitudinal directions to the weld direction. Since the plastic state is incompressible this requires that the extruded material must undergo extensional plastic strain in the z direction vertical down into the plate. As the extrusion zone is deforming plastically, the material outside this zone must remain elastic because after cooling, this elastic region will try to return to its initial conditions and the plastically deformed material will try to retain its plastic deformation state. This results in incompatibility and tensile transverse and longitudinal stresses in weld and compressive through thickness stresses in the weld zone are formed."*

Results on residual stresses in FSW of 3.2 mm thick 304 stainless steel revealed an asymmetric residual stress distribution, with respect to the weld centre-line where the largest gradients in residual stress were on the advancing side due to larger thermal gradients. Longitudinal stresses showed the highest tensile magnitude. Peak residual stress values were located just outside the pin diameter and extended from the crown side toward mid-thickness. These results are presented in Figure 2.58(a) and (b).

(a)



(b)

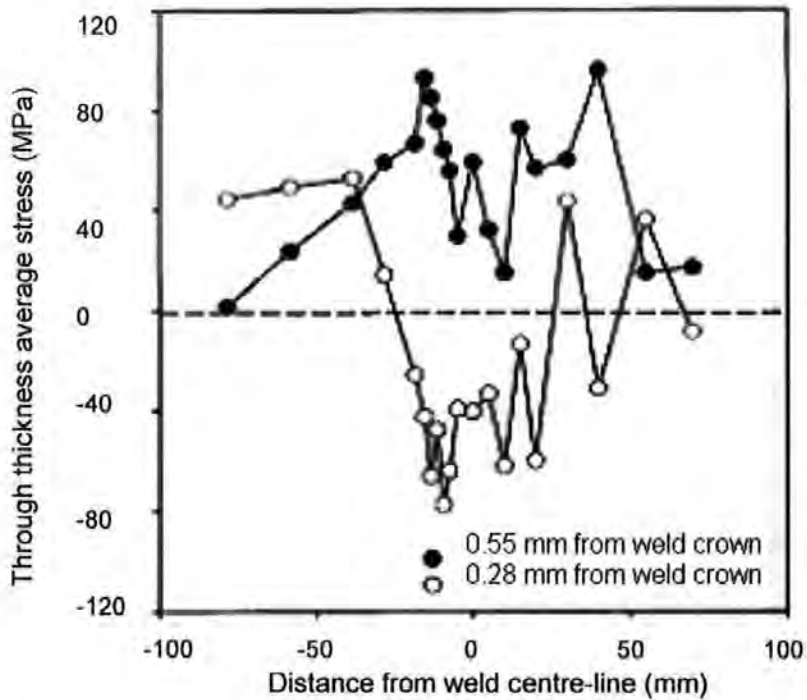


Figure 2.58: (a) Variation of longitudinal stress in FS welds made in 304L stainless steel.  
(b) Variation of transverse stress in FS welds made in 304L stainless steel<sup>1</sup>.

<sup>1</sup>Reynolds, AP et al (2003a)



Data obtained by John et al<sup>1</sup> indicated that residual stresses play a key role in the crack growth in the HAZ parallel to the weld direction for 10mm thick 7050-T7451 aluminium alloy. The magnitude of the fatigue limit depends on microstructure, residual stresses and specimen geometry. For a constant microstructure, center cracked tension specimens had a lower crack growth rate than compact tension specimens through the HAZ at low R-values. This geometry dependence vanished at high R ratios. This observation implies that the residual stresses had an effect on the fatigue crack growth rate.

Bussu and Irving<sup>2</sup> measured the residual stresses in a single FS welded specimen of a 2024-T351 aluminium alloy using hole drilling, and considered their effect on fatigue crack propagation. Longitudinal tensile residual stresses were found with a maximum value of 85% of the parent plate 0.2% proof strength at a position 11 mm away from the plate joint line. Transverse residual stresses varied from a tensile value of 174 MPa on the plate joint line to a compressive value of -192 MPa a distance 25 mm away from this line. It should be noted that very different, and lower, values were measured on a second specimen, which implies that results obtained from the hole drilling technique may be difficult to interpret in the context of life prediction. To assess the effect of residual stresses on crack growth behaviour, the authors subjected the specimens to 2% plastic strain applied orthogonally to the weld axis. Whilst this is effective at reducing residual stress levels it introduces another complexity into fatigue crack growth, as it is not clear that growth rates in strained and unstrained specimens would be the same in the absence of residual stresses. Bussu and Irving<sup>2</sup> inferred a significant effect of the residual stress field on fatigue crack growth but were unable to draw any firm conclusions from their work.

Peel et al<sup>3</sup> investigated (Figure 2.59 (a) and (b)) the residual stress distribution in FSW of annealed 5083 using synchrotron X-ray diffraction. The longitudinal residual stress exhibited an "M"-shaped distribution across the weld similar to the results of Dalle Donne et al<sup>4</sup>. The transverse residual stresses exhibited a peak at the weld centre. The nugget zone was in tension in both longitudinal and transverse directions. Peak tensile residual stress were observed 10 mm from the weld centre-line, a distance corresponding to the edge of the tool shoulder. The

---

<sup>1</sup> John, R et al (2003)

<sup>2</sup> Bussu, G and Irving, PE (2003)

<sup>3</sup> Peel, M et al (2003)

<sup>4</sup> Dalle Donne, C et al (2001)

longitudinal residual stress increased with increasing tool feed rate, whereas transverse residual stresses did not exhibit any evident dependence on the feed rate. A mild asymmetry in longitudinal residual stress profile was observed within the nugget zone with the stresses being  $\pm 10\%$  higher on the advancing side. In a similar fashion, similar to the results obtained by Dalle Donne et al<sup>1</sup>, maximum residual stresses in longitudinal direction (40–60 MPa) were higher than those in transverse direction (20–40 MPa).

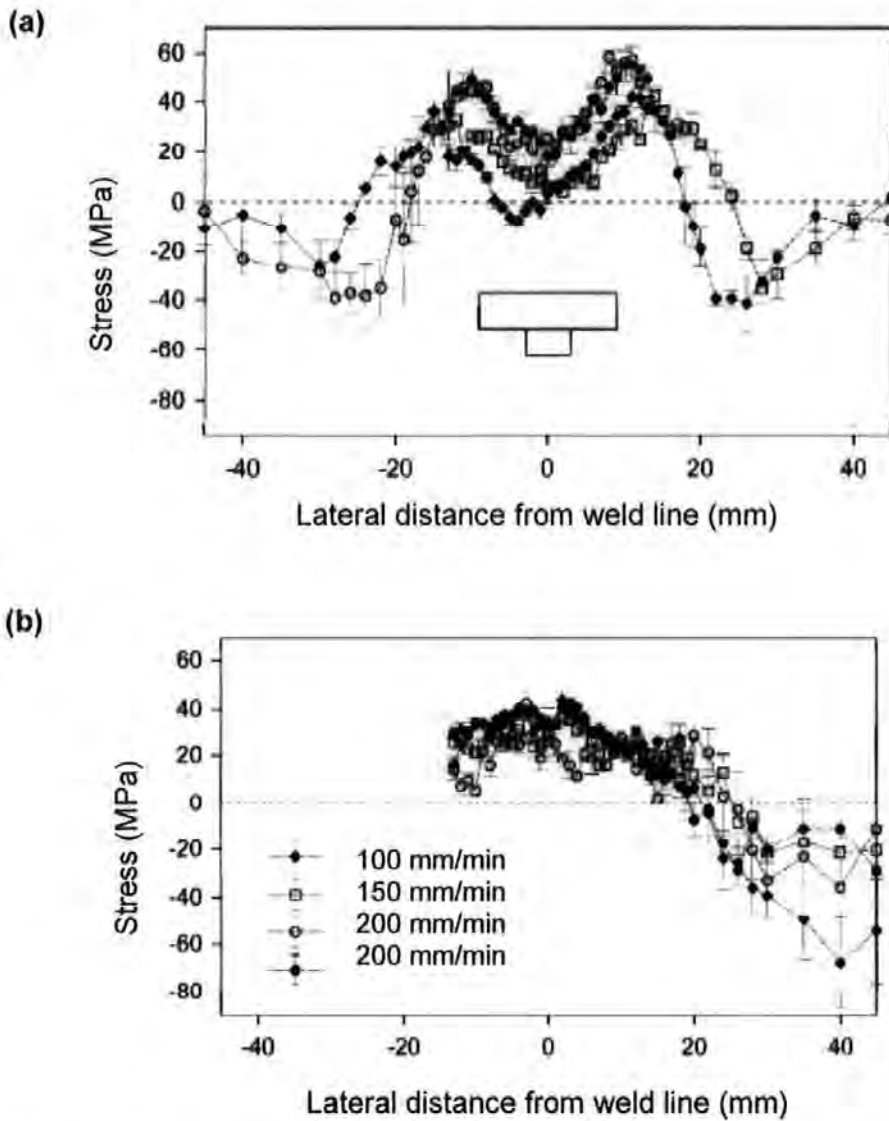


Figure 2.59: (a) Longitudinal residual stress in 5083-AA similar material welds as a function of the lateral distance from the weld line.  
 (b) Transverse residual stress in 5083-AA similar material welds as a function of the lateral distance from the weld line<sup>2</sup>.

<sup>1</sup> Dalle Donne, C et al (2001)

<sup>2</sup> Peel, M et al (2003)

External clamping forces, material properties and dimensions of the plates to be welded will influence the magnitude of the residual stresses but not their shape<sup>1</sup>.

Investigations by James et al<sup>2</sup> on 8 mm thick 5083-H321 revealed that tool feed rate definitely affects fatigue life but that hardness values were little affected by feed rate over the range 80-200 mm/min at a constant rotational speed of 500 rpm. The position of peak tensile residual stresses did not correspond with crack initiation sites.

Sutton et al<sup>3</sup> used neutron diffraction to determine the residual stress distribution in 2024-T3 aluminium alloys. Electro-discharged machined (EDM) combs were used to determine the unstrained lattice parameter<sup>3</sup>. A global ( $d_0$ ) value was used because the variation was reported to be 125 microstrain. Figure 2.60 shows that the residual stress in their specimens was a strong function of the normal (Z) and transverse (T) position and not the longitudinal position. This can be deduced from the observation of very similar residual stress patterns at two different longitudinal positions. Maximum values of the longitudinal stresses were about 105 MPa. The advancing side had larger tensile stress gradients around the edge of the tool shoulder diameter (+9.5 mm).

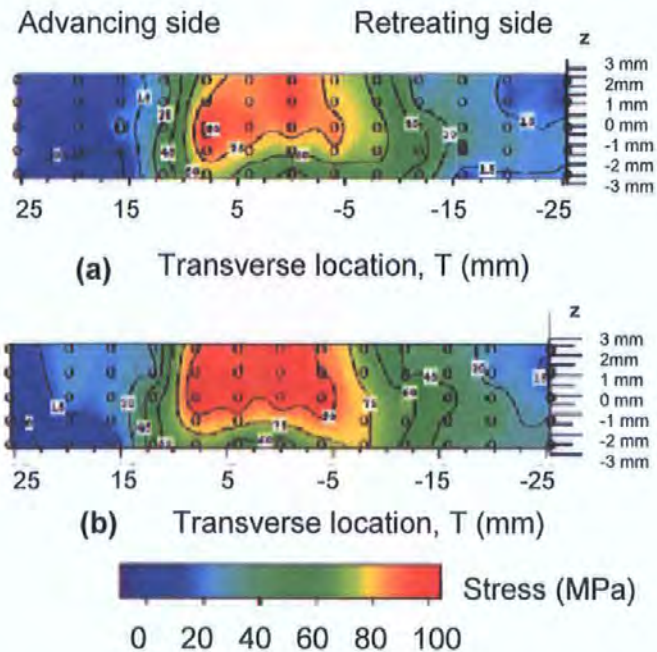


Figure 2.60: Residual stress maps of 2024-T3 for two transverse sections at different longitudinal positions as a function of depth(z) below the surface<sup>3</sup>.

<sup>1</sup> Shi, Q et al (2003)

<sup>2</sup> James, MN et al (2003)

<sup>3</sup> Sutton, MA et al (2002a)

Clearly, maximum residual stresses observed in various friction stir welds of aluminum alloys are generally reported to be well below 100 MPa. The residual stress magnitudes are significantly lower than those observed in fusion welding, and also significantly lower than the yield stress of these aluminum alloys. This should give a significant reduction in the distortion of FSW components and an improvement in mechanical properties.

Most studies on residual stress in FS welds reported in the research literature contain only 2-3 changes in feed rate at a constant rotational speed or 2-3 rotational speeds at a constant feed rate. Residual stresses seem to have an influence on crack growth rates and heat input can be associated with changes in residual stresses. It is clear, from this limited review of some of the available literature, that knowledge of the magnitude of residual stresses at welds is patchy, particularly for aluminium alloys, and that their reported magnitudes vary considerably, even for FS welds where one would expect lower peak values. Part of the problem arises from the incomplete nature of the information gained from hole drilling experiments, and from scatter in the results, as well as from inherent variability of residual stresses along a weld run. Very few researchers have addressed variability along a weld, because of the large size of the experimental matrix required to yield meaningful results. Equally, the difficulty of obtaining complete residual stress information for specimens of a structurally relevant size, has led to a lack of work that considers modification of residual stresses by applied loading.

In this thesis the residual stress data will be related to weld parameters and the force foot print data over a range of feed rate from 85-185 mm/min and rotational speeds of 250-950 rpm. No existing work documents the relationship between process parameters and residual stress in any great detail.

## 2.7 Heat and power input

The heat generated between the tool and the welded plate is a very important parameter in the FSW process. The heat should keep the maximum temperature in the thermal cycle high enough to produce softened material that can be stirred with the pin, and also below the melting temperature of the material to avoid defects and large distortion of the welds. To develop a thermal model for friction

stir welding all the processes of heat transfer due to convection, radiation and conduction into the tool, backing plate and material should be considered. Figure 2.61 illustrates the main features to be considered.

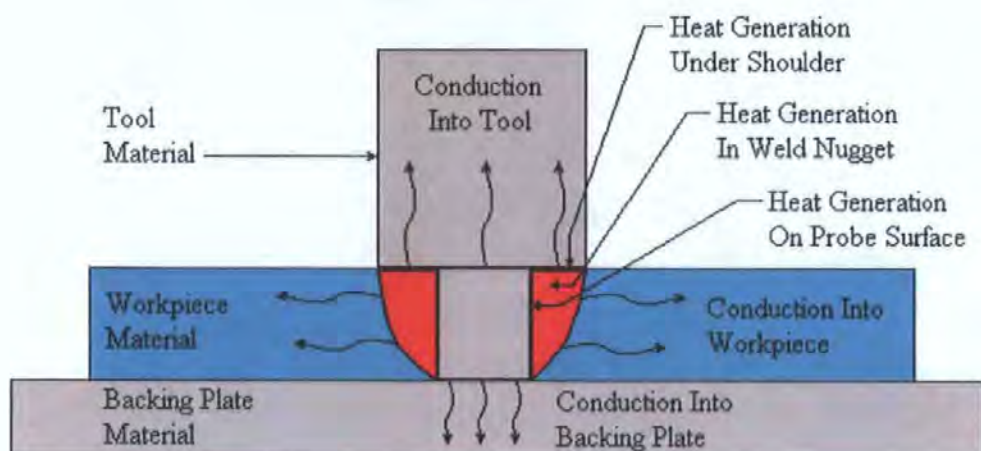


Figure 2.61: Heat processes in the FSW process<sup>1</sup>.

It is therefore extremely difficult to accurately calculate the heat input in friction stir welds. Heat is generated on the material by friction and shearing forces acting on the material around the tool as well as viscous heat dissipation of mechanical energy<sup>2</sup>. The heat is generated by<sup>3</sup>

- (i) the immediate material surrounding the tool. This implies that there is no slipping, so therefore the material flow rate at the contact point of the tool and the material is the tool velocity, and
- (ii) deformation of material that surrounds the tool.

Early research<sup>1,4,5,6,7</sup> indicate that the shoulder is the main contributor to heat input, but Shinoda and Shibata<sup>8</sup> determined that 60% of the heat input was generated by the pin, as indicated by Figure 2.62. The heat generated from the pin should therefore also be considered when formulating models.

<sup>1</sup> Russell, MJ and Shercliff, HR (1999)  
<sup>2</sup> North, TH et al (2000)  
<sup>3</sup> Threadgill, PL and Nunn, ME (2003)  
<sup>4</sup> Chao, YJ and Qi, X (1998)  
<sup>5</sup> Frigaard, ØG et al (1999)  
<sup>6</sup> Gould, JE and Feng, Z (1998)  
<sup>7</sup> Bendzsak, GB et al (2000)  
<sup>8</sup> Shinoda, T and Shibata, D (2000)

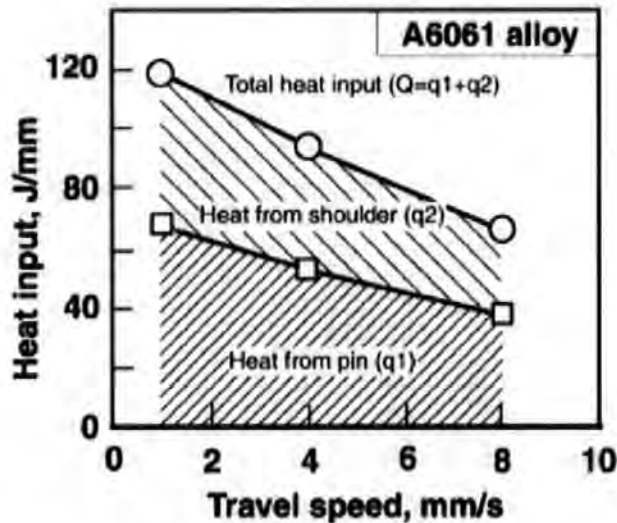


Figure 2.62: Heat input from pin and shoulder<sup>1</sup>.

The heat input to the weld can be divided into four stages<sup>2</sup>

- (i) Stationary heating period: During the dwell period the material beneath the shoulder is preheated to a certain temperature (about 400°C for aluminium alloys) to enable plastic deformation during welding.
- (iii) Transient heating period: The heat starts to build up around the tool shoulder as the tool rotates until saturation occurs.
- (iv) Pseudo-steady-state period: The thermal field around the tool remains constant during the welding operation.
- (v) Post-steady-state period: The reflection of heat from the end plate surface leads to additional build-up of heat around the tool shoulder.

Most of the heat input to the welds arises from friction. The friction developed underneath the tool is given by <sup>3</sup>

$$F_{\text{friction}} = \mu \frac{\text{Pressure}}{\text{Area}} \quad \dots(2.5)$$

where

<sup>1</sup> Shinoda, T (2001)  
<sup>2</sup> Frigaard, ØG et al (1999)  
<sup>3</sup> Dieter, GE (1976)

$\mu$  = coefficient of friction at the specific speed

The local heat generation rate can be calculated as

$$q(r) = \frac{\text{Pressure}}{\text{Area}} v_{\text{slip}} \quad \dots(2.6)$$

where

$$v_{\text{slip}} = \text{relative slip velocity} = \omega r$$

The total heat generated, (considering that there is no pin, only shoulder) according to Frigaard et al<sup>1</sup>, is described as

$$q(r) = \int_0^{r_s} 4\pi^2 \mu P \omega r^2 dr = \frac{4}{3} \pi^2 \mu P \omega r_s^3 \quad \dots(2.7)$$

where

$r_s$  = radius of shoulder

$\omega$  = rotational speed (rpm)

$\mu$  = coefficient of friction at the specific speed

$P$  = pressure distribution across the interface

To have a numerical model is more convenient when expressing equation 2.7 in terms of the contributions to heat input from the shoulder and the pin

$$q(r) = \frac{4}{3} \pi^2 \mu P \omega \sum_{i=1}^n (r_i^3 - r_{i-1}^3) \quad \dots(2.8)$$

The heat contributions at different locations beneath the tool shoulder can be determined by equation 2.8.

The contribution by the pin is usually neglected because the diameter of the pin is much less than the shoulder.

---

<sup>1</sup> Frigaard, ØG et al (1999)

When the pressure is replaced with ( $F_z/\text{Area}$ ) equation 2.8 simplifies to

$$\text{Power} = \frac{4}{3} \pi \mu F_z \omega r_s \quad \dots(2.9)$$

Frigaard et al<sup>1</sup> used a finite difference approach to calculate two and three dimensional heat flow models and to predict the hardness in the weld zone. The coefficient of friction was adjusted in order to ensure that the calculated temperatures at all points do not exceed the melting point of the material.

The tool rotational speed is limited by the necessity of maintaining plasticity without melting the material being welded. The applied pressure should also not exceed the actual flow stress of the material at the operating temperature if a sound weld is to be made<sup>1</sup>. The relationship between process parameters and heat input is not simple since the power is determined by the product of torque and rotational speed. The coefficient of friction is dependent on temperature and slip velocity and is therefore difficult to determine<sup>2</sup>. The speed at which the material flows around the tool is limited by the shear strength of the material. As the temperature increases the frictional coefficient is supposed to decrease and the work of plastic deformation increase. Usually the friction coefficient at the pin surface is considered to be the same as at the shoulder. An effective coefficient of friction ( $\mu_{\text{eff}}$ ) can be determined using the ratio of<sup>3</sup>:

Friction =  $P\mu_{\text{eff}}2\pi r dr$  and Torque =  $P\mu_{\text{eff}}2\pi r^2 dr$  acting on an elementary area of  $dA = 2\pi r dr$  in contact with the plate surface. After integration of these relationships equation 2.10 can be derived

$$\mu_{\text{eff}} = \frac{3}{2} \frac{T}{F_z x r} \quad \dots(2.10)$$

where

$F_z$  = vertical force on the tool (N)

$T$  = torque on the tool (Nm)

$r$  = distance from the tool centre or radius of the tool (m)

<sup>1</sup> Frigaard, ØG et al (1999)

<sup>2</sup> Colegrove, P et al (1999)

<sup>3</sup> Santella, M et al (2003)



The assumptions are made that the pressure and the effective coefficient ( $\mu_{\text{eff}}$ ) do not vary with the position on the tool surface. Santella et al<sup>1</sup> used the relationship in plunge tests to determine the effective coefficient of friction and found that the normal force and tool torque values approximate actual friction stir welding conditions and could be used to represent actual friction conditions for materials being FS welded. In this thesis equation 2.10 was used to determine an approximate value of the friction coefficient of the contact between the tool and welded material.

Russell and Shercliff<sup>2</sup> extended the friction-based model to include the heat generated by shear strength of the material and the tool interface. The heat generated by interfacial shear stress between the material and the tool can be determined by

$$q(r) = \omega \tau r d A \quad \dots(2.11)$$

where

$\tau$  = shear strength of the material at the operating temperature and strain rate

$\omega$  = rotational speed (rpm)

A = area of the tool shoulder

The areas underneath the tool considered by these researchers are shown in Figure 2.63. The contribution by the pin was calculated to be 2% of the total heat generated by the tool.

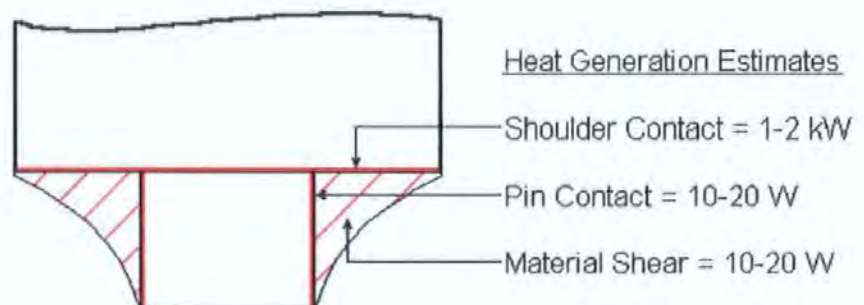


Figure 2.63: Heat generated by specific areas underneath the FSW tool<sup>1</sup>.

<sup>1</sup> Santella, M et al (2003)

<sup>2</sup> Russell, MJ and Shercliff, HR (1999)

Most numerical models have assumed that the material sticks to the tool surface. The model by Colegrove and Shercliff<sup>1</sup> estimates the heat input to 7075-T6 to be 15-18kW compared to the measured 2.6-3.5 kW. This model therefore overestimates the heat input to the material. Colegrove and Shercliff<sup>1</sup>, using experimental and theoretical techniques, concluded that the different tool materials exerted different surface shear stresses on the welded material. They found that the peak temperature of the Al7075-T7351 when welded was near the solidus, that the temperature reached during welding was a function of heat generation, and that changing the rotational speed had little effect on heat generation.

Song and Kovacevec<sup>2</sup> showed that the peak temperature near the tool reached the solidus temperatures. This suggests that a liquid layer exists close to the tool surface which will decrease the shear stresses that can be applied to the material. As a consequence material slip as well as material sticking conditions have been included in some FSW thermal models as will be shown in the following paragraphs.

To develop the sequence of events consider firstly the three dimensional flow and thermal model developed by Colegrove<sup>3</sup>, which determines the total heat generated by adding the contributions of heat generated by shearing of the material, heat generated by frictional heat and the heat generated by frictional heating on the face of the pin. They extended the previous models by adding the frictional heat generated on the pin. Their investigations illustrated that 20% of the total heat is generated by the pin.

Dong et al<sup>4</sup>, included effects of the slip zone around the tool. They presented a coupled thermo-mechanical analysis of a FSW weld, using simplified models. The authors found that frictional heating dominated the upper portion of the weld, and plastic work induced heating dominated the lower section of the weld. The plastic slip zone was due to interactions between the tool and the base material, and they proposed that the stir pin geometry (shoulder diameter and pin height), and the workpiece thickness played a role in the formation of the slip zone. They confirmed the ratio between the translation speed and the rotation speed, referred to as pitch, as an important welding parameter. They proposed that the shoulder

---

<sup>1</sup> Colegrove, P and Shercliff, HR (2003)

<sup>2</sup> Song, M and Kovacevic, R (2002)

<sup>3</sup> Colegrove, P et al (2000)

<sup>4</sup> Dong, P et al (2001)

diameter, pin height and the workpiece thickness played a role in the formation of the slip zone around the tool and the material.

In attempts to understand the formation of the slip zone two conditions for friction can be defined, namely sticking and sliding friction<sup>1</sup>. When the tool slides over the parent plate, a contact shear stress will form over the surface. This can be described using Coulomb's law of friction, namely

$$\text{Stress}_{\text{contact}} = \mu \text{Stress}_{\text{yield}}$$

When the sticking condition is met, the friction stress is approximately equal to the yield shear stress of the material and is independent of the normal force applied to the shear layer<sup>1,2</sup>. The shear stress has an upper limit above which its value is constant, regardless of the value of the applied force in the sliding condition. The coefficient of friction then remains constant and the heat is generated due to plastic work performed on the material in the shear layer. If the contact is characteristic of sliding friction then the coefficient of friction will decrease when the normal force increases. This will be a linear relationship<sup>2</sup>. This is illustrated in Figure 2.64. The max shear stress is usually set to  $UTS/\sqrt{3}$  using the Von Mises relationship.

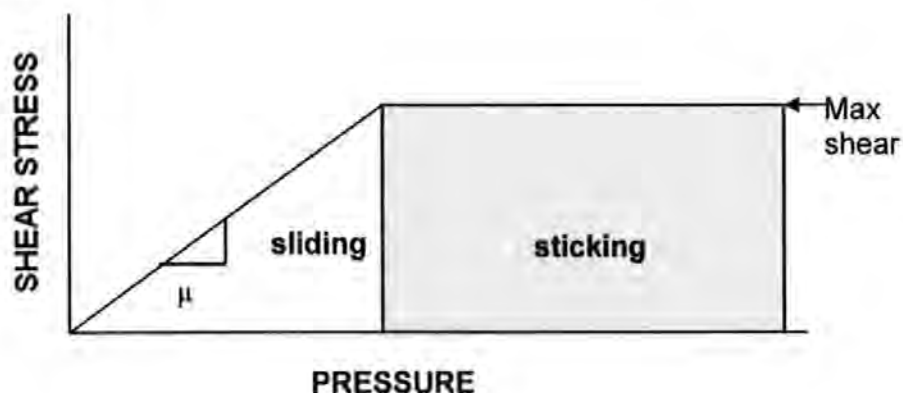


Figure 2.64: Variation of friction with pressure exerted on the tool<sup>2</sup>.

Alternative heat generation models have also been developed based on torque. Khandkar et al<sup>3</sup> present a three-dimensional model that correlates the heat input with the experimentally measured torque measurements. These researchers

<sup>1</sup> Altintas, Y (2002a,2002b)

<sup>2</sup> Xu, S and Deng, X (2002a)

<sup>3</sup> Khandkar, MZH et al (2003)

enabled the prediction of temperature distribution during FSW welds in aluminum 6061-T651 plates. The use of axis-symmetric finite element models based on torque were developed by distributing the power to the different interfaces between the tool and the workpieces, based on the torques generated at the different tool surfaces. Khandkar et al<sup>1</sup> include the effects of the backing plate in their models and prove that cooling or insulating the backing plate alter the thermal profiles and will in turn affect the mechanical properties of the welds. Certain limitations to the model are noted by the authors, such as uncertain values of the variables, normally approximated, for example, thermal contact conductance and the convection coefficient at the bottom surfaces. The authors also propose that the backing plates may have a greater influence on weld quality. The advantage of the torque-based model is that the value of the coefficient of friction is not required.

The heat input is derived as follows:

$$\dot{Q}_{\text{interface}} = \dot{Q}_{\text{tot}} \times \text{Torque generated by interfacial surface} / \text{Total torque} \quad \dots(2.12)$$

The total torque at the shoulder interface can be expressed as

$$M_{\text{shoulder}} = \int_{r_o}^{r_i} \tau r (2\pi r) dr \quad \dots(2.13)$$

The torque at the bottom of the pin is given by

$$M_{\text{pinbottom}} = \int_0^{r_o} \tau r (2\pi r) dr \quad \dots(2.14)$$

The torque at the vertical face of the pin is expressed as

$$M_{\text{pinsurface}} = \tau r_i 2\pi r_i h \quad \dots(2.15)$$

where

$r$  = radial distance from the tool centre

---

<sup>1</sup> Khandkar, MZH et al (2003)

$r_i$  = pin radius

$r_o$  = shoulder radius

$h$  = length of pin

$\tau$  = uniform shear stress

The total torque which is the sum of the three torque components is determined from the average power input

$$P_{av} = M_{tot} \omega \quad \dots(2.16)$$

where

$P_{av}$  = measured experimentally torque x  $\omega$

$M_{tot}$  = total torque

$\omega$  = rotational speed (rpm)

The above equations can be manipulated to relate the heat flux to the radial position on the tool to give

$$q(r) = \frac{P_{av} r}{\frac{2}{3} \pi r_o^3 + 2 \pi r_i^2 h} \quad \dots(2.17)$$

Average heat input in welding has been proposed by other authors in the context of simple energy models. Heat input (J/mm) from the shoulder in FSW is determined from spindle torque measurements that remain reasonably constant once thermal equilibrium is reached and is given by

$$Q = \frac{\text{Power}}{\text{feedrate}} = \eta \frac{2\pi\omega T}{f} \quad \dots(2.18)$$

where

$Q$  = heat (J/mm)

$\eta$  = efficiency factor = 0.9 for Al<sup>1</sup>

$\omega$  = rotational speed (rev/min)

$T$  = Torque (Nm)

$f$  = feed rate (mm/min)

The efficiency factor in this model has been estimated by Lienert and Russell<sup>1,2</sup> as approximately 0.87 - 0.94 for welding aluminium. This means that 87% to 94% of the heat goes into the weld. Contrary to the above results, Johnson<sup>3</sup> indicate that torque should not be considered as the main contributor to energy input; but that  $F_x$  also plays an important role.

The torque based model was extended to include slip zone effects by Schmidt et al<sup>4</sup>. They developed an analytical model that included the sum of the heat input due to sliding and sticking conditions and extended the torque based model. The fractional contributions of each was determined by a state variable ( $\delta$ ) defined as

$$\delta = 1 - \frac{v_{\text{tool}} - v_{\text{material}}}{v_{\text{tool}}} \quad \dots(2.19)$$

where

$v_{\text{tool}}$  = tool velocity that depends on position away from the tool

$v_{\text{material}}$  = velocity of the material at the interface

A value of  $\delta = 0$  equals to pure sliding and when the material sticks to the tool  $\delta$  equals 1.

The expression for the heat at the tool/work piece interface is then given by

$$q_s = \tau_{\text{contact}} \omega r (1 - \delta) \quad \text{with } 0 \leq \delta \leq 1 \quad \dots(2.20)$$

A summary of the various contributions of the heat input by Schmidt et al<sup>4</sup> is shown in Figure 2.65

---

<sup>1</sup> Lienert, TJ (2002)

<sup>2</sup> Russell, MJ (2002)

<sup>3</sup> Johnson, R (2000)

<sup>4</sup> Schmidt, H et al (2004)

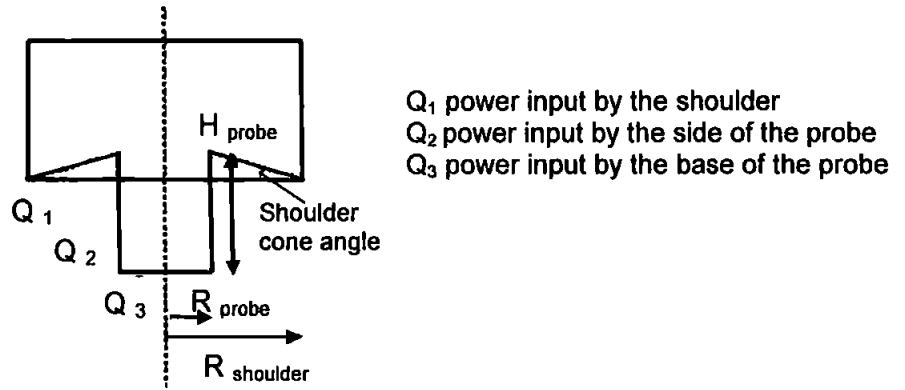


Figure 2.65: Heat model developed by Schmidt et al<sup>1</sup>.

They describe the sliding friction conditions as the state at which the material is elastically deformed and hence moving at zero velocity, while during sticking conditions the velocity of the material increases until it reaches the velocity of the tool. Correction to the above must be made to account for heat loss through the tool and the base plate. Measurement of total power consumption must also be made to account for the losses through the machine bearings and shafts. Their model estimated that the pin contributed about 14% to the total heat flux for 2024Al-T3 aluminium alloy and that the analytical heat generation correlated with the experimental heat generation at 400 rpm and 120 mm/min. Their model was only tested at this one condition.

The various heat contributions in the Schmidt et al<sup>1</sup> model can be determined by the following equations

$$Q_{total} = Q_{sticking} + (1 - \delta)Q_{sliding} \quad \dots(2.21)$$

$$Q_{total} = \frac{2}{3} \pi \omega \left( \delta \frac{\sigma_{yield}}{\sqrt{3}} + (1 - \delta) \mu P \right) \left( R_{shoulder}^3 - R_{probe}^3 \right) (1 + \tan \alpha) + R_{probe}^3 + 3R_{probe}^3 H_{probe} \quad \dots(2.22)$$

where

$Q_{total}$  = total heat generation (W)

$\sigma_{yield}$  = yield strength (Pa)

$\omega$  = the tool angular rotation rate (rad/s)

<sup>1</sup> Schmidt, H et al (2004)

- $R_{\text{shoulder}}$  = tool shoulder radius (m)
- $R_{\text{probe}}$  = pin the tool pin radius (m)
- $\alpha$  = the tool shoulder cone angle
- $H_{\text{probe}}$  = the tool pin/probe height (m)
- $P$  = the contact pressure (Pa)
- $\delta$  = contact state variable

Although it is therefore that many heat input models have been proposed, very little work has been done to relate heat input and power input to the process and input parameters of FSW. It has been found that in general the specific heat input correlates well with pitch<sup>1</sup>. Welds with low pitch are described as "cold welds". Welds made at the same pitch may have differing heat inputs, while a weld with high feed rate and rotational speed will be colder than those with lower welding speeds<sup>2</sup>. The variation of 1/pitch and weld peak temperature is shown in Figure 2.66.

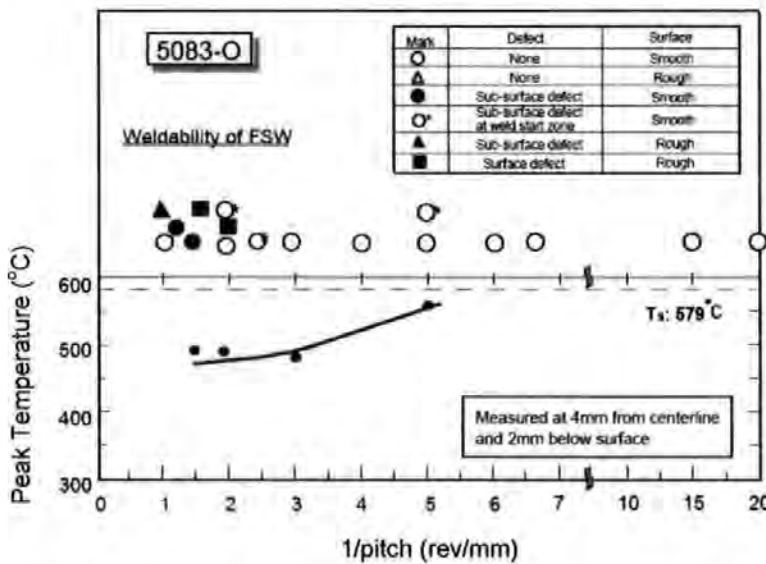


Figure 2.66: The relationship between 1/pitch and peak welding temperature for Al 5083-O<sup>2</sup>.

The work of several authors who did consider the relationship between heat input and process parameters is mentioned below. Lindner et al<sup>3</sup> used the torque based model to determine the heat and power input to FSW. Figure 2.67 (a) shows specific weld energy (that is average heat input) as a function of welding speed and feed rate. As welding speed increases the heat input decreases as a power

<sup>1</sup> Seidel, TU and Reynolds, AP (2001)

<sup>2</sup> Hashimoto, T et al (1999)

<sup>3</sup> Lindner, K et al (2003)



function and may approach a minimum value once feed rates  $> 5$  mm/s. This possibly relates to the formation of a steady-state situation of material-tool interaction and heat transfer. There is a minor effect on rotational speed where, particularly at lower feed rates, lower pitch gives higher energy input.

Figure 2.67 (b) shows the equivalent diagram for power. Power increases sharply with increases in feed rate and again, at lower feed rates, lower pitch values give higher power inputs.

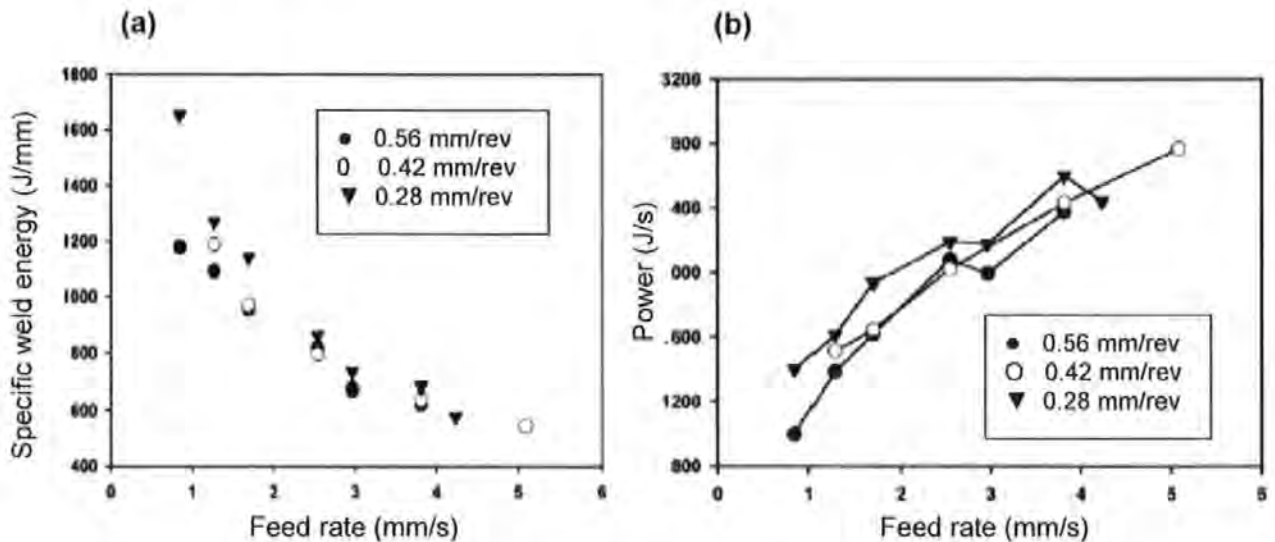


Figure 2.67: (a) Specific weld energy (heat input in J/mm); and (b) Power (Watts) as a function of welding speed (feed rate mm/min) for 7050-T751 aluminium alloy<sup>1</sup>.

In Chapter 3 of this thesis the variation of average heat input and power with feed rate and rotational speed is investigated. The results of this thesis show that as the feed rate increases the average heat input into the weld decreases. The power, however, does not indicate a linear trend with the variation of welding parameters. A maximum power is obtained for the mid range of the data and low power is generated for low rotational speeds and feed rates, as well as high rotational speeds and feed rates. This is quite different to the results given by Lindner et al<sup>1</sup>.

Assumptions made to simplify the various models include constant thermal properties<sup>2</sup>; constant frictional coefficient<sup>3</sup>; non-slippage of the material<sup>4</sup>;

<sup>1</sup> Lindner, K et al (2003)

<sup>2</sup> Russell, MJ and Shercliff, HR (1999)

<sup>3</sup> Frigaard, ØG et al (1999)

<sup>4</sup> Bendzsak, GJ et al (2000)

considering that the shoulder is the only source of heat; taking the material to be a kind of non-Newtonian fluid in CFD models<sup>1</sup>; excluding the rake angle<sup>2</sup>; and not including the backing plate. In practice the thermal properties vary with temperature; the coefficient of friction is likely to be dependent on pressure, slip velocity and temperature gradient; the pin should also contribute to the heat input; and a great amount of heat should be dissipated away via the backing plate.

It is beyond the scope of this thesis to model the heat flow during welding by applying FEA or any other computational method. The accuracy of the models can therefore only be compared to experimental measured data. Assumptions are often made in computing the frictional coefficient, shear stress and thermal conductivity constants when heat dissipated into the backing plate is considered. In general, modeling does assist in determining optimum weld conditions by eliminating numerous amounts of mechanical testing to be done. However, using simulations from heat flow models to determine optimum mechanical properties of FSW, is still in its infancy. In this thesis equations 2.9, 2.10 and 2.18 are used to provide estimates of the heat and power input to the FS welds. Such an approach can only be used to compare weld conditions and should not be considered as accurate quantitative measurements of the heat input to any particular weld.

## 2.8 Summary of findings from existing research literature

Despite the initial industrial success of friction stir welding many obstacles still need to be overcome before FSW becomes a fully developed industrial welding technique. These include:

- (i) development of on-line tool wear and tool breakage sensing systems;
- (ii) development of in-process weld quality inspection system;
- (iii) simulation modelling and tool development to weld high temperature melting materials and to weld at low forces;
- (iv) insight into process physics leading to better predictive modelling of the FSW process;
- (v) better understanding of the influence of process parameters on quality factors, such as tensile strength, fatigue life, and residual stress (The aim here is to enable online prediction of the weld quality during the

---

<sup>1</sup> Bendzsak, GJ et al (2000)

<sup>2</sup> Colegrove, P et al (2000)

welding process and to choose appropriate weld parameters to optimise the performance); and

- (vi) thermo-mechanical modelling combined with improved understanding of residual stress development, in both theoretical and experimental terms.

It is clear from this literature survey that a limited amount of research has been conducted to determine the influence of input parameters (thus tool rotational speed and feed rate) on weld performance, on fracture locations and on the type of defects found at fatigue initiation sites in FS welded 5083-H321 aluminium alloy. All the previous investigations have compared only a relatively small set of weld process conditions with resulting mechanical properties. In this thesis a systematic attempt is made to relate input and process parameters to weld performance, using a matrix of 11 combinations of overlapping process parameters. No existing work documents the relationship between process parameters (forces on the tool, energy input, force footprint plot and tool temperature) and hardness, tensile, residual stress and fatigue performance of FS welds. Additionally, no attempt has been made to generate predictive capability, using surface plots which have also been documented to relate mechanical properties to process parameters. In particular, the novel polar force footprint data are related to energy input to the welds and to residual stress measurements. The net result is a significant improvement in the understanding of linkages between performance, residual stresses, energy input and process parameters.

Monitoring of process data during welding will assist in providing a clearer understanding and better predictive capability of suitable weld conditions as a function of alloy, plate thickness and property requirements of the joint. This will greatly reduce the current empiricism in choice of FSW process parameters, and will be a useful outcome of the work described in this thesis.

### **3. Experimental design for identifying critical process parameters**

#### **3.1 Introduction**

Understanding the influence of process parameters on quality and performance factors, such as weld strength, fatigue life and residual stress, is crucial to enhancing the acceptability of FSW in industry. These investigations are also vital to enable online control of the weld quality during the welding process. Large sets of data are required to advance understanding of these areas, due to the inherent variability in performance parameters and because of the multi-variable nature of welding processes. This means that statistical analysis is an ideal tool to apply to welding research. It provides a means of identifying important factors and their interactions, and of developing statistical models to be used for predicting results or consequences, and can assist in developing an in-depth understanding of the physical processes involved.

Because of the multivariate nature of welding, the selection of technique, process parameters and welding consumables, are generally incompletely optimized. The situation is worsened by the fact that it is not clear whether the observed variables are related to only some or to all of the meaningful process parameters, nor is it clear how these parameters affect the final weld quality, even if "weld quality" can be unambiguously defined. Finally, the lack of mathematical models for the weld process makes it impossible to supplement experimental data by simulation. All these aspects imply that the available experimental data must be used efficiently, looking for the best trade-off between complexity and insight.

The Design of Experiments (DOE) technique, developed by Fisher<sup>1</sup> in England in the 1920's, describes experimental methods used to quantify indeterminate measurements of factors and uncertain interactions between factors statistically, through observance of forced changes made methodically as directed by mathematically systematic tables<sup>2</sup>. The development of appropriate weld procedures for particular geometries, alloys and processes requires extensive experimentation that is time consuming and expensive. The process is further

---

<sup>1</sup> Fisher, RA (1925)

<sup>2</sup> ([http://www.isixsigma.com/dictionary/Design\\_of\\_Experiments\\_-\\_DOE-41.htm](http://www.isixsigma.com/dictionary/Design_of_Experiments_-_DOE-41.htm))

complicated due to the fact that there are multiple sets of variables that could deliver the required welding objectives. Traditionally weld process modeling focused on individual processes in isolation when, in reality, these processes are interrelated<sup>1</sup>.

Reduction in the required experimentation can be accomplished when experiments are constructed according to an experimental array or the DOE method, such as Taguchi's<sup>2</sup>, or with computer generated arrays, or if classical response surface arrays<sup>3,4</sup> are utilized. Researchers often make use of Taguchi methods for screening a large number of factors that might be influential on experimental outcomes and then narrowing these down for a study that is more intensive, using response surface designs. Empirical models of the response surface can then be created using for example regression techniques or neural networks to develop an approximation between the independent variables and the responses within a small region around the optimal value. Since the response surface is generally curved a second order response model is usually applied. The empirical models are used to optimize the process and confirmation tests are then performed on these models.

Approaches used in the past for welding investigations include:

- (i) static Taguchi methods<sup>5</sup>;
- (ii) computer generated models linked to neural networks<sup>6</sup>;
- (iii) heuristic parameter optimization methods such as tolerance boxes<sup>7</sup>; and
- (iv) classical DOE methods such as those of Bukarov<sup>8</sup>

Taguchi methods can address noise factors that are undesired variables, such as ambient temperature, humidity and aging in a part that cannot be controlled by the investigator. Another advantage is that Taguchi methods result in applying less experimental runs than classical "one parameter at a time" methods. Although there are many different approaches to Design of Experiments, Taguchi methods stand out because of their statistical simplicity, ease of use, appeal to engineers,

---

<sup>1</sup> Quintana, P et al (2002)

<sup>2</sup> Park, SH (1996)

<sup>3</sup> Phadke, SM (1989)

<sup>4</sup> Choueiki, MH and Mount-Campbell, CA (1999)

<sup>5</sup> Allen, TT et al (2002)

<sup>6</sup> Noruk, J S (1997)

<sup>7</sup> Harwig, DD (2000)

<sup>8</sup> Bukarov, V (1997)

and proven track record<sup>1</sup>. Artificial neural networks (ANN) offer a coherent approach to modeling virtually any phenomenon with a high degree of accuracy as long as the DOE is sufficiently large.<sup>2</sup> The drawbacks are that these methods are complicated to interpret and they provide limited information about the ability of the process to give consistent welds with a given combination of input settings. The accuracy of neural networks is also difficult to predict unless the training set is very large, because of the many possible ANN implementations and because of performance sensitivities to the choice of the DOE<sup>3</sup>.

In relation to FSW, Record et al<sup>4</sup> applied a 16-run fraction factorial design to investigate the relationship between process parameters in FSW. They were the first to attempt a statistical approach to characterizing the FSW process. Their investigations indicated that feed rate, rotational speed and plunge depth are the most important process parameters. The distance between the welds and the side of the plate influenced the vertical force on the tool.

This chapter describes the experimental strategy and matrix employed in this project as well as the methods of analysis used in this investigation. Taguchi methods were not employed in this investigation, because only two important tool input parameters were identified and the input parameters were calculated based on a set of constant ratios of feed rate/rotational speed and not at equal intervals. Multiple regression analyses were performed in this work to determine the most significant parameters. This is the first time that the interrelationship between process parameters and force polar plot parameters have been investigated. First, however, the FSW system is described and details of the important experimental parameters are given.

## 3.2 Experimental setup for welding

### 3.2.1 Instrumentation

The FSW system used to produce welds is illustrated in Figure 3.1. This image shows the complete experimental setup, consisting of a conventional Nicolas Correa F3U-E CM milling machine reconfigured as a FSW machine. The control

---

<sup>1</sup> Taguchi, G (1986).

<sup>2</sup> Ribardo, C (2000)

<sup>3</sup> Choueiki, MH and Mount-Campbell, CA (1999)

<sup>4</sup> Record, JH (2004)

and monitoring computer and network-distributed client used to obtain experimental data are also indicated.

Performance limits of the machine are:

Spindle Speed (rpm)	min: 28	max: 1400
Feed Speed x-axis (mm/min)	min: 11.2	max: 710
Feed Speed z-axis (mm/min)	min: 4	max: 250

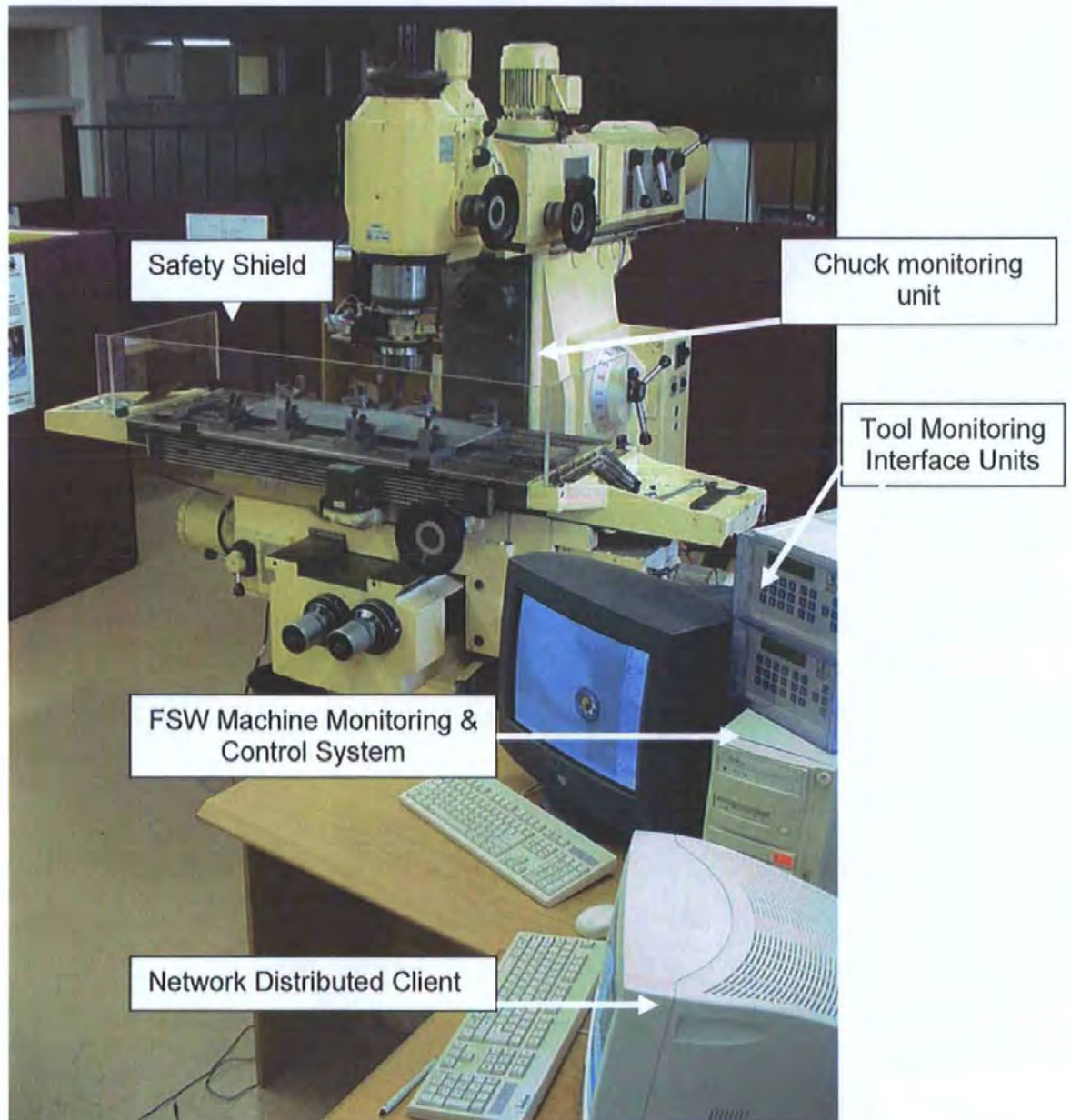


Figure 3.1: Complete experimental setup.

Software architecture was developed by Kruger<sup>1</sup>, using the LAN interface board in the computer that controls the FSW machine. This enables monitoring and controlling of the following stages in the FSW process:

- (i) moving to the weld start position (X and Y axes);
- (ii) starting the spindle at the user specified spindle rotational and plunge speeds;
- (iii) finding the surface of the material by Z-axis motion and by monitoring the vertical force present on the tool;
- (iv) plunging the tool pin to the required depth then allow a dwell period while the material heats up to between 0.6 to 0.8 of the melting temperature of the material being welded. A dwell period of 8s was long enough to obtain a sufficient "plasticized state";
- (v) making the weld seam with the selected spindle rotational speed and horizontal feed;
- (vi) extracting the pin from the material; and
- (vii) Moving the tool to the initial starting position.

An instrumented chuck to measure the dependent FSW process parameters was designed by Blignault<sup>2</sup> and the monitoring system was built by Libra Measuring Instruments (LMI) and is shown in Figure 3.2<sup>2</sup>. The electronics mounted on the chuck allow all the required variables to be sampled, the raw sensor data is signal conditioned and passed to a microprocessor, where it is prepared for transmission to the tool monitoring interface unit. Electrical power is transferred to the chuck using induction and the sampled data is read off the chuck in digital form, using a capacitive technique.

The channels of sampled data are received and processed by the microcontroller housed in the interface unit. The captured data in the controller software is recorded and processed. The user interface displays data in real-time to enable the operator to make control decisions or to allow its use as inputs to a fuzzy logic controller. A thermal insulator, a Tufnol disk (behind the power coil in Figure 3.2) and heatsink promote heat dissipation. A temperature sensor embedded near the electronics was used to monitor the temperature rise, thus preventing damage to

---

<sup>1</sup> Kruger, G (2003)

<sup>2</sup> Blignault, C (2004)



the electronics. The inductive sensor is used to measure the rotational velocity of the tool.

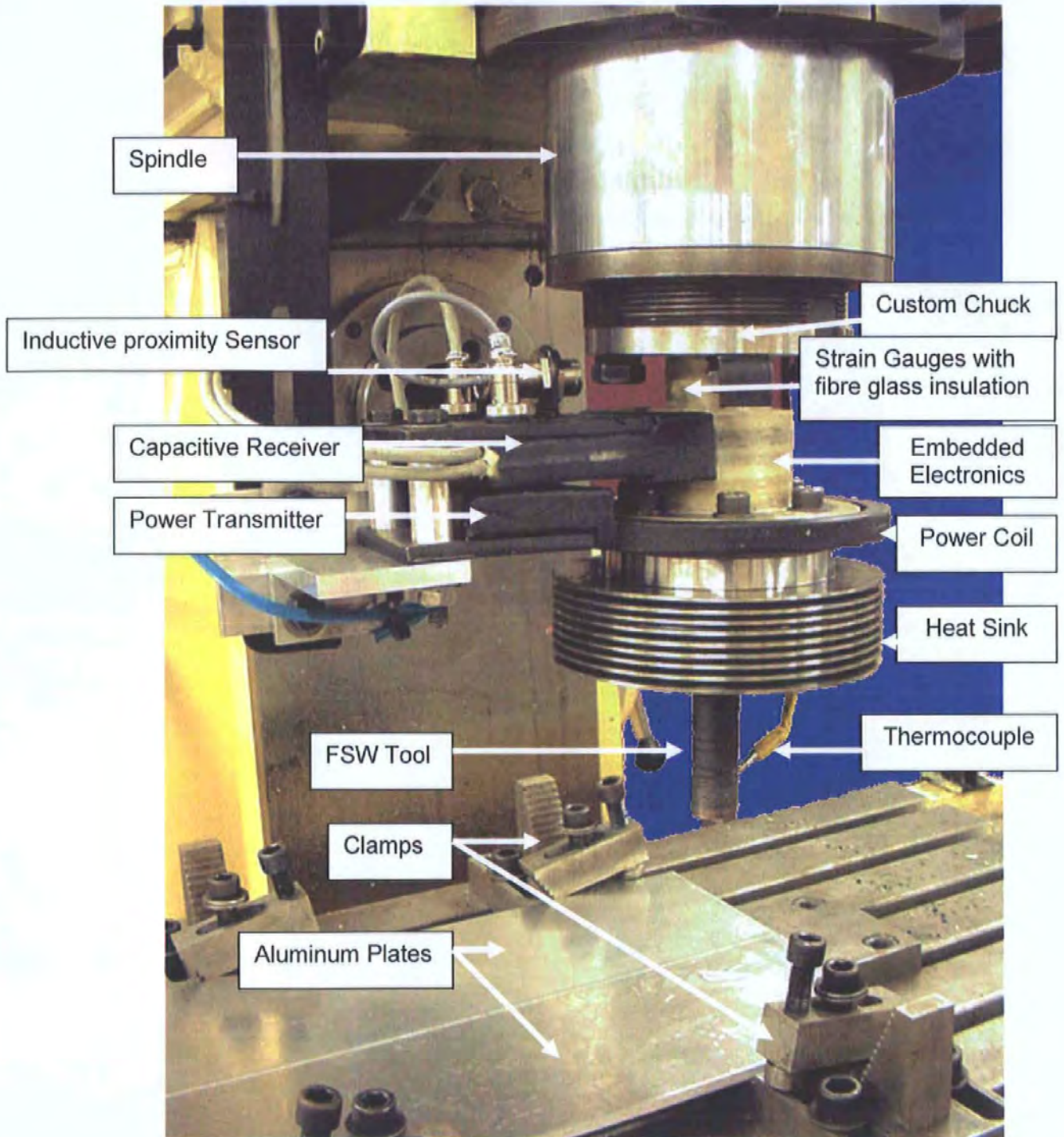


Figure 3.2: Tool monitoring system.

There are four temperature compensating Wheatstone full bridge configurations on the rotating shaft, one each for measurement of Torque,  $F_z$ -force,  $F_x$ -force and  $F_y$ -force. This rotating sensor monitoring unit allows logging of a direct stream of real-time process data including tool torque, tool temperature, and downwards force applied by the tool shoulder to the material, as well as a horizontal force vector that is measured through  $360^\circ$  as the tool rotates during welding. An additional temperature gauge is also mounted within the rotating electronic unit of the tool holder to monitor the potential of overheating. The system will shut down if the threshold level of  $70^\circ\text{C}$  is reached within the unit. A proximity sensor mounted on the receiver measures the exact rotational speed of the tool holder which is displayed in revolutions per minute.

Sensor calibration was performed to ensure that data measurements were reliable. Horizontal and vertical strain gauges were calibrated using a point load cell and the thermocouple was calibrated using a digital thermometer. The repeatability of measurements during a weld run was estimated to be in the range of 100 to 150N for the X and Y forces and 200N for the  $F_z$ -force<sup>1</sup>. The system was initially calibrated and repeatability tests were done at regular intervals by Blignault<sup>5</sup> to ensure that acceptable data would be obtained from the process investigation tests.

### 3.2.2 The force foot print polar plot

The force exerted on the tool by the metal during welding can be shown as a bi-lobed polar plot of a "force footprint" during a single rotation. Figure 3.3 shows typical examples of  $F_x$  and  $F_y$  force footprint plots and demonstrates the variation in their area observed with different process parameters. The positions of the  $F_y$  max are observed to lie in the first and third quadrants of the polar plot, and the  $F_x$  maxima are  $90^\circ$  ( $\pi/2$  radians) out of phase with these. For this thesis it was envisaged to use the angular positions of  $F_x$  and  $F_y$  maxima to interpret aspects of plastic deformation during welding. Software problems prevented this data from being acquired, so all force footprint plots of  $F_x$  and  $F_y$  are presented as having maximum values at  $0^\circ$  for  $F_x$  and  $90^\circ$  for  $F_y$ . However, data for  $F_x$  and  $F_y$  were combined to give resultant force plots (see Figure 3.5) and these plots give the correct relative angular position of the maximum force for each set of process conditions with respect to an arbitrary axis. This has been described as the FSW

force footprint<sup>1</sup>. The research group at the Nelson Mandela Metropolitan University is believed to be the first to report polar plots of force and identify their potential to characterize energy input into the welds. Figure 3.4 defines positive and negative directions as used in this thesis. The maximum force ( $F_x, +ve$ ) is defined as occurring in the opposite direction to that of welding. Forces in the direction defined as negative are usually smaller than those in the positive direction. If the tool was not tilted and was rotated against an applied static position, the positive and negative lobes of the force footprint should be equal<sup>1</sup>. As the tool is tilted at approximately 2.5 degrees and the tool is moving forward against rotational plastic flow around it, the force lobes are generally not equal.

The polar plot provides a graphical representation of the maximum force as a function of tool rotation angle. The maximum force can be used to determine the power exerted by the tool. The lateral component of the force on the tool,  $F_y$ , is perpendicular to the direction of tool feed and therefore does not contribute to the energy required to move along the weld line. It is likely that  $F_y$  has a correlation with weld plastic flow and the efficiency of the bonding process.

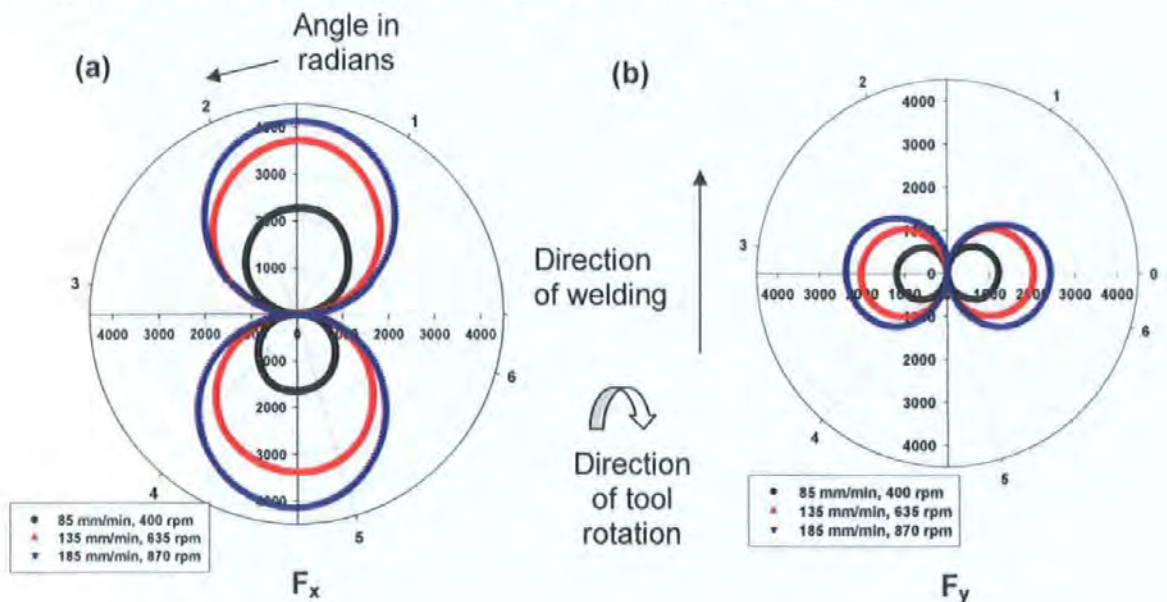


Figure 3.3: Typical polar force plot obtained for FSW using the tool geometry shown in Figure 3.7.

<sup>1</sup> Hattingh, DG et al (2004)

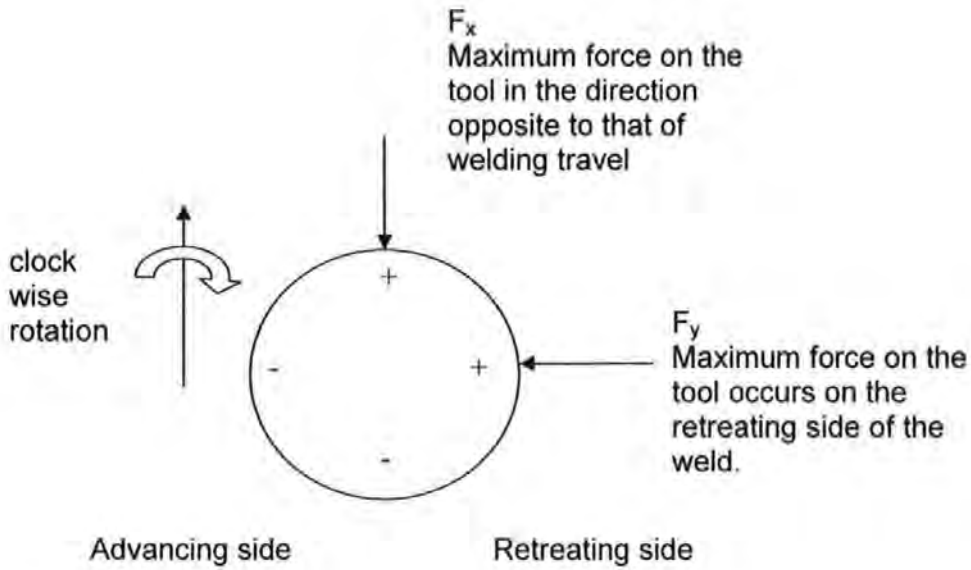


Figure 3.4: Directions of forces on the tool and strain gauge measurements.

A resultant plot of  $F_x$  and  $F_y$  can be obtained by calculating the magnitude of the resultant of  $F_x$  and  $F_y$ ,  $\pi/2$  out of phase, as shown below, for a single illustrative case. Thus the resultant force is given by  $F_{res} = \sqrt{F_x^2 + F_y^2}$ .

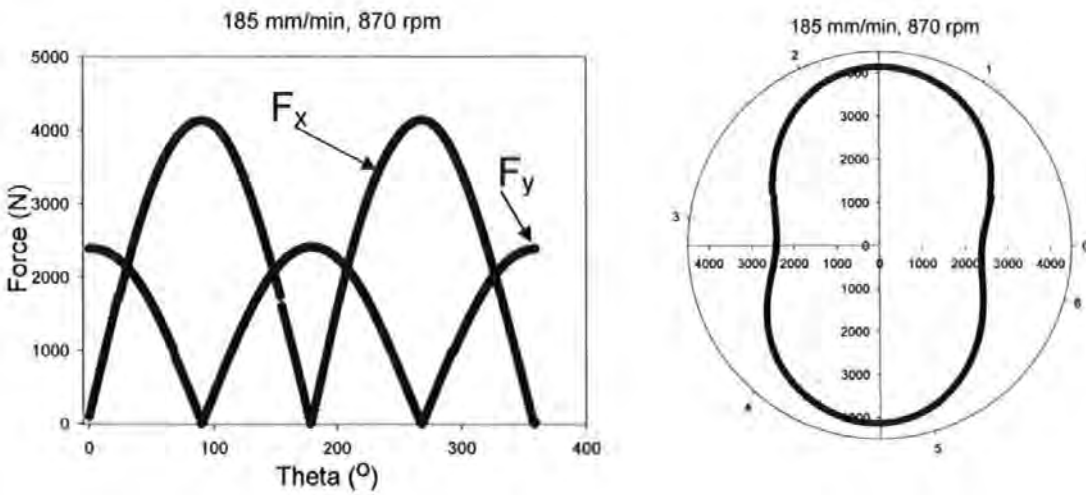


Figure 3.5: Resultant force polar plot of a weld made at a feed rate of 185 mm/min and 870 rpm.

The areas of these plots and the resultant force will be related to tool energy and mechanical properties as a function of process parameters in order to assess their suitability to be used as part of a weld prediction model.

Tool pitch can be defined as the ratio of feed rate over tool rotational speed and should therefore play a key role in the plastic state of the material and in the resulting weld properties. However, at a constant tool rotational speed a faster feed rate for a given value of pitch implies that the tool and material are in contact for less time at a specific point and therefore that less heat can be transferred to the material. There are likely to be threshold combinations of tool rotational speed and feed rate that should be required for a good plasticized state.

To examine the information contained in the force footprint data in detail, a Matlab program was developed to obtain the area of the force footprint lobes for each tool revolution because the data files were quite large for the 750 mm long welds. Videos showing the variation in force footprint along a weld run can be found on the CD provided in appendix A. The videos present the areas of the lobes, the angle of the maximum force and the magnitude of the maximum and minimum force in one revolution as the weld is made. The averages of these areas per revolution were determined for a pseudo-steady state region as explained in section 3.3. The areas can be plotted as force versus radian and the following mathematical relationship can be derived for the integration of a polar plot. The units can be converted to J/s in the following way:

$$\text{Power of polar plot} = (\text{Areas in force versus radian}) * \text{number of rev/s} * \text{pitch} = [\text{J/s}] \quad \dots(3.1)$$

There exists a linear relationship with a coefficient of correlation of 0.99 between the power determined from the polar plots ( $F_x$ ) and the power input determined from the translational forces, as shown in Figure 3.6.

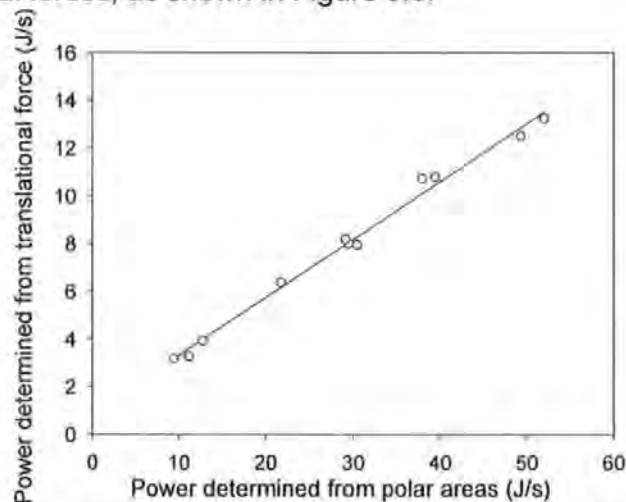


Figure 3.6: Comparison of polar plot data with total power input determined from the translational forces.

### 3.2.3 Experimental conditions

Weld quality is influenced by a number of tool-related parameters, including rotational speed, feed, forging force and tool geometry. Tool speed, feed rate and downward forging force are weld input parameters and can be systematically varied for a single tool geometry.

#### 3.2.3.1 Tool geometry

The tool used to perform the welds in this research study is shown in Figure 3.7 and has a recessed type shoulder of 25.4 mm outer diameter that is intended to create a good flow path for the plasticized material on the surface and also to reduce side flash. The depth of recess was 1.4 mm. The tool was made from W302 (H13) tool steel hardened to 556 HV.

The 10 mm diameter pin has a single flute and a threaded surface respectively intended to improve the static to dynamic volume flow ratio and to assist in the downward auguring effect. The forging action of the tool is enhanced via a forwards tool tilt angle of 2.5 degrees. The pin for welding the 6 mm thick plate of Al 5083-H321 used has 25 threads per inch over a length of 5.7 mm. The scallop on the pin was machined with a major radius of 9 mm and minor radius of 5 mm to a depth of 6 mm at an angle of 30° degrees. Figure 3.7 illustrates the chosen tool geometry.



Figure 3.7: Flute tool geometry used to make the FSW.

The tool can accommodate a thermocouple to give an indication of the tool operating temperature and was designed by Blignault<sup>1</sup>. The tool temperature was measured in the interior of the tool body and is hence more relevant to characterizing tool wear processes than to energy input into the welded joint.

### 3.2.3.2 Input parameters

Since the interrelationship between process parameters in FSW is complex, only feed rate and rotational speed of the tool were altered in this study. A plunge depth was chosen that would keep the tool pin 0.08 mm from the bottom of the plate since this has been proven to be sufficient to eliminate root defects<sup>1,2</sup>. The range selected for feed rate and rotational speed was chosen to be as wide as possible whilst retaining production of reasonably sound welds. This range was assessed for 5083-H321 aluminium alloy at the Nelson Mandela Metropolitan University (NMMU). It was found that sound welds could be made when welding at spindle speeds between 150 and 550 rpm and feed rates (x-axis) between 40 mm/min and 250 mm/min equivalent to pitch ratios (mm/rev) of 0.27-0.45<sup>1</sup>.

A tool-cooling period was used between weld runs to prevent residual heat in the tool affecting the next weld. From practical experience, it was found that only one weld run of 750 mm could be completed every 30 minutes at best. Welds were not made using sequential sets of tool speed and feed but random sets, to reduce any effect of random errors in the results.

Table 3.1 lists the different combinations of tool speed and feed proposed for use in this study. A weld could not be made at 85 mm/min and 173 rpm, because the downwards force measured on the tool was too high which could have led to tool or telemetry system damage. The values given in Table 3.1 are the measured data during welding and are used in all the graphs drawn to determine the relationships between the input and process parameters.

---

<sup>1</sup> Blignault, C(2003)

<sup>2</sup> Seidel, TU and Reynolds, AP et al (2001)

85 mm/min		135 mm/min		185 mm/min	
RPM	Pitch	RPM	Pitch	RPM	Pitch
400	0.21	635	0.21	870	0.21
266	0.32	423	0.32	617	0.3
201	0.42	318	0.42	436	0.42
173	0.5	254	0.51	348	0.53

Table 3.1: Input parameters of FS welds.

### 3.3 Experimental Results

Table 3.2 and 3.3 summarize the various parameters measured during welding under pseudo-steady state conditions as shown in Figure 3.8 (a)-(d) for distances 200 mm to 550mm. The averages of the measured values were determined using a Matlab programme to handle the large number of data points in this region. A decrease in  $F_z$  is detected as the weld run is made. This is probably due to heat flowing into the surrounding matrix and thereby softening it. Thermomechanical modelling by Schmidt and Hattel<sup>1</sup> has also shown this phenomenon. A slight increase in  $F_z$  is generally observed towards the end of the weld run and the reason for this is not known, but may be related to the slight increase in tool temperature observed at the same point in the weld run (Fig 3.8 (c)). It is therefore not advisable to weld for longer than 550 mm using the current experimental set up.

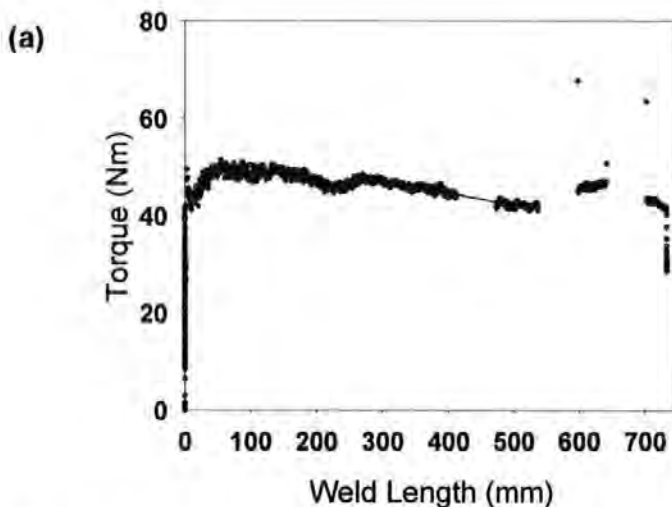


Figure 3.8: (a) Variation of tool torque along the weld.

<sup>1</sup> Schmidt, H and Hattel, J (2005)



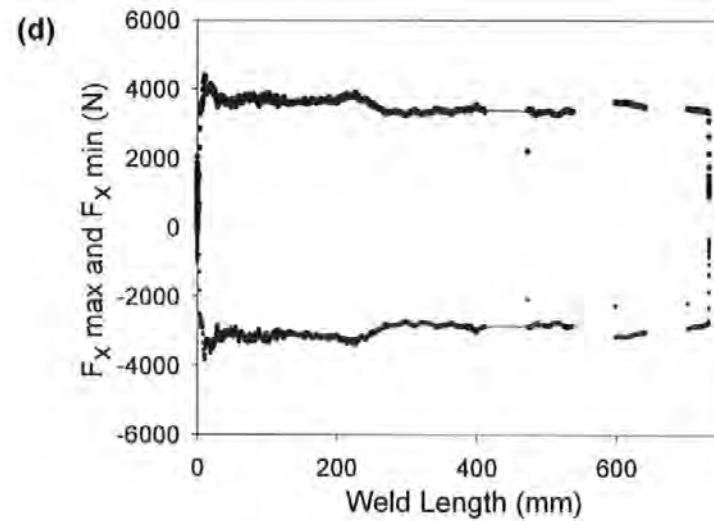
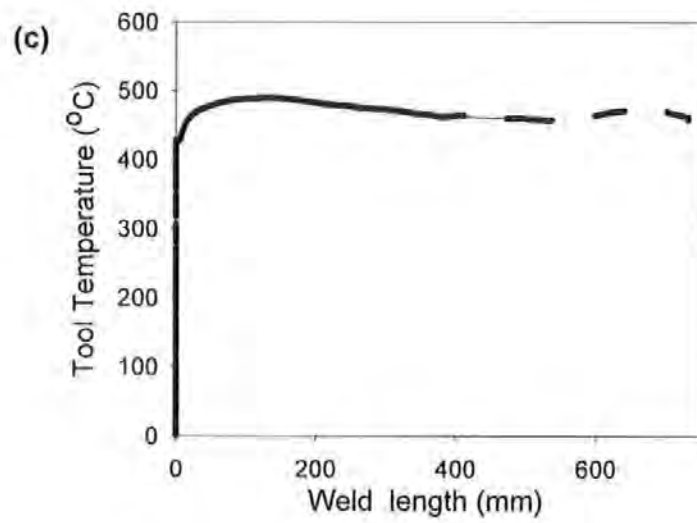
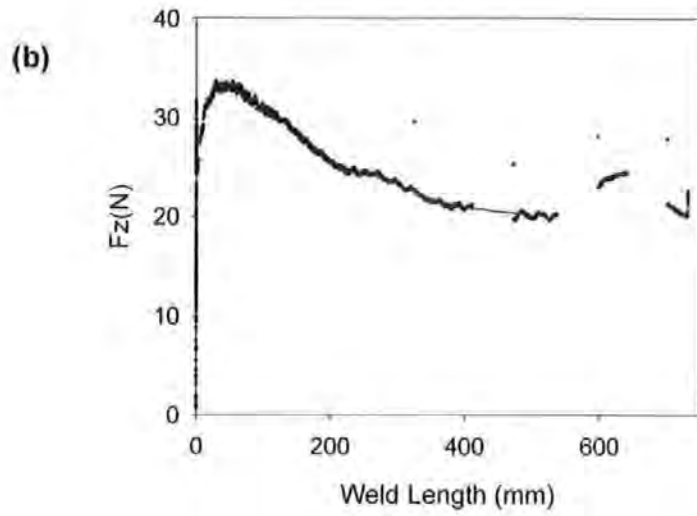


Figure 3.8: (b) Variation of vertical force ( $F_z$ ) along the weld.  
(c) Variation of tool temperature along the weld.  
(d) Variation of  $F_x$  max and  $F_x$  min along the weld.

The data for  $F_z$ , tool temperature, tool torque and  $F_x$  against weld distance were used in the energy calculation given in Table 3.6. Tables 3.2 and 3.3 present process parameters and polar plot data.  $F_z$ , tool torque and  $F_x$  max are measured from strain gauges positioned on the chuck. The standard deviation is also listed in the table and is represented by the abbreviation "SD". The rotational speed determined from encoder measurements are also given in Table 3.2. The data in Tables 3.2 and 3.3 will be related to the tool rotational speed and feed rate via surface plots.

<b>Weld input and process parameters</b>									
Weld	Feed	RPM	Pitch	$F_z$	SD	Torque	SD	Temp	SD
	(mm/min)	(rev/min)	(mm/rev)	(kN)		(Nm)		(°C)	
1	185	436	0.42	25.0	4	46.51	2	474	10
2	135	423	0.32	40.9	2	55.87	2	512	7
3	85	201	0.42	43.7	3	86.84	4	464	8
4	185	870	0.21	32.0	5	25.64	2	524	10
5	135	254	0.51	24.3	3	70.21	5	431	18
6	85	266	0.32	33.2	2	63.59	3	470	8
7	185	348	0.53	41.4	3	69.31	1	497	6
8	85	400	0.21	36.9	2	48.26	1	496	5
9	135	318	0.42	41.4	2	68.69	1	497	6
10	185	617	0.30	34.8	3	26.20	1	528	1
11	135	635	0.20	36.4	4	33.64	1	507	8

Table 3.2: Weld input and process parameters.

<b>Polar plot data</b>						
Weld no	$F_x$ max	SD	$F_y$ max	SD	Fres	SD
	(N)		(N)		(N)	
1	3494	158	-1913	92	3926	192
2	3554	83	-1939	56	4054	96
3	2770	155	-1430	65	3154	100
4	4051	236	-2296	95	4582	200
5	3634	269	-2109	95	4249	186
6	2248	110	-1140	118	2521	124
7	3476	36	-1827	46	3970	72
8	2305	275	-1170	53	2560	117
9	2834	32	-1426	37	3227	52
10	4293	54	-1589	444	4004	156
11	3532	105	-1963	81	2970	195

Table 3.3: Polar plot data.

The percentage deviation from the average  $(SD/average) \times 100$  for all the process parameters is listed in Table 3.4.

Percentage deviation in process parameters					
Weld	$F_z$	Torque	Temperature	$F_x$ max	$F_y$ max
1	±16	±4	±2	±5	±4
2	±5	±3	±1	±5	±2.69
3	±7	±5	±2	±5	±6
4	±13	±7	±2	±3	±6
5	±14	±7	±4	±4	±7
6	±6	±5	±2	±5	±5
7	±7	±2	±1	±5	±1
8	±6	±3	±1	±9	±12
9	±6	±2	±1	±3	±1
10	±10	±3	±2	±23	±3
11	±9	±4	±2	±7	±5

Table 3.4: Percentage deviation in process parameters.

### 3.4 Interrelationship of input and process parameters

As already noted, this study is concerned with two aspects of FSW, namely the energy input and characterizing the plasticized state of the material being welded. The graphical illustration given in Figure 3.9 shows the inter-dependencies among the various parameters that characterize a weld process and the output properties of the weld.

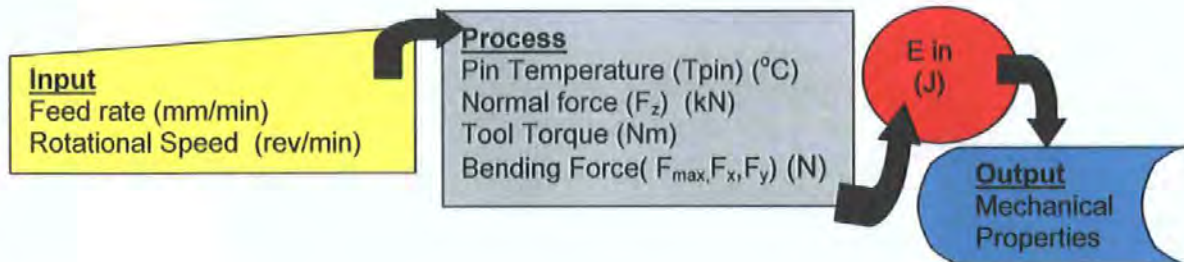


Figure 3.9: Functional relationships model for parameters.

Considering Figure 3.9 the condition of the material determines the values of the process parameters being measured.

In this thesis it is proposed that the measured tool torque represents the energy put into the plasticization of the alloy. The value  $F_x$  max represents the energy put into translating the tool through the material, while  $F_y$  max represents energy used in translating the alloy around the tool to make the weld. Thus the resultant force

$F_{res} = \sqrt{F_x^2 + F_y^2}$  represents the degree of plasticization and the "mixity" of material in the weld. The peak values of  $F_{res}$ ,  $F_x$  and  $F_y$  as a function of process conditions should be relatable to weld properties and defects.

When enough heat has been transferred into the material a good plasticized state is obtained. The resistance to motion is then lower and tool torque,  $F_x$  max and  $F_z$  should decrease to lower values. If the material is soft enough then  $F_z$  will also decrease. This will remain true if the plunge depth is kept constant and the thickness of the material stays the same throughout welding, and such conditions will minimize the possibility of root defects occurring. Polar plot areas will be smaller and tool temperature should be higher.

When the material is not in such a well plasticized state, the values of all the force process parameters should increase.

#### 3.4.1 Energy input to the welds

The methods used to determine the average heat input (J/mm) and frictional power input (J/s) into the weld were discussed in Chapter 2 and the relevant equations from literature are repeated here.

$$Q_{in1} = \eta \frac{2\pi\omega \text{Torque}}{f} = \text{average heat input (J/mm)} \quad \dots(3.2)$$

or

$$P_{in1} = \frac{4}{3} \pi \mu F_z \omega r = \text{frictional power input (J/s)} \quad \dots(3.3)$$

The following parameters were used in the above calculations:

Efficiency ( $\eta$ ) = 0.9

Radius of the tool ( $r$ ) = 12.7 mm

The effective coefficient of friction ( $\mu_{eff}$ ) was determined using

$$\mu_{eff} = \frac{3 \text{ Torque}}{2 F_z x r} \quad \dots(3.4)$$

The distribution of power input between the shoulder and the pin was discussed in Chapter 2, which indicate that some 82% of the heat input is generated by the shoulder if no losses are considered.

Table 3.5 lists the energy calculations as defined by equation 3.3 (frictional power input), the sum of equations 3.5 and 3.6 (total tool power), and equation 3.2 (average heat input). The total power is a translational component, calculated from the  $F_x$  max data determined from the area of the force footprint polar plot from a rotational energy part calculated from torque. Table 3.6 indicates that, at least for this relatively thin plate, the translational power which contributes to total power is small (compare the numerical values in the columns headed Total Tool Power and Frictional Power). It also indicates that torque-based calculations of energy yield similar results to models based on frictional power. This is as expected, but provides independent confirmation that the equations used in this thesis are capable of characterising the FSW process.

<b>Weld no</b>	<b>Total Tool Power (J/s)</b>	<b>Frictional power input (J/s)</b>	<b>Average heat input (J/mm)</b>
1	2134	2124	620
2	2483	2475	990
3	1832	1828	1161
4	2348	2336	683
5	1875	1868	747
6	1775	1771	1125
7	2537	2526	737
8	2025	2021	1284
9	2294	2287	915
10	1706	1693	494
11	2244	2237	895

Table 3.5: Energy calculations and analyses.

Figure 3.10 shows the relationship between heat input and the input process parameters of tool feed and rotational speed. As the feed rate increases the heat input to the weld decreases. The effect on heat input as the rotational speed increases is less clear; at low feed rates energy input goes through a peak as rotational speed increases (see Figure 3.10a) while at high feed rates it goes through a trough. The heat input decreases at a constant pitch as the feed rate increases.

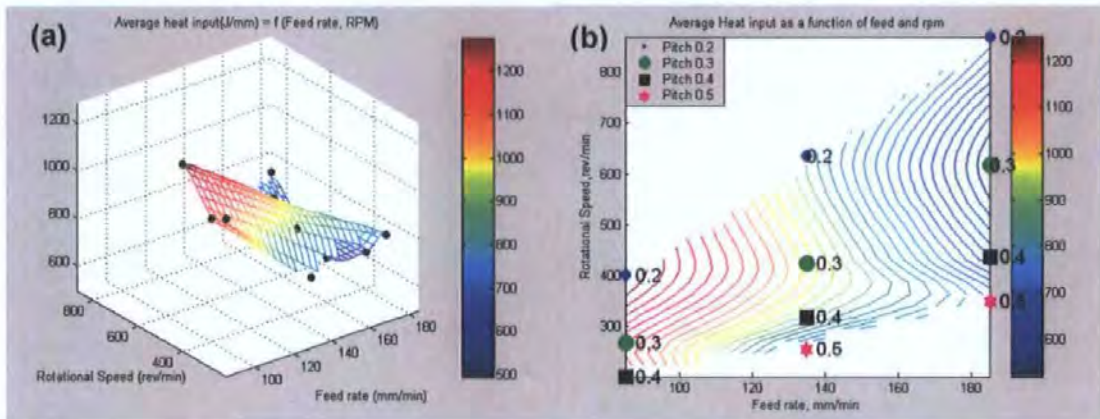


Figure 3.10: (a) 3D plot of heat input versus tool rotational speed and feed rate. (b) Contour plot of heat input versus tool rotational speed and feed rate.

The frictional power input is plotted in Figure 3.11 and shows a maximum value at approximately 400 rpm and 140 mm/min. A complex relationship exists between frictional power input and the input parameters. Local minima in power input occur at a pitch of 0.3 mm/rev at high feed rates and rotational speeds (for example 185 mm/min and 617 rpm) and at low feed rates and low speeds (for example 85 mm/min and 266 rpm). This form of data implies complex plasticity phenomena in the TMAZ.

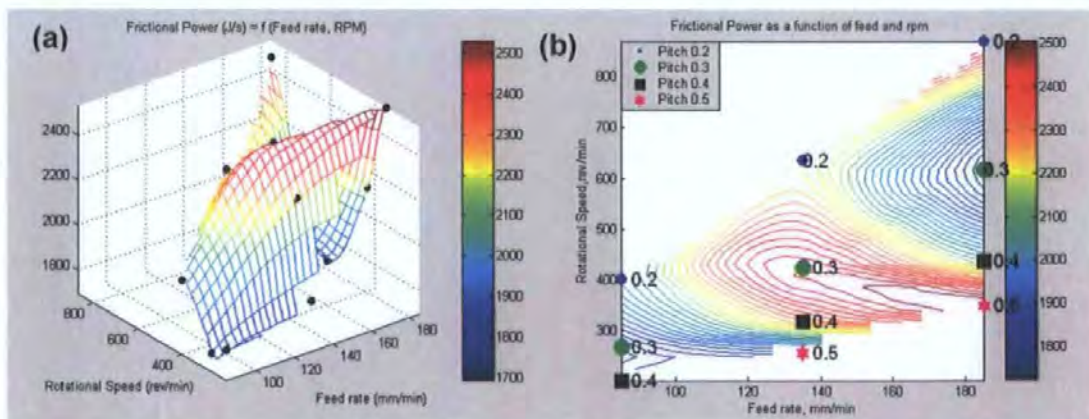


Figure 3.11: (a) 3D plot of frictional power input versus rotational speed and feed rate. (b) Contour plot of frictional power input versus rotational speed and feed rate.

During welding, both translational and rotational forces contribute to the power input into the tool. This thesis also considers such a total tool power model, because the force footprint plots should correlate with the translational energy component. The power input can then be determined from:

$$P_{trans} = F_{max} * feedrate(J/s) \quad \dots(3.5)$$

and

$$P_{rot} = \frac{2\pi\omega T}{60} \text{ (J/s)} \quad \dots(3.6)$$

These equations are based on the assumption that the plunge depth,  $F_x$  max, torque and  $F_z$  all remain approximately constant per revolution during welding. It is quite complex to determine the heat transfer into the material; if the losses due to radiation, convection, conduction and the frictional machine losses are considered, then an energy balance of the system could be described as:

Power input to FS machine ( $V \cdot I$ ) = Translational energy from the tool + rotational energy from the tool + Energy input due to the normal force + machine losses.

Heat transfer to the material = Frictional heat + heat generated due to plastic flow - losses due to conduction, convection and radiation.

Thermodynamic properties change with temperature and accurate values are not available, heat losses were not determined and therefore the simplified power approach summarized determined by equations 3.5 and 3.6 was used.

The surface plot of total power on the tool calculated from rotational and translational forces acting on it (Figure 3.12) shows a reasonable agreement with the  $F_z$  profile illustrated in Figure 3.18(d) as a function of tool feed rate and rotational speed. Figure 3.12 shows similar power input trends to Figure 3.11, as a function of tool feed rate and rotational speed, with distinct regions of minimum power input.

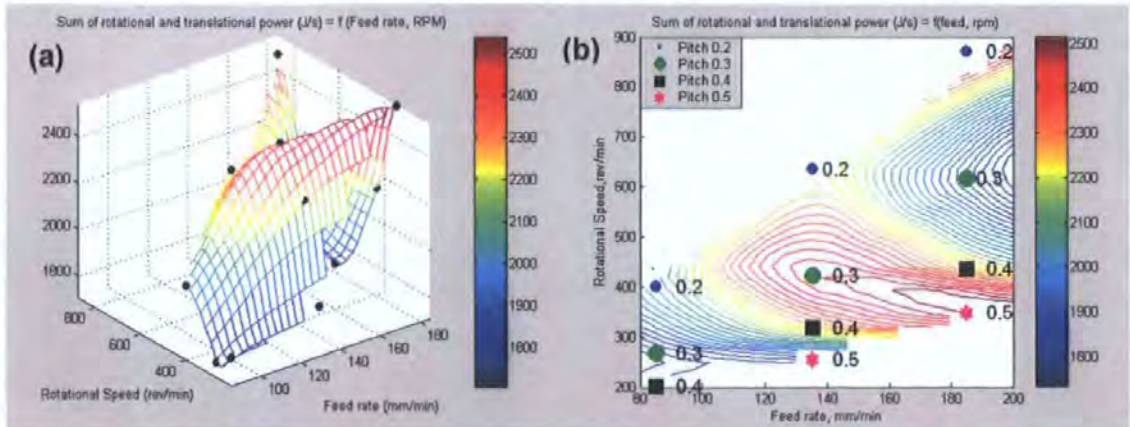


Figure 3.12: (a) 3D plot of the sum of rotational and translational power input versus rotational speed and feed rate.  
 (b) Contour plot of the sum of rotational and translational power input versus rotational speed and feed rate.

The question now arises as to how to characterize a good plasticized state of the material and how does the plasticized state relate to the process parameters. The plasticized state is largely controlled by feed rate and rotational speed as explained in the literature review, in Chapter 2. Equation 3.7 indicates that the width of the plasticized state( $\xi$ ) is proportional to  $\omega^2/f^1$ .

$$\xi = \mu\beta\alpha\omega \left( \frac{R\omega}{f} \right) \left( \frac{R}{k_{th}(T_{solidus} - T_{ambient})} \right) = \left( \frac{\omega^2}{f} \right) (\mu\beta R^2\alpha) \left( \frac{1}{k_{th}(T_{solidus} - T_{ambient})} \right) \dots(3.7)$$

This is a simplification, since some of the parameters like the viscosity are a function of temperature and cannot be considered as a constant in the equation. This simplified approach shows that the plasticized state is strongly dominated by the choice of rotational speed. The assumption will be made in this investigation that  $\omega^2/f$  represents a measure of the plasticized state of the material.

If  $\omega^2/f$  is plotted against effective coefficient of friction (equation 3.3) a linear relationship is observed.

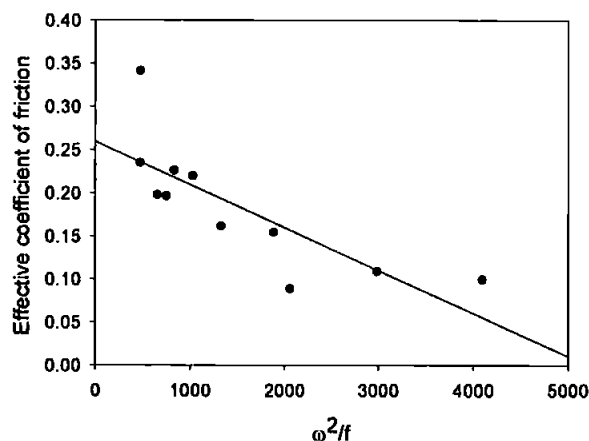


Figure 3.13: The relationship between  $\omega^2/f$  and the effective coefficient of friction.

The variation of  $\omega^2/f$  with respect to the process parameters is also investigated. Figure 3.14 shows the general trend, for increasing  $\omega^2/f$  as a function of vertical force ( $F_z$ ), tool temperature, tool torque and forces  $F_x$  max and  $F_y$  max.

<sup>1</sup> North, TH et al (2000)



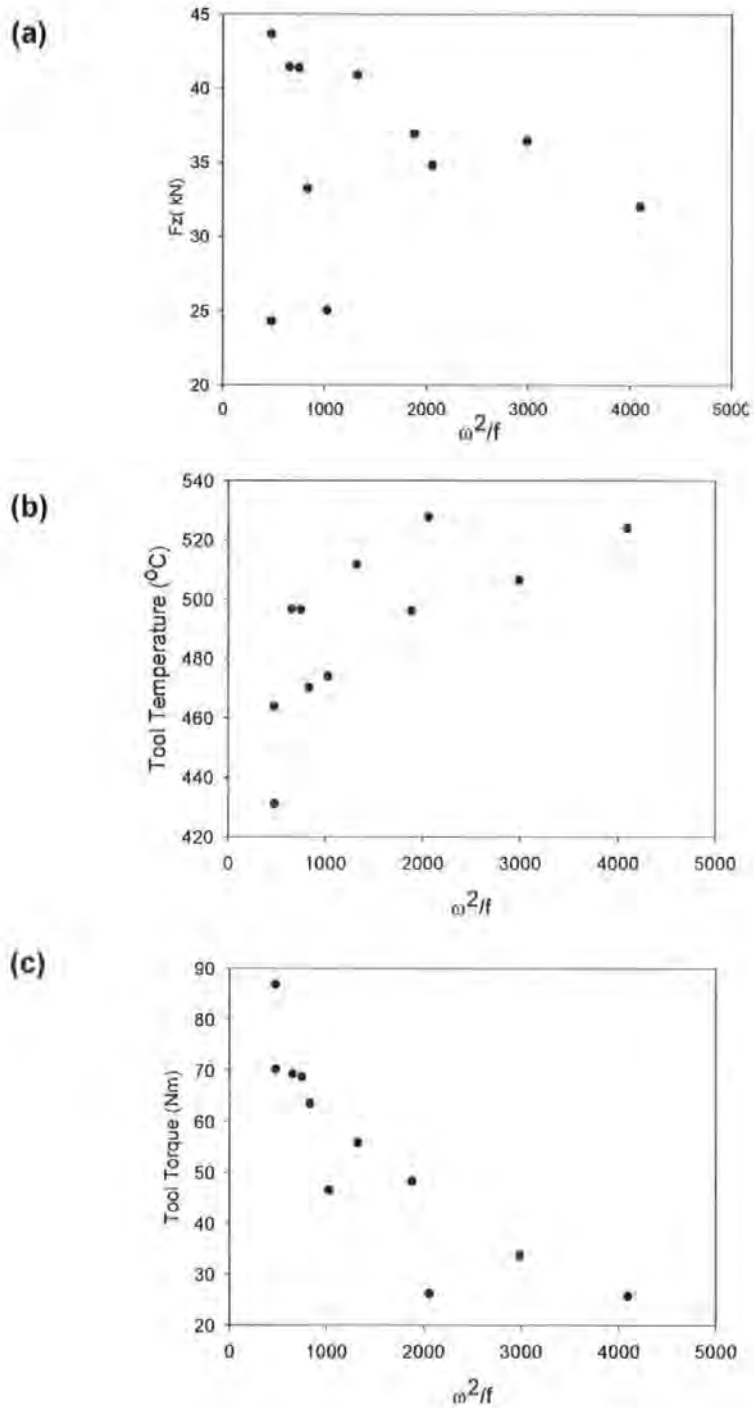


Figure 3.14: (a) Normal force versus  $\omega^2/f$ .  
 (b) Tool temperature versus  $\omega^2/f$ .  
 (c) Tool torque versus  $\omega^2/f$ .

Figure 3.14 (a) shows that when increasing values of  $\omega^2/f$  there is no clear relationship between  $F_z$  and  $\omega^2/f$ . However, reasonably linear relationships exist between  $\omega^2/f$  and tool temperature or tool torque. The value of  $\omega^2/f$  (thus the width of the plasticized region) increases as either tool temperature increases or tool

torque decreases. Figure 3.14 (c) shows that tool torque decreases for increasing  $\omega^2/f$  values. Since the coefficient of friction decreases with increasing  $\omega^2/f$ , energy input is greater, leading to lower shearing forces on the tool. A meaningful relationship between process parameters and  $\omega^2/f$  can now be summarized, as shown in Figure 3.15. The effective coefficient of friction and the tool temperature could be used as an indication of the plasticized state of the material and plastic flow processes.

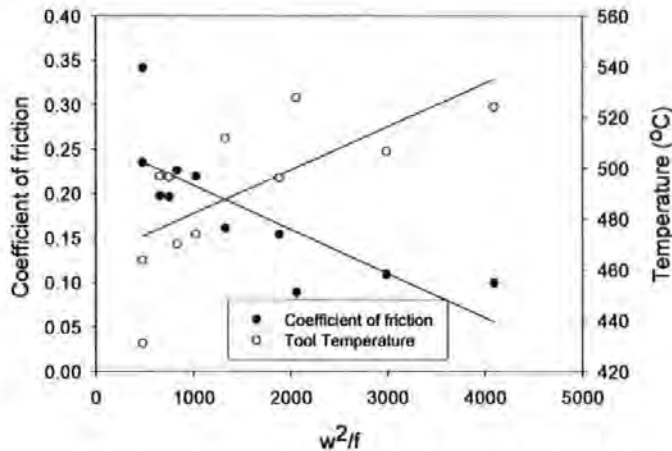


Figure 3.15: A comparison between the effective coefficient of friction, tool temperature and  $\omega^2/f$ .

A relationship can now be determined between  $\omega^2/f$  and the process parameters tool temperature,  $F_z$  and Torque. Since  $\omega^2/f$  is proportional to tool temperature and inversely proportional to effective coefficient of friction hence the following equation can be derived:

$$\text{Plasticized width } (\xi) \propto \omega^2/f = C \cdot \text{tool temperature} / \text{coefficient of friction} \quad \dots(3.8)$$

where  $C=0.44$  is a constant derived from the following linear relationship given in Figure 3.16 and the coefficient of friction is a function of (Torque/ $F_z$ ) as given by equation 3.3.

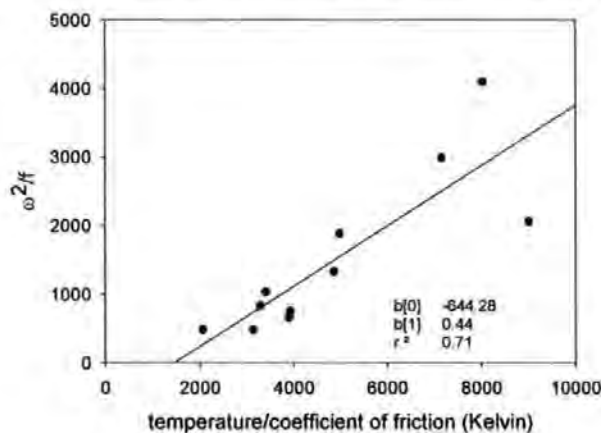


Figure 3.16: The parameter ( $\omega^2/f$ ) versus temperature/coefficient of friction

### 3.4.2 Regression models of weld parameters<sup>1,2,3</sup>

In this section an attempt is made to determine meaningful relationships between the input parameters and output variables via a statistical analysis. The results of the multiple regression analyses of the process parameters are shown in Table 3.7. An observed output from the welding process, (for example tensile strength) can be written as a function of the levels of input variables such as feed rate and rotational speed.

$$y = f\{a_1, a_2, a_3, \dots\} + \epsilon_r \quad \dots(3.9)$$

where

$y$  = output response variable (UTS)

$a_1, a_2, \dots$  = input variables ( feed rate and speed)

$\epsilon_r$  = statistical random error term with a normal distribution which is a measurement of the error on the response

The expected output response can then be represented as a contour plot where two input variables form the axes in the plane of the paper and the output response forms the perpendicular axes. The contours show conditions giving a constant response. The first step in mathematical modelling is then to determine a suitable output approximation for the output response as a function of the input process variables.

If the response is well modelled by a linear relationship then the mathematical approximation is given by

$$y = a_1 + b_1x_1 + b_2x_2 + \dots a_kx_k + \epsilon_r \quad \dots(3.10)$$

The method of least squares is used to determine the coefficients in the model. This method chooses the coefficients so that the sum of the squares of the errors is minimized and is given by.

---

<sup>1</sup> Park, SH et al (1996)

<sup>2</sup> Navidi, Y (2007)

<sup>3</sup> Montgomery, DC (1976)

$$L = \sum_{i=1}^n (y_i - a_0 - \sum_{j=1}^k a_j x_{ij})^2 \quad \dots(3.11)$$

The least squares estimators  $a_0, \dots, a_k$  satisfy

$$\left. \frac{\partial L}{\partial a_0} \right|_{b_0, b_1, \dots, b_k} = -2 \sum_{i=1}^n \left( y_i - b_0 - \sum_{j=1}^k b_j x_{ij} \right) = 0 \quad \dots(3.12)$$

The difference between the observed  $y$  and fitted  $\hat{y}$  is referred to as the residual.

The variance,  $\sigma^2$ , is given by

$$\sigma^2 = \frac{SS_E}{n-p} \quad \dots(3.13)$$

where

$$SS_E = \text{residual sum of squares or error given by } \sum_{i=1}^n (y_i - \hat{y}_i)^2$$

$n-p$  = degrees of freedom

The value of  $\sigma^2$  depends on the form of model that is fitted to the data. A larger variance indicates that there is more unexplained variability resulting from the model.

The significance of regression is tested by using

$$S_{yy} = SS_R + SS_E \quad \dots(3.14)$$

where

$$S_{yy} = \text{total sum of square} = \sum_{i=1}^n y_i^2 - \frac{(\sum_{i=1}^n y_i)^2}{n}$$

$SS_R$  = regression sum of squares

$SS_E$  = residual sum of squares

A regression coefficient ( $a_0 = a_1 = \dots = 0$ ) if

$$F_o = \frac{SS_R / k}{SS_E / (n - k - 1)} = \frac{MS_R}{MS_E} \quad \dots(3.15)$$

exceeds the value  $F_{\alpha, k, n-k-1}$ . If the P-value for the statistic  $F_o$  is less than 0.05 and  $(a_o \neq a_1, \dots \neq 0)$  then the parameter is considered to be statistically significant. The probability-level (p-level) is the probability that the residuals are solely the result of random error (chance). The lower the probability, the less likely it is that the difference occurring is by chance<sup>1</sup>. This test procedure is called an analysis of variance and can be summarized as shown in Table 3.6 below.

Source of variation	Sum of squares	Degrees of freedom	Mean square	F-statistic
Regression	$SS_R$	k	$MS_R$	$MS_R / MS_E$
Error of Residual	$SS_E$	n - k - 1	$MS_E$	
Total	$S_{yy}$	n - 1		

Table 3.6: Analyses of variance.

The coefficient of multiple determination  $R^2$  measures the amount of reduction in the variability of y, obtained by using regressor variables in the model and is given by

$$R^2 = 1 - \frac{SS_E}{S_{yy}} \quad \dots(3.16)$$

The values of the coefficient of the multiple determinations  $R^2$  fall in the range  $0 \leq R^2 \leq 1$ . A value of 0 means 0% of the data can be described by the regression model. A value of  $R^2$  close to 1 does not necessarily imply a good fit. Adding a variable to the model will always increase  $R^2$  regardless if this is statistically significant or not. Large  $R^2$  values could give poor predictions of new observations of the mean response. Therefore  $R^2$  adjusted values are rather used and is given by

$$R^2_{adj} = 1 - \frac{SS_E / (n - p)}{S_{yy} / (n - 1)} \quad \dots(3.17)$$

<sup>1</sup> Zeelie, B (2002)

A small variation between  $R^2$  and  $R^2$  adjusted indicates that only statistical significant variables are contributing to the model. Adding a variable to a model usually causes the sum of squares to increase and the error sum of squares to decrease. Adding an unimportant variable could increase the mean square error and therefore decrease the usefulness of the model.

The model adequacy should be tested before exploring optimisation of the model otherwise it may lead to misleading results being obtained.

The P values for the F-statistic distribution were used as an indication as to whether a parameter should be included in a model or not. The value of  $P < 0.05$  implies that at least one of the chosen parameters are significant and rejects the null hypothesis that none of the independent variables are significant. However, a P-value of 0.05 means that there is a 5% chance that the relationship emerged randomly and a 95% chance that the relationship is real. If the coefficient of a variable equals zero it implies that the variable does not significantly influence the value of  $y$ . The coefficient of the variable indicates how much an increase in its value will change the dependent variable.

The FSW parameters were related to each other, as explained in Figure 3.8. Table 3.7 lists the regression models for the process and input parameters. The process parameters  $F_z$ , tool torque, tool temperature and  $F_x$  max are related to feed rate and rotational speed as presented by equations (a) to (d). The regression analyses of total tool power, determined from equation (3.3) and (3.4), as a function of feed rate and rotational speed is given in equation (e). The regression analyses of the frictional power input and average heat input is given by equations (g), (h) and (i), (j), respectively. The relationship of the areas of the polar plot determined in J/s as a function of feed rate and rotational speed is given in equation (f).

The P-values in bold have high significance, since  $P < 0.05$  and those in black are less significant, since  $P > 0.05$ . If a value is less significant it does not necessarily imply that you can eliminate that variable completely from the equation, but rather that the variable does not contribute to a large variation in the dependent function.  $F_y$  max was not included in this analyses because  $F_x$  max is much larger than  $F_y$  max forces and would not have a large effect on altering the weld properties.

Eq	Regression models for process parameters versus input parameters	Input parameter's P-value	
a	$F_z = 39 - 0.001 \text{ feed} - 0.006 \text{ rpm}$ $R^2 = 0.04$ ; $R^2_{adj} = -0.23$	Feed rate RPM	0.992787 0.679977
b	$\text{Torque} = 89.5 + 0.06 \text{ feed} - 0.10 \text{ rpm}$ $R^2 = 0.86$ ; $R^2_{adj} = 0.82$	Feed rate RPM	0.543674 <b>0.000871</b>
c	$\text{Temperature} = 439 + 0.08 \text{ feed} + 0.10 \text{ rpm}$ $R^2 = 0.59$ ; $R^2_{adj} = 0.48$	Feed rate RPM	0.739594 <b>0.057403</b>
d	$F_x \text{ max} = 1245.7 + 13.16 \text{ feed} + 0.57 \text{ rpm}$ $R^2 = 0.76$ ; $R^2_{adj} = 0.70$	Feed rate RPM	<b>0.010637</b> 0.308724
	<b>Regression models for energy input versus input and process parameters</b>	<b>Input parameter's P-value</b>	
e	Total Translational and Rotational Power in $= 1680 + 3.2 \text{ feed} + 0.03 \text{ rpm}$ $R^2 = 0.18$ ; $R^2_{adj} = -0.05$	Feed rate RPM	0.379123 0.880916
f	Power in polar plot ( $F_x \text{ max}$ ) = $-9.9 + 0.2 \text{ feed} + 0.03 \text{ rpm}$ $R^2 = 0.72$ ; $R^2_{adj} = 0.64$	Feed rate RPM	0.055919 0.100346
g	Frictional power input = $1684 + 3.04 \text{ feed} + 0.02 \text{ rpm}$ $R^2 = 0.17$ ; $R^2_{adj} = -0.06$	Feed rate RPM	0.386899 0.970779
h	Frictional power input = $-5519 - 24.7 F_z + 18.2 \text{ Torque} + 0.06 F_x \text{ max} + 14.9 \text{ Temp}$ $R^2 = 0.37$ ; $R^2_{adj} = -0.13$	$F_z$ Torque Temp $F_x \text{ max}$	0.67649 0.413931 0.377557 0.779443
i	Heat input = $1649 - 5.8 \text{ feed} + 0.1 \text{ rpm}$ $R^2 = 0.86$ ; $R^2_{adj} = -0.82$	Feed rate RPM	<b>0.001081</b> 0.657076
j	Heat input = $4578.05 + 27.14 F_z - 9.22 \text{ Torque} - 0.29 F_x \text{ max} - 0.54 \text{ Temp}$ $R^2 = 0.87$ ; $R^2_{adj} = 0.82$	$F_z$ Torque Temp $F_x \text{ max}$	0.226444 0.259506 0.282447 <b>0.012182</b>
	<b>Regression models for effective coefficient of friction versus input parameters</b>	<b>Input parameter's P-value</b>	
k	Effective coefficient of friction = $0.28 + 0.0003 \text{ feed} - 0.0003 \text{ rpm}$ $R^2 = 0.69$ ; $R^2_{adj} = 0.60$	Feed rate RPM	0.570229 <b>0.011231</b>

\* Eq= equation number

Table 3.7: Multiple regression analyses.

Table 3.7 illustrates that feed rate and rotational speed's relationship with the normal force ( $F_z$ ) has quite a complex, nonlinear relationship (equation (a)). This can be seen for the adjusted  $R^2$  value, which indicates that only 23% of the data is explained by the regression model. The sign of the coefficients indicates that a decrease in feed rate will increase  $F_z$  and an increase in rotational speed should decrease  $F_z$ . One would expect the plunge depth to play a role in the magnitude of the  $F_z$  force and that it would also be influenced by the hardness of the material. The softer the material the smaller the  $F_z$  force should be.

Rotational speed is the key parameter to change the magnitude of tool torque (equation (b)) and tool temperature (equation (c)) because the P value is less than

0.05 for tool torque and approximately 0.05 for tool temperature. A change in feed rate should not have a lesser influence on the tool torque than a change in rotational speed, since the coefficient of feed rate is less than the coefficient of rotational speed. Increasing rotational speed should decrease the tool torque and vice versa for feed rate. The adjusted  $R^2$  value = 0.82 indicates that 82% of the data fits the regression model.

Feed rate predominantly affects  $F_x$  max shown by equation (d). Increasing feed rate and rotational speed will increase  $F_x$  max, since the coefficients of these parameters are positive. A change in feed rate will greatly affect the value of  $F_x$  max compared to the rotational speed, since the coefficient of feed rate is 13.16 and the coefficient of tool rotational speed is only 0.57.

The total translational and rotational power equation (e) generated from the translational and rotational forces has a non-linear relationship with feed rate and rotational speed, since the adjusted  $R^2$  value is -0.06. An increase in both feed rate and rotational speed should increase the total translational and rotational power input, since the coefficients are positive. Feed rate will alter the total translational and rotational power more than the rotational speed, since the coefficient of feed rate is 3.12 and the coefficient of rotational speed is less, namely 0.03. Tool temperature seem to be the only process parameter that will have a reasonable correlation with frictional power input, as shown in equation (h), since the P-value is the lowest compared to the other process parameters. Figure 3.17 shows a correlation between the frictional power input and tool temperature. The correlation coefficient,  $R^2$  for this model is 0.67 when the data for weld 10 is eliminated.

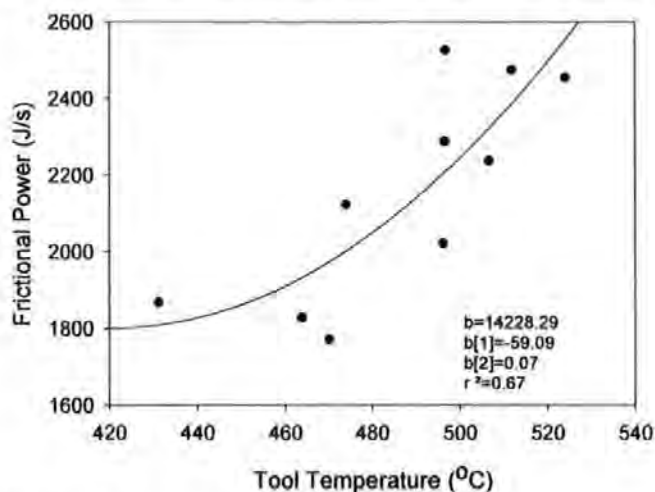


Figure 3.17: Frictional power versus tool temperature.



Examining the polar plots (equation (f)) revealed that the areas of the lobes have a strong dependency on feed rate and are slightly influenced by rotational speed.

The average heat input into the FS welds is strongly dependent on variation in feed rate and  $F_x$  max as shown in equation (i) and (j). The coefficient of feed rate is negative (equation (i)) therefore increasing feed rate results with a decrease of the heat input while increasing rotational speed, increases the heat input.

### 3.4.3 Surface plots of process parameters versus rotational speed and feed rate

In the following sections, the relationships between the measured process parameters and the input variables of feed rate and rotational speed are investigated. The relationships between the energy equations and the input variables are also determined. Three-dimensional mesh plots and two-dimensional contour plots, obtained using Matlab, are shown in Figures 3.18 (a)-(g). The surface plots were constructed from the data in Tables 3.2 and 3.3. These plots more clearly reveal the dependency of measured process parameters on feed rate, rotational speed and pitch. The possibility exists of using the plots to determine ranges of values where local maxima and/or minima in the process conditions are located. Note that the surface mesh is constructed through the actual data and is not a smoothed representation according to a specific mathematical relationship. Since variability exists in the monitored data, these plots should be considered only as an initial step towards determining optimum weld conditions. They show general trends in the data and indicate possible mathematical relationships that could be used to model these trends. These plots therefore provide a useful depiction of the interrelationship among the process parameters.

### 3.4.3.1 Tool torque versus feed rate and rotational speed

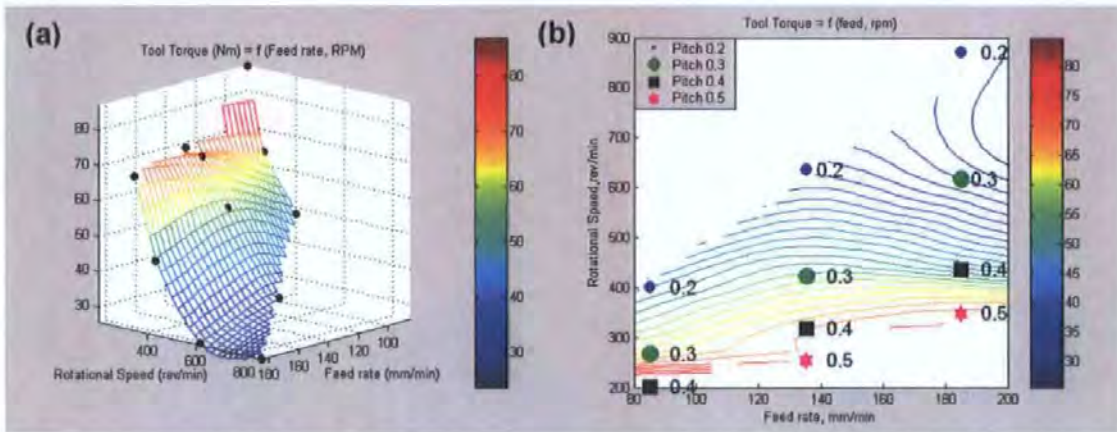


Figure 3.18: (a) 3D plot of torque versus rotational speed and feed rate.  
(b) Contour plot of torque versus rotational speed and feed rate.

Figures 3.18 (a) and (b) indicate that the highest spindle torque values are obtained for all feed rates at low rotational speeds (between 200 and 300 rpm). As the rotational speed increases, at constant feed rates, the torque on the tool decreases significantly. Changes in the feed rate at a given rotational speed result in smaller changes in the tool torque. The tool torque is mostly affected by the rotational speed. These observations agree with results obtained by Johnson et al<sup>1</sup> and correlate with the regression analysis (equation (b)). At a constant value of feed rate, tool torque increases as pitch increases. At a constant pitch (for example increasing feed rate and rotational speeds), tool torque decreases. This indicates an insufficient level of energy input at a constant pitch value at low feed rates, such that the plasticized state was less “fluid” and increased the torque on the tool. This agrees with the inverse relationship between torque and  $\omega^2/f$  in Figure 3.14 (c). The power on the tool has an inverse relationship with torque, as shown in Figure 3.11(b). This implies that higher frictional power input leads to lower torque on the tool.

<sup>1</sup> Johnson, R (2001)

### 3.4.3.2 $F_z$ force versus feed rate and rotational speed

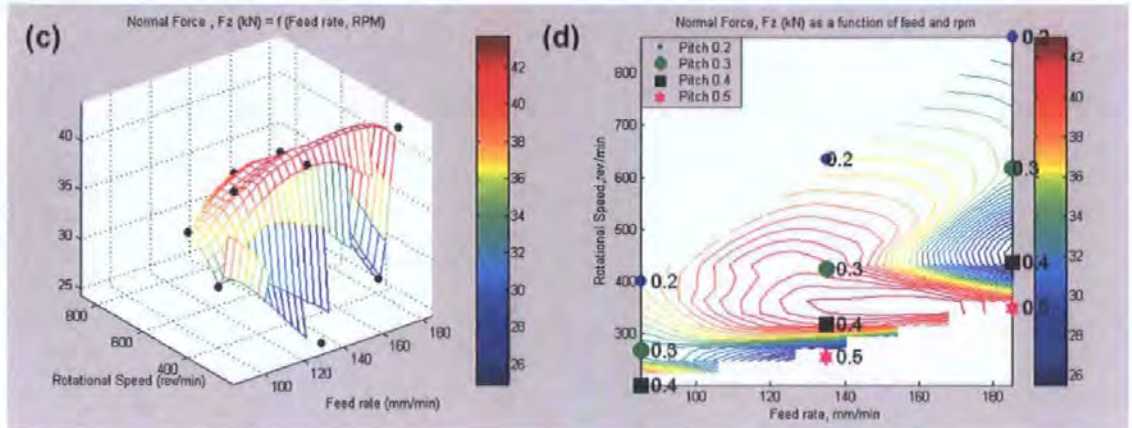


Figure 3.18: (c) 3D plots of  $F_z$  versus rotational speed and feed rate.  
(d) Contour plots of  $F_z$  versus rotational speed and feed rate.

There exists a complex non-linear relationship between the  $F_z$  force, feed rate and rotational speed as seen in Figures 3.18 (c) and (d). The contour plot indicates that there are two distinct regions of low  $F_z$ , corresponding with low rotational speeds and low feed rates, and with high feed rates and medium rotational speeds. These are separated by a region of speed and feed combinations, giving rise to high  $F_z$ . Clearly, this data are reflecting changes in the plastic flow processes during welding. They therefore need to be linked to weld output parameters, such as mechanical and fatigue performance, before conclusions can be drawn regarding weld process optimization. This discussion is continued in Chapters 4 and 6. The form of this data may change if the alloy is different in its responses to plastic strain. Aluminium alloy 5083-H321 is a strain hardening alloy at room temperature and heat treatable aluminium alloys may behave differently.

These results are completely different to any data thus far published in research literature. This is due to the fact that a larger range of data were investigated in this thesis. For instance, work by Ulysse<sup>1</sup> show that the axial ( $F_z$ ) and shear forces on the pin increase as the welding speed increases, regardless of rotational speed. In addition, he found that, for a fixed welding speed, increasing the rotational speed has the effect of decreasing the forces acting on the pin. The opposite effect of the welding and rotational speeds is observed for the welding temperature of 7050-T7451 aluminium alloy. The dependence of the pin forces on tool speeds  $F_z$  can be directly attributed to the strain-rate and temperature-dependent flow stress used in the model developed by Ulysse<sup>1</sup>.

<sup>1</sup> Ulysse, P (2002).

### 3.4.3.3 Tool temperature versus feed rate and rotational speed

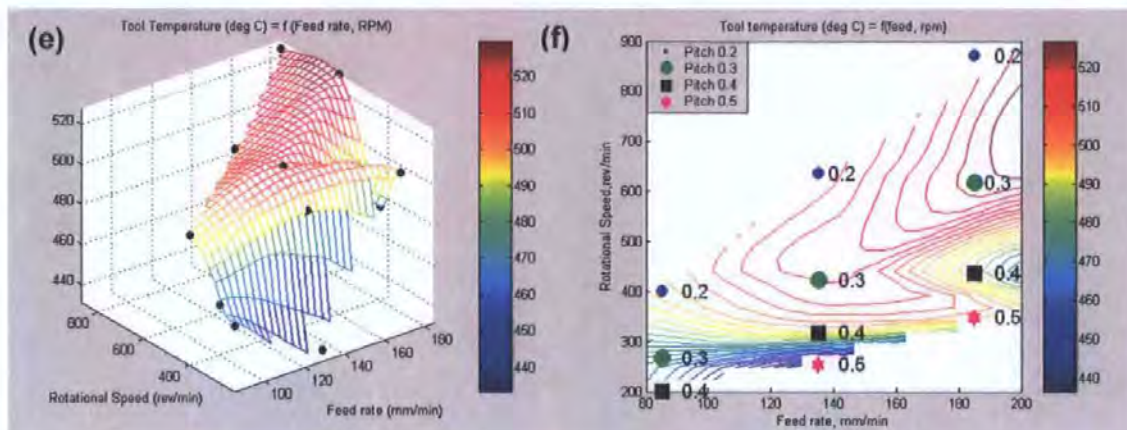


Figure 3.18: (e) 3D plot of tool temperature versus rotational speed and feed rate.  
(f) Contour plot of tool temperature versus rotational speed and feed rate.

Figure 3.18 (e) and 3.18 (f) show 3D and contour plots of the tool temperature measured by a K-type thermocouple positioned at the centre of the tool shoulder. Higher temperature regions will correspond to a lower flow stress in the material and possibly to an increase in dynamic recrystallisation processes<sup>1</sup>. It is clear that the tool temperature is mostly affected by rotational speed and increases with an increase in rotational speed and hence with energy input. The lowest feed rate and rotational speed conditions produce low temperatures. The tool temperature can be observed to decrease at a constant value of feed rate, with increase in pitch. Since an increase in pitch results in increased tool torque values, it is implied that less energy was put into the weld. The observed increase in temperature is believed to be a result of higher frictional forces applied to the tool as pitch increases. This is later confirmed in Figure 3.20.

Comparing the various contour diagrams allows observations to be drawn about the interaction between the process parameters. Torque values are dominated by tool rotational speed, increasing steadily as rotational speeds decrease. They show only a slight dependency on feed rate, generally being slightly higher at the mid-range of feed rates for a given value of rotational speeds. In contrast, both  $F_z$  and tool temperature show similar behaviour with two distinct regions of low values separated by a region of high values. Clearly therefore, the influential material and process parameters are the same for  $F_z$  and tool temperature. As the bulk of the

<sup>1</sup> Blum, W et al (1996)

heat input is known to derive from the tool shoulder, it is not surprising that larger contact forces give higher temperature. This observation is supported by the close similarity between contour plots of the total power input into the weld (Figure 3.11 (b)) and the contour plot of  $F_z$  (Figure 3.18(d)). Clearly, both temperature and power input are closely linked with the contact force and the tool shoulder.

### 3.4.3.4 $F_x$ and $F_y$ forces versus feed rate and rotational speed

Figure 3.18 (g) and (h) show 3D and contour maps of peak  $F_y$  max readings. Higher  $F_y$  max values occur in the range below 140 mm/min and 400 rpm. Both feed rate and tool rotational speed have a significant effect on peak values of  $F_y$ .

$F_y$  max seems to be the inverse of  $F_x$  max, which is plotted in Figures 3.18 (i) and 3.18 (j). This should be true, because when one strain gauge on the tool post measures a maximum for  $F_x$  max, the other strain gauge reading  $F_y$  max is positioned  $90^\circ$  out of phase.

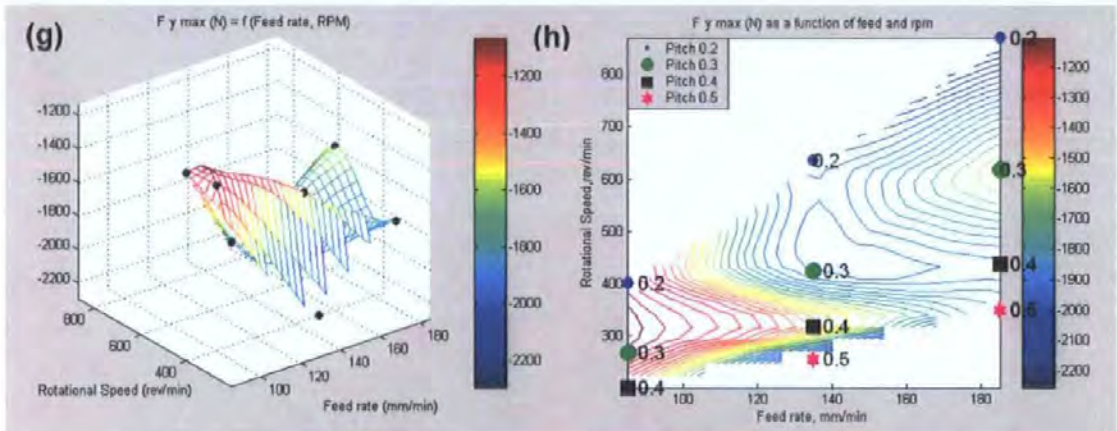


Figure 3.18: (g) 3D plot of  $F_y$  max versus rotational speed and feed rate.  
(h) Contour plot of  $F_y$  max versus rotational speed and feed rate.

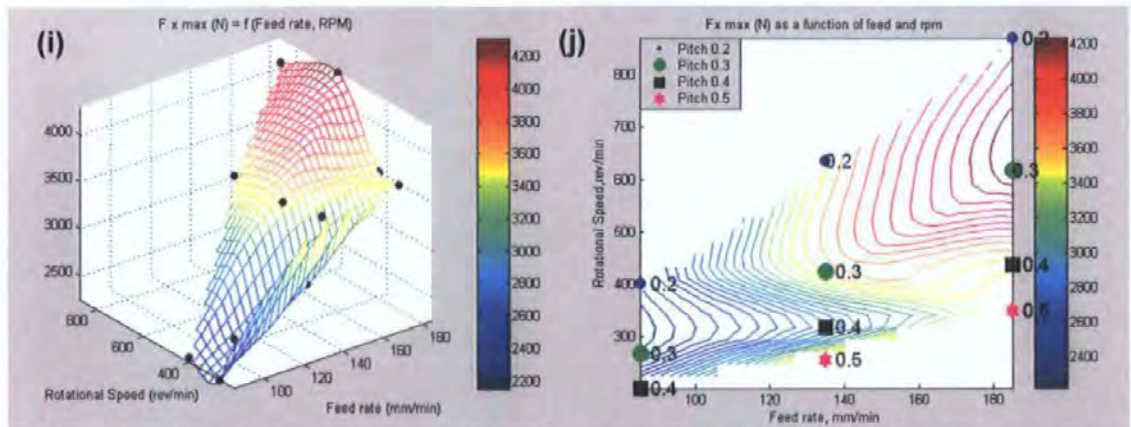


Figure 3.18: (i) 3D plot of  $F_x$  max versus rotational speed and feed rate.  
(j) Contour plot of  $F_x$  max versus rotational speed and feed rate.

The resultant force obtained combining  $F_x$  and  $F_y$  as a function of rotational speed and feed rate is indicated in Figures 3.18 (k) and 3.18 (l). It is clear that higher values of resultant force are obtained in the midrange of feed rates between 135 to 185 mm/min and rotational speed of 400 and 600 rpm. Lower values of rotational speed and feed rate produce lower resultant forces on the tool. Increase in frictional power (Figure 3.11(b)) on the tool corresponds with regions of higher resultant forces on the tool.

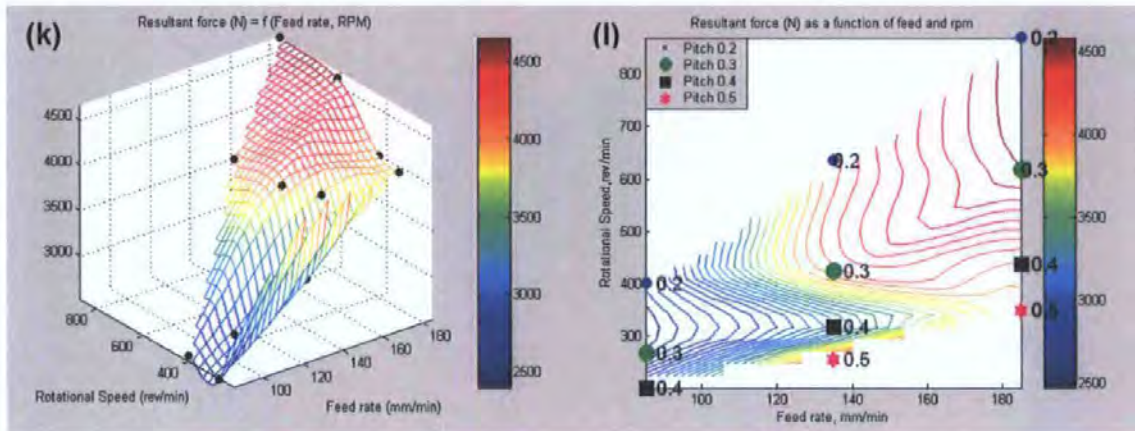


Figure 3.18: (k) 3D plot of the resultant polar plot areas versus rotational speed and feed rate.  
 (l) Contour plot of the resultant polar plot areas versus rotational speed and feed rate.

#### 3.4.4 The dependence of the coefficient of friction on process parameters

FSW can be considered as partially a forging process. The forging pressure in metal working is usually described by<sup>1</sup>

$$P = \sigma_o g(f)h(c) \quad \dots(3.21)$$

where

$\sigma_o$  = flow resistance of the material (flow stress) which is a function of temperature, strain and strain rate

$g(f)$  = an expression for the friction on the tool work piece

$h(c)$  = a function for the geometry of the tool and deformation

<sup>1</sup> Dieter, GE (1976)

There should therefore exist a relationship between normal force, tool temperature and the coefficient of friction that could aid in the understanding of the FSW process. Figures 3.19 (a)-(f) show the dependence of the coefficient of friction on all the measured process parameters.

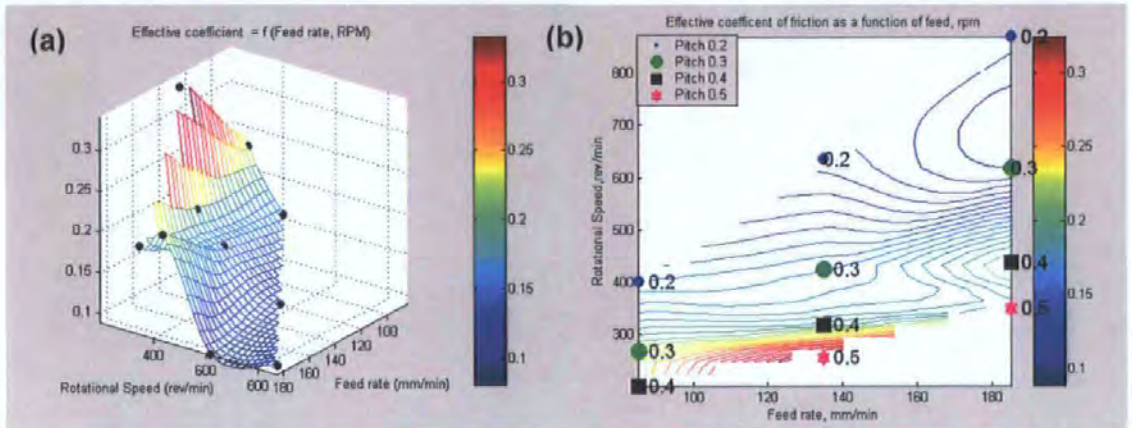


Figure 3.19: (a) 3D plot of effective coefficient of friction versus rotational speed and feed rate.  
 (b) Contour plot of effective coefficient of friction versus rotational speed and feed rate.

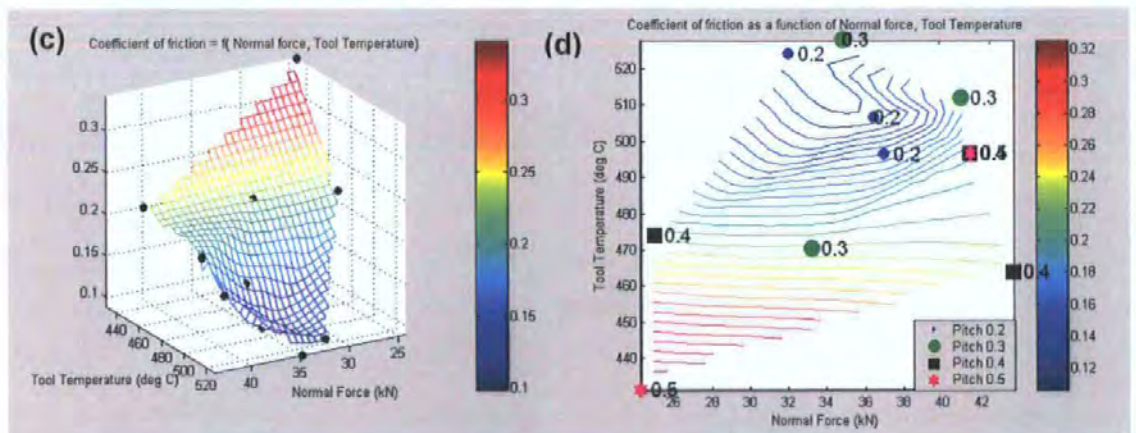


Figure 3.19: (c) 3D plot of effective coefficient of friction versus normal force and tool temperature.  
 (d) Contour plot of effective coefficient of friction versus normal force and tool temperature.

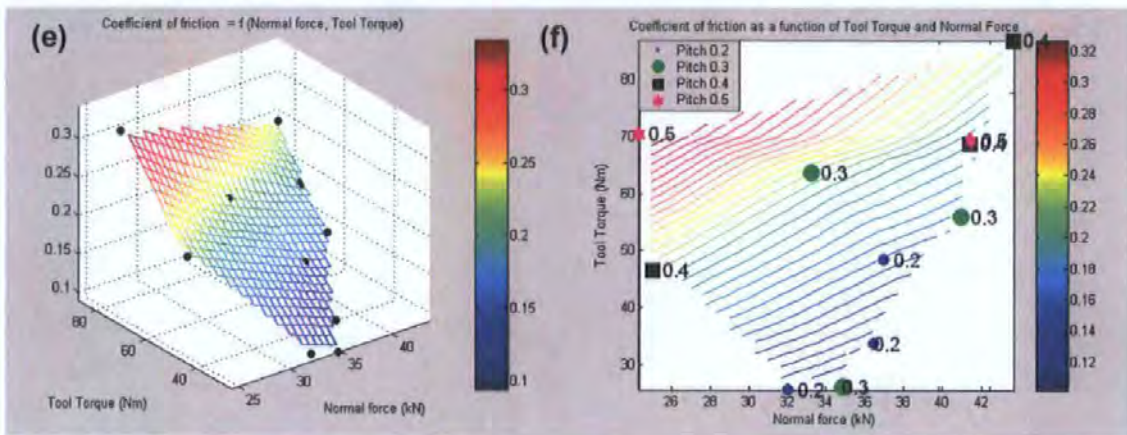


Figure 3.19: (e) 3D plot of effective coefficient of friction versus tool torque and normal force  $F_z$ .  
 (f) Contour plot of effective coefficient of friction versus tool torque and normal force  $F_z$ .

The effective coefficient of friction shows similar trends to tool torque as a function of feed rate and rotational speed. A higher coefficient of friction implies that a larger torque is exerted on the tool and therefore that less energy was put into the weld. Lower coefficient of friction values correspond with lower heat input (Figure 3.10). An inverse relationship can be found between tool temperature and the coefficient of friction. This means that high tool temperature readings correspond with low coefficient of friction values.

Figure 3.19 (e) and (f) indicate that the coefficient friction is only slightly affected by increases in the normal force  $F_z$ . As the coefficient of friction decreases, the rate of plastic deformation increases. It seems as if higher pitch values produce large values of the coefficient of friction.

As might be expected, there is a definite linear relationship between measured tool temperature and the coefficient of friction as indicated by Figure 3.20. The coefficient of friction increases as the tool temperature decreases because the material has a higher yield strength and is more resistant to plastic deformation<sup>1,2</sup>.

<sup>1</sup> Altintas, Y (2000)

<sup>2</sup> Blum, W et al (1996)



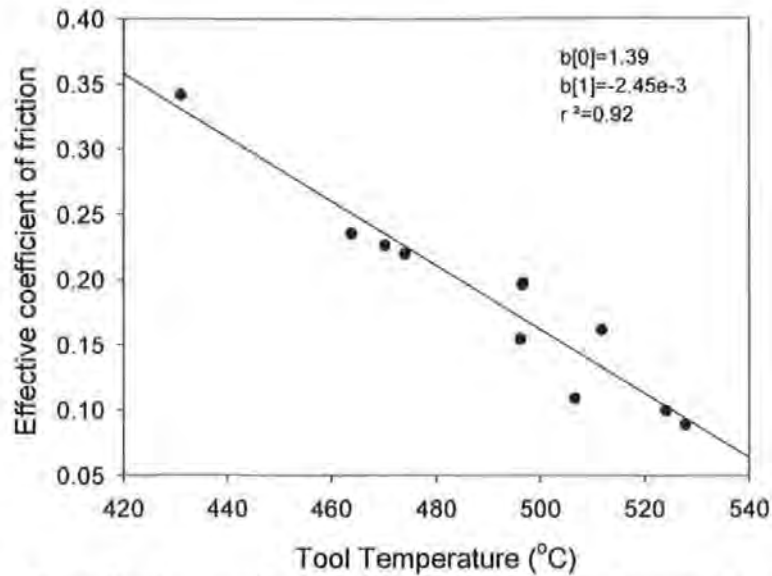


Figure 3.20: The effective coefficient of friction versus tool temperature and normal force.

When the normal force  $F_z$  decreases the coefficient of friction increases and this corresponds with low temperature values. The coefficient of friction summarizes thermal as well as plasticity effects in FSW. The effective coefficient of friction values obtained are in the range of coefficients usually determined for metal-metal contact interfaces<sup>1</sup>.

### 3.5 Conclusions

This chapter attempted to identify some of the dominant influences on trends in the most important weld process parameters. It is clear from the results and discussion that monitoring of vertical downwards force reaction on the tool, applied tool torque and subsequent tool temperature would provide a much-improved way of assessing the attainment of suitable welding conditions in the metal. This alone would eliminate some of the empiricism currently attendant on selection of suitable weld process parameters under changing alloy/joint conditions.

In this chapter it has been found that the tool rotational speed is a key parameter controlling the magnitude of tool torque, tool temperature and effective coefficient which is the ratio of torque over vertical downwards force. The heat input to the weld is more strongly dependent on the changes of feed rate than rotational speed in the range of this investigation.

<sup>1</sup> Brandes, EA and Brook, GB (1992)

The highest spindle torque values are obtained at all feed rates with low rotational speed (between 200 and 300 rpm).

The contour plot of  $F_z$  (Figure 3.18 (c) and (d)) versus tool speed and feed rate indicates that there are two distinct regions of low  $F_z$ , corresponding with low rotational speeds and low feed rates, and with high feed rates and medium rotational speeds. These are separated by a region of speed and feed contributions giving rise to high  $F_z$ . Clearly, these data are reflecting changes in the plastic flow processes during welding.

The lowest feed rate and rotational speed conditions produce low temperatures. The tool temperature can be observed to decrease at a constant value of feed rate with increase in pitch. Since an increase in pitch gives increased tool torque values implying that less energy is put into the weld, per unit time the observed increase in temperature is believed to be a result of higher frictional forces on the tool. This is justified by the good linear relationship (coefficient of correlation  $R = 0.92$ ) between the coefficient of friction and tool temperature. Higher  $F_z$  values correspond with higher tool temperatures.

The plots of frictional power on the tool indicates that more energy into the weld results in an increase in temperature, less friction on the tool and therefore a greater plasticized state during welding. The frictional power input shows a maximum value at approximately 400 rpm and 140 mm/min. Local maxima in power input occur with a pitch of 0.3 at high feed rates rotational speeds (for example 185 mm/min and 617 rpm) and at low feed rates and low speeds (for example 85 mm/min and 266 rpm). This form of data implies complex plasticity phenomena in the TMAZ.

The heat input into the weld could not be related to the parameter  $w^2/f$ . The energy model (equation 3.2) did show that as the feed rate increases, the heat input to the weld decreases.

A linear relationship with  $r = 0.99$  was obtained between the total frictional power and total tool power models (thus the sum of rotational and translational energies). The frictional power determined by equation (3.3) and (3.4) was used to compare

the mechanical properties with the welds and will be discussed in the following chapters.

The area contained within the polar plot of reaction forces on the tool had a good correlation with the power input into the weld. It should therefore provide an indication of the defect population and the dynamic performance of the welds. Thus, weld soundness and performance should be able to be explicitly linked to process conditions (such as tool pitch, which is defined as weld travel increment per revolution) as a function of alloy and tool design. Predictive capability can be developed which will give a substantial improvement in the selection of appropriate welding conditions for various combinations of alloy, plate thickness, tool design, and production rates.

The resultant force on the tool determined from a polar plot has an inverse relationship with the heat input model. As expected, larger heat input results in smaller forces on the tool.

The next chapters link the process parameter maps to residual stress distribution in the welds and to weld properties and performance.

## **4. Microstructure, defect occurrence, tensile strength and Vickers hardness of FSW**

### **4.1 Introduction**

Weld microstructure depends upon welding parameters such as energy input and feed rate which determine the heating and cooling effects during welding. Final weld characteristics which are affected by properties of the base metal include<sup>1</sup>:

- (i) the range of melting points of the constituent elements;
- (ii) the solubility of hydrogen in molten aluminium;
- (iii) oxide characteristics; and
- (iv) thermal and non-magnetic characteristics.

The fine grain structure found within FSW nugget zones would generally be considered beneficial to the mechanical properties of these welds. An understanding of the microstructural evolution during FSW as a consequence of changes in process parameters and the associated microstructural effects on mechanical and physical properties such as fatigue, crack growth and toughness is critical to developing a predictive methodology. Such an understanding would bring broader acceptance and, inevitably new applications for this innovative technology.

### **4.2 General properties of Aluminium 5083 – H321**

Aluminium alloy 5083 is used in the fabrication of lightweight, high-speed marine vessels<sup>2</sup>. These alloys have good welding characteristics and resistance to corrosion in marine atmospheres. This material is cold worked, thus strain hardened to increase the dislocation density in the material and is also stabilized by a low temperature thermal treatment of  $350\text{ }^{\circ}\text{C} \pm 5\text{ }^{\circ}\text{C}$  for 2-3 hours. This softens the material slightly and increases the ductility<sup>3</sup>. This temper is also performed to overcome localized recovery within the grains that reduce the tensile properties. The movement of dislocations is impeded by precipitates at grain boundaries and internal strains around precipitates that is Guinier-Preston (GP) zones. Intermediate precipitates may be nucleated in or around stable GP zones

---

<sup>1</sup> Dickerson, PB(1993)

<sup>2</sup> Shankar, K and Wu, W (2001)

<sup>3</sup> Polmear, IJ (1995)

or at lattice defects such as dislocations. Al 5083-H321 contains no age-hardening precipitates. During the fabrication of wrought aluminium alloys such as H<sub>2</sub>, Cl, Ar and N<sub>2</sub> may be used. Hydrogen is very soluble in Al at high temperature and may be entrapped in the solid structure after production that could lead to porosity. Mg is highly soluble in Al at high temperatures and offers the largest amount of solid solution strengthening for this material. Mg increases the rate of work hardening, which is the most important strengthening mechanism in Al 5083. If the concentration of Mg increases from 0.2% wt to 6% wt there is a 0.2% proof strength increase from 120 MPa to 300 MPa<sup>1</sup>. The Mn is included to increase the recrystallisation temperature and complement the strengthening effect of the Mg<sup>2</sup>. Precipitates typically expected to form in alloys of this type are (Fe, Mn, Cr)<sub>3</sub>SiAl<sub>12</sub>, Mg<sub>2</sub>Si, Al<sub>3</sub>Mg<sub>2</sub> and Cr<sup>3</sup>. If more than 5.5% Mg is present Mg<sub>5</sub>Al<sub>8</sub> may form in slip bands and grain boundaries, which may lead to stress corrosion cracking in corrosive environments. Small percentages of Mn and Cr raise the recrystallisation temperature and may also increase the tensile properties for a given magnesium content. Mn can precipitate in the form (Al<sub>6</sub>Fe,Mn) if more than 0.3% Mn is present in the alloy<sup>3</sup>. Small dispersoids less than 1 µm of Al<sub>6</sub>(Fe,Mn) could retard recrystallisation by hindering the motion of grain boundaries and larger particles that act as nucleation sites for recrystallised grains<sup>4</sup>. Mg<sub>2</sub>Si are usually semi coherent rods that form directly from GP zones along the directions <100>, (001)β//<100>; [100]β//[011] slip planes on {111} along <110> directions, and occur due to line defect dislocations. These precipitates could be fcc or hexagonal in nature. The nominal composition of Al 5083-H321 is shown in Table 4.1.

Al	Cr	Cu	Fe	Mg	Mn	Si	Ti	Zn
94.8	0.05-0.25	0.1	0.4	4-4.9	0.4-1	0.4	0.15	0.25

Table 4.1: Nominal wt% of Al 5083-H321.

#### 4.3 Specimens taken from the weld

Transverse tensile (T) and fatigue (F) samples were machined from the FS welds at the positions as indicated in Figure 4.1. The residual stress

<sup>1</sup> Brandes, EA and Brook, GB (1992)

<sup>2</sup> Polmear, IJ (1995)

<sup>3</sup> Lee, SL and Wu, SE (1988)

<sup>4</sup> Humphreys, FJ and Hatherly, M (2002)

(R) specimen is also shown. Optical macrographs (M) and hardness measurements were taken from a specimen of the FS weld at position 450 to 493 mm. This chapter presents macrographs, fractographs, tensile and hardness investigations. The residual stress and fatigue investigations are discussed in Chapter 5 and 6 respectively.

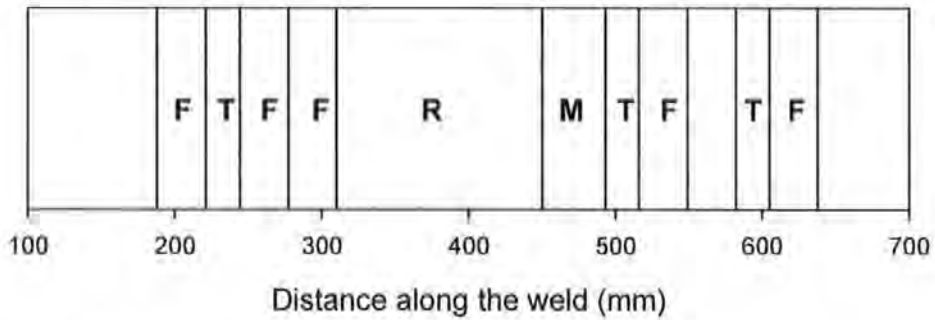


Figure 4.1: Position of specimens taken from the friction stir welds.

#### 4.4 Microstructural specimen preparation

Samples of size  $30 \times 5 \times 6 \text{ mm}^3$  were cut using a Struers Minitom precision cut-off machine from the weld using water as coolant and mounted for metallographic examination using a thermoplastic resin. The microstructure of the 5083-H321 aluminium alloy was revealed by mechanical grinding/polishing, using a Motopol Grinder/Polisher 2000, followed by electro-etching. Grinding of the surface started with 600 grit SiC paper followed by 1000 or 1200 grit SiC paper until a uniform surface finish was attained. Water was used for lubrication. Initial polishing was undertaken using  $15 \mu\text{m}$  diamond compound followed by  $3 \mu\text{m}$  and  $1 \mu\text{m}$  diamond compounds for 3, 3 and 2 minutes respectively. Hyprez Fluid, Type W, was used for lubrication. Final polishing was completed using a colloidal silica ( $\text{SiO}_2$ ) or aluminium oxide ( $\text{Al}_2\text{O}_3$ ) suspension for 20 to 30 seconds.

Electro-etching was performed using an electrolyte consisting of a 2% solution of fluoroboric acid,  $\text{HBF}_4$  (5 ml  $\text{HBF}_4$  (40%) diluted with 100 ml of distilled  $\text{H}_2\text{O}$ ). The cathode was stainless steel, the surface area of which was much greater than that of the anode (surface to be polished). The maximum surface area of the anode left exposed was  $250 \text{ mm}^2$  (ideally the maximum area should be restricted to  $100 \text{ mm}^2$ , but the production of macrographs required larger areas to be etched), the remainder being masked with either tape or Lacomit varnish. The specimens were

electro-polished at a voltage of between 20 - 30 volts for periods of 2 to 2.5 minutes.

The L-T, L-S and T-S planes corresponding to the longitudinal, rolling direction, the transverse and short transverse faces of a rectangular shape are designated in accordance with ASTM E616, as shown in Figure 4.2.

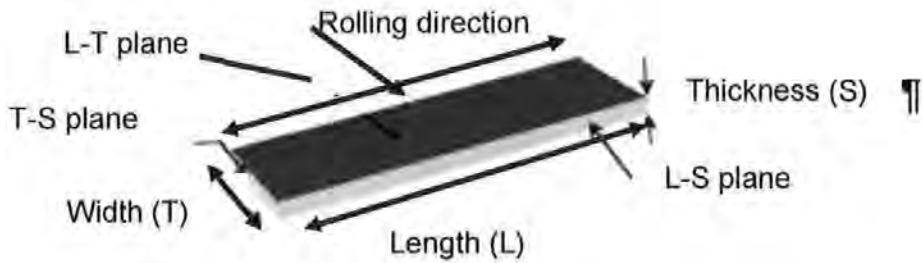


Figure 4.2: Identification of planes for a rectangular plate.

#### 4.5 FS weld microstructure

##### 4.5.1 Macrostructure variation as a function of process parameters

Table 4.2 shows a comparison of all the macrographs taken along the T-S plane for welds made at different input parameters given in Table 3.2. The advancing side is on the right and the retreating side is on the left in all the figures of this study, unless stated otherwise.

Flaws and pseudo-bond defects (section 2.6.1) were observed at the regions indicated on the images in Table 4.2 and enlargements of some of the flaws are also shown. These defects could be caused by insufficient metal flow and low heat input to the weld. A fine pseudo-crack can be seen in welds 2,3,6,7 and 9 depicted as an S-shaped dash-dotted line. In the case of weld 2 the pseudo-crack is wider at the upper surface of the weld and becomes thinner towards the centre of the weld cross section and towards the bottom of the weld; weld 2 also had the lowest tensile strength. Welds 1,8 and 9 contained several voids while welds 2,4 and weld 11 contained root-type defects. As the pseudo-bond defect in weld 9 is fairly limited in extent, it will be referred to as a sub-surface, lapping type defect.


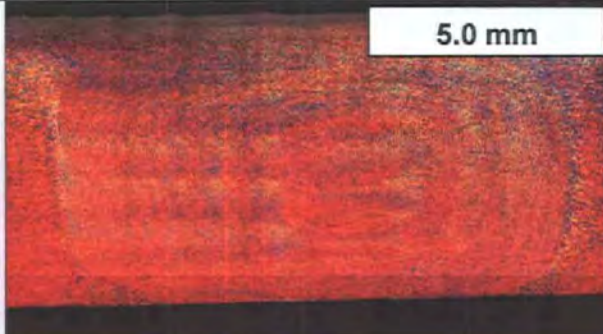
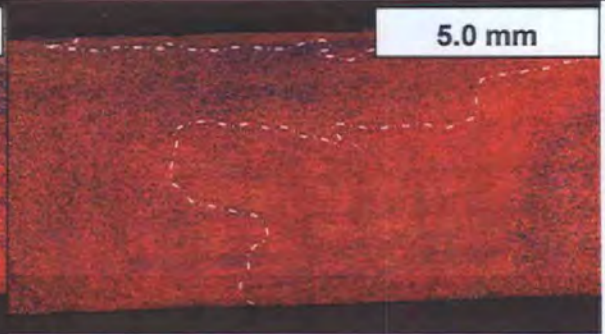
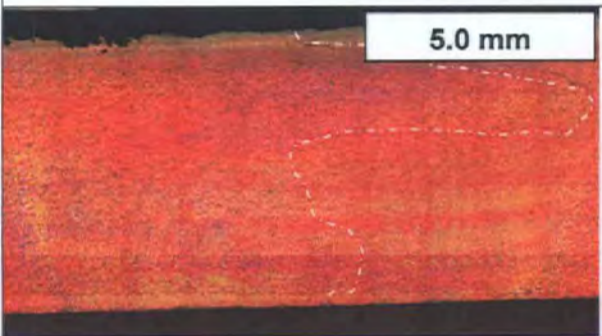
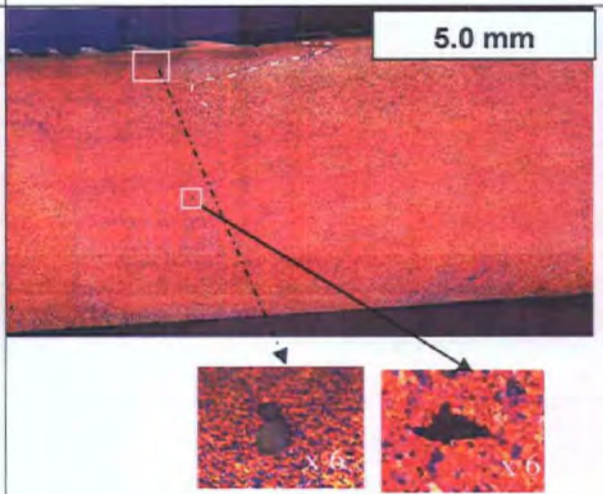
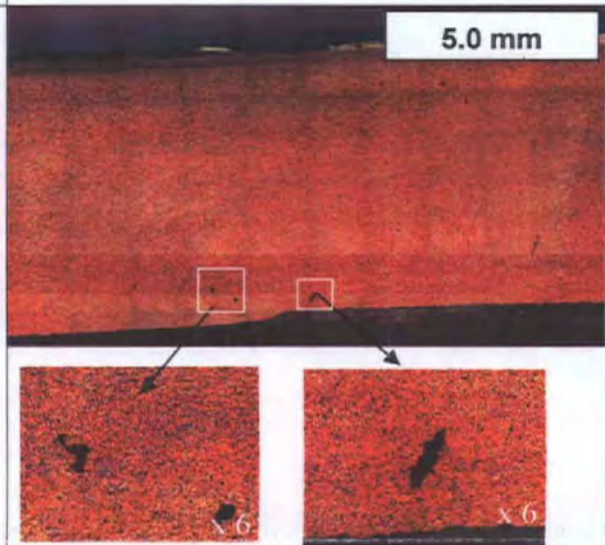
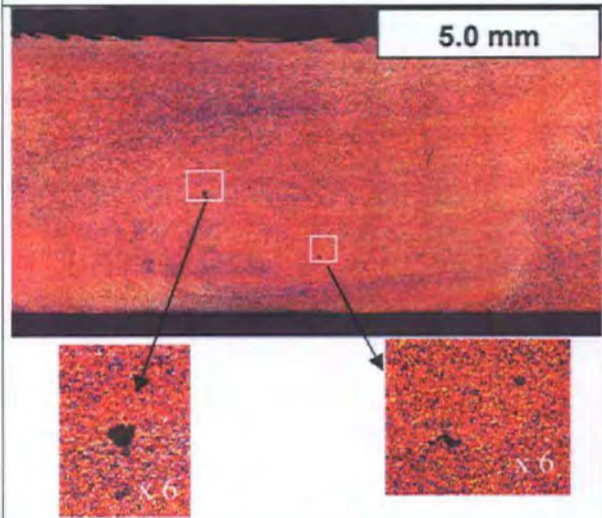
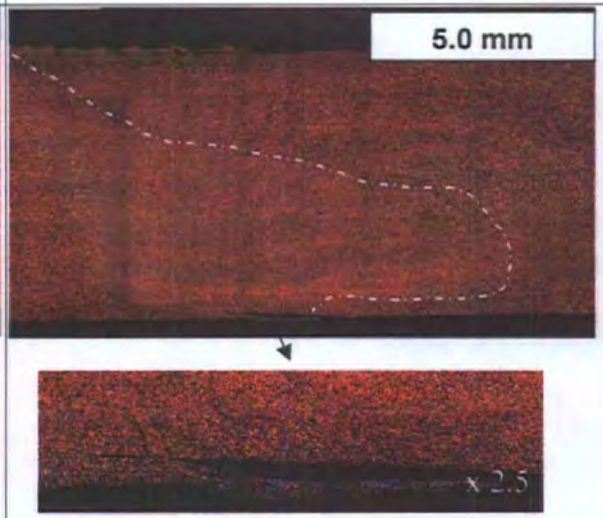
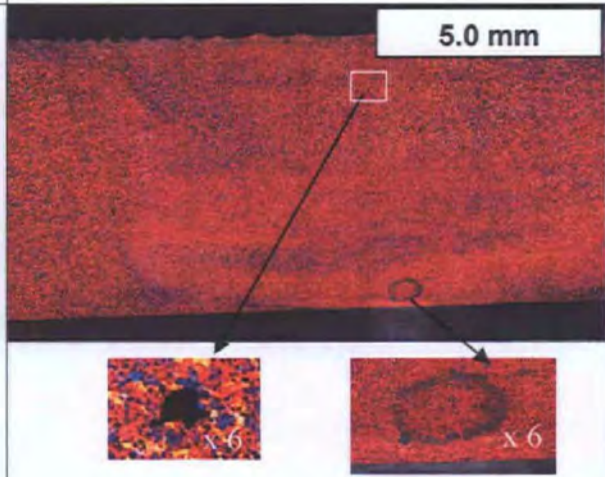
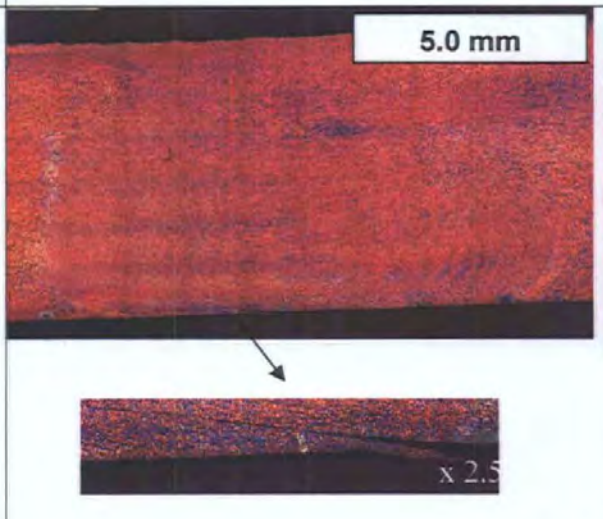
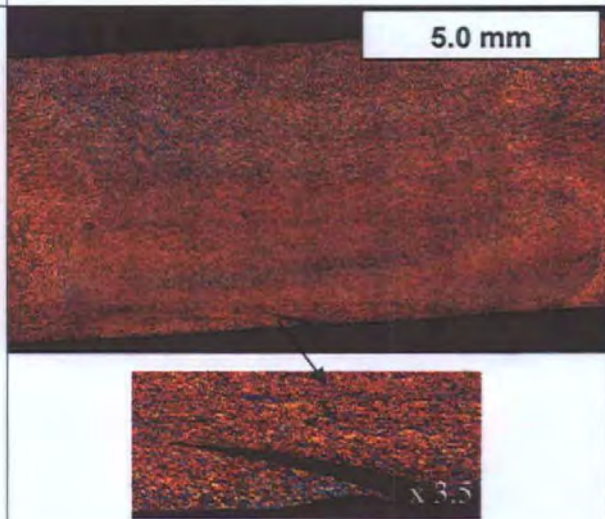
Feed rate : 85 mm/min	Feed rate : 135 mm/min	Feed rate :185 mm/min
<p data-bbox="300 188 719 230">Weld 3 :201 rpm, Pitch 0.42</p>  <p data-bbox="320 632 875 742">The white dashed line represents so-called pseudo-bond defects or lazy -S defects.</p>	<p data-bbox="902 188 1321 230">Weld 5: 254 rpm, Pitch 0.51</p> 	<p data-bbox="1505 188 1924 230">Weld 7: 348 rpm, Pitch 0.53</p> 
<p data-bbox="300 820 712 862">Weld 6:266 rpm, Pitch 0.32</p> 	<p data-bbox="902 820 1323 862">Weld 9:318 rpm , Pitch 0.42</p> 	<p data-bbox="1505 820 1919 862">Weld 1:436 rpm, Pitch 0.42</p> 
<p data-bbox="300 1452 710 1494">Weld 8:400 rpm, Pitch 0.21</p> 	<p data-bbox="902 1452 1317 1494">Weld 2:423 rpm, Pitch 0.32</p> 	<p data-bbox="1505 1452 1928 1494">Weld 10: 617 rpm, Pitch 0.3</p> 
<p data-bbox="902 2084 1317 2126">Weld 11:635 rpm, Pitch 0.2</p> 	<p data-bbox="1505 2084 1919 2126">Weld 4:870 rpm, Pitch 0.21</p> 	

Table 4.2: Photo montages of weld cross sections.



The concentric rings seem to become flatter and the nugget wider as the vertical downwards force increased. This can clearly be illustrated at each feed rate in Table 4.3. The TMAZ is indicated, approximately, with black lines on the pictures.

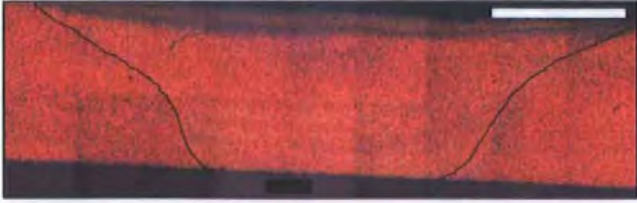

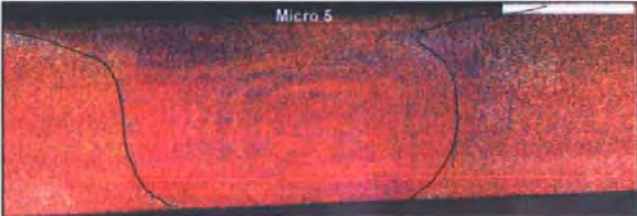
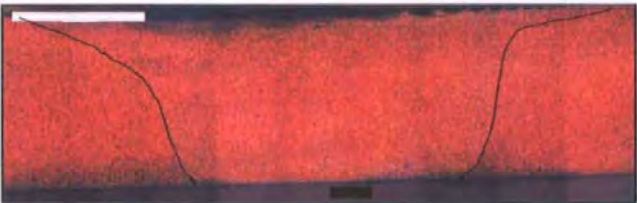


85 mm/min		Parameters
	weld 6	<b>33.2 kN</b> 283 rpm
	weld 3	<b>44.7 kN</b> 213 rpm
135 mm/min		
	weld 5	<b>24.3 kN</b> 270 rpm
	weld 9	<b>41.4 kN</b> 338 rpm
185 mm/min		
	weld 1	<b>25.0 kN</b> 463 rpm
	weld 7	<b>41.4 kN</b> 370 rpm

Table 4.3: Variation of the nugget zone with respect to  $F_z$  (the bar in the macrograph is equal to 5mm).

The types of defects identified from these macrographs, are summarized in Table 4.4.

Weld no	Defect type
1,8,9,10	Voids
2,6,7	Pseudo steady bond-(lazy S) defect
3	Pseudo steady bond-(lazy S) defect Porosity defect
2,4,10,11	Root defect
9	Sub surface, lapping type defect

Table 4.4: Defect type identified on the macrographs.

#### 4.5.2 Effect of weld parameters on defects

The emphasis in this section is placed on defect occurrence in welds as a function of energy input and polar plot data. The formation of defects in welds was explained in Chapter 2 as being related to either energy input, fluid dynamics of the tool and/or the forces acting on the tool.

The variation of defect occurrence with rotational speed and feed rate is depicted in Figure 4.3. It is difficult to draw firm conclusions from this limited data set, but some trends are apparent.

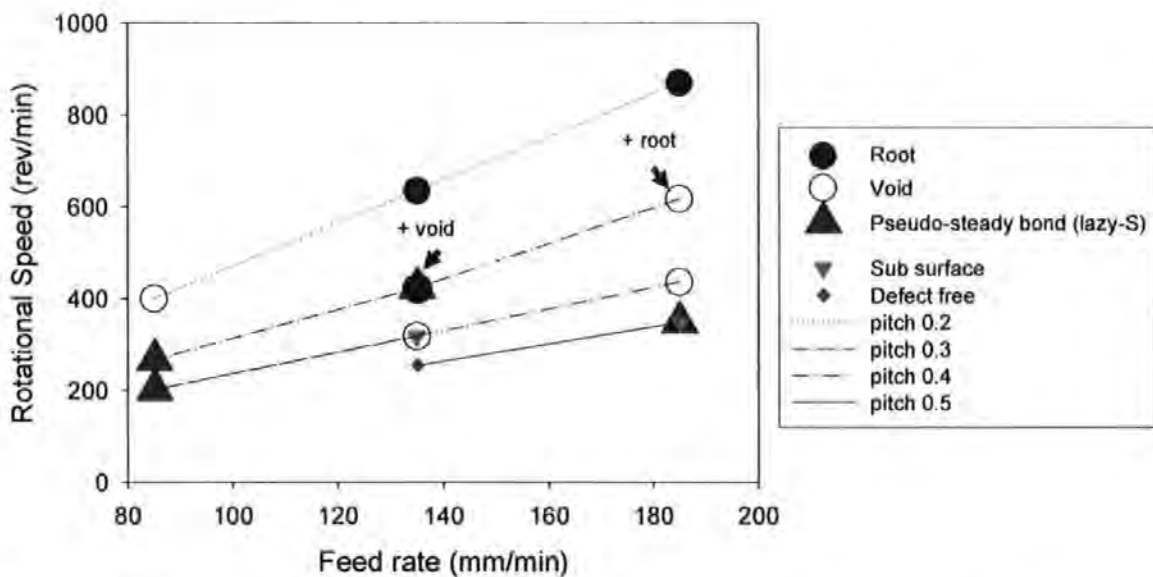


Figure 4.3: Relationship of the occurrence of defects to feed rate and rotational speed.



A typical tensile stress-strain relationship is shown in Figure 4.6. The rest of the graphical data can be found on the CD in the folder labeled CH4 tensile tests.

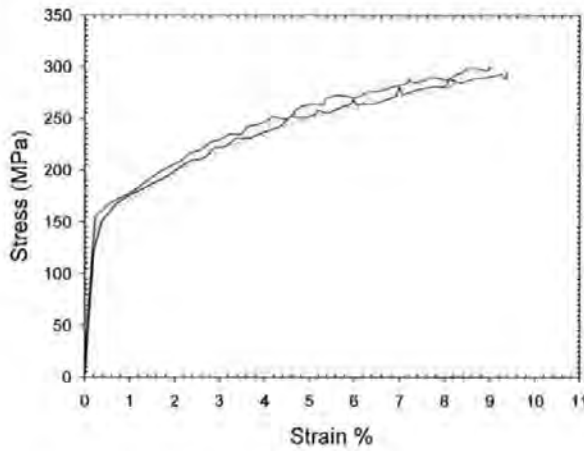


Figure 4.6: Tensile results for weld 6.

#### 4.6.1 Variation of UTS and 0.2% proof strength along the weld

Table 4.5 gives the tensile data as the average of three tests for the parent plate. Table 4.6 gives the tensile strength data, and Table 4.7 gives the 0.2% proof strength as an average of three tests of all the welds.

Property	Sample1	Sample2	Sample3	UTS
UTS	382	365	366	371 ± 10
Yield	261	251	251	254 ± 6

Table 4.5: Tensile results of the parent plate in MPa.

Weld no	Ultimate Tensile Strength Along Weld (MPa)			Average UTS (MPa)	SD (MPa)
	221 mm	493 mm	582 mm		
1	290	297	280	289	9
2	276	245	203	241	36
3	324	324	290	313	20
4	297	232	234	254	37
5	296	313	314	308	10
6	318	311	315	315	4
7	297	278	306	294	15
8	311	311	303	308	4
9	305	208	307	273	57
10	308	319	302	310	8
11	307	310	301	306	5

Table 4.6: Tensile results of the welds in MPa.

Weld no	0.2% Proof Strength Along Weld (MPa)			Average 0.2% Proof strength (MPa)	SD (MPa)
	221 mm	493 mm	582 mm		
1	180	162	170	171	9
2	145	143	170	153	15
3	160	162	160	161	1
4	146	142	145	144	2
5	165	166	165	165	1
6	163	156	175	165	10
7	*	144	155	150	8
8	140	142	152	145	6
9	146	143	146	145	2
10	151	153	141	148	6
11	146	144	133	141	7

\* no measurement was possible

Table 4.7: 0.2 % Proof stress along the weld.

Figure 4.7 shows graphically the variation in tensile strength along the weld. Welds 2,4,7, and 9 show substantial difference in trends for tensile strength along the welds to the rest of the specimens. In particular, welds 4,7 and 9 show an increase in tensile strength towards the end of the weld run. This is contrary to the behaviour shown by the other welds. The conclusion is that weld properties may vary along the weld in non-systematic ways that may reflect alignment and weld clamping. This is likely to complicate interpretation of process conditions that lead to optimum welds. In this thesis the problem is recognized and data are taken and compared from consistent positions along the welds.

It is interesting that UTS is much more affected between weld positions than proof strength, for example weld 9 and weld 1 in Figure 4.7. One possible reason is that the pseudo-bond defects in weld 1 and 9 are being triggered once yielding has occurred. Hence pseudo-bond defects appear less influential of proof strength than UTS, thus they are triggered by a certain level of plastic deformation during fracture and can be correlated with previously reported strain-partitioning defects, although they may simply be cases of low interfacial strength between adjacent onion skin layers.

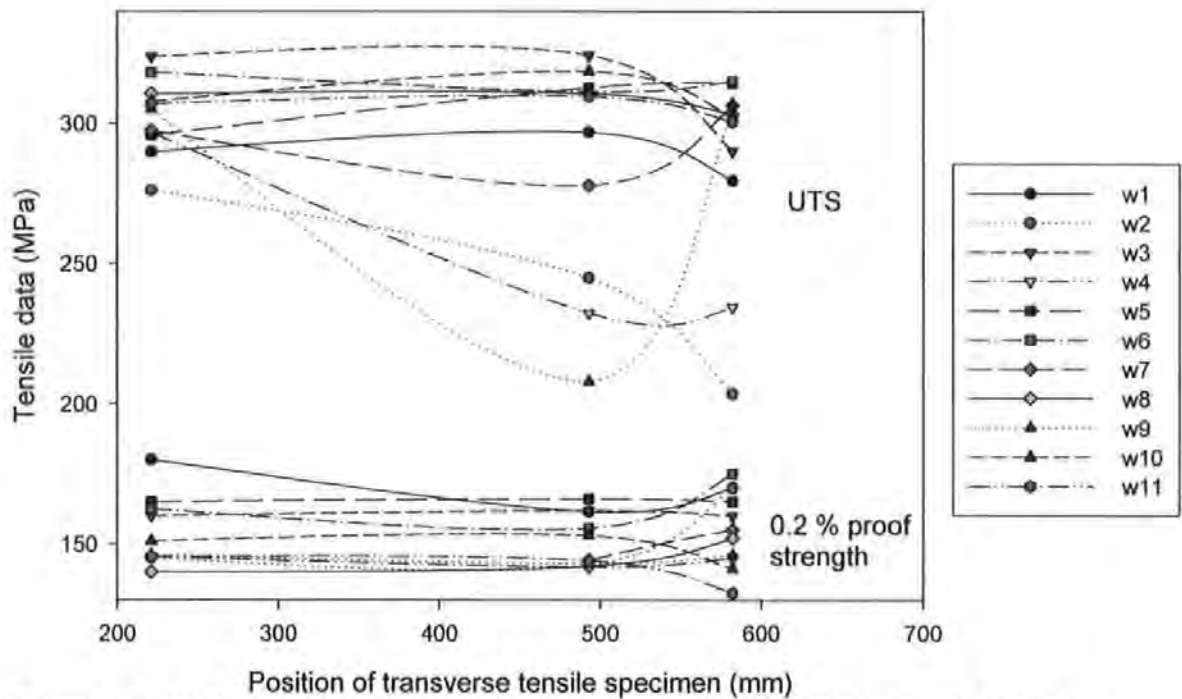


Figure 4.7: Variation of ultimate tensile strength and 0.2% proof strength along the weld length.

#### 4.6.2 Tensile fracture surfaces

Table 4.8 shows a comparison of the fractographs taken along the L-S plane for welds made at different input parameters.

Root defects were identified for welds 2 and 4 at all the positions along the weld. This feature is clearly shown in Figure 4.8 (a) and (b). These fractographs show that the root of the weld did not completely bond with the weld. Occasional root defects were observed on tensile specimens for weld 10. Weld 11 showed an insignificant root defect in one specimen. This does correspond with the root defects identified on the fractographs of the T-S plane of the welds specimen given in Table 4.2.

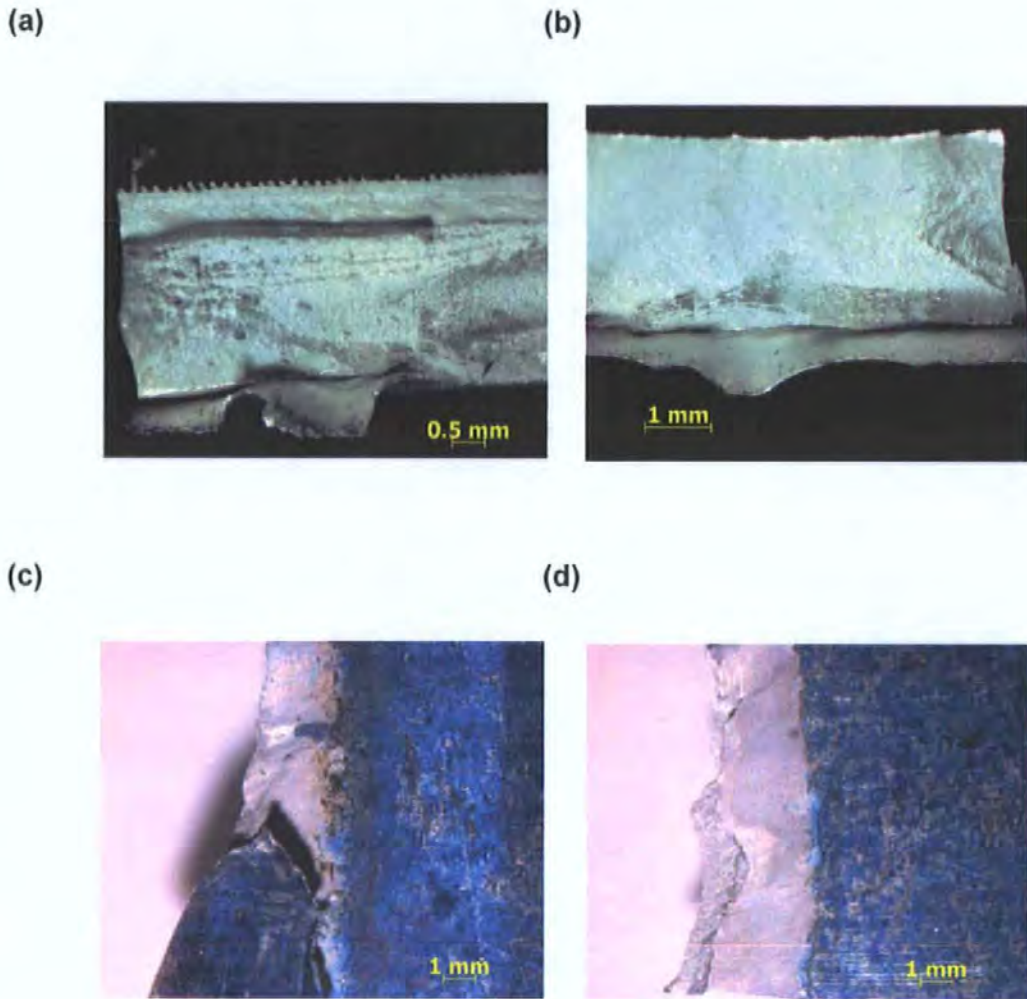


Figure 4.8: Fractographs illustrating root defects for  
 (a) weld 2 at position 221 mm along the weld.  
 (b) weld 4 at position 221 mm along the weld.  
 (c) weld 2 at position 221 mm at the root of the weld.  
 (d) weld 4 at position 221 mm at the root of the weld.

A number of the tensile fracture surfaces shown in Table 4.8 display large planar regions on the fracture surface which can be related to the rotary flow processes occurring in the weld metal, for example weld 1,2,4,5,7 and 9. Weld 5, in particular, demonstrates that regular arrays of voids opened up during fracture from pseudo-bonds between adjacent layers of metal spaced at the tool pitch distance.

However, tensile fracture surfaces showed existence of onion skin defects<sup>1</sup> quite clearly for this weld and will later be referred to as onion skin defects. Certain positions on the fracture surface of weld 5 clearly show the link between surface

<sup>1</sup> James MN, et al (2003)

and root defects as a function of the pitch-related onion skin layers. This is due to the Poisson's contraction that occurred during fracture. The original defects would have been planar pseudo-bonds in the alloy.

The effect of these pseudo-bond and planar defects on mechanical properties appears to be limited, except in certain cases where they occur over a high percentage of the fracture surface. Thus three groups of welds can be distinguished in terms of their performance characterized as a weld performance factor that is: relative to the parent plate:

- (i) welds 3,5,6,8,10 and 11 have weld factors in the range 82-85%;
- (ii) welds 1,7 and 9 have weld factors in the range 74-79%; while
- (iii) welds 2 and 4 have weld factors in the range 65-68%.

The situation is somewhat different in terms of 0.2% proof strength with welds 4,7,8,9,10 and 11 having proof strength values in the range 56-59% of the parent plate, while welds 1,2,3,5, and 6 have proof strength values in the range 60-67% of the parent plate. It should be noted that these values of weld factor compare well with other reported values for 5083-H321 alloy. For instance, Peel<sup>1</sup> reported weld factor values in the range 41-67% for 3mm plate in his work, and reported that other researchers had found weld factors of 87-97%. The 0.2% proof strength values reported by Peel<sup>2</sup> were 145-154 MPa, which are very similar to those found in this study, thus 141-171 MPa. The parent plate in Peel's study had a UTS of 457 MPa and a 0.2% proof strength of 392 MPa. As 5083-H321 is a strain hardening alloy and the FSW process leads to extensive recrystallisation in the weld nugget and TMAZ, it is not surprising that weld proof strength values are very similar in the two studies.

---

<sup>1</sup> Peel, M (2005)



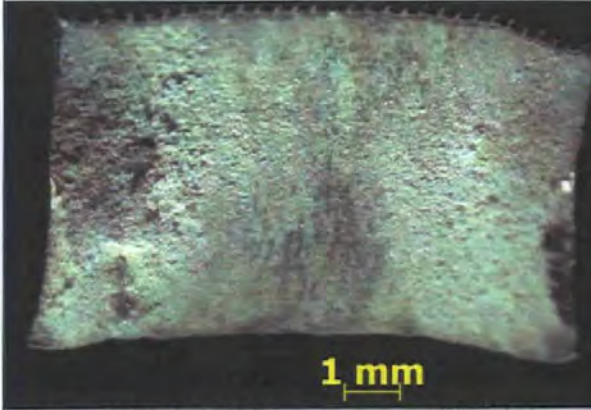
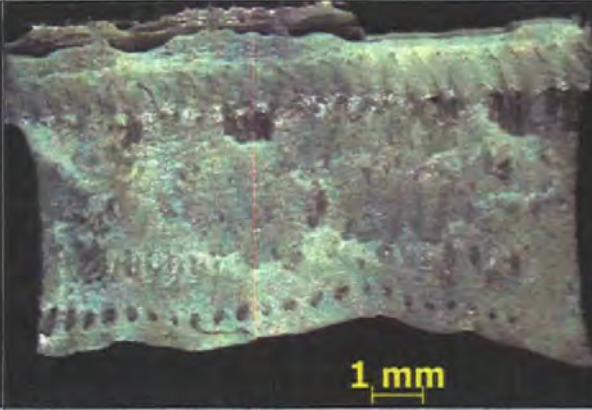
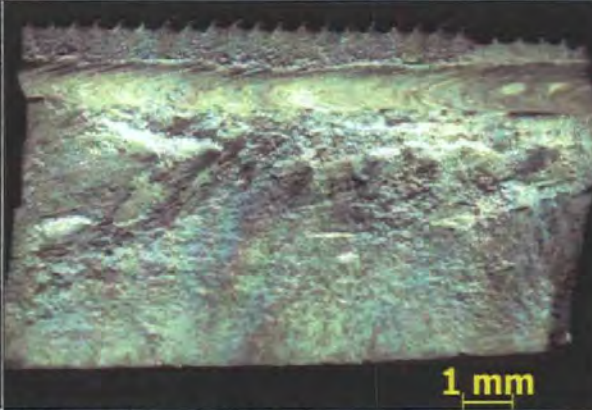
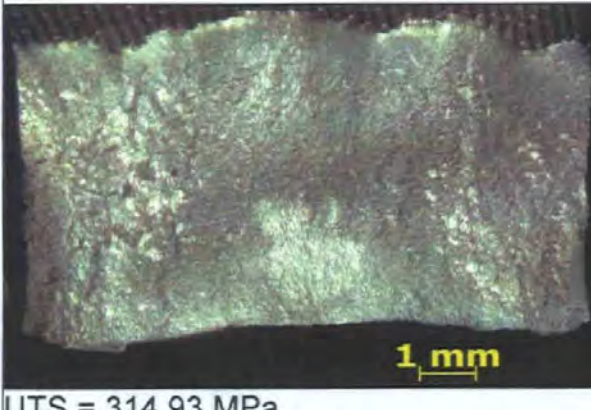
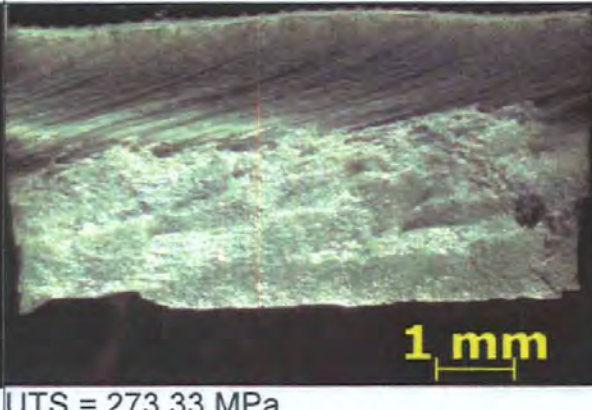

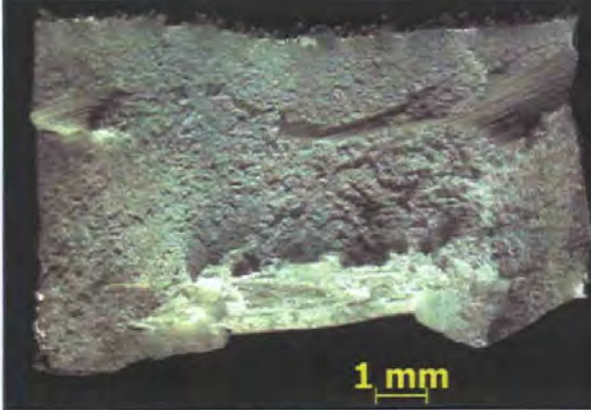
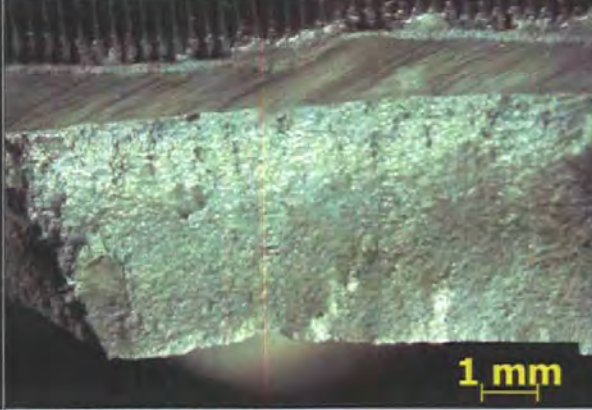
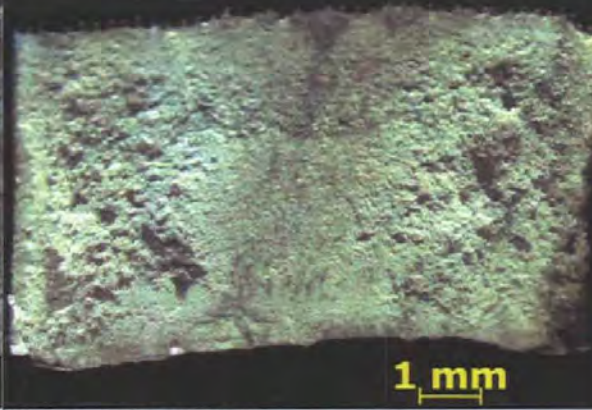
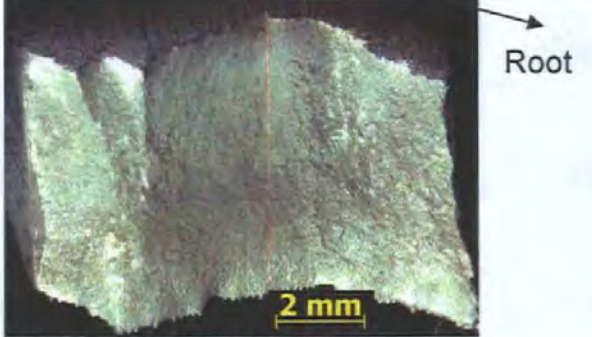
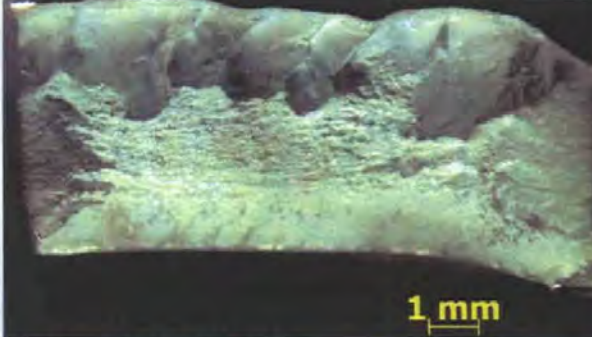
Feed rate : 85 mm/min	Feed rate : 135 mm/min	Feed rate :185 mm/min
Weld 3 :201 rpm, Pitch 0.42	Weld 5: 254 rpm, Pitch 0.51	Weld 7: 348 rpm, Pitch 0.53
		
UTS = 312.81 MPa 0.2% proof strength = 160.63 MPa	UTS = 307.69 MPa 0.2% proof strength = 165.37 MPa	UTS = 293.87 MPa 0.2% proof strength = 149.60 MPa
Weld 6:266 rpm, Pitch 0.32	Weld 9:318 rpm , Pitch 0.42	Weld 1:436 rpm, Pitch 0.42
		
UTS = 314.93 MPa 0.2% proof strength = 164.37 MPa	UTS = 273.33 MPa 0.2% proof strength = 145 MPa	UTS = 288.8 MPa 0.2% proof strength = 170.5 MPa
Weld 8:400 rpm, Pitch 0.21	Weld 2:423 rpm, Pitch 0.32	Weld 10: 617 rpm, Pitch 0.3
		
UTS = 308.2 MPa 0.2% proof strength = 144.7 MPa	UTS = 241.45 MPa 0.2% proof strength = 152.5MPa	UTS = 309.57 MPa 0.2% proof strength =148.33 MPa
	Weld 11:635 rpm, Pitch 0.2	Weld 4:870 rpm, Pitch 0.21
		
	UTS = 305.73MPa 0.2% proof strength = 140.67MPa	UTS = 254.47MPa 0.2% proof strength = 148.33MPa

Table 4.8 : Optical fractographs of FSW tensile fractures.

The formation of the planar facets in the shoulder region of the fracture surfaces can be explained by relating these features to frictional power input, as shown in Figure 4.9. Larger frictional power corresponds with greater plastic deformation in the tool shoulder region. The tool shoulder side of the weld lies at the top of each optical macrograph shown in Figure 4.9.

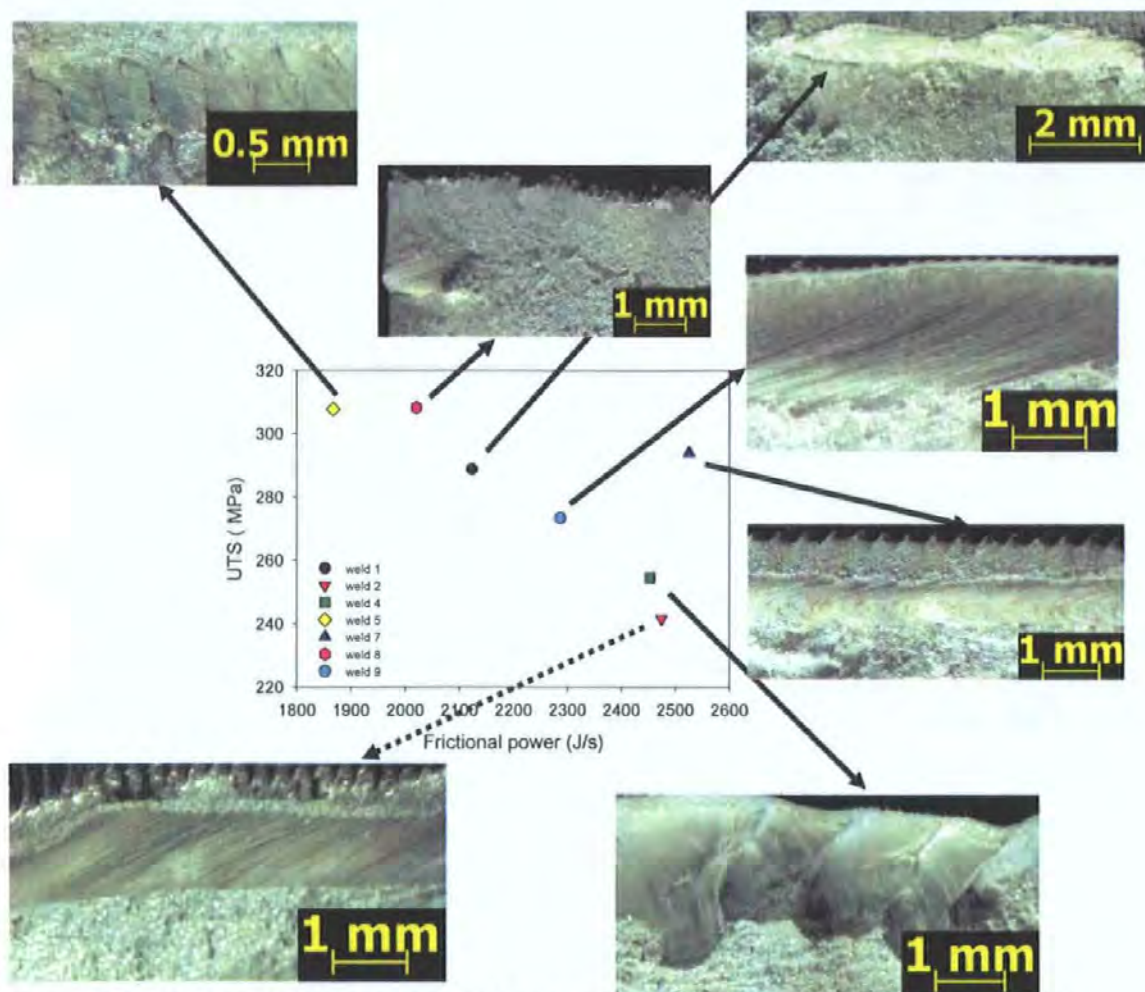


Figure 4.9: Tensile fractographs of the shoulder region of the welds as a function of UTS and frictional power.

Weld five showed the most prominent onion skin related features, with the distances between the layers equal to the weld pitch of 0.51 mm/rev. The holes seen at the root side of the weld also corresponds to distances equal to the weld pitch for this weld that is, 0.49 mm. Weld four also showed fracture surface features related to the onion skin layers quite clearly, but indicated more plastic deformation.

Table 4.9 summarizes the gross defects observed on the tensile fracture surfaces and in the macrographs and will be used to relate defects to welding parameters.

When a shear fracture occurred after tensile testing an entry of "shear" was made in Table 4.9. The defects that occurred more frequently are highlighted in bold.

Weld no	Weld position			Conclusions
	221 mm	493 mm	582 mm	
1	planar section and onion skin defects	planar section and onion skin defects	planar section and onion skin defects	<b>planar section and onion skin defects</b>
2	root defects and planar section and pseudo-bonds	root defects, planar section	root defect and planar section	<b>root defects, planar section</b>
3	shear	shear	planar section and	<b>shear</b>
4	root defect	root defect planar section	root defect and planar section	<b>root defects and planar section</b>
5	shear	onion skin	shear	<b>shear, onion skin defects</b>
6	shear	shear	shear	<b>shear</b>
7	planar section	planar section	shear	<b>planar section</b>
8	planar section onion skin defects on root side	planar section onion skin defects on root side	shear	<b>onion skin defects planar section</b>
9	shear	shear	planar section	<b>shear, planar</b>
10	Shear, onion skin defects and root defects	shear	shear and root defect	<b>shear, root defects</b>
11	shear	shear	shear	<b>shear</b>

Table 4.9: Summary of defects detected in tensile fractured specimens of FSW.

It is evident from Table 4.8 that welds containing planar sections also contain onion skin defects. Table 4.8 showed evidence of pseudo bonds as S-shaped features shown on welds 2,3,6 and weld 7. No confirmation could be obtained of this feature on the tensile fracture surfaces because welds 2 and 7 contained planar regions and onion skin whereas welds 3 and 6 were shear fractures as listed in Table 4.9. These defects were added to the comparison (shown in Figure 4.3) to see if they do change the UTS of FSW.

#### 4.6.3 Variation of UTS and 0.2 % proof strength with weld parameters

The interrelationship of UTS with the process parameters was investigated to try and determine the process parameters that might be used as a predictor of optimum tensile properties. Thus Figure 4.10 presents contour plots of UTS as a function of tool speed and feed rate.

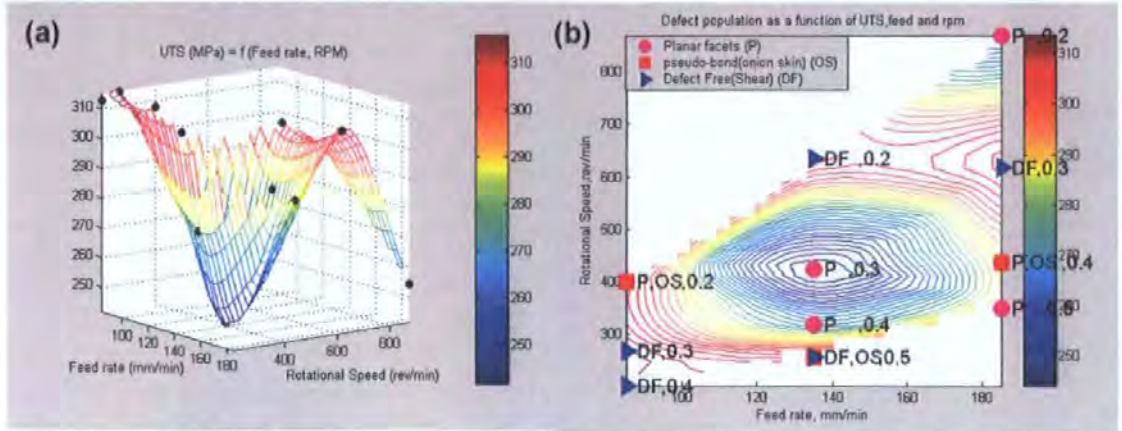


Figure 4.10: (a) 3D plot of UTS versus rotational speed and feed rate.  
(b) Contour plot of UTS versus rotational speed and feed rate.

High values of UTS can be seen to correspond with defect free welds and is clearly correlated with feed rate and rotational speed. Planar facets correspond with low UTS regions. Pseudo-bond defects occur at tool speeds around 400 rpm for all feed rates. Weld 5 had the lowest rotational speed and the most prominent onion skin layers. The rotational speed has the greatest influence on the formation of the onion skin layers. A minimum UTS point is located at approximately 140 mm/min and 400 rpm. This plot seems to be the inverse of that observed for the total frictional power input to the weld and hence the difference in power input measured from the centre of the tool (see Figure 3.11 (b)).

The interpretation of this contour plot data is that plastic flow processes must underlie the observed trends. These processes occur in discrete regions and, certainly over the mid-range of feed rates considered (100-200 rpm), there are two separate regimes that give rise to high strength welds at any particular pitch value. High strength welds are observed at both high and low pitch values, but not at intermediate values. This demonstrates that although pitch is a useful characterizing parameter in discussing weld process conditions it is not as good as a predictive parameter for mechanical properties in FSW. Frictional power would be a better predictor and is shown in Figure 4.11.

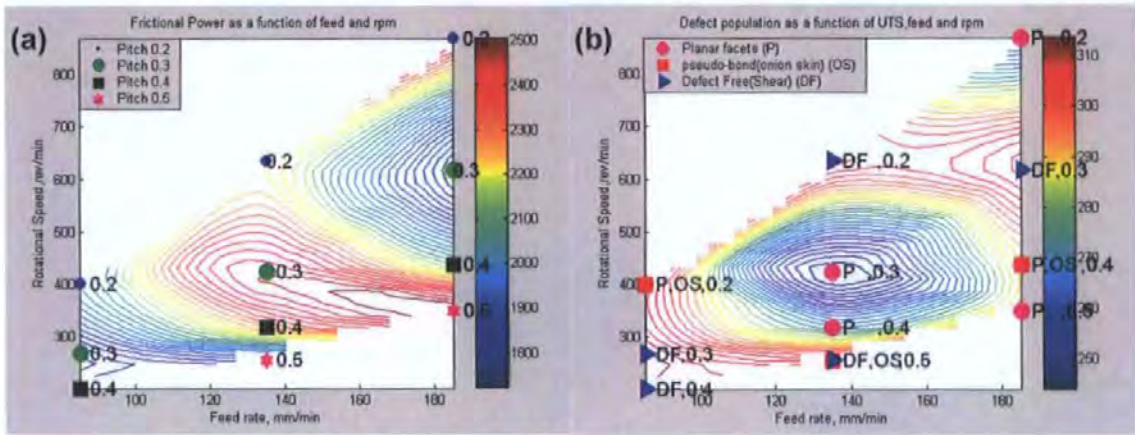


Figure 4.11: Comparison between (a) frictional power and (b) UTS.

Figure 4.12 indicates the success of a predictive model for UTS based on frictional power input.

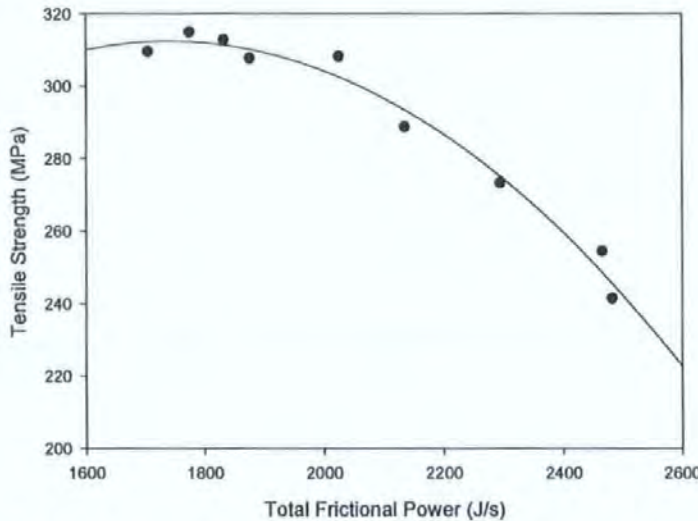


Figure 4.12: Tensile strength as a function of tool frictional power.

Adjusted  $R^2$  values of 0.97 could be obtained after two data points (weld 2 and weld 7) that had large studentized residuals were eliminated from the data set. The model is then given by

$$UTS = -328.44 + 0.7(\text{Power}) - 0.0001(\text{Power}^2)$$

The interrelationship of 0.2% proof strength with the process parameters was investigated to try and determine the process parameters that might be used as a predictor of optimum proof strength properties. Thus Figure 4.13 presents contour plots of 0.2% proof strength as a function of tool speed and feed rate.

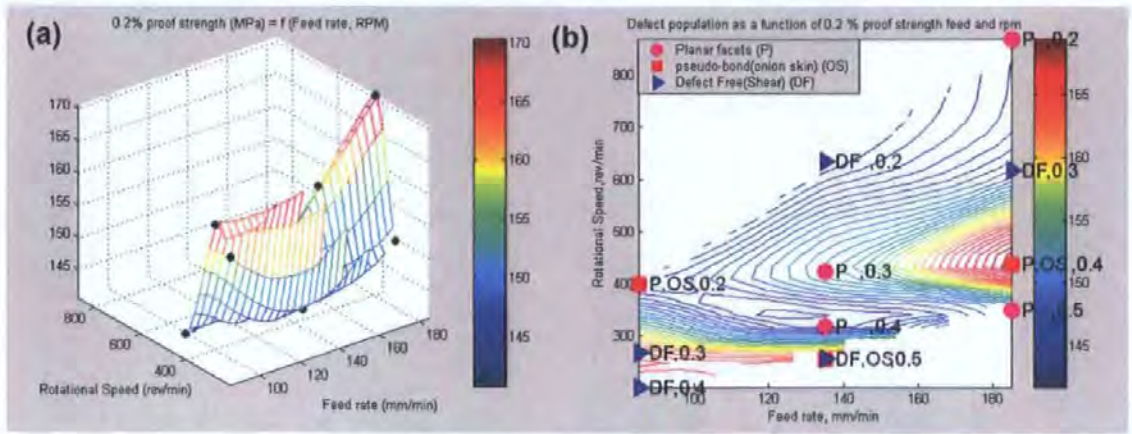


Figure 4.13: (a) 3D plot of UTS versus rotational speed and feed rate.  
 (b) Contour plot of UTS versus rotational speed and feed rate.

It is quite evident that the variation of 0.2% proof strength and UTS with tool speed and rotational speed are not identical. Defect free welds correspond to high and low 0.2% proof strength. This is due to the fact that different processes trigger the occurrence of yielding and ultimate tensile strength. The highest yield strength occurs at low feed rates and tool speeds as well as the highest feed rates and mid range tool speeds. Pseudo-bond defects correspond to high and low 0.2% proof strength regions and no systemic influence of pseudo-bonds on the 0.2% proof strength could be obtained.

Other weld process parameters were also modelled but did not produce regression coefficients as good as that found for frictional power for UTS. P-values, < 0.05 are significant parameters. The results are given in Table 4.10.

Regression models for UTS versus weld parameters	Parameters	P- value
UTS=327- 0.16 feed - 0.03 rpm R <sup>2</sup> =0.19 R <sup>2</sup> <sub>adj</sub> = -0.04	Feed Rpm	0.586972 0.596232
UTS= 1340 + 5.08 F <sub>z</sub> -2.41 Torque -2.20 Temp + 0.03 F <sub>x</sub> max + 0.07 F <sub>y</sub> max R <sup>2</sup> = 0.82; R <sup>2</sup> <sub>adj</sub> = 0.61	F <sub>z</sub> Tool Torque Tool Temperature F <sub>x</sub> max F <sub>y</sub> max	0.152918 0.08492 <b>0.050167</b> 0.146696 <b>0.056862</b>
Regression models for 0.2% proof strength versus weld parameters	Parameters	P- value
0.2% proof strength=164 - 0.002. feed – 0.03 rpm R <sup>2</sup> =0.48; R <sup>2</sup> <sub>adj</sub> = 0.34	Feed Rpm	0.977277 0.087474
0.2% proof strength= 177 – 0.85 F <sub>z</sub> +0.36 Torque -0.03 Temp + 0.005 F <sub>x</sub> max + 0.009 F <sub>y</sub> max R <sup>2</sup> =0.75; R <sup>2</sup> <sub>adj</sub> = 0.43	F <sub>z</sub> Tool Torque Tool Temperature F <sub>x</sub> max F <sub>y</sub> max	0.506893 0.450415 0.929133 0.516598 0.442016

Table 4.10: UTS and 0.2% proof strength regression models.

The above analyses reveal that tool temperature and  $F_y$  max seem to be parameters that could contribute significantly to changes in UTS, but there is not a large difference in P-values with respect to the process parameters. Quadratic models of these parameters and UTS were attempted and the  $R^2$  values for tool temperature, tool torque,  $F_z$  and  $F_y$  max were respectively 0.22, 0.08, 0.02 and 0.19.  $F_y$  max and tool temperature are the best process parameter predictors of the variation in UTS. This is not surprising since both parameters vary with energy input to the welds. Figure 4.14 shows a contour plot of UTS as a function of tool temperature and  $F_y$  max (which Table 4.10 indicated as a significant contributor to UTS). This figure indicates that this type of defects occur for any applied  $F_y$  max force. The presence and type of defects are therefore a complicating factor in making predictions of high tensile strength process conditions. If plastic flow processes combine with certain alloy compositions (of which 5083-H321 is known to be one) new defect types, such as strain partitioning induced defects, may occur<sup>1</sup>. Nonetheless, this work has demonstrated that robust predictive models of tensile strength can be developed.

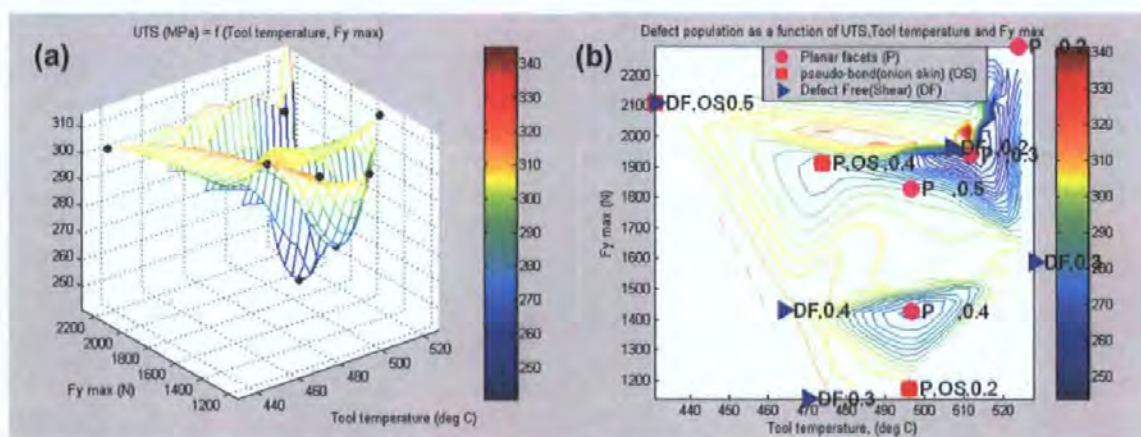


Figure 4.14: Tensile strength as a function of (a) tool temperature and (b)  $F_y$  max.

There is a reasonable correlation between an increase in UTS and a decrease in the parameter  $\omega^2/f$ , which is an indication of the plasticized width during welding, as shown in Figure 4.15. This is understandable if it is assumed that an increase in heat input will decrease the tensile strength of the material. A correlation coefficient of 0.68 was obtained after eliminating the data for welds 2 and 9.

<sup>1</sup> James, MN et al (2004)

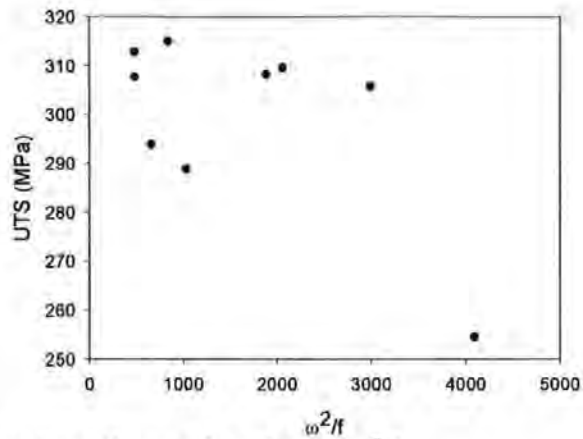


Figure 4.15: Tensile strength as a function of  $\omega^2/f$ .

The regression analyses on 0.2% proof strength did not show any good correlations.

#### 4.7 Micro hardness results

Micro hardness testing was undertaken using a Buehler Micromet 5103 automated micro hardness tester at the Facility for Materials Engineering (FaME38) at the ILL-ESRF Grenoble, France (see Figure 4.16). Measurements were made on the T-S plane across the weld at 1 mm intervals in the T-direction. A load of 200 gf was employed, with a loading time of 10 seconds. Vickers hardness measurements were calculated using the software developed by Buehler.

The measured value of the micro-indentation hardness of a material is subject to several sources of errors. According to the ASTM 384 standard a 1% error in the applied force and 0.5% error in the measured diagonal can contribute to a 1% error in the final measurement. An error in the angle of the indenter does not have a significant effect on the result.

Each indentation was therefore examined to determine whether the software had chosen the correct contrast, thus correctly identifying the indentation and not including other etched sections with the same contrast. Indentations that did not appear symmetrical were eliminated. Figure 4.17 shows an example of an indentation made on the sample.





Figure 4.16: Buehler Micromet 5103 micro hardness tester at FAME38 in Grenoble, France.

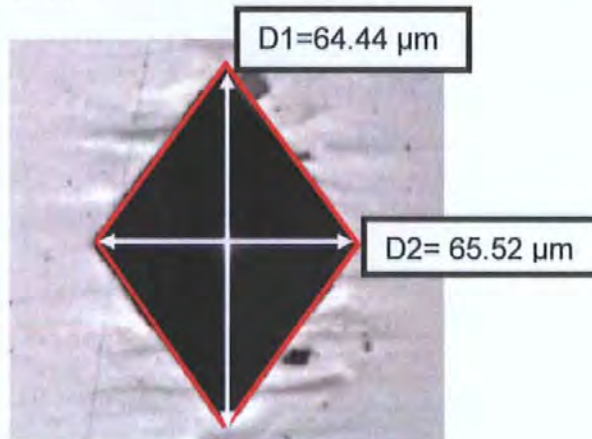


Figure 4.17: An example of a micro hardness indentation.

The Vickers hardness,  $\text{kgf/mm}^2$  was determined using

$$HV = 1854.4 \frac{P}{d^2} \quad \dots (4.1)$$

where

$P$  = force in gf

$d$  = mean diagonal length of the indentation in  $\mu\text{m}$ .

#### 4.7.1 Relationship between rotational speed and hardness

Figure 4.18 shows the variation of Vickers hardness with rotational speed for three feed rates. The data is taken on a transverse cross section of the weld (S-T plane) and the 0 mm position represents the weld centre-line. The corresponding parent plate hardness is shown on all figures as horizontal lines drawn at

approximately 102 HV. The mechanical and heat input to the welds softens the material by about 22%-26% in the centre of the weld around the position of the pin diameter. This corresponds with other reports on the hardness of this material being between 70 – 80 HV after welding<sup>1</sup>.

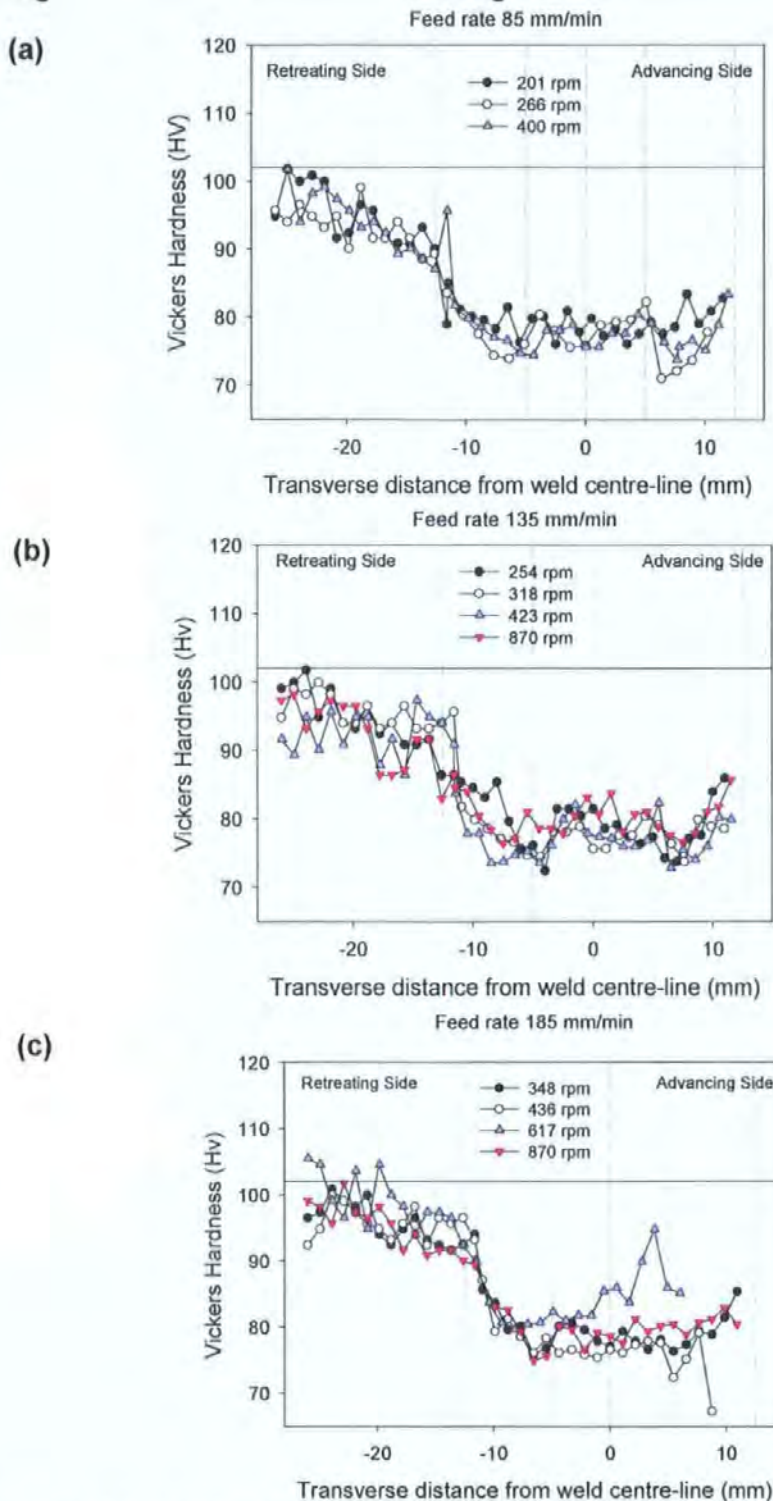


Figure 4.18: (a) Hardness versus rotational speed for a feed rate of 185 mm/min.  
 (b) Hardness versus rotational speed for a feed rate of 135 mm/min.  
 (c) Hardness versus rotational speed for a feed rate of 85 mm/min.

<sup>1</sup> Larsson, H et al (1998)

Since at a constant feed rate a decrease in rotational speed should give a slight decrease in heat input to the welds, one might expect the hardness value in the region -10 mm to +10 mm to decrease with increasing rotational speed. This is not evident in Figure 4.20 (a)-(c) at any of the three feed rates considered, which indicates that the recrystallisation that occurs in the nugget dominates the hardness in the alloy.

#### 4.7.2 Relationship of Vickers hardness with increasing feed rate and rotational speed at constant pitch

Figure 4.19 shows the variation in Vickers hardness at constant pitch values as both feed and speed increase. With a constant pitch value the heat input per unit length decreases as the feed rate and rotational speed increases simultaneously (Figure 3.10). An increase in hardness values is therefore expected. This cannot be seen to be generally true. This again indicates that recrystallisation that occurs in the nugget dominates the hardness for 5083-H321 aluminium alloy.

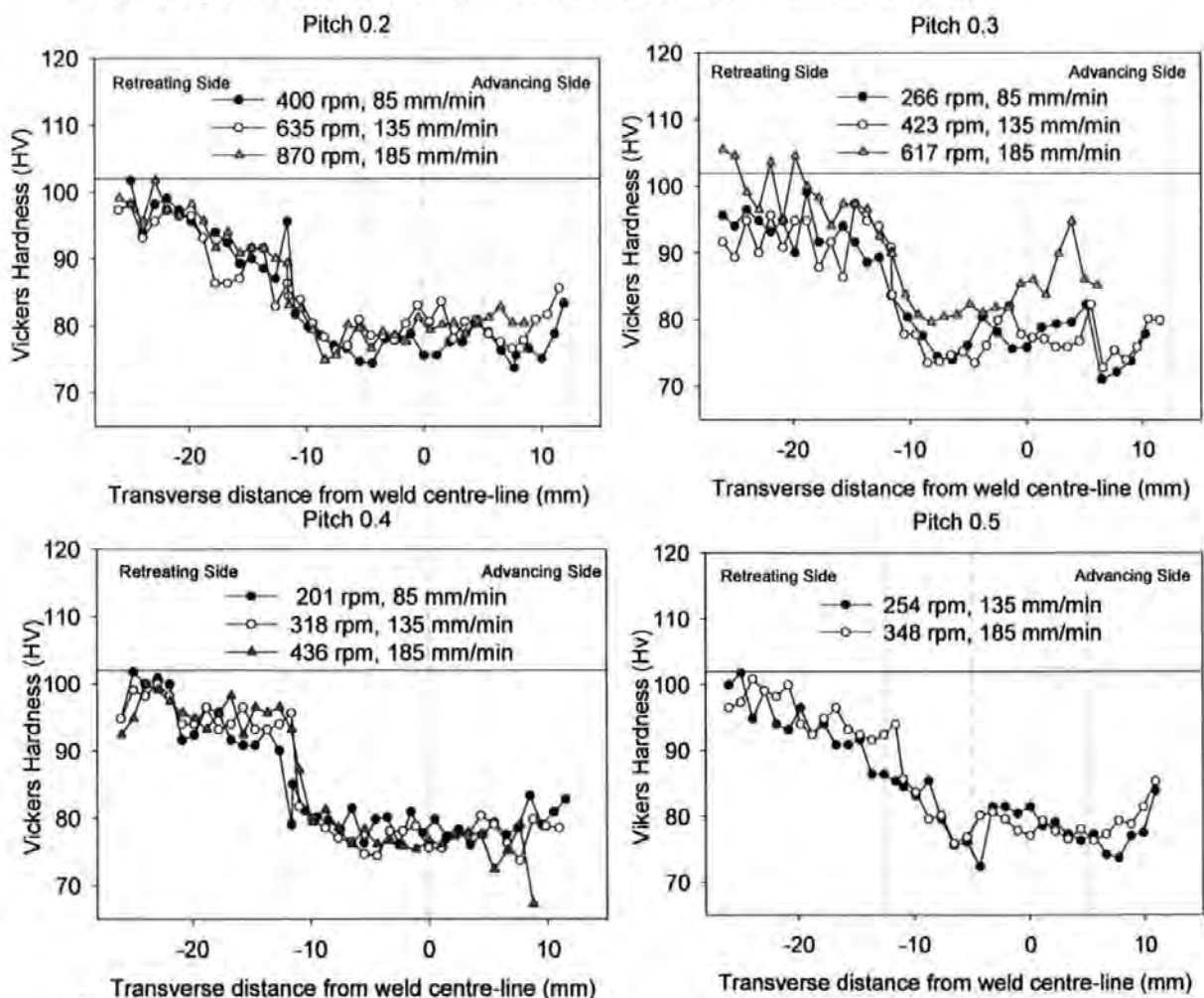


Figure 4.19: Trends of Vickers hardness versus pitch.

### 4.7.3 Comparison between hardness and process parameters

The average values of all the hardness measurements in the nugget region, at 3 mm below the tool shoulder side of the welds were calculated and are shown in Figure 4.20 and 4.21, together with a similar plot for frictional power and heat input. Generally speaking, in aluminium alloys there is a correlation between hardness values and tensile strength. As Figure 4.12 indicates, showing a good correlation between tensile strength and frictional power, an inverse correlation would be expected between hardness and frictional power. Figure 4.12 shows clear evidence of such a correlation. Frictional power therefore appears to be a good predictor of hardness and tensile strength.

An increase in frictional power gives lower hardness values. Thus and therefore more softening of the parent material. In this strain hardening 5083-H321 alloy, however, mechanical properties are a more subtle combination of plastic flow and power input. The downwards force is therefore likely to play an important role in the hardness generated at this position in the weld. At 3 mm below the tool shoulder side of the weld, the heat input model indicates that lower heat input corresponds with higher hardness values.

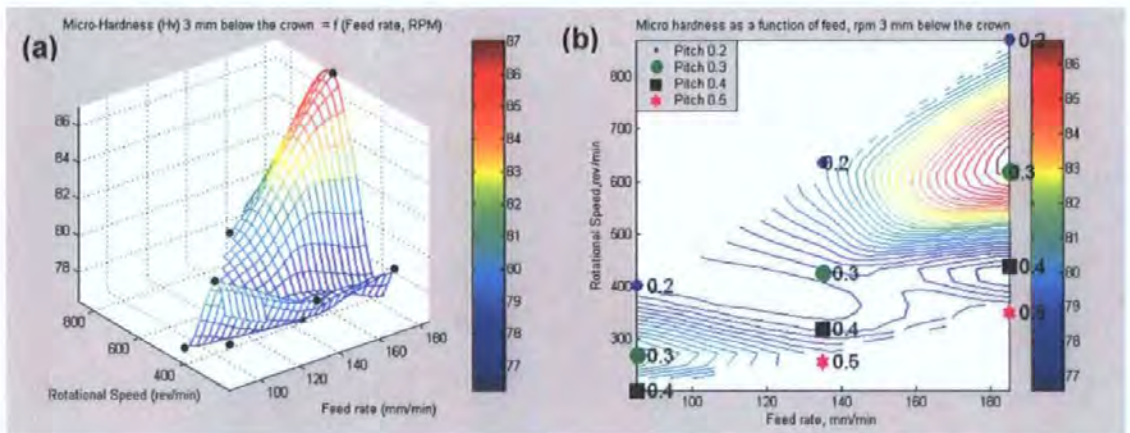


Figure 4.20: (a) 3D plot of Vickers hardness values 3 mm below the crown of the weld versus input process parameters.  
(b) Contour plot of Vickers hardness values 3 mm below the crown of the weld versus input process parameters.

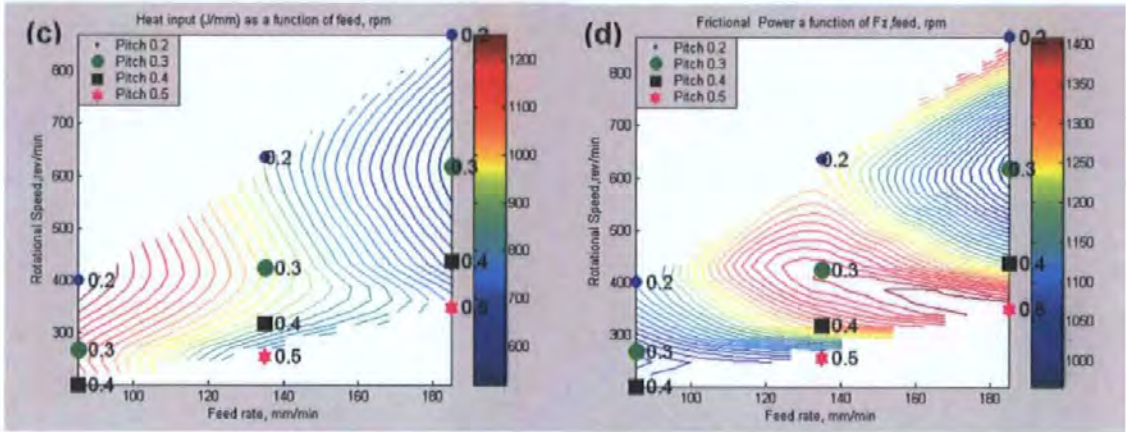


Figure 4.21: (c) Contour plot of heat input and as a function of feed rate and rotational speed.  
 (d) Frictional power input as a function of feed rate and rotational speed.

#### 4.8 Conclusions

The following conclusions can be drawn from the discussion so far:

- (i) The tensile strength is a direct function of the total frictional power (Figure 4.11) and decreases with increasing frictional power input.
- (ii) The planar type defect at approximately 1.5 mm from the shoulder side of the weld correlates excellently with the frictional power in the welds (Figure 4.9).
- (iii) Hardness 3mm below the tool shoulder correlates fairly well with the inverse of frictional power (thus lower frictional power is equal to higher hardness values (Figure 4.20 (b) and (c)).

## **5. Determination of residual stress in FSW using synchrotron radiation**

### **5.1 Introduction**

During welding, the thermal contraction of weld metal is resisted by the colder surrounding metal as well as by the plastic flow in the material. This results in residual stresses that considerably affect the mechanical properties and service life of engineering components.

This chapter presents detailed stress profiles obtained for welds using synchrotron X-ray diffraction. It also discusses the experimental setup used during the strain measurements conducted at the European Synchrotron Radiation Facility (ESRF) on the FSW Al 5083-H321 samples. Residual stress data was investigated as a function of varying input and process parameters. Very little information is available in the research literature on the influence of process parameters (that is forces on the tool, tool torque or tool temperature) on the residual stresses resulting from FSW 5083-H321 aluminium alloys. Recent studies have investigated the residual stress variation with rotational speed in 2024-T3 and 5083-H321<sup>1,2</sup>. Most studies on residual stress in FS welds reported in the research literature contain only 2-3 changes in input parameters, that is, feed rate at a constant rotational speed or 2-3 rotational speeds at a constant feed rate<sup>1,2</sup>. In this study eleven experimental conditions are investigated. Stress maps are also correlated and discussed in the context of the heat input into the welds. The results are presented as a series of 'performance surface maps' as a function of energy input and weld pitch (defined as tool travel increment per revolution). This allows predictions to be made of favourable process parameters for particular combinations of weld property characteristics.

Detailed knowledge of the residual stress and strain distributions is indispensable in linking process parameters with mechanical properties and fatigue performance. Points of high residual stresses are often associated with stress concentrations which lead to local yield and plastic flow and alter the residual stress in an applied load cycle through plastic relaxation or cyclic hardening under fatigue loading<sup>3</sup>.

---

<sup>1</sup> Shukla, AK and Baeslack, WA (2006)

<sup>2</sup> Steuwer, A et al (2006)

<sup>3</sup> James, MR and Lu, J (1996)

The presence of residual stresses is known to affect both the initiation and growth of fatigue cracks, through changes to the effective mean stress experienced during fatigue cycling. Higher mean stresses generally give higher crack growth rates and faster crack initiation<sup>1</sup>. Tensile residual stresses will add to applied stress levels and lead to fracture at lower loads than might be expected<sup>1</sup>. Since residual stresses can have such a large influence on the life of engineering components, these were investigated for the FSW made for this study.

## 5.2 Residual stress definitions

James and Lu<sup>1</sup> give a definition of residual stress as a stress state which exists in the bulk of a material at rest without application of an external load. Residual stresses arise due to a misfit in the material that cannot be accommodated by the distortion of the material. These misfits arise due to different regions of the material experiencing different rates of thermal inputs (that is thermal misfits) or due to different regions of the material or phases present deform differently (that is shape or plastic misfits)<sup>2</sup>. All residual stress systems are self-equilibrating over the whole system. The resultant force and the moment which they produce, must be zero.

The residual stresses are generally classified into three categories that are related to the scale that is measured in the material<sup>3</sup>:

- (i) Type I, macroscopic residual stresses, which are of a scale larger than the grain size of the material;
- (ii) Type II, micro-residual stresses (inter-granular), of a magnitude equal to or less than the grain size often resulting due to the presence of different phases or constituents in a material; and
- (iii) Type III, intra-granular, micro-residual stresses that range over several atomic distances within a grain because of the presence of dislocations and other crystalline defects.

The actual residual stress state at a point comes from the superposition of the above stress categories. Figure 5.1 shows the three types of residual stresses.

---

<sup>1</sup> James, M R and Lu, J (1996)

<sup>2</sup> Hutchings, MT et al (2005)

<sup>3</sup> Withers, PJ and Bhadeshia HKDH (2001)

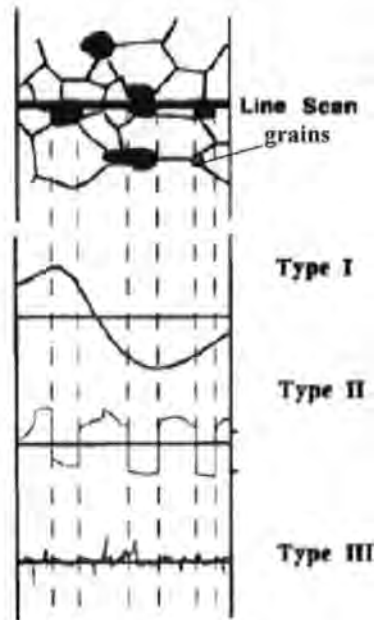


Figure 5.1: The different types of residual stresses<sup>1</sup>.

### 5.3 Techniques used to measure residual stresses

Residual stresses can be determined using either destructive or non-destructive techniques. Methods such as hole drilling, crack compliance, curvature and layer removal and contour methods all require damage of the material in order to take measurements and a mathematical analysis in order to determine the residual stresses in the material. Non-destructive techniques do not cause any damage to the sample, e.g. if layers are not removed from the sample and these techniques include ultrasonic, raman, magnetic, synchrotron X-ray, low intensity X-ray and neutron diffraction. To choose an appropriate technique depends on the material being investigated, the size of the part, the type of data required and the availability of equipment. Table 5.1 summarizes the major attributes of various residual stress measurement techniques briefly<sup>2,3,4,5</sup>. X-ray, synchrotron X-ray and neutron diffraction methods can measure uniaxial, biaxial and triaxial (not for X-ray) macro- and micro-stresses whereas the other techniques, listed in Table 5.1, only measure uniaxial and biaxial macro stresses.

<sup>1</sup> Fitzpatrick, ME et al (1997)

<sup>2</sup> Wilthers, PJ( 2001a)

<sup>3</sup> James, NM ( 2006)

<sup>4</sup> Steuwer, A (2006)

<sup>5</sup> Fitzpatrick, ME and Lodini, A (2003)



Method	Principle, advantages and limitations	Resolution, penetration and sampling volume	Material type
Hole Drilling	This method measures in plane stresses from distortion caused by stress relaxation in plates using rosettes. Many sources of error arise due to the shape and dimensions of the hole, surface conditions and non orthogonal hole drilling. The size of the rosette and hole-to-hole interference limits spatial resolution. Yielding can occur during hole drilling close to the surface of the sample, and this will lead to inaccurate measurements. Strain can be measured up to a depth equal to the diameter of the drilled hole.	<u>Resolution</u> 50-100 $\mu\text{m}$ depth <u>Penetration</u> Equal to Hole diameter <u>Sampling size</u> 1-2 mm in diameter 1-2 mm deep	Metals Plastics Ceramics
X-ray Diffraction	The shifts in the position of Bragg peaks, caused by elastic strain induced in a sample, is used to determine strain. Grains are therefore considered as atomic strain gauges. This method requires <ul style="list-style-type: none"> <li>(i) layer removal for depth measurements by using, for example, electro polishing techniques;</li> <li>(ii) the need to deduce principal stress directions (or measure 6 components of strain tensor);</li> <li>(iii) suitable lattice planes to be chosen; and</li> <li>(iv) The <math>\sin^2\Psi</math> technique to be applied and does not require <math>d_0</math> measurements.</li> </ul> Limitations include : the whole specimen must fit inside the diffractometer when measurements are taken; errors can arise from rough surfaces, e.g. welds; only near surface information can be measured; and this method is sensitive to surface preparation.	<u>Resolution</u> 20 $\mu\text{m}$ depth 1 mm wide <u>Penetration</u> 5 $\mu\text{m}$ - Ti 50 $\mu\text{m}$ - Al 1 mm layers <u>Sampling size</u> 0.1-1 $\text{mm}^2$ 0.05-0.1 mm	Metals Ceramics
Synchrotron Diffraction	This technique is discussed in detail in sections 5.6 to 5.10. Synchrotron X-ray advantages include: <ul style="list-style-type: none"> <li>(i) <math>10^{12}</math> times brighter than laboratory X-ray source. 20-300 keV beam with small wavelength <math>\approx 0.3 \text{ \AA}</math>;</li> <li>(ii) Much higher penetration</li> </ul>	<u>Resolution</u> 20 $\mu\text{m}$ lateral 1 mm in-line <u>Penetration</u> >500 $\mu\text{m}$ 20 mm – Al <u>Sampling</u>	Metals Ceramics

	<p>depths (&gt;20 mm in Al) than laboratory X-rays;</p> <p>(iii) Narrow beam and small sampling volume;</p> <p>(iv) Fast measurements ~ 20s per data point; and</p> <p>(v) low scattering angles ~ 10-20° depending on (h k l) planes investigated; and</p> <p>(vi) Standard diffraction techniques being used with synchrotron X-ray measurements.</p> <p>One limitation is that the gauge volume has an elongated diamond shape that could make strain measurements in certain directions not feasible due to long paths lengths into the material. This technique is best applied to thin plates.</p>	<p><u>size</u> 0.1 mm<sup>3</sup></p>	
Neutron Diffraction	<p>Neutrons are scattered by an electron cloud or nuclei. Constructive interference leads to the generation of intensity peaks from Bragg reflected planes. Time of flight of the reflected beam is used to determine strain. Major advantages are:</p> <p>(i) high penetration depths of ~100 mm in Al and ~ 25 mm in steel;</p> <p>(ii) high spatial resolution – can measure to within 0.2 mm of surface;</p> <p>(iii) narrow beam (slits);</p> <p>(iv) full 3-d strain maps via strain scanning of specimen at the same time can be obtained;</p> <p>(v) automated translation and rotation of a specimen;</p> <p>(vi) strain measurements during fatigue, bending or tensile testing (that is in service measurements) can be taken; and</p> <p>(vii) time of flight measurements can be taken to obtain strains from different phases present in the same sample at the same time. This is possible because different hkl reflections will take different amounts of time to reach the detector.</p>	<p><u>Resolution</u> 500 μm</p> <p><u>Penetration</u> 100 mm – Al 25 mm – Fe 4 mm - Ti</p> <p><u>Sampling size</u> &gt;1 mm<sup>3</sup></p>	Metals Ceramics

	The only limitation is that this technique is more expensive than Synchrotron X-ray radiation and highly qualified scientists are required to take strain measurements.		
Curvature Layer Removal	Measures in plane stresses by changes in curvature of a strip coated on the sample. The accuracy is limited by the minimum measurable curvature. Near surface stresses cannot be measured with this technique.	<u>Resolution</u> Variable <u>Penetration</u> Not applicable <u>Sampling size</u> Not applicable	All
Magnetic	Ferromagnetic properties are sensitive to the internal stress state in the sample. The magnetic domains closely aligned with stress are strained. The stress-induced magnetic anisotropy leads to the rotation of the magnetic field away from the applied direction. A sensor coil can monitor these small rotations. When no rotation is observed, principal stress axis and the magnetic axis are aligned. This technique is sensitive to the micro structural and chemistry changes in the sample. No universal or agreed method of data interpretation is available.	<u>Resolution</u> 1 mm <u>Penetration</u> 20-300 $\mu\text{m}$ <u>Sampling size</u> >2 mm <sup>2</sup>	Ferro-magnetic
Ultrasonic	The velocity of ultrasonic waves are sensitive to stress in materials. The changes in speed provide a measure of the average stress along the wave path through the material. Measurements are affected by microstructural changes in the sample. Difficulties arise in separating multi-axial stresses.	<u>Resolution</u> 5 mm <u>Penetration</u> >100 mm <u>Sampling size</u> 1-400 mm <sup>2</sup>	Metals Ceramics
Raman	Laser light causes atomic bonds to vibrate in certain liquid and solid materials. This gives characteristic fluorescence luminescence lines of wavelength and intensity. Raman lines shift with changes in hydrostatic stress. This is a surface technique for samples that are not optically transparent.	<u>Resolution</u> 0.5 $\mu\text{m}$ <u>Penetration</u> Surface <u>Sampling size</u> -	Ceramics Polymers Silicon carbide Alumina-zirconia Epoxy Sapphire Fibre composites

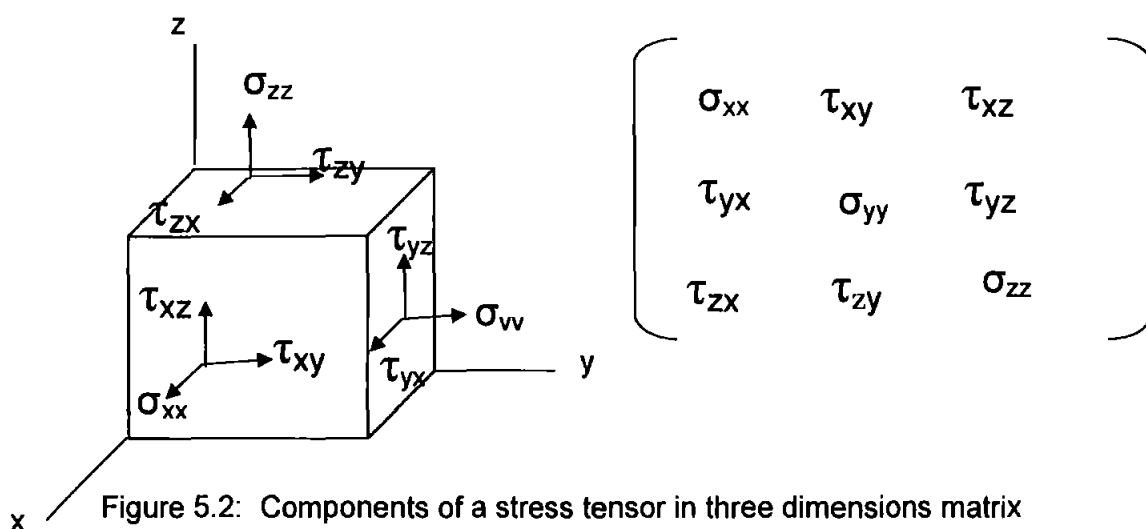
Table 5.1 : Summary of various measurement techniques and their characteristics to determine residual stresses.

The non-destructive tool used to measure residual stresses in this investigation is synchrotron X-ray radiation. This was chosen because accurate data could be obtained without any damage to the specimen and measurements could be taken through the thickness of the 6 mm Al 5083-H321 plate. Laboratory X-ray diffraction techniques only allow measurements up to a depth of 50  $\mu\text{m}$  in aluminium.

#### 5.4 Continuum mechanical definition of stress and strain

The internal force acting on a small area  $dA$  of a plane that passes through a point  $P$  can be resolved into three components: one normal to the plane and two parallel to the plane<sup>1</sup>. The normal component divided by  $dA$  gives the normal stress (usually denoted by  $\sigma$ ), and the parallel components divided by the area  $dA$  give the shear stress (usually denoted by  $\tau$ ). These stresses are average stresses, as the area  $dA$  is finite; but when the area  $dA$  is allowed to approach zero, the stresses become stresses at the point  $P$ . It can be proved by equilibrium that the stresses on any plane can be computed from the stresses on three orthogonal planes passing through the point. The three planes are normally chosen to be the  $x$ -,  $y$ -, and  $z$ -planes. As each plane has three stresses, the stress tensor has nine stress components which completely describe the state of stress at a point.

Stress is a second order tensor quantity with six degrees of freedom, but can be described completely by six terms due to symmetry as shown in Figure 5.2.



<sup>1</sup> Dieter, GE (1989)

In the generalized stress tensor notation, the tensor components are written as  $\sigma_{ij}$  where  $\sigma_{ij}$  is the stress on the  $i$  face acting in the  $j$  direction of a cube. The relationship between stress and strain can be obtained by applying Hooke's law and is given by

$$\sigma_{ij} = \sum_{kl} C_{ijkl} \cdot \epsilon_{kl} \quad \dots(5.1)$$

where

$C_{ijkl}$  = stiffness tensor

$\sigma_{ij}$  = stress at a point

$\epsilon_{kl}$  = strain at a point

If three normal stresses at a point are known, the strain caused by each component of stress can be derived. The total strains in three directions for an elastically isotropic material can be represented by the following equations:

$$\begin{aligned} \epsilon_x &= \frac{1}{E} [\sigma_x - u(\sigma_y + \sigma_z)] \\ \epsilon_y &= \frac{1}{E} [\sigma_y - u(\sigma_x + \sigma_z)] \\ \epsilon_z &= \frac{1}{E} [\sigma_z - u(\sigma_x + \sigma_y)] \end{aligned} \quad \dots(5.2)$$

where

$\epsilon_x, \epsilon_y, \epsilon_z$  = strain in directions x, y and z

$E$  = Modulus of elasticity

$\sigma_x, \sigma_y, \sigma_z$  = stress in directions x, y and z

$u$  = Poisson's ratio

Alternatively, stresses in three directions can be represented by strains in three directions, as shown in equation (5.3):

$$\sigma_x = \frac{E}{(1-2u)(1+u)} [(1+u)\epsilon_x + u(\epsilon_y + \epsilon_z)]$$

$$\begin{aligned}\sigma_y &= \frac{E}{(1-2\nu)(1+\nu)} \left[ (1+\nu)\epsilon_y + \nu(\epsilon_x + \epsilon_z) \right] \\ \sigma_z &= \frac{E}{(1-2\nu)(1+\nu)} \left[ (1+\nu)\epsilon_z + \nu(\epsilon_x + \epsilon_y) \right]\end{aligned}\quad \dots(5.3)$$

where

$\epsilon_x, \epsilon_y, \epsilon_z$  = strain in directions x, y and z

E = Modulus of elasticity

$\sigma_x, \sigma_y, \sigma_z$  = stress in directions x, y and z

$\nu$  = Poisson's ratio

Because of the linear relationship between the elastic strain and stress, the theory above can be applied for a three-dimensional strain and stress analysis. The calculations developed are valid for all polycrystalline materials, provided that:<sup>1</sup>

- (i) they are homogeneous and not anisotropic;
- (ii) they contain no crystallographic texture;
- (iii) show small grain size < 100  $\mu\text{m}$  (If not the case, this could lead to too few grains in the required orientation that produces a diffracted volume that is not large enough for good scattering statistics);
- (iv) the grain size is not too large. Peak intensities will vary for measurements at a specific wavelength while the sample is rotated about a plane normal to the plane of diffraction<sup>2</sup>); and
- (v) they are free from stress or composition gradients in the material. A stress gradient needs to be determined and it is difficult to distinguish between stress and composition gradients.

## 5.5 The biaxial stress case

The stress state of a body can be simplified to a biaxial stress state if loading occurs in the plane of the plate and the thickness of the plate is much smaller than the other dimensions. The biaxial conditions have been applied to thin welded

---

<sup>1</sup> Lu, J et al (1996)

<sup>2</sup> Vamas (2001)

plates<sup>1,2</sup>. The assumption that the stress perpendicular to the plate is zero is made in this thesis. Therefore, for a biaxial stress, state  $\sigma_z = 0$ , and equation (5.3) simplifies to<sup>3</sup>

$$\sigma_x = E \frac{\epsilon_x + \nu \epsilon_y}{1 - \nu^2}$$

$$\sigma_y = E \frac{\epsilon_y + \nu \epsilon_x}{1 - \nu^2}$$

.....(5.4)

where

$\epsilon_x, \epsilon_y$  = strain in directions x, y, and z

E = Modulus of elasticity

$\sigma_x, \sigma_y$  = stress in directions x, y and z

$\nu$  = Poisson's ratio

## 5.6 Determination of strain and stress from X-ray diffraction (XRD) data

A short synopsis of diffraction based calculation of strain in specimens will now be given. For diffraction based stress determination we use Bragg's law. When a monochromatic X-ray is incident on a solid material, it will be scattered at specific angles by the atoms composing the material. The wavelength of the radiation should be comparable or less than the inter-atomic spacing to produce a diffraction pattern. This scattering generates a path difference between the incident and scattered beam. For constructive interference the two beams will be in phase if the path difference is equal to an integral number of wavelengths. The path difference, as shown in Figure 5.3, is given by  $2h=2d \sin\theta$ .

---

<sup>1</sup> Reynolds et al (2003)

<sup>2</sup> James, MN et al (2004)

<sup>3</sup> James, MN et al (2004)

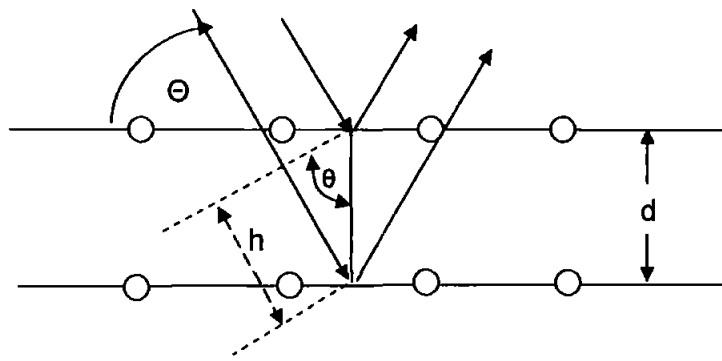


Figure 5.3: Determination of the interplanar spacing.

Braggs law is given by

$$n\lambda = 2d\sin\theta \quad \dots(5.5)$$

where

$n$  = order of reflection (  $n=1,2,3,\dots$  )

$\lambda$  = the wavelength of the X-ray or neutron beam

$d$  = the separation of the diffracting crystal planes

$\theta$  = the Bragg diffraction angle

The scattering angle measured in diffraction techniques will be twice the Bragg angle. The assumption made in deriving the Bragg equation is that the incident angle equals the angle of reflection. For a perfect unstressed single crystal, the lattice spacing between atoms is constant at a given temperature. The diffraction peaks in synchrotron X-ray radiation will be based on several crystallites and, therefore,  $d$ -values calculated will resemble mean values over all the crystallites yielding macroscopic stress levels.

In the absence of applied and residual stresses inside a specimen, the lattice space for a given plane family will be the same regardless of individual orientations. When the specimen is under stress, the lattice spacing will be different in relation to the orientations of planes. By measuring the change of lattice spacing, from the displacement of the diffraction peak, the elastic strain can be derived. The lattice is therefore used as an internal strain gauge.



Residual stresses change the spacing of the non-strained lattice and the lattice strains can therefore be evaluated from angular shifts of the diffraction lines. The shift in the peak will move to lower values for lattice planes in tension and, as a result, the planes in compression due to Poisson's effect will shift peaks to higher angle values.

The strain measured from the shift in the diffraction peak position is the elastic strain corresponding to the direction of the scattering vector that is normal to the diffracted planes and thus is directed along the line that bisects the incident and diffracted beam<sup>1</sup>.

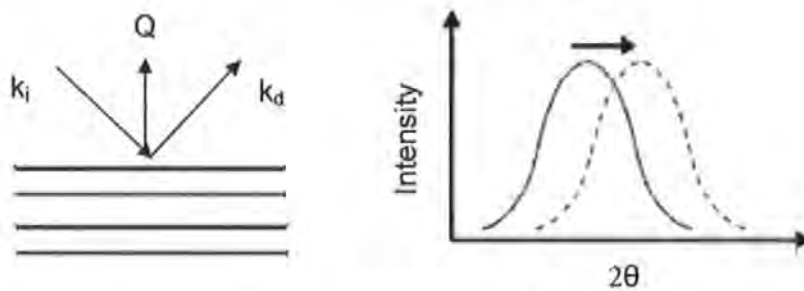


Figure 5.4: Diffracting geometry showing incident ( $k_i$ ), diffracted  $k_d$  and the direction of the scattering vector  $Q$ .

The wavelength ( $\lambda$ ) of the photons produced in XRD can be determined from <sup>2</sup>:

$$E = \frac{hc}{\lambda}$$

$$\lambda(\text{\AA}) = \frac{12.389}{E(\text{keV})} \quad \dots(5.6)$$

where

$E$  = X-ray energy

$h$  = Planck's constant

$c$  = speed of light

<sup>1</sup> Withers, PJ (2001b)

<sup>2</sup> Withers, PJ et al (2002)

## 5.7 The $\sin^2\psi$ method<sup>1,2,3</sup>

For many years the  $\sin^2\psi$  method has been applied in X-ray diffraction analysis. This is an excellent technique to determine residual stresses in a sample when residual strain measurement can be made in three directions simultaneously at a position in the sample. One advantage of the  $\sin^2\psi$  method is that the reference parameter ( $d_0$ ) is not required. This method is especially used for heat treatable alloys where a variation in  $d_0$  values is expected across the measuring length of the sample. The derivation of the equation used in this method will now be discussed.

Figure 5.5 shows the defined angular arrangement used to determine the stress in a specimen. The principal stresses are taken parallel to the x, y and z direction as indicated in Figure 5.5.

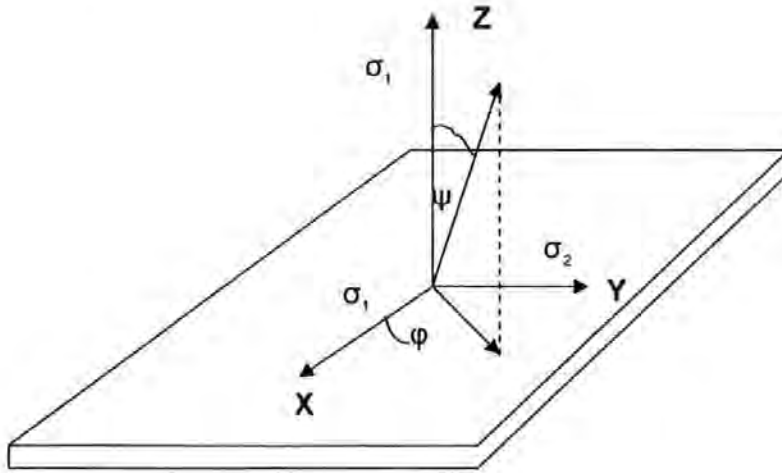


Figure 5.5: Angular arrangement to determine the stress component in the  $\psi$  direction.

The direction cosines are given as

$$\begin{aligned} \alpha_1 &= \sin \psi \cos \phi \\ \alpha_2 &= \sin \psi \sin \phi \\ \alpha_3 &= \cos \psi = \sqrt{1 - \sin^2 \psi} \end{aligned} \quad \dots(5.7)$$

Since the material is considered to be isotropic the assumption is made that the material is deformed into an ellipsoid. This yields

<sup>1</sup> Cullity, BD (1967)

<sup>2</sup> Kaelble, EF (1967)

<sup>3</sup> Klug, HP and Alexander, LE (1974)

$$\frac{X^2}{\sigma_1^2} + \frac{Y^2}{\sigma_1^2} + \frac{Z^2}{\sigma_1^2} = 1 \quad \dots(5.8)$$

Any point on the surface of the ellipsoid represents the components of a normal stress given by

$$\sigma_n = \sigma_1 \alpha_1^2 + \sigma_2 \alpha_2^2 + \sigma_3 \alpha_3^2 \quad \dots(5.9)$$

Hence the stress in a given direction  $\psi$  is given by

$$\sigma_\psi = \sigma_1 (\sin \psi \cos \varphi)^2 + \sigma_2 (\sin \psi \sin \varphi)^2 + \sigma_3 \cos^2 \psi \quad \dots(5.10)$$

When  $\psi = 90^\circ$  the above equation simplifies to

$$\sigma_\varphi = \sigma_1 \cos^2 \varphi + \sigma_2 \sin^2 \varphi \quad \dots(5.11)$$

The strain in the  $\psi$  direction is given by

$$\epsilon_\psi = \epsilon_1 (\sin \psi \cos \varphi)^2 + \epsilon_2 (\sin \psi \sin \varphi)^2 + \epsilon_3 \cos^2 \psi \quad \dots(5.12)$$

For thin plates the normal stress will be zero if the penetration depth is small and one can therefore assume that  $\sigma_3 = 0$ . For the biaxial stress state (discussed in section 5.5), the above equations then simplify to

$$\epsilon_\psi = \frac{1+\nu}{E} (\sigma_1 \cos^2 \varphi + \sigma_2 \sin^2 \varphi) \sin^2 \psi + \epsilon_3 \quad \dots(5.13)$$

Substituting equation (10) in (8)

yields

$$\sigma_\varphi = (\epsilon_\psi - \epsilon_3) \frac{E}{(1+\nu) \sin^2 \psi} \quad \dots(5.14)$$

The quantity  $(\epsilon_\psi - \epsilon_3)$  is determined by measuring the  $d$  spacing of a specific plane when oriented perpendicular to the  $\psi$  direction and approximately normal to  $Z$ . Thus

$$\epsilon_\psi - \epsilon_3 = \frac{d_\psi - d_u}{d_u} - \frac{d_z - d_u}{d_u} = \frac{d_\psi - d_z}{d_u} \quad \dots(5.15)$$

where

$d_u$  = unstressed spacing.

Since the measurement of  $d_u$  is quite difficult,  $d_u$  is set equal to an approximated value  $d_z$ .

Thus using Bragg's law equation 5.15 changes to

$$\epsilon = \frac{d - d_0}{d_0} = -\cot\theta(\theta - \theta_0) = 1 - \frac{\sin\theta_0}{\sin\theta} \quad \dots(5.16)$$

The determination of the strain free lattice parameter will be discussed in section 5.10. Combining equations 5.14 and 5.15 yields

$$d_\psi = \frac{d_z(1+\nu)}{E}(\sigma_\psi \sin^2 \psi) + d_z \quad \dots(5.17)$$

Equation 5.17 predicts a linear relationship between  $\sin^2\psi$  and  $d_\psi$ . The slope of this graph will be related to the in plane stress  $\sigma_\psi$  and the intercept will be equal to the out of plane lattice spacing  $d_0$ . Any deviation from this linear relationship can be due to stress gradients, texture, anisotropy or insufficient counting statistics<sup>1</sup>.

## 5.8 Elastic anisotropy

Different lattice reflections exhibit a range of elastic responses to a macroscopic stress field due to the elastic anisotropy of individual crystallites in a material. In the elastic regime these effects are linear and hence most diffraction planes can be used to determine the macrostress. In the plastic regime certain diffraction peaks introduce greater anisotropy between the behaviours of different crystallographic lattice planes<sup>2</sup>. Figure 5.6 depicts this behaviour.

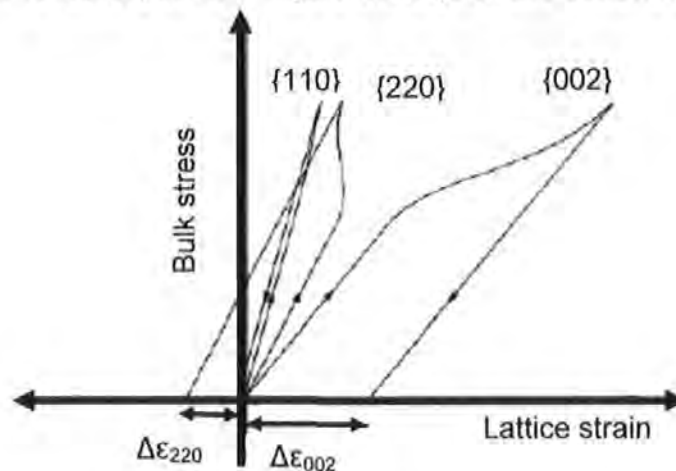


Figure 5.6: Behaviour of different lattice planes under loading perpendicular to the planes for elastic anisotropic materials such as steel<sup>3</sup>.

<sup>1</sup> Hauk, V (1997)

<sup>2</sup> ISO standard (2001), Claussen et al (1998), Pang et al (1998)

<sup>3</sup> Dye, D et al (2001)

The different reflection planes react differently to loading applied to the material and may show different behaviour from the response of the bulk of the material as a result of anisotropy in the elastic and plastic behaviour of the material<sup>1</sup>. The (311) reflection was used in this study due to its relative insensitivity to small intergranular strain development and will therefore be a representative of the bulk macroscopic stress of the material<sup>1,2</sup>. It is assumed that the atomic spacing between (311) planes in aluminium will be equal regardless of the orientation of the lattice planes relative to the sample surface in a stress-free specimen. The lattice spacing will be expanded or compressed elastically (by an amount dependent upon the orientation of the lattice planes) by any stress present in the specimen.

Aluminium is essentially elastically isotropic and the diffraction constants can therefore be described in terms of the bulk modulus without introducing a significant error. The Young's modulus of Al 5083-H321 was taken in this work as 69 GPa for the (311) reflection and Poisson's ratio was 0.3<sup>2</sup>.

## 5.9 Strain measurement using synchrotron X-ray diffraction methods at beamline ID31

### 5.9.1 The production and advantages of synchrotron X-ray diffraction

All experiments in this project were performed at the beamline ID31 of the European Synchrotron Radiation Facility (ESRF), Grenoble, France during beam-time allocated under experiment ME 992. The following is a brief introduction of the ID31 beamline.

The advantages of synchrotron X-ray radiation include<sup>3,4</sup>

- (i) high X-ray energies that provides wavelengths less than 0.1 Å ;
- (ii) low absorption edges and high attenuation lengths to measure depths greater than the conventional X-ray sources;

---

<sup>1</sup> Pang, JWL et al (1998)

<sup>2</sup> Clausen, B et al (1998)

<sup>3</sup> Hutchings, MT et al (2005)

<sup>4</sup> Withers, PJ (2001b)

- (iii) high intensity and collimation of beams that allow rapid data acquisition rates in the order of seconds and milliseconds; and
- (iv) low level of angular divergence and narrow energy bandwidths that lead to peak widths that are symmetric and narrow ( $\sim 0.01^\circ$  full width half maximum)

Synchrotron X-ray radiation is produced in the direction of motion during magnetically induced bending of relativistic electrons by dipole magnets. At the European Synchrotron Radiation Facility (ESRF) in Grenoble the electron energy reaches about 6 GeV before it is circulated in vacuum in a circle guide tube of 884 m circumference. Photons are emitted tangentially to the beam at points where bending magnets or insertion devices, undulators, are placed and are used by the experimental stations or beam lines. This phenomenon is shown in Figure 5.7.

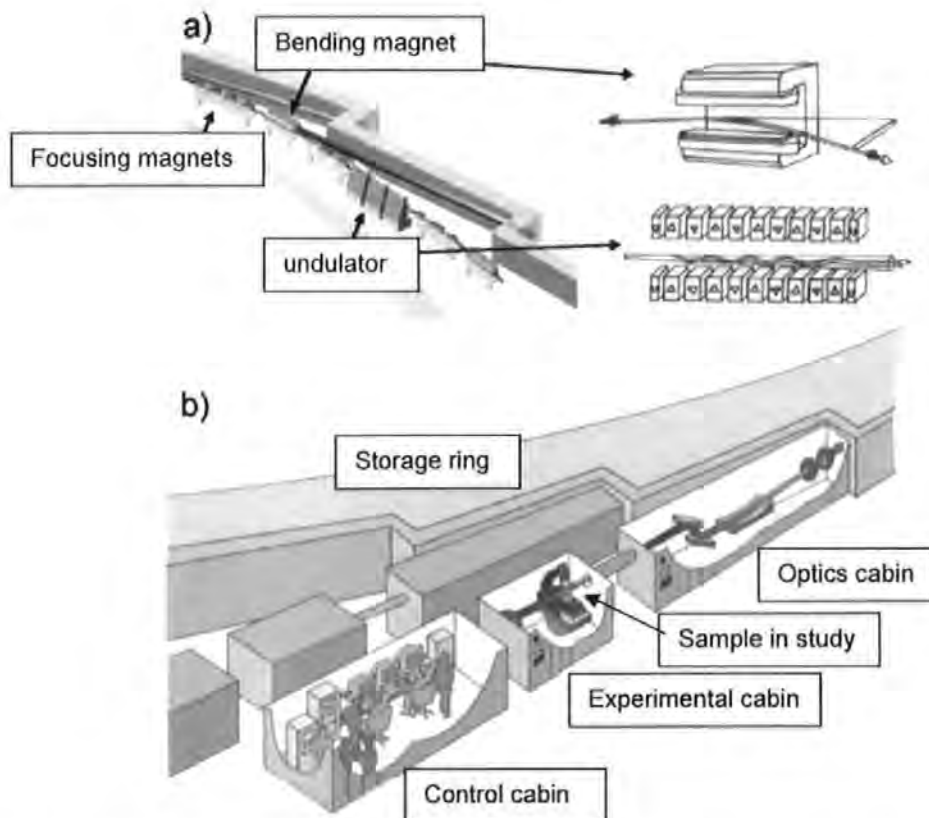


Figure 5.7: (a) Movement of the beam through bending magnets and undulators. (b) Example of a beam line station.

The peak intensities, peak widths at half maximum (FWHM) and the scattering angle are measured during synchrotron X-ray investigation. In this thesis the scattering angle was used to determine longitudinal and transverse residual stresses. The FWHM values will also be related to the heat input during FSW and will be discussed in section 5.17.

### 5.9.2 Setup on beam line ID31

Very intense narrow polychromatic beams of highly collimated and penetrating energetic X-ray photons of wavelengths less than 0.1 Å may be produced. This enables strain measurements to be made that are characterized by low scattering angles. A single Si(111) crystal is usually used as a monochromator from which a desired wavelength is obtained by altering the diffraction angle. Synchrotron X-ray strain scanning techniques were used in this project because of the high spatial resolution due to intense beams of 10 μm-1 μm<sup>1</sup>. The depth to which these measurements can be made depends on the X-ray energy and absorption characteristics of the materials.

Specifications for the beamline's operational range are<sup>1</sup>:

- (i) an energy range of 5 - 60 keV;
- (ii) very high angular resolution with an optimal instrumental contribution to the peak width of 0.006° (the actual peak width is normally greater and is determined by the nature of the sample);
- (iii) an energy resolution around 1 eV at 10 keV (i.e.  $\Delta E/E < 10^{-4}$ ); and
- (iv) beam definition between 10 μm to 1 mm.

The beamline was operated at 60 keV, corresponding to a fixed wavelength of 0.2065 Å, which generates peaks up to a limit of 1 Å in d-spacings. The incident and receiving slits were opened to 1 mm x 1.3 mm with the diffraction angle  $2\theta = 9.68^\circ$ .

The horizontally collimated beam has a flux large enough to ensure that data can be collected more rapidly with excellent statistical quality of peak shape by having more photons available on the specimen. The attenuation of the beam in a material decreases the intensity of the peaks and may limit the scope of the

---

<sup>1</sup> [http://www.esrf.fr/exp\\_facilities](http://www.esrf.fr/exp_facilities)

experimental investigation. Data acquisition and storage are carried out by dedicated computers and electronic systems. The raw data comprise a diffraction peak in the form of photon counts over one specific angle range in specified small steps. To obtain the best estimate of the diffraction peak centre, a standard peak profile fitting routine based on either Gaussian, Lorentzian or Pseudo-Voigtian distribution is used to fit the measured diffraction profile to rectify the problem of peak asymmetry due to geometric, hardware and other effects<sup>1,2,3,4</sup>. The symmetrical Gaussian function is often suitable for the elastic regime and the Lorentzian- shaped curve, a curve that contain tail sections, is suitable for the plastic regime. The peak uncertainties were approximately  $10 \times 10^{-6}$  strain and much less than the VAMAS Technology Trends assessment document of  $100 \times 10^{-6}$  strain<sup>5</sup>.

### 5.9.3 The gauge volume and slit system

The incident slit is situated on a rectangular slit holder between the monochromator and the sample and defines the incident synchrotron beam on the sample. The diffracted beam slit is placed between the sample and the detector on a slit holder mounted on the bracket of the detector. The area in the detector where synchrotron X-rays enter is defined by the aperture of the detected beam slit. An analyser is usually mounted before the detector to select only near-parallel radiation and to eliminate surface aberration effects.

The gauge volume from which the synchrotron beam is diffracted, is defined by a series of slit systems as depicted in Figure 5.8.

---

<sup>1</sup> Otto, JW (1997)

<sup>2</sup> Webster, PJ and Kang,WP( 2002)

<sup>3</sup> Wilson, AJC (1973)

<sup>4</sup> Hutchings, MT et al (2005)

<sup>5</sup> Webster, GA (2001)



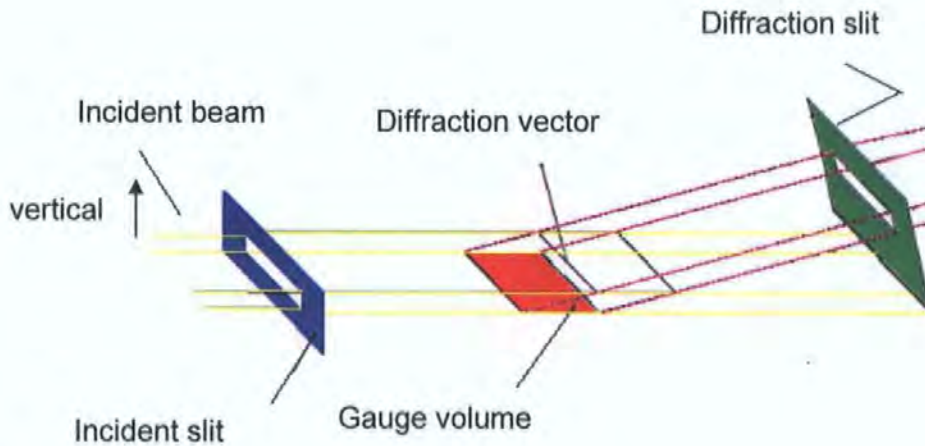


Figure 5.8: Slit system and gauge volume.

The vertical gap of the incident slit generally can be from 0.05 mm to 1 mm. The vertical gap of the diffracted beam slit is usually the same as that of the incident slit. The corresponding horizontal gaps can be up to 10 mm. At low angles ( $\tan 2\theta \approx \tan \theta$ ) and the gauge volume length perpendicular to the scattering vector is given by<sup>1</sup>

$$(l_i + l_d) / 2\theta \quad (5.18)$$

where

$\theta$  = Bragg diffraction angle

$l_i$  = incident aperture width

$l_d$  = width of the diffracted beam aperture

Systematic shifts in the peak position can be obtained if the gauge volume leaves the sample because there will be a difference between the angle implied by the diffractometer and the actual angle measured from the centre of gravity position in the partially filled gauge volume as indicated by Figure 5.9<sup>2</sup>. Since the scans were performed along the centre-line of the plate thickness, this was not a problem in this investigation.

<sup>1</sup> Withers, PJ (2000b)

<sup>2</sup> Owen, RA (2002)

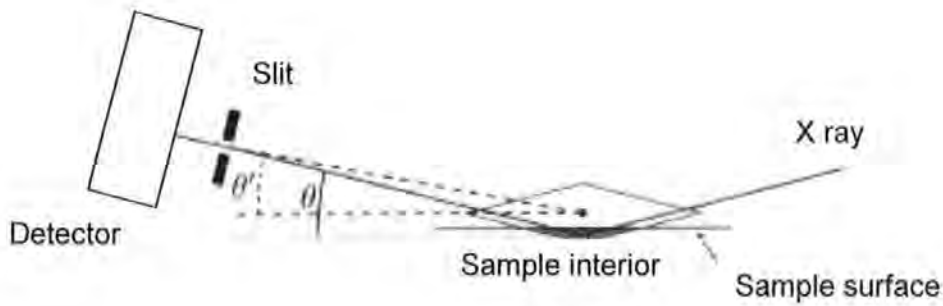


Figure 5.9: The influence of an incomplete gauge volume on the shift in the diffraction angle<sup>1</sup>.

#### 5.9.4 Determining the position of strain measurement

The point where the axis of the sample table crosses the centre axis of the incident beam was found using an accurate and rigidly mounted optical alignment system that consists of a theodolite and a level. This allowed positioning of the sample relative to this reference point with a precision of  $\pm 0.1$  mm. The incident and diffraction slit systems were thereafter accurately positioned to define the position of the gauge volume at the reference point. An intensity scan was used to determine the edges of the plate. There was a slight misalignment in the FSW across the weld region. The advancing and retreating side of the FS welds were therefore scanned separately and 4 to 6 data points were scanned at the same positions to match the points of overlap.

#### 5.10 Strain-free lattice data

Once the diffraction peak positions are found for various points in a sample the strain distribution can be derived from equation 5.16. The strain-free reference diffraction angle  $\theta_0$  is found from a strain-free sample of the same kind of material which allows calculation of  $d_0$  the lattice strain-free parameter. The lattice parameter is sensitive to a number of effects namely macroscopic load, instrumental aberrations, chemical composition and temperature. Various methods to determine  $d_0$  will be discussed in the next paragraph.

<sup>1</sup> Owen, RA (2002)

A variety of methods may be used to obtain strain-free lattice data. If the  $d_0$  value does not vary across the sample due to texture or microstructural effects then measurements from a section in a "strain free" region may be used. Another method involves taking a stress-free powder or an annealed sample of the same material in the same microstructural conditions of the specimens of interest. Methods such as the following may be used: small coupons in which the macroscopic strain is relaxed, or the application of strain balance and boundary conditions, or the  $\sin^2\psi$  method (which requires no d-zero values). Obtaining the strain-free lattice spacing is not trivial, particularly for a welded joint in a cold-rolled alloy, where the thermo-mechanical treatment causes significant micro-structural variation between weld metal and parent plate and where a gradient in  $d_0$  exists across the TMAZ and HAZ<sup>1</sup>.

To ascertain the  $d_0$  variation, the tooth-comb technique was used in this thesis<sup>2</sup>. Teeth approximately 2 x 2 mm in section and 10 mm long were electro-discharge machined (EDM) into the edges of specimens cut both transverse to the FS weld through the complete TMAZ and HAZ zone to the plate edge, and in the direction parallel with the weld. Figure 5.10 illustrates an EDM sample cut from FS weld specimen 4. Note that the tooth comb section has been completely removed from the FSW specimen and is held in place for synchrotron measurement by double sided tape.

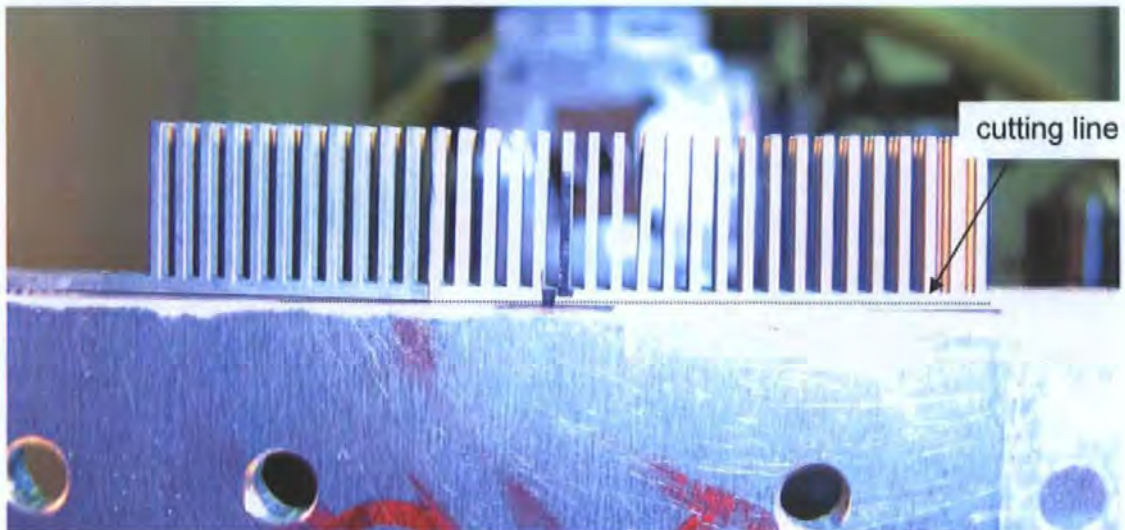


Figure 5.10: Illustration of EDM  $d_0$  sample consisting of several rows of 32 teeth machined transverse to the weld and extending across the plate thickness.

<sup>1</sup> Fitzpatrick, ME and Lodini, A (2003)

<sup>2</sup> Hughes, DJ et al (2004)

Results by Hughes<sup>2</sup> showed that no significant variation in strain could be determined between three combs at different positions from the crown of the weld in 5383-H321 aluminium alloys. Measurements in this thesis were therefore only taken from the centre comb of the EDM sample. It was assumed that any stresses would be largely relaxed close to the ends of the teeth and thus the position represents the strain-free reference lattice condition<sup>1</sup>. The texturing and microstructural variation in the parent plate microstructure is therefore taken into account. The recrystallisation of grains in the weld nugget and TMAZ implies that  $d_0$  in this region will have the same values both along the weld and transverse to it<sup>2</sup>.

Measurements of the lattice strain as a function of position along the teeth are shown in Figure 5.11 for one of the FSW specimens (welds 4). Data are shown for teeth at positions along the length of the plate, -12.5 mm to 12.5 mm associated with the nugget, -30 mm to -35.5 mm and 30 mm to 40 mm well away from the nugget. The distance 0 mm represents the centre position of the weld. This data shows that a small variation of interplanar distances exists at points far away from the weld and a larger scatter exists in the fine-grained recrystallised weld nugget region. This is believed to reflect texture effects and genuine grain-to-grain variation in local stresses arising from the cold rolling treatment inherent in the H321 condition<sup>3</sup>.

Region a, shown in Figure 5.11, corresponds to distances on the advancing side of the weld and show a region of interplanar distances much lower than those distances found in other regions. This could imply that two d-zero values could be present one in the parent plate and one in the weld region. There was an overlap (region b) for the same regions away from the centre of the weld on the retreating side with the weld region. Unfortunately, a longer length of measurements will be required to determine accurate d-zero values using the EDM method.

It would be preferable to have measurements of  $d_0$  EDM samples for each weld. However, in the allocated experimental beam-time this was not possible.

---

<sup>1</sup> James, MN et al (2004)

<sup>2</sup> Hughes, DJ et al (2004)

<sup>3</sup> James, MN et al (2004)

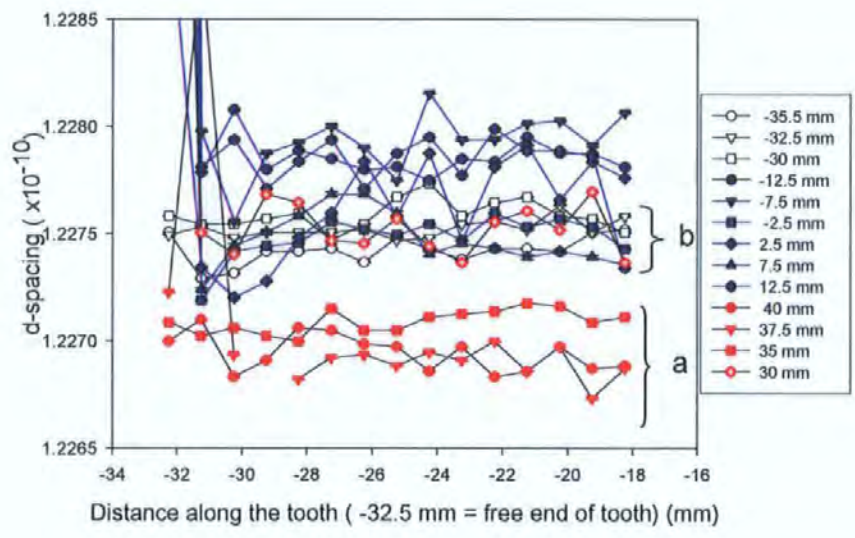


Figure 5.11: Measurements of  $2\theta$  as a function of position along teeth for a toothcomb specimen parallel to the weld and cut from the parent plate (weld 4: 185 mm/min, 870 rpm).

As expected for a non-precipitation-hardening alloy, very little variation has been found by the comb method, of the order of  $4 \times 10^{-4} \text{ \AA}$ , (for weld 4 and weld 8) and therefore a global  $d_0$  method was used. The relative strain for each weld is shown in Figure 5.12. This shows that the variation of strain determined by this method is about 50 micro strain.

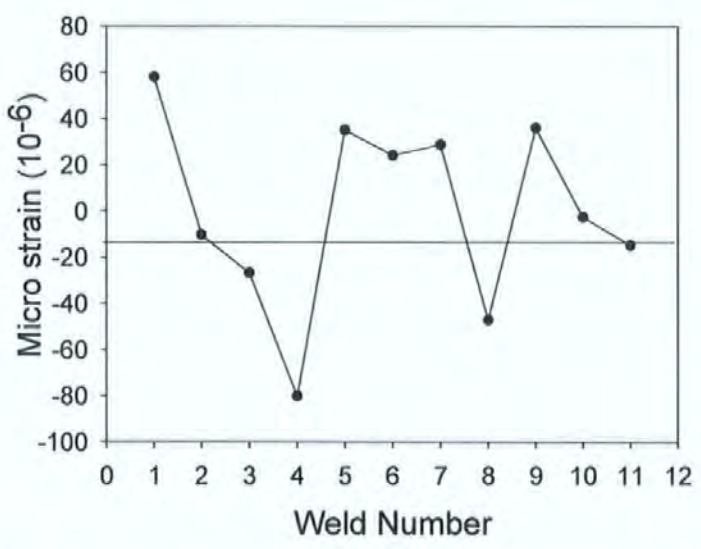


Figure 5.12: The variation of the unstrained lattice parameter expressed as strain between welds.

## 5.11 Longitudinal and transverse strain and stress in FSW

It is assumed in this work that the thermal gradients created during welding leads to thermal misfits where different regions of the welds will cool at different rates leading to the creation of residual stresses in the FSW.

In order to determine the residual stress in the FSW the longitudinal and transverse residual strain were measured at a depth of approximately 3 mm into the weld in the direction transverse to the weld over the central region of the 750 mm long weld. This region is most likely to correspond with pseudo steady-state conditions, and hence it should be possible to correlate the data with welding parameters. FEA modelling results by Chen and Kovacevic<sup>1</sup> show that the longitudinal and lateral stress contours had the predicted maximum stress located in the middle of their 240 × 50 × 6 mm 6061-T6 Al alloy plates.

A single line at mid-thickness was scanned in the longitudinal and transverse direction to the weld. An example of a sample is shown in Figure 5.13. These scans were compared to the process parameters and are illustrated in section 5.12. The point spacing was at 1 mm intervals to obtain a smooth strain profile up to distances of 60 mm towards the retreating and advancing side, as measured from the weld centre-line.

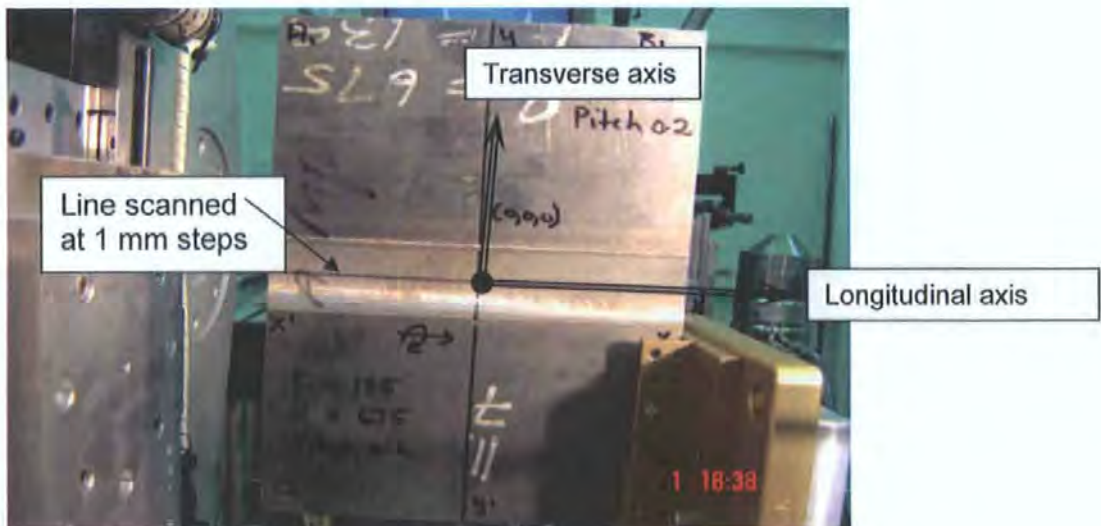


Figure 5.13: Strain measurements sample for weld 11.

<sup>1</sup>Chen, C and Kovacevic, R (2003)

However, it is possible that the stress state may be significantly different at the starts and ends of the plates, where the conditions are not steady-state. In all cases, the basic assumptions regarding the stress and strain distribution in the plates are that their principal directions are determined by the symmetry of the plates, with  $\sigma_x$  and  $\sigma_y$  being perpendicular and parallel to the welding direction respectively, and that  $\sigma_z$  corresponds to the plate normal (through-thickness direction). It is also assumed that the stress state is essentially two dimensional with a negligible through-thickness residual stress and that the plate has only moderate texture. This is probably a reasonable assumption because in the present work, the maximum temperatures during FSW are much lower than in fusion welding, and the plate thickness of 6 mm is much less than the weld width of 25 mm.

Figure 5.14 shows the variation of the longitudinal residual stress at distances from -60mm to +60 mm from the weld centre-line. The results show that the largest residual longitudinal stress is in the weld direction and that this is in tensile within 25 to 19 mm from the centre of the weld and is balanced by compressive residual stresses in the parent plate. This phenomenon agrees with the descriptions of residual stresses given by Masubuchi<sup>1</sup> and Easterling<sup>2</sup> namely that the weld region is forced into tension and is balanced by compressive residual stresses in the parent material.

The features in the longitudinal residual stress data correlate with known thermo-mechanical influences occurring during the FSW process. Small peaks are seen within a range of 5 mm from the centre of the weld towards the advancing and retreating side which can be related to the plastic flow induced by the rotation of the FSW tool pin (with a diameter of 10 mm). The longitudinal residual stress rises to maximal values close to the diameter of the tool shoulder of 25.4 mm. These effects can therefore be related to the thermo-mechanical effects induced by the shoulder on the material in the TMAZ. The longitudinal residual stress finally decreases over the rest of the specimen and reaches a minimum value at about 40 mm on either side of the weld centre-line. The peak longitudinal residual stresses vary in the range 66 to 100 MPa for the selected input FSW parameters.

---

<sup>1</sup> Masubuchi, K (1980)

<sup>2</sup> Easterling, K (1992)

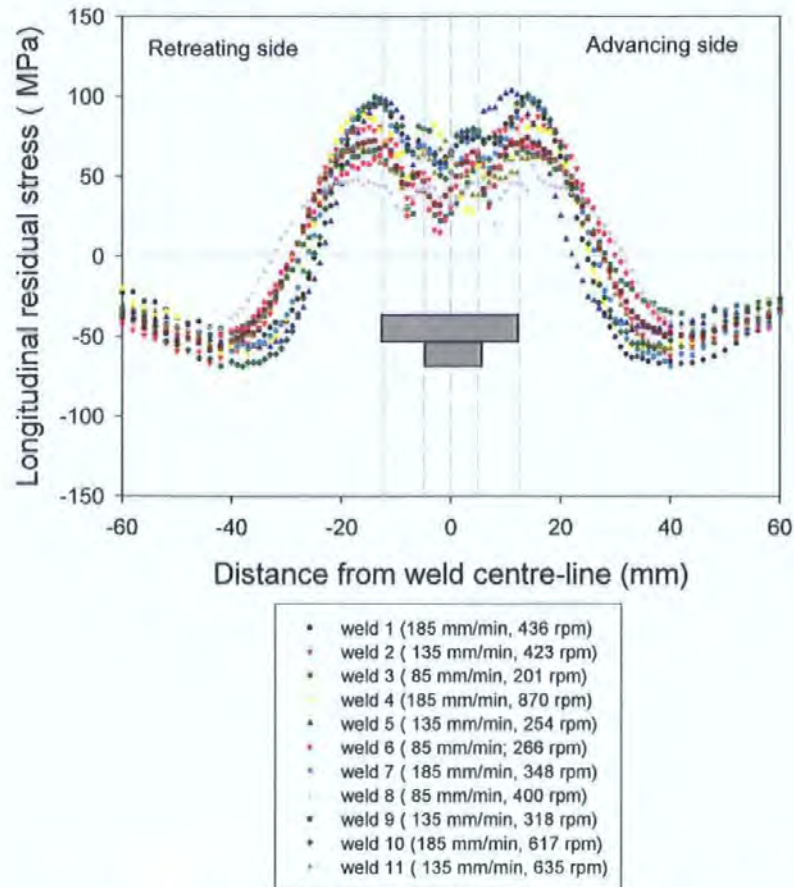


Figure 5.14: The residual longitudinal stress profile at the mid section across the weld .

The transverse residual stress data is shown in Figure 5.15. The residual stress in the transverse direction remains tensile at distances from -40 mm to +40 mm from the weld centre-line while the longitudinal residual stress becomes compressive beyond distances of 20 mm and -20 mm from the weld centre-line. The transverse residual stress varies in the range 38-54 MPa and is approximately 30% - 76% lower than the longitudinal residual stress. This can be compared to fusion welding, where the residual stress of the welded plate is usually close to the yield strength of the parent plate<sup>1</sup>. The transverse residual stress also shows greater scatter in results than the longitudinal residual stress. The longitudinal tensile and compressive stresses are in approximate balance.

Maximum values in the residual stresses in both the longitudinal and the transverse directions are in the proximity of the shoulder diameter, also been

<sup>1</sup> Mishra, RA and Ma, ZA (2005)



reported by Chen and Kovacevic<sup>1</sup>. This is believed to be caused by the high temperature and high shear force at the shoulder periphery edge in this region. The transverse stress data can therefore be correlated with known thermomechanical influences during the FSW process. The transverse and longitudinal residual stresses were slightly larger on the advancing side of the welds. This is expected since larger temperatures are often found on the advancing side of FSW<sup>2,3</sup>.

It is quite evident that the peak longitudinal and transverse stresses as well as the widths of the residual stress profiles vary with rotational speed and feed rate. The relationship between the peak stresses and widths of the residual stress profiles with the input and process parameters will be investigated in sections 5.12 to 5.14.

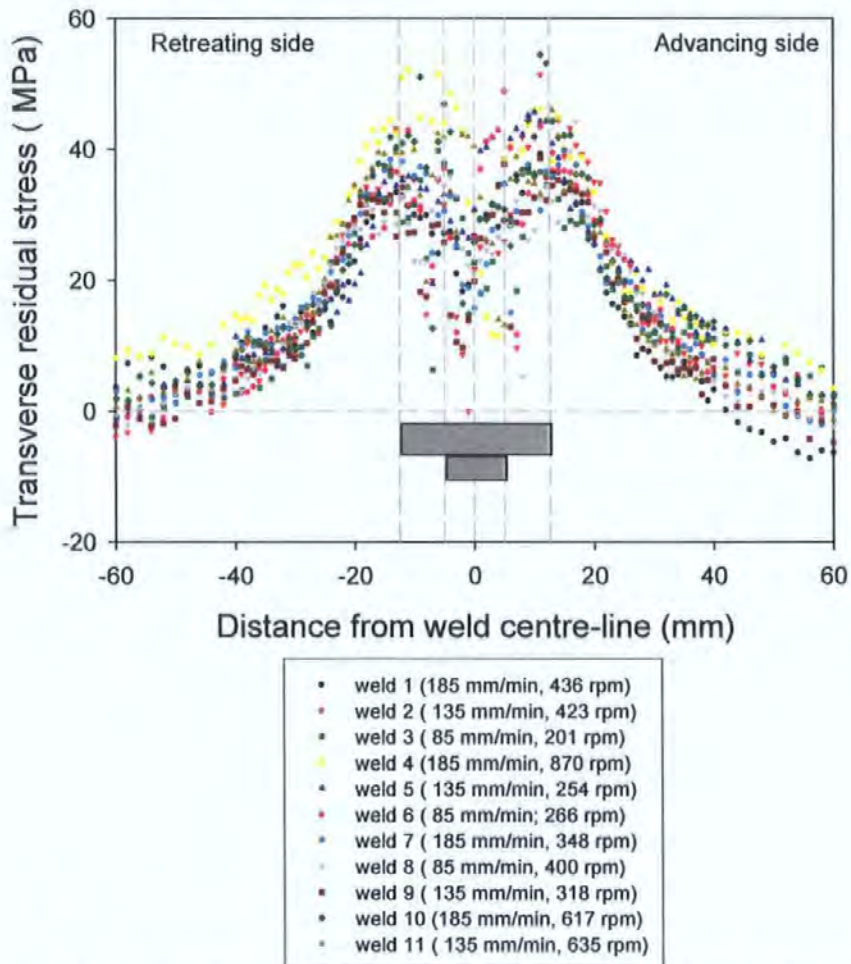


Figure 5.15: The residual transverse stress profile at the mid section across the weld .

<sup>1</sup> Chen, C and Kovacevic, R (2003)

<sup>2</sup> Arbegast and Hartley (1998)

<sup>3</sup> Sutton, MA et al (2002a)

## 5.12 Variation of residual stress data with respect to process parameters in FSW

This section discusses the variation of the residual stress profiles with FS weld input parameters. These results are given as an example and introduction to section 5.15 where surface plots are shown. All the data are not shown in this section because it is not always easy to see general trends from these figures. The general trends were not consistent for all the welds and surface plots were needed to summarize the data and obtain general trends. These surface plots compare the peak stresses in each profile with input and process parameters.

Figure 5.16 shows the variation of longitudinal stress with respect to the rotational speed at a constant feed rate of 135 mm/min. This feed rate was in the midrange of the data set. These plots clearly show that the width between the longitudinal stress peak profile increases with increased rotational speed and increasing pitch. The maximum longitudinal stress also decreases with increasing tool speed except for 318 rpm (weld 9). Table 5.2 summarizes the process parameters for these welds.

Weld	Feed	RPM	Pitch	$F_z$	Torque	Temp	Q in	Long max	Frictional Power
	(mm/min)	(rev/min)	(mm/rev)	kN	Nm	°C	J/mm	MPa	J/s
5	135	254	0.51	24.3	70.21	431	747	103	1868
9	135	318	0.42	41.4	68.69	450	915	74	2287
2	135	423	0.32	40.90	55.87	512	990	88	2475
11	135	635	0.20	36.43	33.64	507	895	68	2237

Table 5.2: FSW parameter data for welds at 135 mm/min.

The data in Table 5.2 do not provide any explanation why weld 9 does not fit in the general trend observed. For example, if heat input was the only parameter that influenced the magnitude of the tensile longitudinal stresses, then the heat input for weld 9 (747 J/mm) should have been greater than weld 2 (990 J/mm), to indicate that increasing heat input produces a decrease in longitudinal stresses.

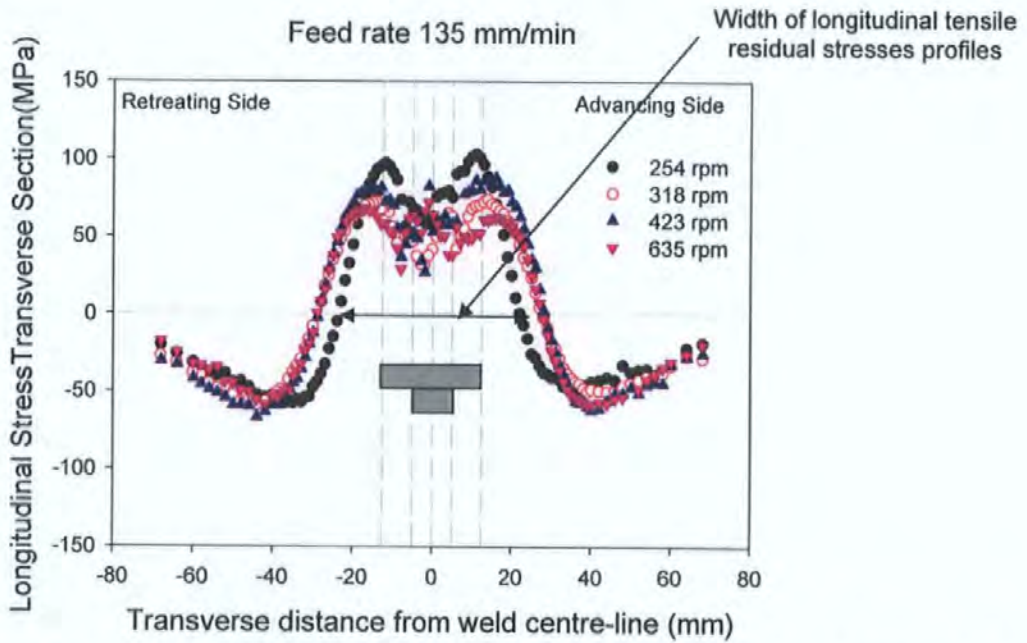


Figure 5.16: Longitudinal stress for a feed rate of 135 mm/min as a function of tool rotational speed.

Figure 5.17 shows the variation of transverse stress with respect to the rotational speed at a constant feed rate of 135 mm/min. No consistent trend can be obtained for the peak maximum positions or the widths in the peak profiles from Figure 5.16. This is further analyzed in section 5.13 and 5.14.

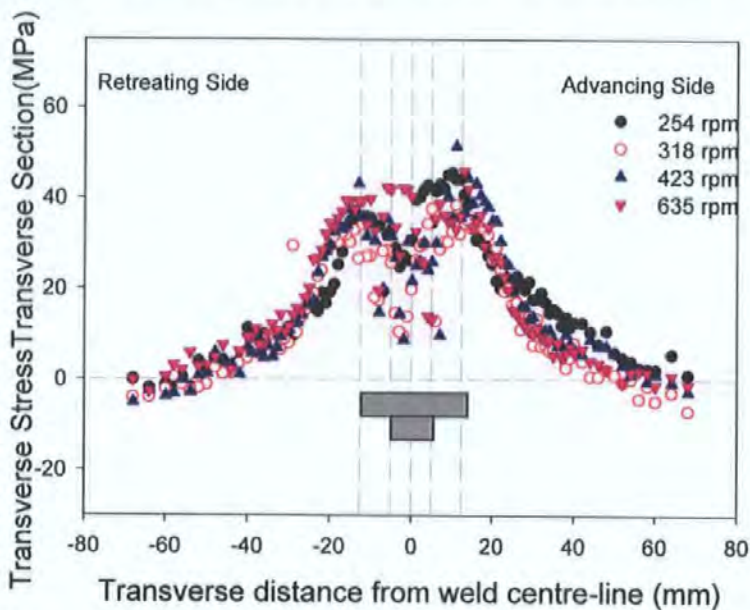


Figure 5.17: Transverse stress for a feed rate of 135 mm/min as a function of tool rotational speed.

Figure 5.18 shows the longitudinal residual stress distribution across the as-welded transverse section (3mm from shoulder side of the weld) of welds made with a constant pitch of 0.2 mm/rev, but at different combinations of tool speed and feed. The peak magnitude of the residual stress increases significantly at the same pitch as the feed rate and rotational speed increases simultaneously. The tensile peaks become less rounded and the pin peak becomes more emphasized. Associated with this is a decrease in spacing of the peak profiles in the stress distribution. This data implies that more deformation is put into the weld zone as tool speed and feed increase at a constant pitch, and that the spread of heat energy outside the weld zone is less.

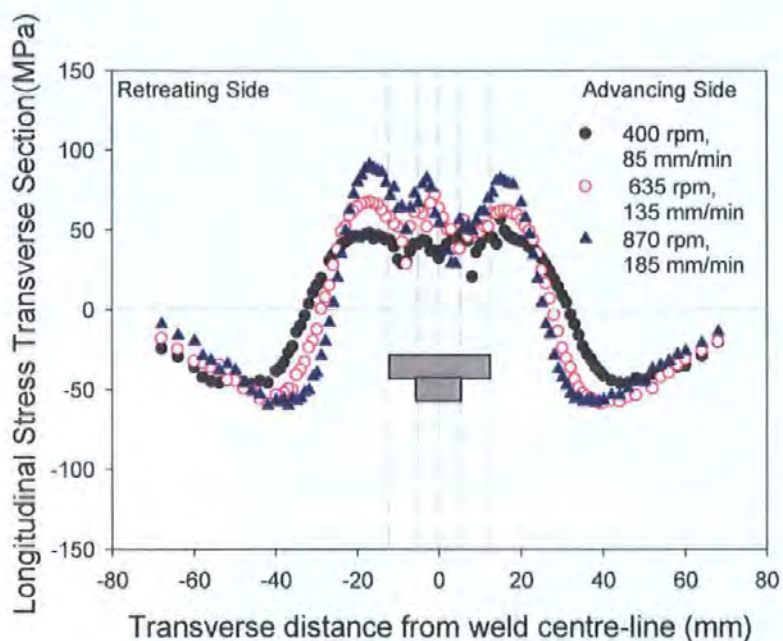


Figure 5.18: Longitudinal stress at a pitch of 0.2.

The force in the direction of welding increased from 2303 N to 4051 N at pitch 0.2. This correlates with the observation that the maximum longitudinal stress increases at pitch 0.2 for increasing tool speeds and feed rates. At a constant pitch of 0.2, as the feed rate and rotational speed increases, the heat input to the welds decreases (Figure 3.10) and hence a larger force will be exerted on the tool.

The transverse stresses in Figure 5.19 show a similar trend but the variation is not as large as in the longitudinal direction. The widths of the peaks decrease with increasing feed rate and rotational speed. This again relates to an increase in heat input.

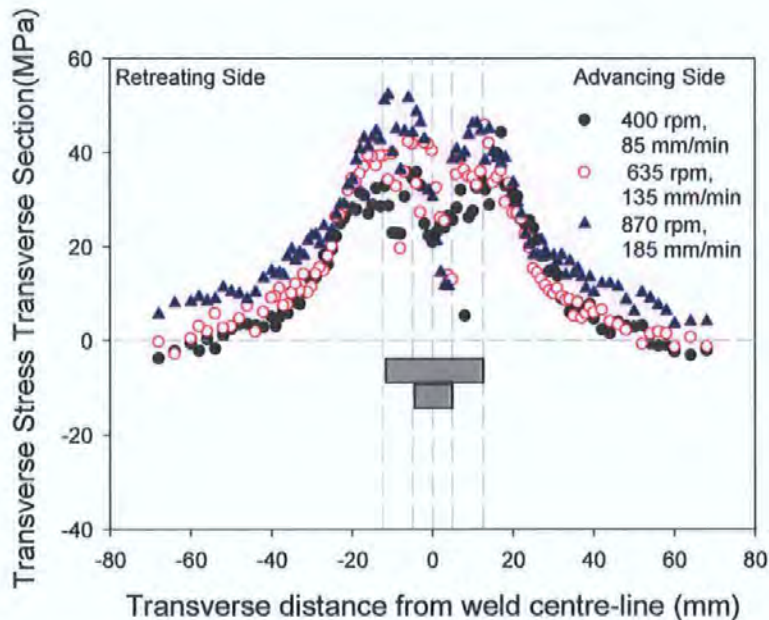


Figure 5.19: Transverse stress at a pitch of 0.2.

A comparison between residual stress contour plots and the contour plots in Chapters 3 and 4 are now investigated. A statistical analysis is first performed to determine critical parameters that correlate with the residual stress in FSW.

### 5.13 Regression analyses

Statistical analyses were performed to relate process parameters with longitudinal and transverse residual stress and are summarized in Table 5.3. Significant process parameters are identified by calculating P-values. P-values less than 0.05 indicate process parameters whose coefficient will not be zero in the regression model. Values that have been bolded in Table 5.3 are parameters that will be statistically significant for the residual stress data.

The analyses in Table 5.3 indicate that feed rate,  $F_z$ , tool torque and  $F_x$ max are statistical significant parameters for the peak tensile longitudinal stresses since these parameters have P-values < 0.05 shown in equations (a) and (b). This is not surprising since all these process parameters vary with energy input. The rotational speed with a P-value of 0.013 is also a significant parameter for the transverse maximum stresses since the P-value is less than 0.05, but to a lesser extent than the feed rate because the coefficient for feed rate is larger than the

coefficient of rotational speed. Increasing the rotational speed in equation (e) and (a) will increase the maximum residual transverse stress and decrease the maximum longitudinal residual stresses as indicated by the coefficient of this term. The process parameters  $F_{xmax}$ ,  $F_z$ , tool torque and tool temperature have P-values that are close in magnitude and the multiple regression analysis could not indicate which of these parameters are significant for the peak transverse residual stresses and widths of the transverse residual stress profiles.

Eq.	Regression models for process parameters versus longitudinal stress data	Input parameter	P- value
(a)	Max tensile Long stress = $40 + 0.42 \text{ feed rate} - 0.03 \text{ rpm}$ $R^2=0.78$ ; Adj $R^2=0.72$	Feed rate RPM	<b>0.000816</b> 0.064672
(b)	Max tensile Long stress= $-332 - 3.6 F_z + 1.4 \text{Torque} + 0.83 \text{Temp} + 0.02 F_x$ $R^2=0.94$ ; Adj $R^2=0.90$	$F_z$ Torque Temp $F_{xmax}$	<b>0.003457</b> <b>0.003443</b> 0.011433 <b>0.001136</b>
(c)	Width of Long stress profile= $65 - 0.11 \text{ feed} + 0.01 \text{ rpm}$ $R^2=0.54$ ; Adj $R^2=0.43$	Feed rate RPM	<b>0.016566</b> 0.226278
(d)	Width of Long stress profile= $73 + 0.39 F_z - 0.16 \text{Torque} - 0.001 F_x - 0.007 \text{Temp}$ $R^2=0.95$ ; Adj $R^2=0.91$	$F_z$ Torque Temp $F_{xmax}$	0.121401 0.113974 0.990408 <b>0.000187</b>
	Regression models for process parameters versus transverse stress data	Input parameter	P- value
(e)	Max tensile trans stress = $44.18 - 0.07 \text{ feed rate} + 0.03 \text{ rpm}$ $R^2=0.56$ ; Adj $R^2=0.45$	Feed rate RPM	0.114057 <b>0.012796</b>
(f)	Max tensile trans stress= $152 + 0.67 F_z - 0.45 \text{Torque} - 0.21 \text{Temp} + 0.001 F_x$ $R^2 0.23=$ ; Adj $R^2=0.13$	$F_z$ Torque Temp $F_{xmax}$	0.420752 0.188194 0.379758 0.879383
(g)	Width of trans stress profile= $56.95 - 0.02 \text{ feed} + 0.02 \text{rpm}$ $R^2=0.23$ ; Adj $R^2=0.04$	Feed rate RPM	0.776841 0.195614
(h)	Width between trans stress profile= $-49.71 - 0.5 F_z + 0.006 \text{Torque} + 0.05 F_x + 0.002 \text{Temp}$ $R^2=0.20$ ; Adj $R^2=-0.33$	$F_z$ Torque Temp $F_{xmax}$	0.737443 0.991763 0.907438 0.766129

Table 5.3: Regression analyses of the longitudinal and transverse residual stresses. (Eq.= equation number)

### 5.14. Residual stress and heat input

The variation between the longitudinal residual stress data and the average heat input was investigated. The maximum longitudinal residual stresses are larger for less average heat input and the widths of the peak profiles increase with heat input, as shown in Figure 5.20. Hot welds have lower residual stresses, possibly because the heat is distributed over a larger volume of material and less thermal mismatch is created between the weld and the parent plate. The correlation coefficient was 0.76 and 0.69 for the peak stresses and width of the profiles respectively. The correlation coefficient between the transverse residual stress and the average heat input was 0.04 and does not give good linear models.

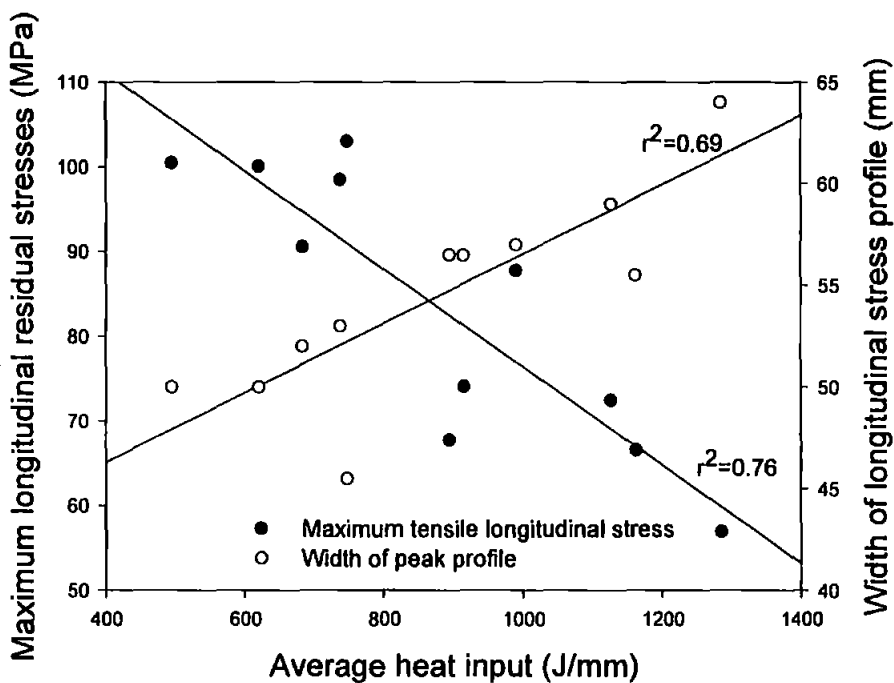


Figure 5.20: Features of residual stress profile as a function of average heat input.

### 5.15 Surface plots of transverse and longitudinal residual stresses

Three dimensional plots of the process parameters were investigated to see if models could be obtained to optimize residual stresses. The relationship of pitch with respect to residual stresses can also be investigated with these plots.

Figure 5.21 shows a comparison between the input process parameters and the maximum tensile longitudinal and transverse residual stresses. Figure 5.21 (a) illustrates that the maximum tensile longitudinal residual stress increases at a

constant pitch as the feed rate and tool speed increase. The tensile residual stress increases with increasing feed rate at constant rotational speeds. The longitudinal stresses decrease at a constant feed rate for decreasing rotational speeds. As the feed rate increases at constant rotational speeds, the longitudinal residual stresses increase. The maximum longitudinal residual stress values are obtained above 185 mm/min and less than 635 rpm. One would expect that plastic deformation that results in equiaxed grains would result in lower residual stresses measured in the nugget region. As the rotational speed increases at constant feed rates, the maximum transverse residual stresses increase. This is opposite to the longitudinal stresses. The lowest transverse stresses are obtained for rotational speeds less than 400 rpm for all feed rates.

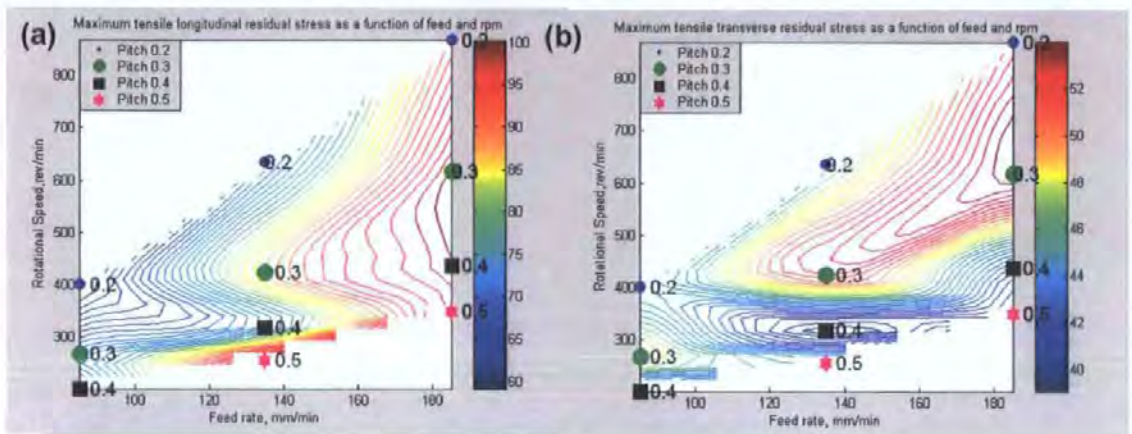


Figure 5.21: Comparison between maximum tensile residual stresses of (a) longitudinal and (b) transverse directions as a function of tool rotational speed and feed rate.

### 5.16 Residual stresses and the force footprint

It is believed that the loads applied to the tool affect the residual stresses. The forging force ( $F_z$ ) causes extra compression and expansion of the surface material. The applied torque causes the asymmetric stress distribution, since the rotational forces on the advancing side cause additional expansion compared to the retreating side leading to smaller tensile stresses on the retreating side<sup>1</sup>. There is a strong correlation between the polar areas as well as the maximum longitudinal stresses. The areas of the polar plots also decrease with increasing feed rate and tool speed, which correlates with a decrease in energy (Figure 3.10) as seen in

<sup>1</sup> Shi, Q et al (2003)



Figure 5.22. The polar plots of tool force indicate that energy input into the weld (represented by area of the plot,  $F_x$  max) steadily increases with tool feed and speed. Taken in conjunction with the mechanical property, metallographic and dynamic performance data, insight into weld processes should therefore be extracted. Similar trends were observed for pitch 0.3, 0.4 and 0.5 given in the appendix Figure 8.1.

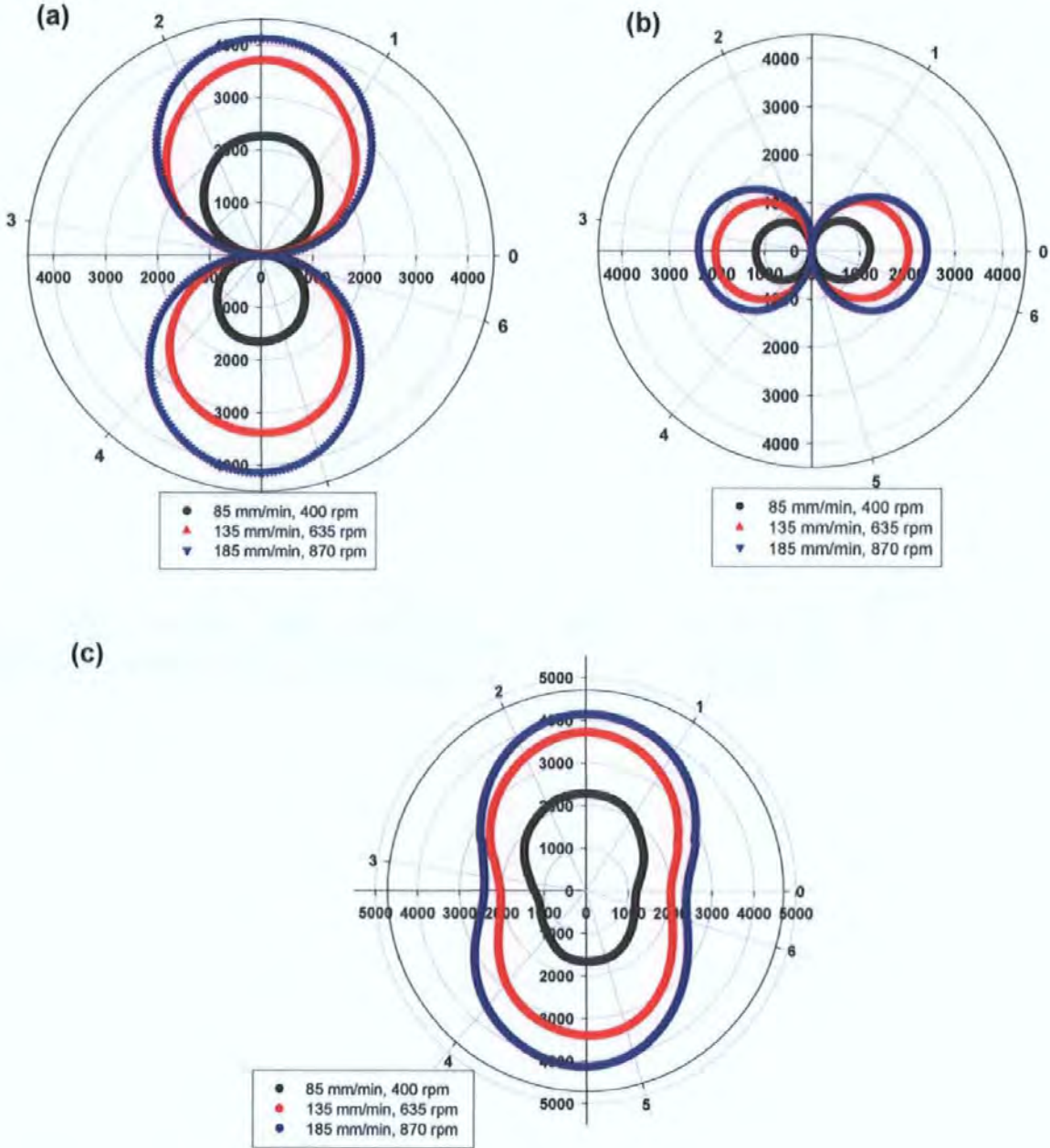


Figure 5.22:(a) Polar plots of  $F_x$  for pitch 0.2.  
 (b) Polar plots of  $F_y$  for pitch 0.2.  
 (c) Resultant polar plots for pitch 0.2.

Table 5.4 gives the weld parameters and residual stress data at pitch 0.2. The average heat input decreased with 44% and the  $F_x$  max polar plot power increased with 434% as indicated by Table 5.4. An increase in  $F_x$  max and the power determined from the polar plot areas (translational energy) are compared with an increase in longitudinal residual stresses. Similar trends are observed for the transverse residual stresses. The width between the longitudinal stress profile decreased as the rotational speed and feed rate simultaneously increased.

Weld	Feed (mm/min)	Speed (rev/min)	Fz (kN)	Fx max (N)	Fy max (N)	Heat (J/mm)	Fx max (J/s)	Long stress (MPa)	Trans stress (MPa)	Width (mm)
8	85	400	37	2303	1170	1284	1.7	57	44	64
11	135	635	36	3532	1963	839	4.6	68	46	56
4	185	870	32	4051	2295	682	7.2	91	52	52

Table 5.4: Summary of weld parameters and residual stress data.

From this discussion it is clear that the development of residual stress and strains during welding reflects a complex interplay between applied forces, energy input, temperature gradients and material flow properties.

Section 5.13 indicated that feed rate, rotational speed and  $F_x$  max are significant parameters in changing the longitudinal residual stresses. Figure 5.23 show the relationship between the longitudinal residual stresses and  $F_x$  max. The correlation coefficient for this model is 0.58.

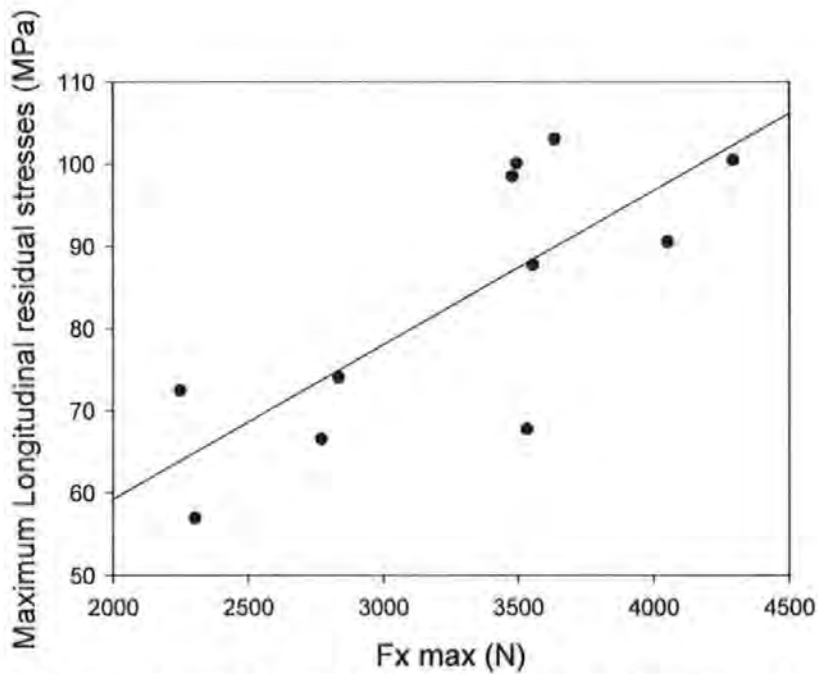


Figure 5.23: Maximum tensile longitudinal and transverse stress as a function of  $F_{x\max}$ .

A reasonable correlation could be found with the resultant force and the maximum longitudinal residual stresses (Figure 5.24). The correlation coefficient was 0.58. The resultant force could be used as an indicator of the variation in the longitudinal stresses.

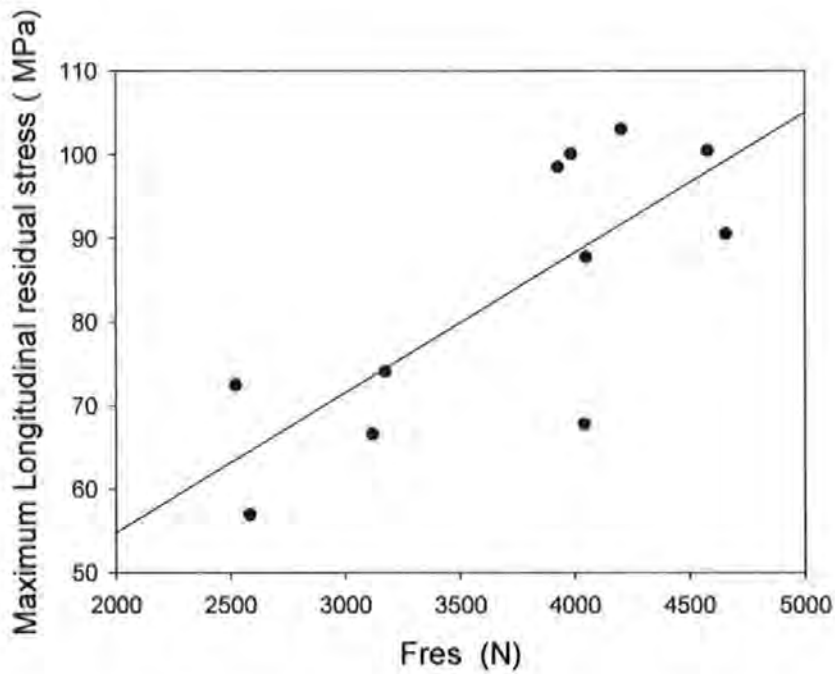


Figure 5.24: Maximum tensile longitudinal and transverse stress as a function of the resultant force.

## 5.17 FWHM results in FSW

The full width at half maximum (FWHM) obtained from the diffraction peak widths provides a measure of the microstrain and plastic deformation in materials<sup>1</sup>. The FWHM measurements are therefore proportional to the dislocation density and should indicate the regions of the different zones in the weld as discussed in section 2.5.1 in Chapter 1. The FWHM measurements are the lowest in the nugget area as a result of lower dislocation density. The distances -10 mm and 10 mm in Figure 5.25 correspond to the nugget in the FS welds. A larger dislocation density is expected for the parent plate as the parent plate is strain hardened and hence cold rolled. The distances -60 mm and 60 mm in Figure 5.25 correspond to the parent plate region. The results obtained in this thesis support studies on 5083 aluminium by Peel<sup>2</sup>, which show a good linear correlation with Vickers hardness and FWHM measurements (this could also be found using data in this thesis), and similar variations of FWHM with the dislocation density of the FS welds. Figure 5.25 shows two FWHM measurements for welds with different heat inputs. It can clearly be seen that the peak is wider for the hottest weld, indicating that the HAZ would have been wider for this weld.

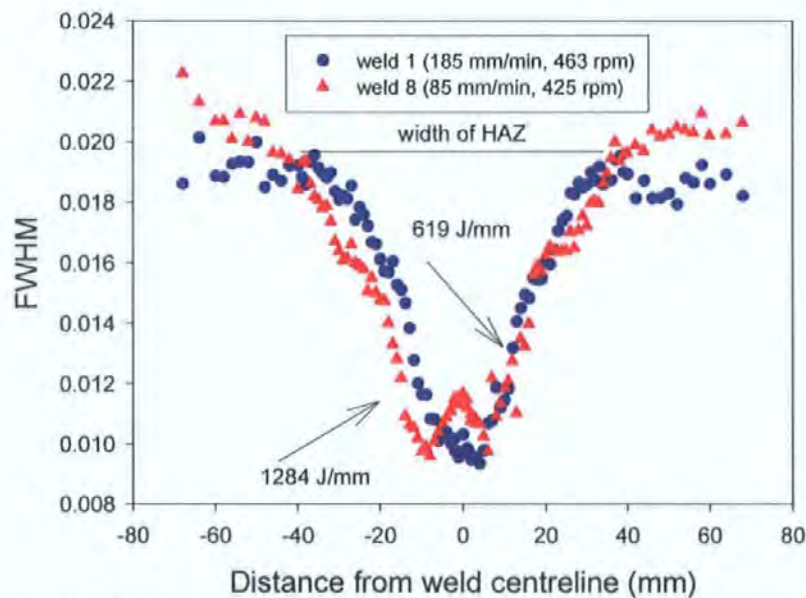


Figure 5.25: FWHM for welds 1 and 8.

<sup>1</sup> Hutchings, MT et al (2005)

<sup>2</sup> Peel, M (2005)

Figure 2.26 shows the widths of the HAZ (illustrated in Fig. 5.25) as a function of the average heat input. These regions represent the length of the HAZ at the mid depth of the plates.

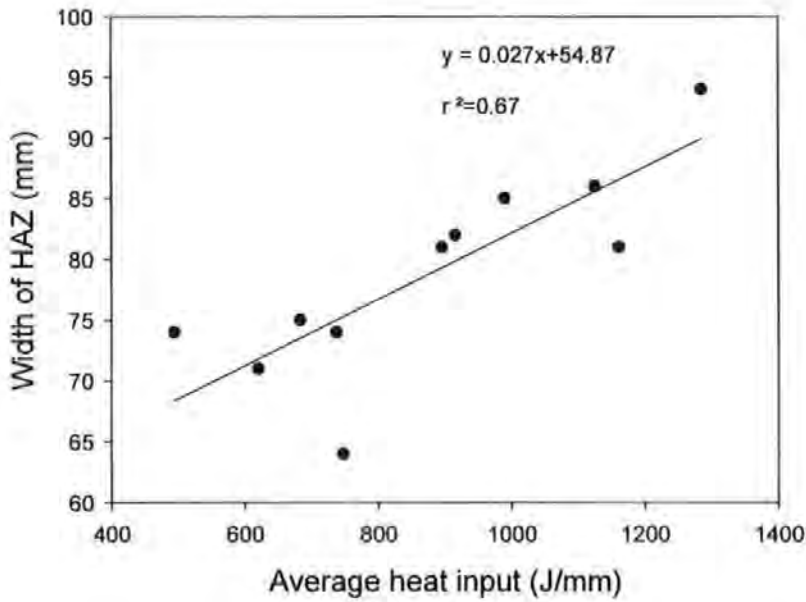


Figure 5.26: Regression between width of the HAZ and the average heat input.

A very good correlation between the average heat input and the widths of the HAZ were obtained. A larger average heat input model is therefore a good indication of a wider region in which the heat is distributed in the weld zone during FS welding.

## 5.18 Results of residual stress mapping at various weld positions

### 5.18.1 Transverse and longitudinal stress at 10 mm intervals along the weld

Figure 5.27 shows the Transverse Block Scans measuring transverse strains along transverse sections of welds 2, 5 and 11. The positive co-ordinate axis is also shown. The co-ordinate system is defined as follows: the X-direction is in the same direction as that in which the tool traverses during welding; the Y-direction is directed towards the advancing side of the weld; and the Z-direction is directed from the centre of the plate towards the tool shoulder and is thus perpendicular to the X-Y plane. Weld 2 was scanned only along the centre-line and welds 5 and 11 contained five 50 mm long scans at 15 mm intervals, with measurements taken

through the thickness of the plate at  $z = 0, -1, -2, -3, -4, -5, -6$ . Scans commenced at  $-10$  mm on the  $y$ -plate axis. Welds 2, 5 and 11 were scanned to obtain longitudinal and transverse strains on the same transverse sections of the welds, as shown in Figure 5.27, and at the same measurement positions. The scan along the transverse axis in this case was at  $60$  mm. These scans were made for welds at a single feed rate of  $135$  mm/min and increasing rotational speeds of  $254, 423$  and  $635$  rpm in an attempt to observe the variation of the residual stress through the thickness of the plate at different process parameters. Stress balancing was not done on the data for all the maps shown in this thesis because only part of the weld was scanned and not the complete width of the plate.

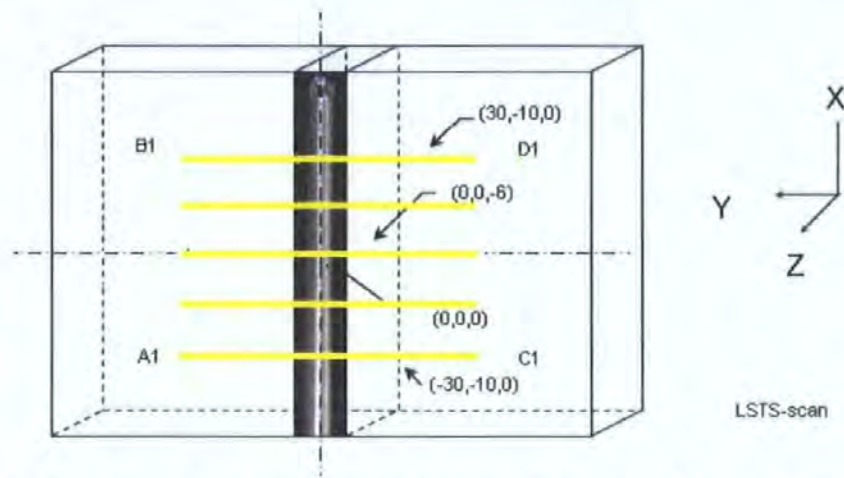


Figure 5.27: Example of Longitudinal scan on transverse section of weld (LSTS - scans).

Figure 5.28 shows the longitudinal stress maps of the transverse section for welds made at a single feed rate of  $135$  mm/min and increasing rotational speeds of (a)  $254$ , (b)  $423$ , and (c)  $635$  rpm. The advancing side is on the right hand side of each figure. The pin diameter of  $10$  mm and the shoulder diameter of  $25.4$  mm are indicated by dashed lines in Figure 5.28. The longitudinal stresses originate in the longitudinal shrinkage of the weld with respect to the colder plate material, leaving the weld in tension and the plate in compression. This can clearly be seen in Figure 5.28 where the region beyond  $30$  mm (parent plate region) is in compression and the region  $-15$  mm to  $15$  mm (weld region) in tension. The maximum tensile residual stress is obtained on the advancing side close to the edge of the shoulder. The coordinates of the maximum longitudinal tensile stress for each map are:

- (i)  $(9, 823, -1)$  for weld 5 with a maximum longitudinal residual stress of  $115$  MPa;

- (ii) (15.51,-1) for weld 2 with a maximum longitudinal residual stress of 42 MPa; and
- (iii) (15.00, -1) for weld 11 with a maximum longitudinal residual stress of 24 MPa.

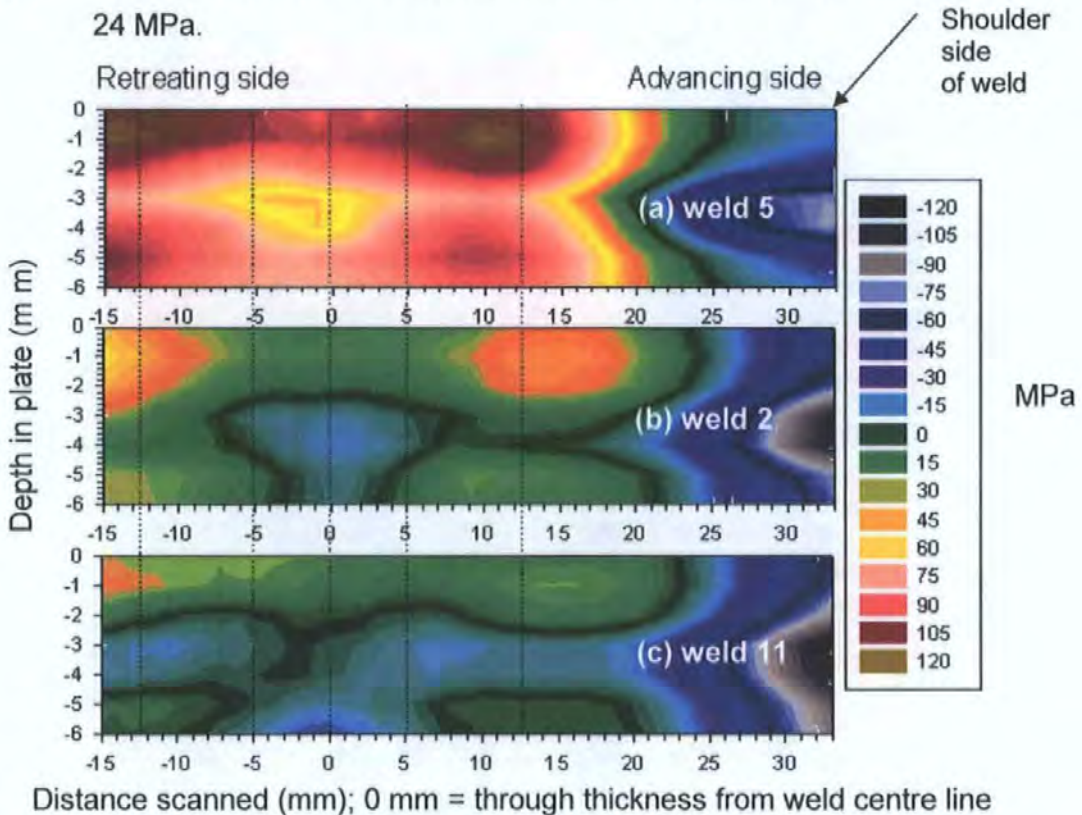


Figure 5.28: Longitudinal stress maps of the transverse section for welds made at a single feed rate of 135 mm/min and increasing rotational speeds of (a) 254 rpm, (b) 423 rpm and (c) 635 rpm.

As the rotational speed therefore increases, the peak longitudinal residual stresses occur at greater distances from the weld centre-line. This is expected as a larger heat input results in a greater volume of material being heated. As the heat input increases, the longitudinal stresses become less tensile. This is expected as a larger heat input results in a greater volume of material being heated and less thermal mismatch being created between the parent plate and weld metal.

Within the pin diameter, maxima and minima residual stress points are seen, with the larger of the two closer to the shoulder side of the weld. On the shoulder side of the weld, over  $\approx 1.5$  mm, a smaller area becomes less tensile as the rotational speed increases.

Table 5.5 gives the process parameters measured at these weld conditions. The vertical force increases significantly by 67% from 254 rpm to 423 rpm and 50% from 254 rpm to 635 rpm. This indicates that the vertical downwards force could have an effect on the magnitude of the stresses at this position. The downwards force could constrain the expansion of the material during welding and therefore decrease the residual stresses.

<b>Weld</b>	<b>Rotational speed (rev/min)</b>	<b>Vertical downwards force (kN)</b>	<b>Temperature (°C)</b>	<b>Torque (Nm)</b>	<b>Heat input (J/mm)</b>	<b>Max Stress at (0 mm) MPa</b>
W5	254	24	431	70	747	115
W2	423	41	512	56	990	42
W11	635	36	506	34	894	24

Table 5.5: Process parameters at 254, 423 and 635 rpm.

The transverse residual stress is shown in Figure 5.29. The transverse residual stresses originate from the transverse shrinkage of the weld with respect to the plate material, causing a small distortion of approximately two degrees upwards normal to the weld centre-line. Figure 5.29 shows a high compressive region for a depth of -2 to -3 mm into the plate for weld 2 and 11. Weld 5 had lower tensile transverse stresses in this region than regions close to the root and shoulder side of the weld. The transverse residuals stresses are larger at the root side of the welds. The transverse and longitudinal residual stresses show approximate stress balance in the top and bottom half of the plate. There is a large variation in transverse stresses through the depth of the plate. A larger region around the pin is in compression as the heat input increases. This could be a result of different thermal gradients being created around the tool at the different heat inputs.



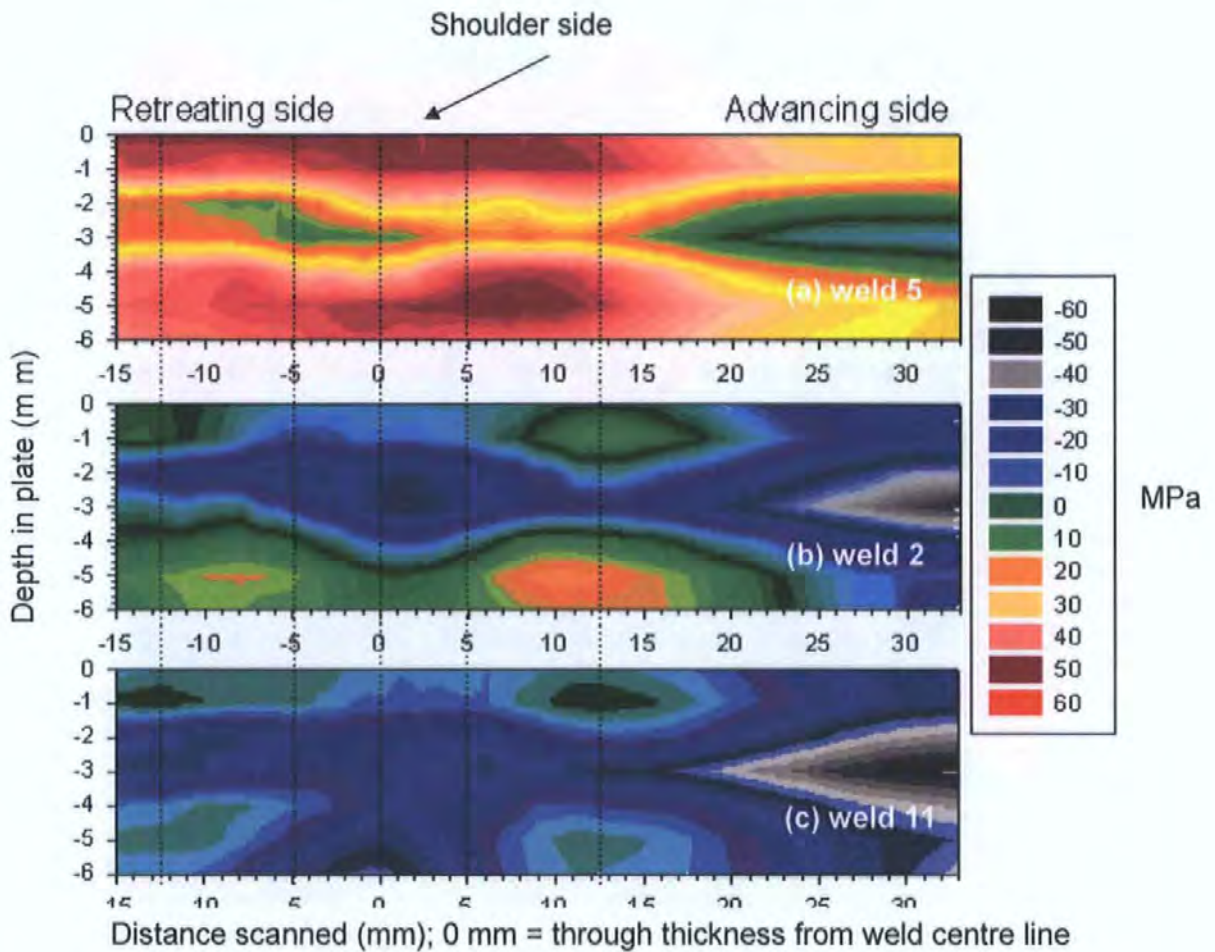


Figure 5.29: Transverse stress maps of the transverse section for welds made at a single feed rate of 135 mm/min and increasing rotational speeds of (a) 254 rpm, (b) 423 rpm and (c) 635 rpm.

Transverse and longitudinal residual stress maps for weld 5 and 11 are shown in Figures A.2 to A.5 and are given in the appendix. These scans were made at 15 mm intervals in order to determine whether the residual stresses varied along the weld. The figures clearly show that the residual stresses in both directions show similar features of the variation of the residual stresses in the depth of the plate. This would imply that the process conditions during welding remain constant.

The effects of the shoulder during FSW result in larger areas of tensile residual stresses being created. One would expect the tensile residual stress regions to be the regions where fatigue initiation is most likely to take place. It is interesting to note that, in regions close to the shoulder side of the weld, planar facet defects were detected on fatigue samples. The type of defects present at the fatigue initiation sites on the FSW fatigue samples is investigated in Chapter 6.

### 5.18.2 Transverse and longitudinal stress maps of longitudinal weld sections on the advancing side of the weld

Welds 5 and 11 were also scanned to obtain longitudinal and transverse strains along longitudinal sections of the weld as shown in Figure A.6 to A.9 listed in the appendix. Strains were measured over a length of 58 mm along the weld centre-line, at distances 5, 10 and 35 mm from the weld centre-line. These lines represent the centre-line of the weld, approximately the edge of the pin, approximately the edge of the shoulder and parent plate material respectively. The results clearly indicate that the parent plate had the highest stress values and the welded region had lower stress due to the combined effect of thermal and mechanical forces applied to the plate.

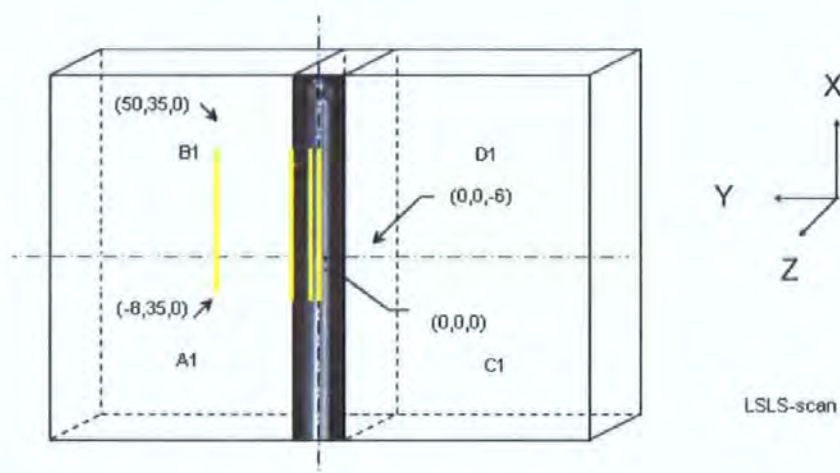


Figure 5.30: Example of longitudinal scans on the longitudinal section of the weld (LSLS-scans).

These figures show that the longitudinal and transverse residual stress is quite uniform through the length of the plate at depths of 0 mm to -3 mm, -3 mm to -5 mm and -5 to -6 mm. This again indicates that the welding conditions remained the same along this length of the weld. The longitudinal sections match the transverse positions of 0 mm, 5 mm, 10 mm and 35 mm for the transverse maps given in Figures 5.28 and 5.29 at the weld centre-line. The combined transverse sections and longitudinal sections could perhaps be used to model the residual stress around weld 5 and weld 11. This data could be used to verify a FEM model which is beyond the scope of this thesis.

## 5.19 Conclusions

In this chapter, the variation of residual stress with input and process parameters for a series of FSW was compared. In all the welds made, the region around the weld line was characteristic of tensile stresses and was balanced by the compressive stresses in the parent plate. The longitudinal strains and stresses are approximately two to three times larger than the transverse strains and stresses, but approximately 22% to 40% of the 0.2% proof strength of the parent material. The largest stress magnitude was obtained on the shoulder side of the weld. Feed rate plays a dominant role in the changes in the maximum longitudinal residual stresses, and the peak longitudinal residual stress increases as feed rate increases. Feed rate and rotational speed can be chosen from the prediction maps to obtain low tensile longitudinal residual stresses.

$F_x$  max contributes the most to the changes in the tensile longitudinal stresses. It is interesting to note that feed rate as well as  $F_x$  max has a strong dependence on the changes of widths of the longitudinal stress profiles.

No process parameter showed a good correlation with the peak transverse residual stresses. It seems that torque could play a role in the variation of transverse residual stresses.

There is a strong dependence on pitch and the force footprint polar areas, as well as the variation of pitch and the peak longitudinal residual stresses. The areas of the polar plots also decrease with increasing feed rate and tool speed which correlates with a decrease in energy as seen in Figure 5.20. A linear correlation of 0.82 could be obtained for the longitudinal residual stresses and the average heat input. In general, greater heat input results in lower residual longitudinal stresses.

An excellent correlation could be obtained with the FWHM and HAZ widths and the average heat input into the welds. This indicates that larger average heat input does indicate a greater HAZ for FSW.

The 2D stress maps indicated that the process conditions of the welds remained constant for the length measured since the longitudinal and transverse residual stress remained uniform for transverse sections of the welds and was also uniform for similar depths for longitudinal sections of the FS welds.

## 6. Fatigue life in FSW aluminium 5083-H321 as a function of process conditions

### 6.1 Introduction

In this chapter the intention is to address the occurrence of specific fractographic intrinsic defect 'indications' for FS welded fatigue present in this project. It examines the role of process-structure interactions, both in generating such defect indications, and in considering the effect of these defects on dynamic performance of the welds. This leads to some general conclusions as to the manner in which FSW process parameters might be optimized so as to minimize any detrimental influence of such defects on fatigue and fracture. This chapter includes a brief introduction to the relevant theory of fatigue and a discussion of the fatigue tests conducted on all the welds.

### 6.2 Background to Fatigue

Fatigue of metals refers to the process of micro-plastic deformation, crack initiation and subsequent crack propagation, resulting from the application of variable or constant amplitude cyclic stresses, usually significantly below the material's tensile strength<sup>1</sup>. Fatigue tests can be conducted under either strain controlled or force controlled conditions to determine the fatigue strength of a material, which refers to the sustainable stress amplitude at a given number of cycles and which is obtained from a stress versus number of cycles (S-N) plot. Low-cycle fatigue tests are done at high loads and short lifetimes  $<10^4$  cycles. Fatigue life prediction is usually done via strain-based models in low-cycle fatigue since these conditions usually involve effects of yielding<sup>2</sup>. Stress based models are applied for high cycle fatigue tests<sup>3</sup> where cyclic life is greater than  $5 \times 10^3$  cycles in which the strain is largely confined to the elastic range. In this thesis the range from  $10^4$  to  $2 \times 10^6$  cycles will be termed as medium cycle fatigue and the range  $>2 \times 10^6$  cycles as high cycle fatigue.

The nomenclature associated with constant amplitude loading and used in this thesis is summarized in Figure 6. Here  $\sigma_a$  is the allowable alternating stress,  $\sigma_n$  is

---

<sup>1</sup> ASM International (1991)

<sup>2</sup> Bannantine et al (1990)

<sup>3</sup> Collins, JA (1993)

the fully reversed fatigue strength at  $R = -1$ , and  $\sigma_m$  is the mean stress at which the allowable alternating stress is determined.

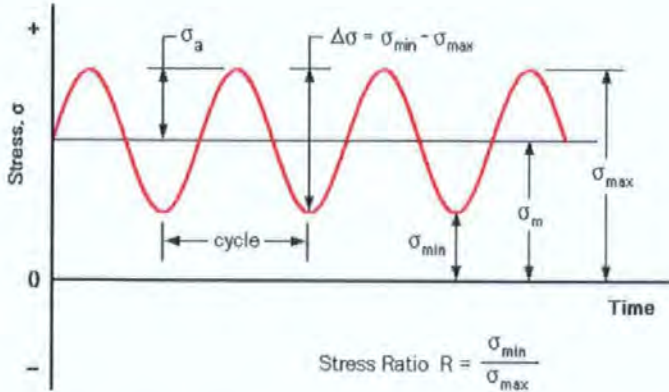


Figure 6.1: Typical loading parameters used to characterize cyclic loading.

### 6.3 Experimental setup

#### 6.3.1 Fatigue testing instrument

A Servohydraulic FastTrack™ Instron 8810 fatigue machine, shown in Chapter 4, was used to conduct the fatigue tests.

#### 6.3.2 Fatigue specimens

A CNC milling machine was used to cut fatigue specimens transverse to the weld with dimensions as illustrated in Figure 6.2. These samples concur with the requirements of ASTM E 466 – 96.

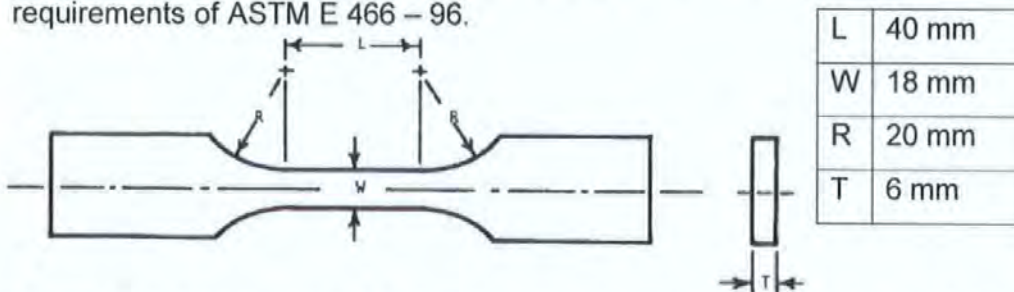


Figure 6.2: Dimension of fatigue specimen according to ASTM E 466-96<sup>1</sup>.

After final machining, the characteristic surface on the top of the weld was removed with a surface grinder whereafter samples were polished with 400 grit followed by 1200 grit SiC paper to remove the circumferential markings of the

<sup>1</sup> ASTM (1995)

initial polishing phase and to eliminate any sharp edges remaining on the sample that could create notch effects during fatigue loading. The characteristic marks on top of the FSW were removed, since any rough marks on a fatigue specimen usually act as fatigue initiation sites. It was shown by James and Hattingh<sup>1</sup> that this was true for FSW. This thesis focuses on investigating the effect of intrinsic defects in FSW, rather than such surface effects.

Fatigue specimens were placed under uniaxial constant amplitude sinusoidal loading to ensure constant load acting over the cross section of the sample. A value of  $R=0.1$  was chosen to ensure only tensile loads acting on the sample and to make certain no rubbing damage to the fracture surface would be induced during crack growth. The fatigue tests were conducted according to ASTM standard E 466 – 96. Alignment was checked to ensure no induced bending.

The aim of the tests was to obtain cycles to failure data for all welds at the same cyclic load and to relate these values and their variation to process parameters. Specimen failure was defined as a 15% decrease in applied load or run out at  $2 \times 10^6$ . The welds were tested in a random order to exclude any variation in results arising from any systematic effects that may be associated with the material or testing machine. Fatigue testing was done at the same load for each specimen while maintaining the same R ratio.

### 6.3.3 Determining the constant stress to apply to all specimens

There is usually a considerable scatter in fatigue data, with a decreasing scatter in fatigue life observed as the stress increases. Sufficient data is therefore required to identify statistically meaningful trends. Three or four stress levels above the fatigue limit are usually adequate to define the general shape of the S-N curve. Tests should then be repeated at these levels. Little<sup>2</sup> provides guidelines for replications and number in fatigue testing. For research and development results a minimum of 6-12 specimens are required, which includes 33-50% replication. The five fatigue samples available for each FSW were not enough to obtain statistically meaningful fatigue life S-N plots. It was therefore decided to run 5 samples at the same applied stress and to use the average of these values in comparing effects of the FSW parameters and fatigue life.

---

<sup>1</sup> James, MN and Hattingh, DG (2002)

<sup>2</sup> Little, RE (1975)

The uncertainty in life is greater than the uncertainty in stress. The variability of the data around the mean fatigue life remains fairly constant up to  $1 \times 10^6$  cycles to failure and increases significantly for lives longer than this. The distribution of fatigue data at a specific stress level, such as  $\log N$ , has a Gaussian distribution. The variability of the data can be determined from the standard deviation of  $\log N$ . Methods do exist to determine S-N curves for small numbers of samples. A single sample can be tested at a stress level below the fatigue limit and if it does not fail it can be retested at intervals of 1-3% of UTS, until failure is reached. This method can only be applied if the samples are not susceptible to strain aging which can artificially increase the fatigue strength through "coaxing".

Al 5083-H321 is strain hardened and each specimen has a variable fatigue strength which value varies from sample to sample. It is therefore difficult to determine the fatigue limit accurately and hence we need to test several groups of specimens at several stresses. The measured tensile strength of the parent plate was approximately 360 MPa, thus 14% higher than the parent plate data available in the literature. The fatigue limit of this alloy in literature equals 168 MPa at  $2 \times 10^6$  cycles thus adding 14% gives a value of 192 MPa, which should be an estimate of the fatigue limit at  $2 \times 10^6$  for the parent plate at  $R=-1$ . This value would be higher at  $R=0.1$ . The S-N curve of the parent plate was found as shown in Figure 6.3 and used as a guideline to determine the conditions to apply to all the weld samples. Figure 6.3 indicates that a fatigue life of  $10^6$  cycles corresponds to a stress of approximately 216 MPa at  $R = 0.1$ .

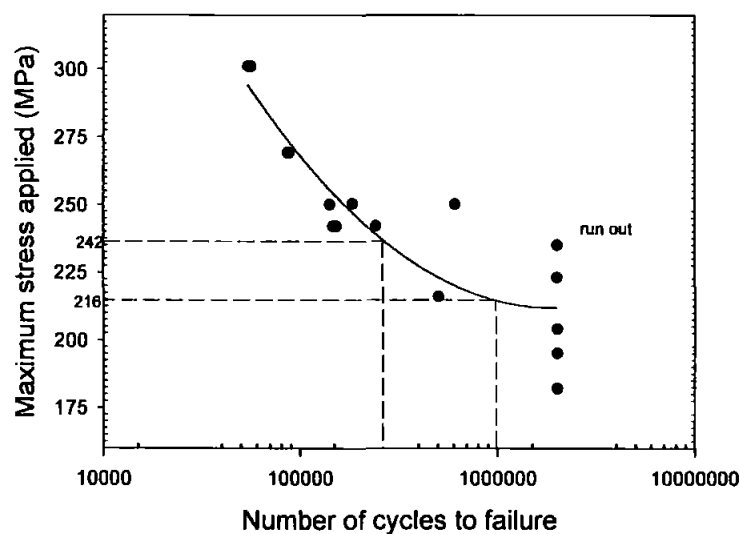


Figure 6.3: Experimental data obtained for the parent plate cut in the rolling direction.



A few initial tests were conducted to decide upon a load to apply to all welds in order that no run-outs occur.

Weld	UTS(MPa)	Stress applied (MPa)	Fatigue life
11	306	216	20653210
10	310	242	29780
1	289	269	23850

Table 6.1: Initial trials to investigate fatigue life.

Table 6.1 did not show any systematic trend. A mid-range stress of 242 MPa was chosen, which should give fatigue lives between  $1 \times 10^4$  and  $1 \times 10^6$ . Previous work on this alloy has indicated that the pseudo-bond defects were activated at higher levels of plastic strains and their effects are therefore more likely to be influenced at shorter fatigue lives<sup>1</sup>. Less scatter in fatigue data is usually associated with an increase in applied stress.

#### 6.4 Fatigue life of FSW

The variation of fatigue properties along the weld length was first investigated and is presented in Figure 6.4. The fatigue data is also presented in Table 6.2. There is a decrease in fatigue life up to 200 mm followed by an increase. There is a slight scatter in the data; but fatigue measurements always produce scatter in the results. The type of defects obtained for a specific weld also show variation. The defects will be discussed in sections 6.6 and 6.7. Five measurements done at each specific stress level are statistically acceptable. The indicated variation in the standard deviation and error measurements is quite high. This variation should be borne in mind when the results are interpreted.

Weld number	Average No Cycles	SD
1	16792	14868
2	12746	26362
3	50000	59818
4	32694	35131
5	28624	30579
6	68798	22944
7	45021	26985
8	21616	7295
9	19202	14886
10	85897	40902
11	74433	38047

Table 6.2 Average fatigue data for five samples taken along the weld.

<sup>1</sup> James, MN and Hattlingh, DG (2002)

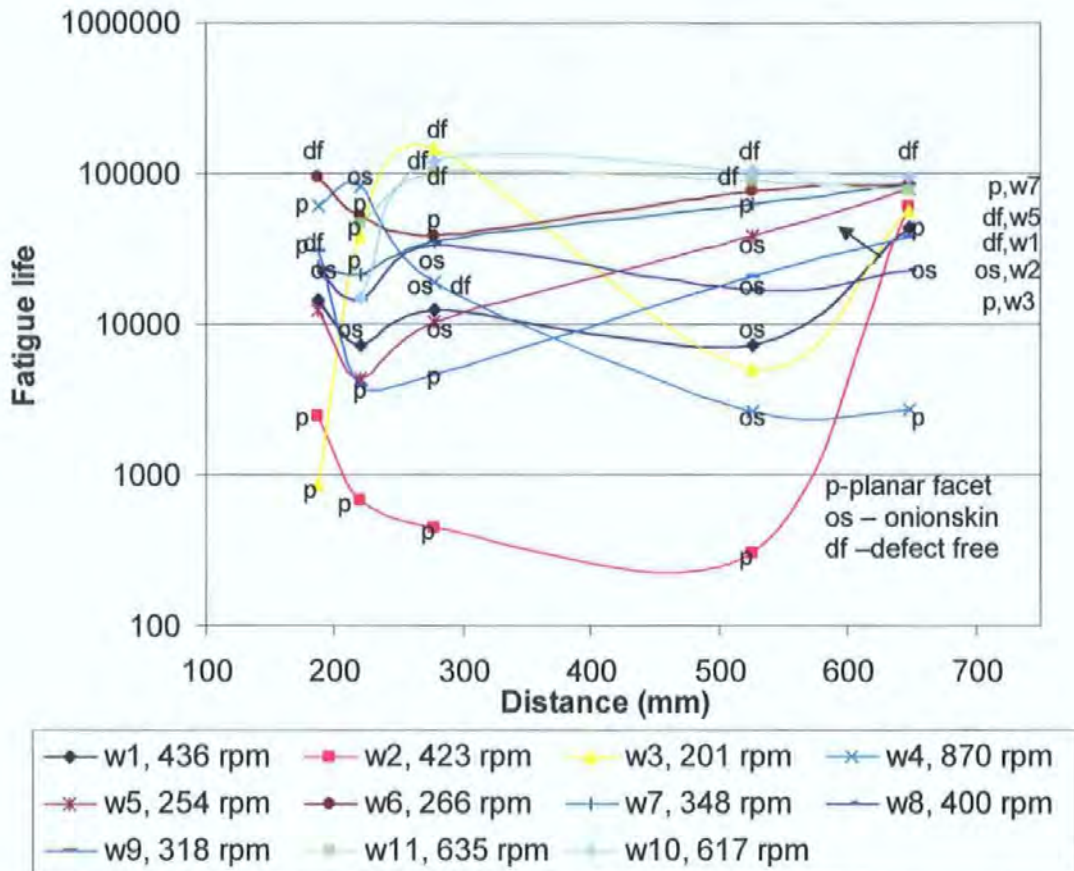


Figure 6.4: Variation of fatigue life and defects for each sample at different positions along the weld.

### 6.5 Statistical analyses of fatigue data

Table 6.3 lists the statistical analyses done on the fatigue data to attempt to find a suitable model for fatigue life and process parameters. A regression analysis to relate the process parameters with fatigue life to determine whether, any online monitored process parameters can be used to predict fatigue life, is also shown in Table 6.3.

The analyses reveal that no parameter could be considered to be statistically significantly for the fatigue life, since all the P-value are  $> 0.05$ . This indicates that there is a 95% change that the parameters are not significant. The optimization of fatigue life therefore requires a complex combination of parameters. Process parameter maps were investigated to see if any trends were apparent. This is shown in Figure 6.5 which gives tool feed, speed and pitch as a surface plot of fatigue life.

Regression models for process parameters versus input parameters	Input parameter's P- value	
fatigue =33525 -4.49 feed - 25.4rpm $R^2= 0.04$ ; $R^2_{adj}=-0.23$	Feed rate RPM	0.98823 0.669151
fatigue=695946 +5103 Fz -2286Torque +8.5 F <sub>x</sub> max-1503 Temp $R^2= 0.28$ ; $R^2_{adj}=-0.29$	F <sub>z</sub> Torque Temp F <sub>x</sub> max	0.350454 0.264441 0.320956 0.658698
Fatigue=172874 - 37 heat -45 power $R^2= 0.39$ ; $R^2_{adj}=0.22$	Heat Frictional Power	0.268495 0.10712

Table 6.3: Statistical analyses of fatigue data.

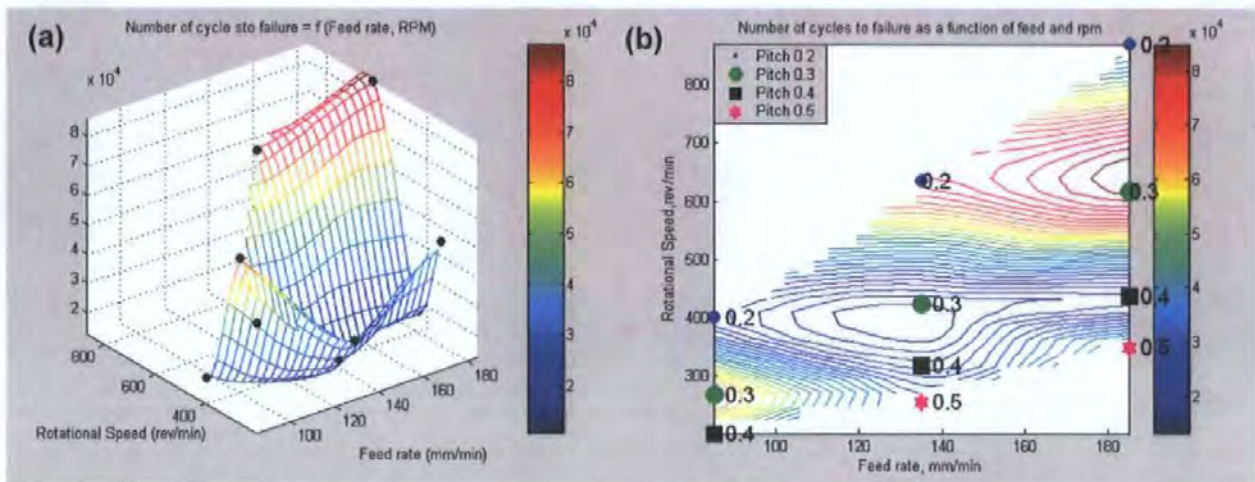


Figure 6.5:(a) 3 D map of fatigue life as a function of feed rate and rotational speed.

(b) Contour map of fatigue life as a function of feed rate and rotational speed.

Figure 6.5 shows that higher lives are obtained at feed rates  $> 180$  mm/min and above 550 rpm and also at low speeds and feeds. A minima is obtained at approximately 350 rpm and 135 rev/min. It is interesting to note that regions of high and low fatigue cycles correspond with low and high vertical downwards force. There is an approximate inverse relationship between frictional power (Figure 3.11 (a) and (b)) and fatigue life (Figure 6.5 (a) and (b), Figure 6.6 (a)).

Interestingly fatigue life, UTS, and the frictional power show similar trends (Figure 6.6 (b)). There is a decrease in fatigue life as the frictional power on the tool increases up to 1200 J/s. Thereafter the fatigue life seems to increase again. These relationships show general trends, indicating that lower UTS values correspond with lower fatigue life values. If weld 11 is excluded from the results,

the correlation coefficient of the relationship becomes 0.83 between frictional power and fatigue life.

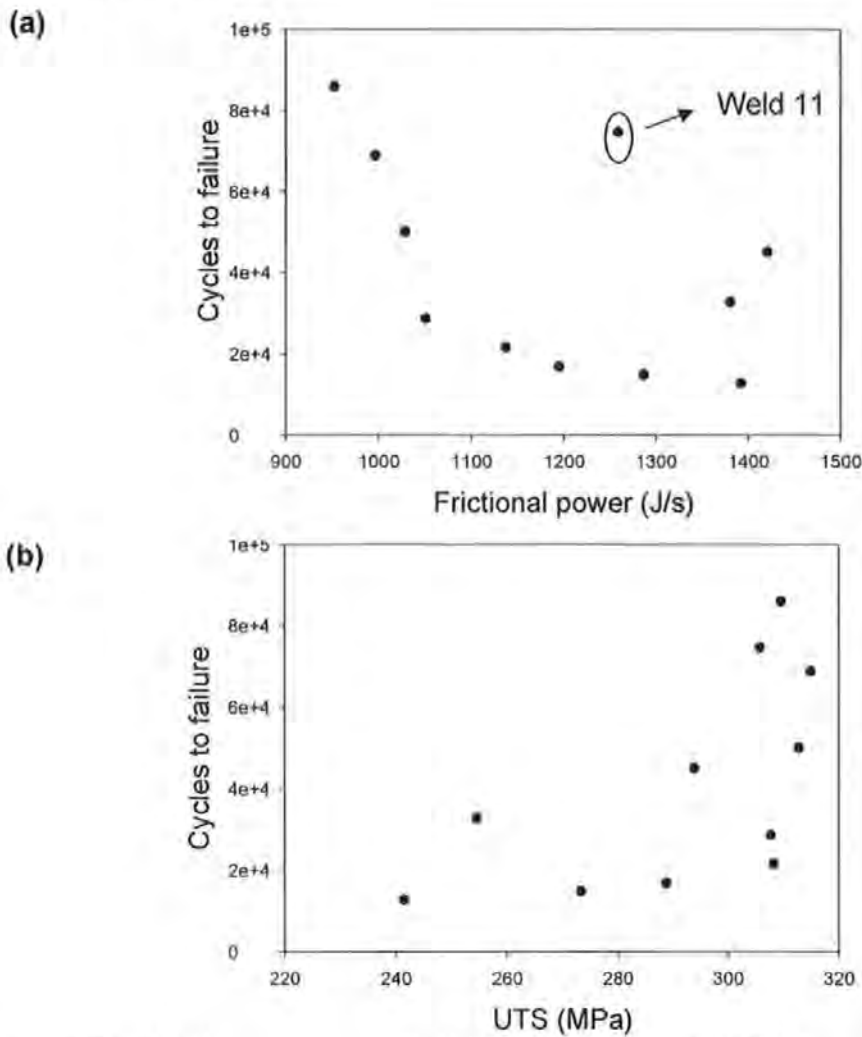


Figure 6.6: Fatigue compared to (a) frictional power (b) UTS.

### 6.6 Defects in FS welds of Al 5083-H321

Fractography was performed on the welded fatigue samples to determine fracture surface features and identify the types of defects present at the fatigue initiation sites in an endeavour to link fatigue life variability with defect type and occurrence. Two linked types of defects were observed on the samples, namely onion skin (OS) defects and planar facets (PF). Figure 6.7(a) shows onion skin defects observed at the fatigue regions of weld 5.

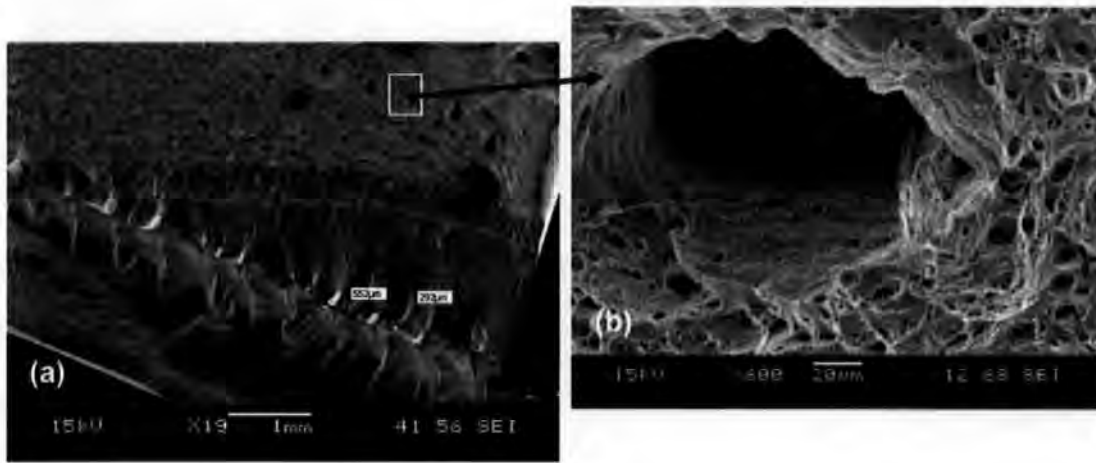


Figure 6.7: (a) Fatigue onion skin defect for weld 5 (135 mm/min, 254 rpm).  
 (b) Fatigue void like feature for weld 5 (135 mm/min, 254 rpm).

These defects are formed close to the shoulder side of the weld and are related to the weld pitch of 0.5 mm. At approximately 2 mm from the root of the weld two rows of void-like features are seen (Figure 6.7 (b)). A possible reason for the formation of these voids is that there was not enough heat available to allow good mixing for the pin profile used in this thesis ( heat input to weld 5 was medium low, 747 J/mm).

Weld 8 also contained onion skin defects in the fatigue regions, as well as void like features at the root of the weld as shown in Figure 6.8. The void-like features were related to the pitch of weld 8 in some regions, which is 0.2 mm/rev. There were regular intervals of approximately 0.5 mm between most void-like features on weld 8. Weld 8 had the highest heat input (2021 J/mm) and a medium vertical force of 24 kN. Heat input therefore does not seem to play a role in the formation of these features since weld 5 was a cold weld. The sample size is too small to draw sound conclusions. The formation of these features must also be related to the flow dynamics around the pin. Weld 8 is less regularly defective than weld 5- supposition is that the extremes of heat input (high and medium-low) more likely to cause onion skin defects, but that they are worse under cold weld conditions.

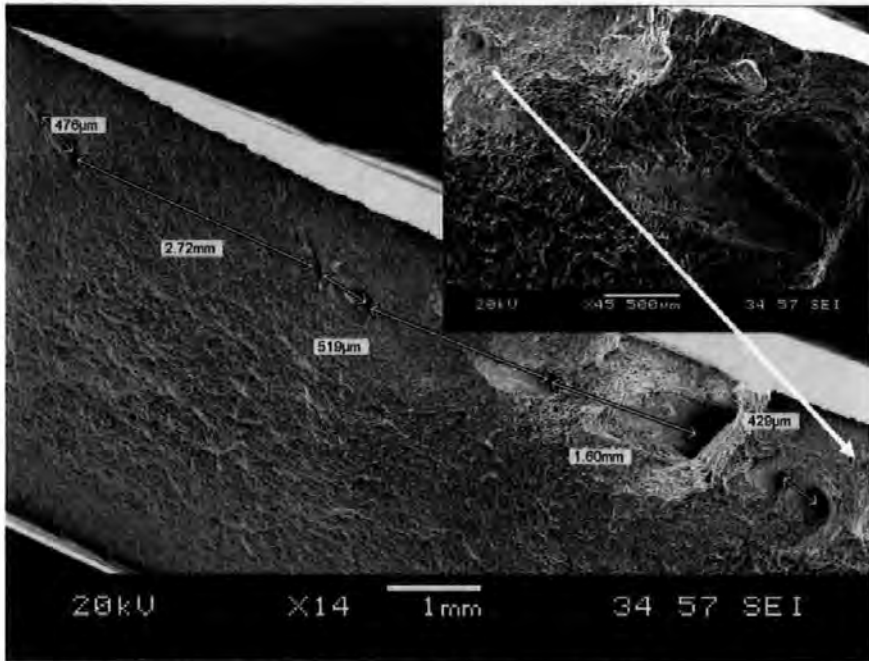


Figure 6.8: Onion skin defects for weld 8 (85 mm/min, 400 rpm, pitch 0.21).

Planar facets were also found associated with fatigue crack initiation sites, as is shown in Figure 6.9.

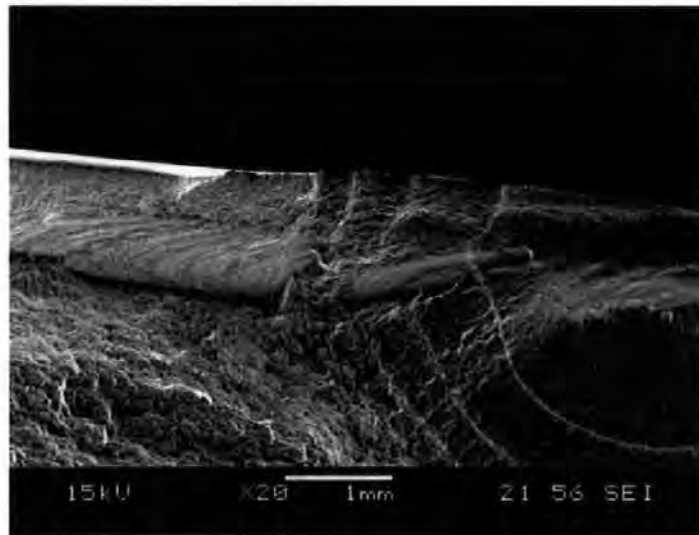


Figure 6.9: Optical micrograph indicating planar facets at fatigue initiation site for weld 6 (85 mm/min, 266 rpm, pitch 0.3).

The majority of such planar facets formed around 1-2 mm below the shoulder side of the weld. Welds 2, 3, and 9 also exhibited planar facets as shown in Figure 6.10. Specimens with larger planar defects generally had lower fatigue lives than specimens where onion skin defects occurred.

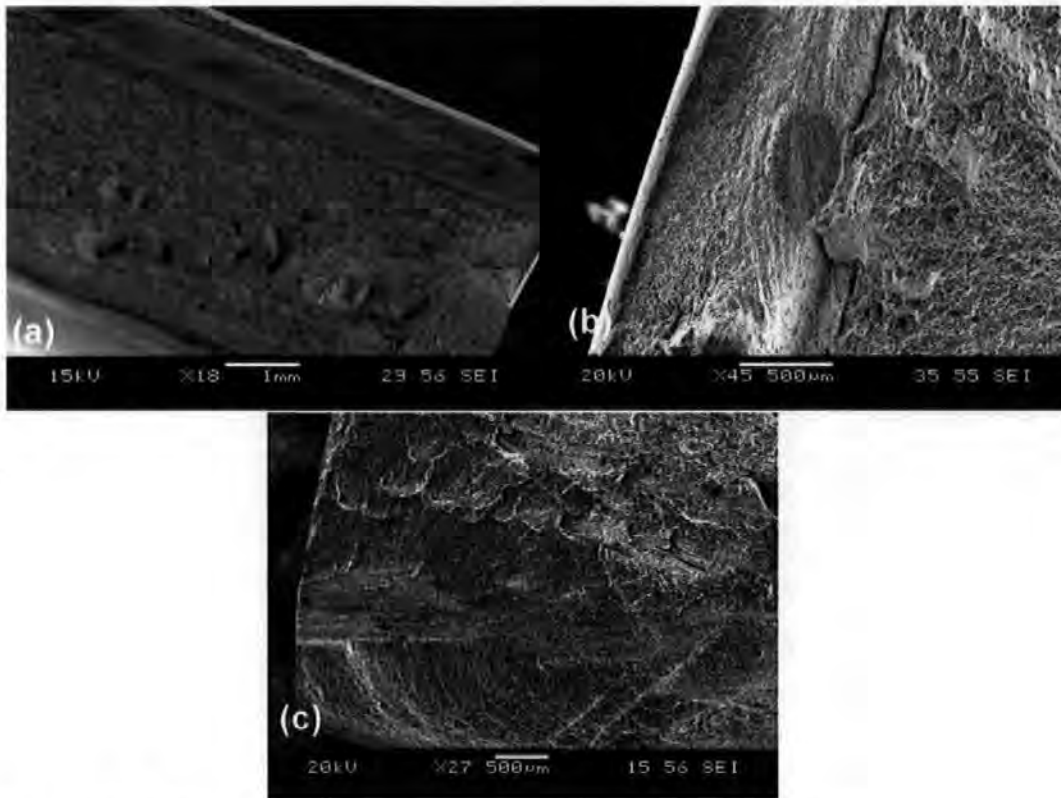


Figure 6.10: Planar facets for (a) weld 2 (b) weld 3 and (c) weld 9.

#### 6.7 Defect population in FSW 5083-H321 aluminium alloy

Table 6.4 lists the defect types observed on fatigue samples of the FSW in this thesis.

Fatigue lives of weld samples and Defect classification at initiation site.					
Sample no	RPM Rev/min	Feed mm/min	Pitch mm/rev	No fatigue cycles to failure	Defect type
1.1	185	436	0.42	7165	OS defects
1.14	185	436	0.42	42744	No defects
1.2	185	436	0.42	14527	Planar facet
1.3	185	436	0.42	7110	OS defects
1.5	185	436	0.42	12415	OS defects
2.1	135	423	0.32	300	Planar facet
2.14	135	423	0.32	59880	OS defects
2.2	135	423	0.32	2430	Planar facet
2.3	135	423	0.32	670	Planar facet
2.5	135	423	0.32	450	Planar facet
3.1	85	201	0.42	5076	Planar facet
3.14	85	201	0.42	56861	Planar facet
3.2	85	201	0.42	852	Planar facet
3.3	85	201	0.42	38700	Planar facet
3.5	85	201	0.42	148510	No defects
4.1	185	870	0.21	2597	OS defects
4.14	185	870	0.21	2666	Planar facet
4.2	185	870	0.21	59324	Planar facet
4.3	185	870	0.21	79930	OS defects

4.5	185	870	0.21	18954	No defects
5.1	135	254	0.53	38107	OS defects
5.14	135	254	0.53	78172	No defects
5.2	135	254	0.53	12315	OS defects
5.3	135	254	0.53	4358	OS defects
5.5	135	254	0.53	10169	OS defects
6.1	85	266	0.32	76249	No defects
6.14	85	266	0.32	84663	No defects
6.2	85	266	0.32	92855	No defects
6.3	85	266	0.32	52098	Planar facet
6.5	85	266	0.32	38126	Planar facet
7.1	185	348	0.53	62783	Planar facet
7.14	185	348	0.53	83113	Planar facet
7.2	185	348	0.53	23755	Planar facet
7.3	185	348	0.53	20806	OS defects
7.5	185	348	0.53	34647	OS defects
8.1	85	400	0.21	16624	OS defects
8.14	85	400	0.21	22122	OS defects
8.2	85	400	0.21	22000	OS defects
8.3	85	400	0.21	14205	OS defects
8.5	85	400	0.21	33133	OS defects
9.1	135	318	0.42	20544	Planar facet
9.14	135	318	0.42	36742	No defects
9.2	135	318	0.42	30380	Planar facet
9.3	135	318	0.42	3811	Planar facet
9.5	135	318	0.42	4535	Planar facet
10.1	185	617	0.30	101573	No defects
10.13	185	617	0.30	99562	No defects
10.14	185	617	0.30	94264	No defects
10.3	185	617	0.30	14705	OS defects
10.5	185	617	0.30	119380	No defects
11.1	135	635	0.21	99943	No defects
11.13	135	635	0.21	88663	No defects
11.14	135	635	0.21	77531	No defects
11.3	135	635	0.21	46374	No defects

Table 6.4 Optical classification of fatigue fracture surfaces.

A ranking order was determined using equation 6.1 to examine the possible relation of process parameters to the type of defects that occur during FSW in this thesis.

$$x = \frac{\text{measurement} - \frac{1}{2}(\text{minvalue} + \text{maxvalue})}{\frac{1}{2}(\text{minvalue} - \text{maxvalue})} \quad \dots\dots 6.1$$

The following ranking was used, as shown in Table 6.5.

High	Med high	Medium	Medium low	Low
from	between	from	Between	from
1 to 0.75	0.25 and 0.75	-0.25 to 0.25	-0.25 and -0.75	-0.75 to -1

Table 6.5: Ranking order used in this thesis.



The results can be displayed as a set of histograms (Figure 6.11) that show the percentage of each type of defect occurring in a specific range of process parameters.

In summary, these histograms show that:

- (i) vertical force ( $F_z$ ) = category 3 (~31-36 kN) gives highest frequency of defect-free welds; higher  $F_z$  values favour planar facets (PF), lower  $F_z$  favour onion skin defects (OS);
- (ii) temperatures in category 4 (~504°C) give the best relative frequency of defect-free welds; category 4 also gives highest relative % of PF and OS defects;
- (iii) torque values in category 4 (~34 kNm) give best relative frequency of defect-free welds. PF tend to occur at higher torque categories compared to OS;
- (iv) Heat and power input in category 3 (~0.9 kJ, 2300J/s) gives best relative frequency of defect-free welds. PF facets occur in medium heat input and high frictional power input. OS defects are favoured by medium heat input and medium to low frictional power;
- (v) medium high resultant force ( $F_{res}$ ) in category 3 (~1800 N) favours OS defects and category 2 (~1300 N) favours PF. The greatest probability of defect-free welds occur at medium-low and medium-high  $F_{res}$ ; and
- (vi)  $F_x$  max values in category 2 (~2500 N) and 4 (~3600 N) give highest relative frequency of defect free welds and PF. Category 4 also gives best relative frequency of OS.

Planar defects occur at high vertical downwards forces, power and torque and medium low temperature as well as lower heat input. This indicates a possible rationale for the formation of the planar facets, namely:

Higher torque implies that it is more difficult to move the layer of material that rotates around the tool from the advancing to the retreating side over the layer that advances with the tool. It could also be possible that the design of the tool shoulder plays a major role in improving the flow dynamics of the material underneath the tool and that an improved design could eliminate these planar facets.

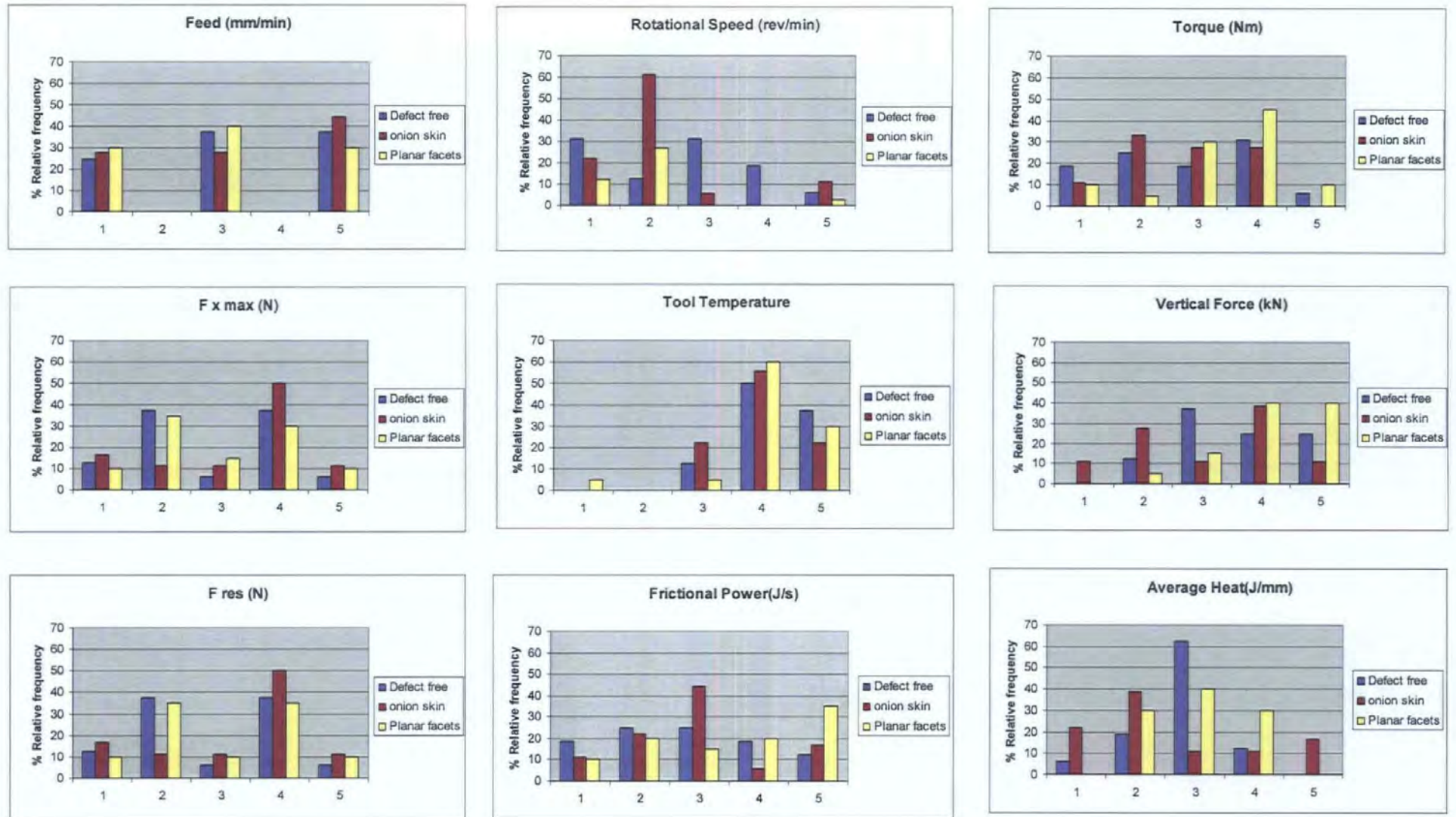


Figure 6.11: Histograms relating FSW parameters with defect types.

The onion skin defects occur at process parameters in lower ranges compared to the planar facets. Lower torque values indicate that the difficulty of shearing the material around the tool does not play a role in the formation of the onion skin defects.

The defect population in tensile and fatigue fracture samples, ultimate tensile strength and fatigue life as a function of frictional power and input parameters, is illustrated in Figure 6.12. The following conclusions can be drawn by interpreting Figure 6.12:

- (i) the same defects occurred on tensile and fatigue samples at the same welding conditions;
- (ii) low tensile strength concur with low fatigue life and high tensile strength concur with high fatigue life;
- (iii) high frictional power corresponds with low fatigue life and low tensile strength;
- (iv) weld 10 and 11 were defect free welds (185mm/min, 617rpm and 135mm/min, 635 rpm);
- (v) welds 4, 5 and 8 contained onion skin defects;
- (vi) welds 1, 2, 3, 6, 7 and 9 contained planar facets;
- (vii) the formation of the type of defects does not give a linear relationship with frictional power. This is investigated further in Figure 6.13; and
- (viii) the planar facets do correlate with frictional power, where the planar facets become less prominent for less frictional power, clearly shown in Figure 4.11, Chapter 4.

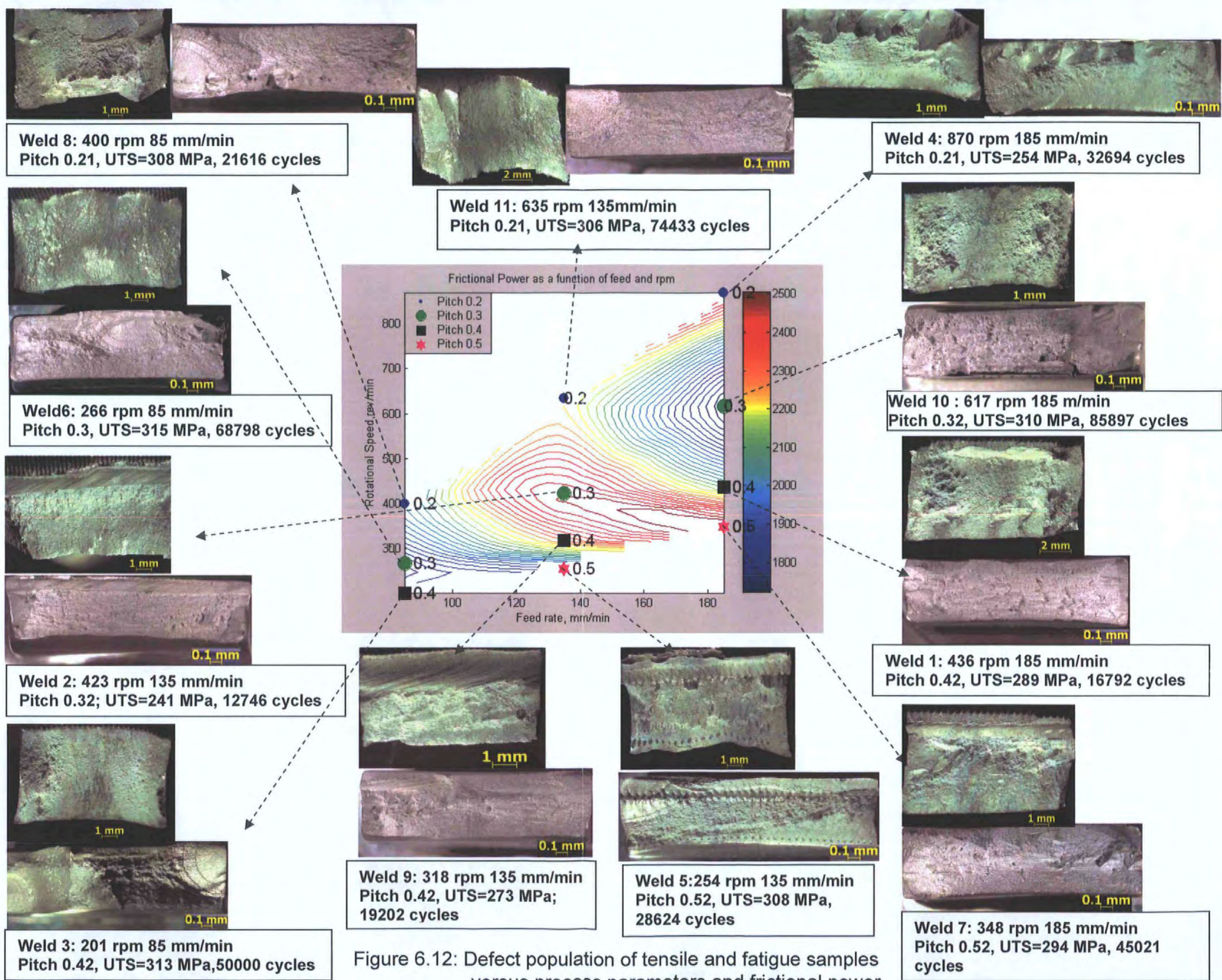


Figure 6.12: Defect population of tensile and fatigue samples versus process parameters and frictional power.

Figure 6.13 presents the fatigue life data for all the individual specimens tested in this thesis.

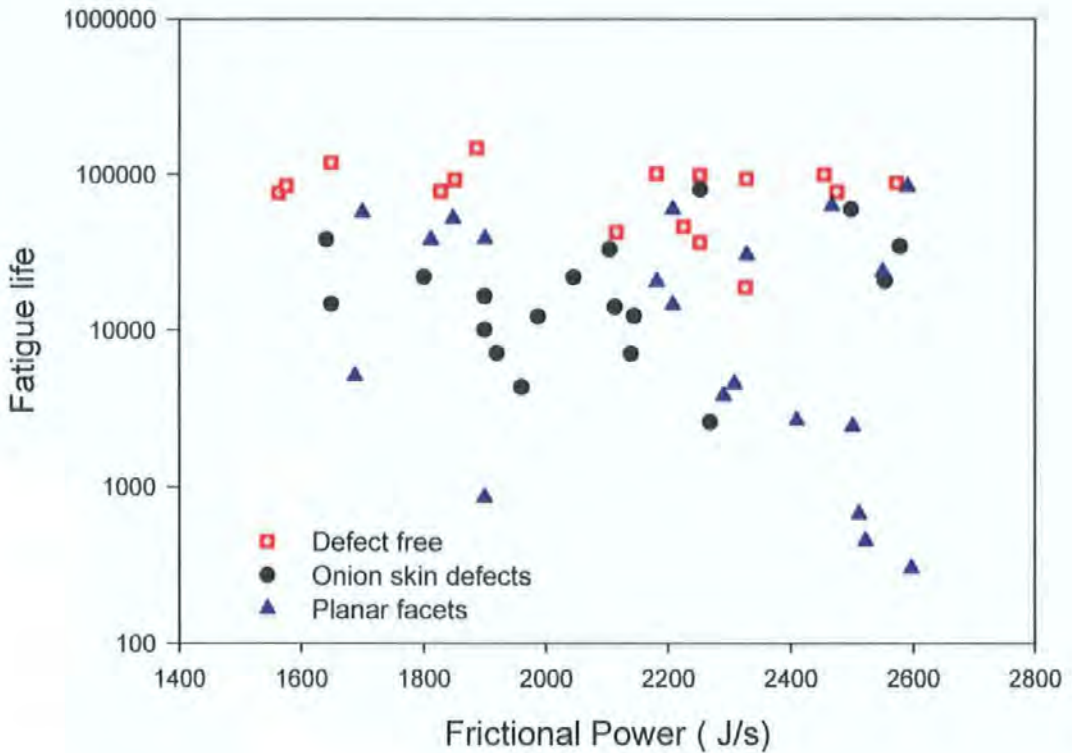


Figure 6.13: Fatigue life as a function of defect type and frictional power input.

The fatigue life of specimens containing onion-skin defects shows a slight increasing trend as frictional power increases, while those specimens containing planar defects show a bifurcation in behaviour as frictional power increases. These trends can be explained in terms of the relative sizes of the defects, and their extent across the weld, which reflect the underlying plastic flow processes in the TMAZ. These, in turn, reflect frictional power input and hence process parameters. Fatigue life is highly sensitive to influences on the crack initiation phase and to the existence of any easy growth routes in-plane with the fatigue crack. Whilst it could be argued that any influences on crack initiation would have a small effect in the low cycle fatigue regime, the fracture surfaces shown in Figures. 6.7 and 6.9 indicate that the pseudo-bond defects in this alloy offer significantly enhanced crack initiation sites and are often associated with crack growth over several millimetres. It is clear that optimum fatigue life requires both defect-free welds and frictional power input below about 1900 J/s.

## 6.8 Residual stress and fatigue life

Generally, when a larger stress is applied the number of fatigue cycles to failure becomes less. If the residual stresses play a role in altering the fatigue life one might expect that an increase in the transverse tensile stresses associated with welding to decrease the fatigue life because these stresses would add to those from the load applied on the sample. The previous section has shown that defect free samples had the largest fatigue lives. Weld 10 gave the highest fatigue life and ratios of the longitudinal and transverse tensile residual stresses for all welds were determined using weld 10's data as reference. All the other welds had lower longitudinal residual stresses than weld 10, thus one would have expected that the fatigue lives should have been higher than weld 10. However, the fatigue lives were actually less, as shown in Table 6.5. The welds that had defects (except for weld 6) have 20-50% of the fatigue life of weld 10. It is therefore assumed that the defects play a major role in decreasing the fatigue life and not the residual stresses. For example, weld 11 contained no defects and had similar longitudinal tensile residual stresses compared to weld 10 (max). Although these welds were made at the same feed rate and weld 11 was made at a larger rotational speed, the fatigue life for weld 11 was 86% of the maximum and weld 9 22%, thus much lower. This must have been the result of the defect present and not the residual stress.

For the transverse stresses welds 2, 4, 5, 6 and 11 have similar deviations: approximately 90% of the largest, weld 10. The transverse stresses are lower than weld 10 and therefore have a smaller effect in increasing the mean stress. A lower stress should be applied to the sample, which should lead to an increase in the fatigue life. For a 16% decrease in transverse residual stresses weld 11 caused a 13% decrease in fatigue strength, and weld 5 a 67% decrease in fatigue strength for the same transverse residual stress in the sample, therefore the defects play a greater role in decreasing the fatigue life.

Weld number	Long Stress (MPa)	Long ratio	Trans Stress (MPa)	Trans ratio	Fatigue life	Number of cycles ratio	defect type
w1	100.08	1.00	41.85	0.77	16792	0.20	os
w2	87.74	0.87	51.38	0.94	12746	0.15	p
w3	66.56	0.66	39.73	0.73	49999	0.58	p
w4	90.54	0.90	52.18	0.96	32694	0.38	p
w5	103.03	1.03	45.60	0.84	28624	0.33	os
w6	72.44	0.72	48.84	0.90	68798	0.80	p,df
w7	98.50	0.98	39.72	0.73	45020	0.52	p,os
w8	56.92	0.57	44.26	0.81	21616	0.25	os
w9	74.03	0.74	38.63	0.71	19202	0.22	p
w11	67.76	0.67	45.90	0.84	74432	0.87	df
w10	100.48	1.00	54.41	1	85896	1.00	df

Table 6.5: Comparison between fatigue lives and residual stress data.

## 6.9 Conclusions

In this chapter the influence of process parameters on the fatigue strength is investigated. It was found that none of the process parameters exclusively influence the changes of the fatigue life. The variation of the fatigue strength with the process parameters are therefore non linear complex relationships. The frictional power on the tool does show a trend with the fatigue life and there was a comparison with the ultimate tensile strength. Unfortunately the models were not good with a correlation coefficient of 0.4. The models did show trends of higher tensile strength corresponding with higher fatigue life, as well as an inverse relationship between frictional power and fatigue life. The scatter usually obtained with fatigue data could lead to the difficulty of obtaining good correlation in the data. More tests conducted at the same point could lead to an improved statistical correlation.

The defect population of the fatigue specimens were also investigated and were correlated with the process parameters. For FS welds in this 5083-H321 alloy, the fatigue performance is dominated by defect-crack path interactions. Defect free samples gave the highest fatigue life. Varying process parameters like tool speed and feed effects defect type and presence much more strongly than microstructure in the nugget or TMAZ. Low frictional power is a useful guide to obtain high quality welds. Low torque is also beneficial, but rotational speed is

the most influential parameter. A rotational speed of 617-635 rpm and 870 rpm gave the lowest torque values. At 870 rpm there was a greater occurrence of onion skin defects occurred than at 617-635 rpm. This implies that plastic flow around the tool is critical to defect occurrence and this is why the frictional power (a function of torque and rotational speed) showed a correlation between tensile and fatigue life. Planar facets are detrimental to fatigue life and they occur at higher vertical force,  $F_z$  and higher torque values.

The surface contour plots can be used to link weld parameters with power and heat input. Tensile and fatigue properties of the welds are related to power and heat input. Using instrumented FS welding machines, guidance can be given on process conditions to achieve an optimum performance.



## **7. Summary of results and suggestions for future work**

This dissertation investigates a process window of the influence of input and output FSW process parameters on the quality and mechanical properties of 6 mm friction stir butt welded 5083-H321 aluminium alloy. The intention was to determine whether the online monitoring system's data can be used to predict weld properties. The following important results were obtained:

- (i) The rotational speed is the key parameter to change the magnitude of tool torque, tool temperature and effective coefficient of friction. The highest spindle torque values are obtained at all feed rates with low rotational speed (between 200 and 300 rpm). The average heat input to the weld is strongly dependent on the changes of feed rate. An increase in feed rate decreases the average heat input.
  
- (ii) The plots of frictional power on the tool indicates that more energy into the weld results in an increase in temperature, less friction on the tool and therefore a greater plasticized state during welding. Comparisons between the frictional power on the tool and process parameters were conducted. The frictional power on the tool has a complex relationship with feed rate and rotational speed and shows a similar trend with regard to the vertical force on the tool. The contour plot of  $F_z$  reflects changes in the plastic flow processes during welding, where two distinct regions of low  $F_z$ , corresponding with low rotational speeds and low feed rates, and with high feed rates and medium rotational speeds are seen. These are separated by a region of speed and feed contributions, giving rise to high  $F_z$ . Higher  $F_z$  values correspond with higher tool temperatures. The frictional power also shows a good quadratic relationship with tool temperature, with a correlation coefficient of 0.67. The area contained within the polar plot of reaction forces on the tool had a good correlation with the power input into the

weld. This should provide an indication of the defect population and the dynamic performance of the welds. Thus, weld soundness and performance should be able to be explicitly linked to process conditions (such as tool pitch, which is defined as weld travel increment per revolution) as a function of alloy and tool design. Predictive capability can be developed, which will give a substantial improvement in the selection of appropriate welding conditions for various combinations of alloy, plate thickness, tool design, and production rates. The Vickers hardness 3mm below the tool shoulder correlates fairly well with the inverse of frictional power (thus lower frictional power is equal to higher Vickers hardness values).

(iii) The resultant force on the tool determined from a polar plot has an inverse relationship with the heat input model. As expected, larger heat input results in smaller forces on the tool. There is a strong influence of pitch on the polar areas and the peak longitudinal residual stresses. The areas of the polar plots also decrease with increasing feed rate and tool speed, which correlates with a decrease in energy as seen in Figure 5.20. A linear correlation of 0.82 could be obtained for the longitudinal residual stresses and the average heat input. Greater heat input in general results in lower residual longitudinal stresses.

(i) The relationship  $w^2/f$ , which is proportional to the plasticized width of the material around the tool, gives a relationship between process parameters i.e tool torque, vertical downwards force and tool temperature. The effective coefficient of friction ( $\mu_{\text{eff}} = \frac{3 \text{ Torque}}{2 F_z x r}$ ) decreases linearly as the tool temperature increases.

- (i) In all the FS welds the region around the weld line was characteristic of tensile stresses and was balanced by the compressive stresses in the parent plate. The longitudinal stresses are approximately 2 to 3 times larger than the transverse stresses, but approximately 22-40% of the 0.2% proof strength of the material. The largest stress was obtained on the shoulder side of the weld. Residual stress became more compressive as feed rate increased. Feed rate plays a dominant role in the changes of the maximum longitudinal stresses. All the process parameters are statistically significant parameters for the peak tensile longitudinal residual stresses. No process parameter showed a good correlation with the peak transverse residual stresses. It seems that torque could play a role in the variation of transverse residual stresses.
  
- (ii) The longitudinal residual stress maps were constant through the length of the plate at depths of 0 mm to -3 mm, -3 mm to -5. mm and -5 to -6 mm indicated that the process conditions of the welds remained constant for the length measured. These maps could be used to verify a FEM/FEA or analytical model to determine the 3D residual stress profile around the tool.

In summary, Figure 6.12 shows the variation of tensile and fatigue data and defect types with frictional power input. Figure 6.12 clearly show that low frictional power regions correspond with high tensile and fatigue strength and defect free specimens. High UTS correlate with defect free welds. Rotational energy between 650 and 400 produce defect free welds. Planar facets correspond with low UTS regions and the degree of plastic deformation of the planar facets correlates well with frictional power. Higher frictional power corresponds to greater plastic deformation. Pseudo-bond defects occur at tool speeds around 400 rpm for all feed rates. Weld 5 had the lowest rotational speed and the most prominent onion skin layers. The rotational speed has the greatest influence on the formation of the onion skin layers. A good inverse relationship between the frictional power on the tool and tensile strength could be obtained. There was not a good correlation

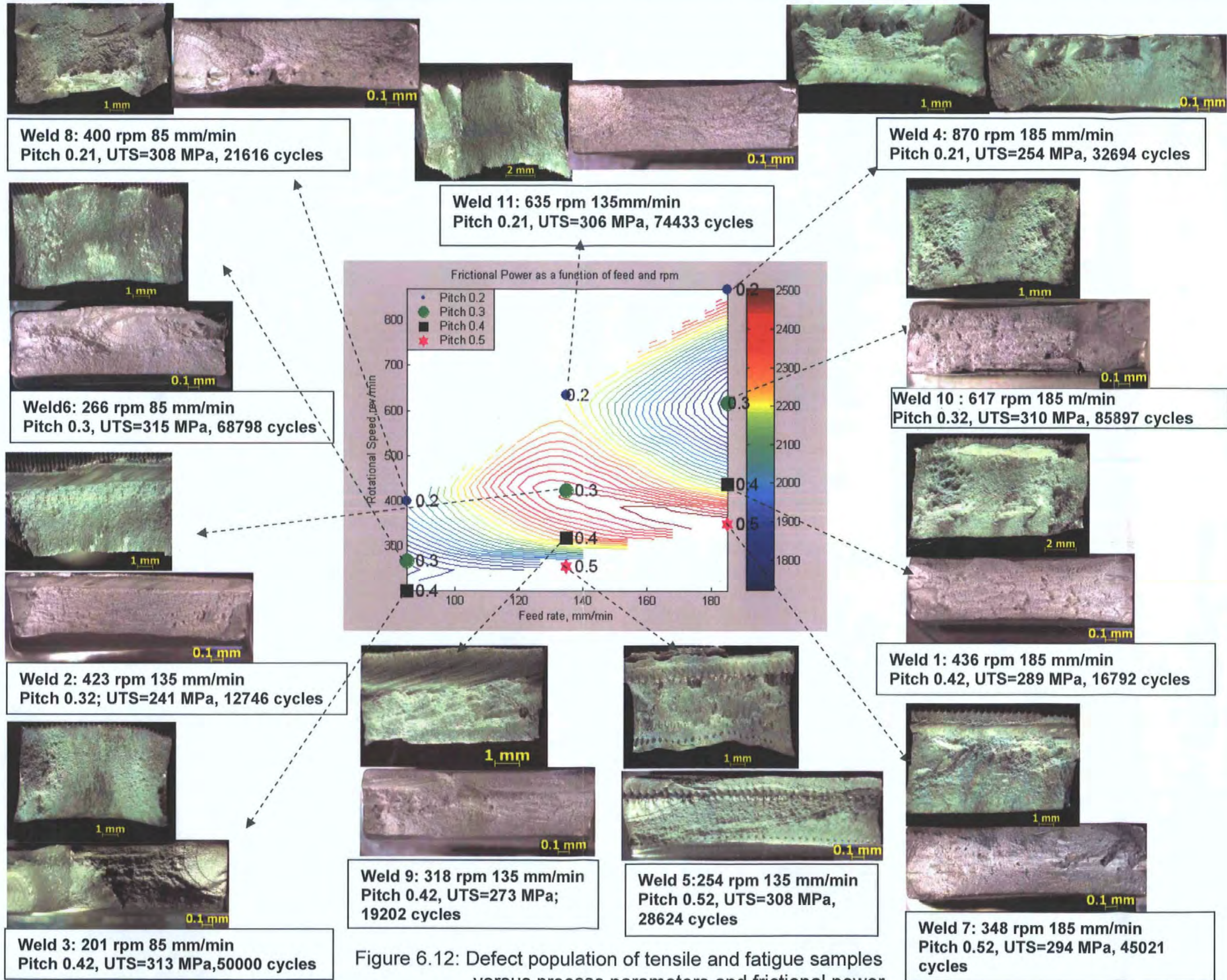


Figure 6.12: Defect population of tensile and fatigue samples versus process parameters and frictional power.

welds with the aid of thermo-couples, even though these measurements are difficult to obtain. The peak temperature of the welds could then be related to process parameters, grain size and residual stresses.

- (iii) The fatigue tests in this thesis should be extended to obtain S-N curves where fatigue life at lower applied loads are determined. This will clarify the process window and reason for the occurrence of onion skin defects and planar facets in FSW. It would also be interesting to investigate the changes of the residual stresses with applied loading or shot peening to try to improve the fatigue life of the samples. Since residual stresses have a detrimental effect on the fatigue life, an investigation into the reduction of residual stresses using post weld heat treatments or tensioning of the welds will be beneficial. This will include relationships between the parameters like temperature, forces applied and the microstructure and mechanical properties of the welds.
- (iv) A FEM or analytical model could be useful to predict the changes of the process parameters on mechanical properties of the weld and to support the data found in this thesis.
- (v) Investigating different tool profiles and welding materials such as precipitate hardened alloys for example 6061-T6 could also extend the investigation in this thesis to determine the effects of tool design and weld material on the:
  - (a) microstructure, for example grain size and hardness;
  - (b) fatigue properties and residual stresses;
  - (c) types of defects on the fatigue specimens; and
  - (d) fracture toughness and crack growth studies.

This would expand the data base about knowledge of FSW.

between the 0.2% proof strength and UTS. The defect population of the fatigue specimens were also investigated and it was found that planar facets are detrimental to fatigue life and they occur at higher vertical downwards force, ( $F_z$  and higher torque values). The variation of the fatigue strength with the process parameters is a non-linear complex relationship. The frictional power on the tool does show an inverse trend with the fatigue strength and there was a comparison with the ultimate strength. The scatter usually obtained with fatigue data could lead to the difficulty of obtaining good correlation in the data. More tests conducted at the same point could lead to an improved statistical correlation.

It is clear from the results and discussion that monitoring of vertical downwards force reaction on the tool, applied tool torque and subsequent tool temperature would provide a much-improved way of assessing the attainment of suitable welding conditions in the metal. This alone would eliminate some of the empiricism currently attendant on selection of suitable weld process parameters under changing alloy/joint conditions.

The following suggestions can assist in obtaining a better insight into FSW and support the current data obtained in this thesis:

- (i) Since the microstructure of the material was affected by the pin movement, and not only the heat input from the shoulder, this indicated that the flow of the material around the tool could also have an effect on the residual stresses and Vickers hardness developed in the weld and it would be interesting to investigate the flow dynamics of the specific tool at various weld settings, by using either a metal insertion technique (like Cu layers) or introducing particles in the material or by stopping the tool during welding. The latter will produce the most accurate results but is very costly because the tool will have to be destroyed each time.
- (ii) The relationship between grain size, hardness and residual stress with respect to process parameters could be investigated in a greater depth. It would be useful to determine the peak temperature in the

## References

- Allen, TT; Richardson, RW; Tagliabue, DP and Maul, GP. (2002) Statistical process design for robotic GMA welding of sheet metal: an optimization procedure minimizes cycle time while achieving small fractions of nonconforming welds. *Supplement to The Welding Journal*. May. Pp. 69-S-77-S.
- Altintas, Y. (2000)  
*Manufacturing Automation: metal cutting mechanics, machine tool vibrations and CNC design*. Cambridge University Press: New York.
- American Society for Testing and Materials (ASTM). (1995) Standard practice for conducting force controlled constant amplitude axial fatigue tests of metallic materials – E 446-96. *Annual Book of ASTM Standards*. Section 3 - Metals test methods and analytical procedures. Vol 03.01 Metals-mechanical testing; elevated and low temperature tests; metallography. Philadelphia.
- Aota, K; Okamura, H; Masakuni, E and Takai, H. (2001) Heat inputs and mechanical properties in friction stir welding. Proceedings of the 3<sup>rd</sup> International Symposium on Friction Stir Welding: Kobe, Japan. 27-28 September. TWI(UK). Retrieved: CD-ROM.
- Arbegast, WJ and Hartley, PJ. (1998) Friction Stir Weld Technology Development at Lockheed Martin Michoud Space Systems- An Overview. Proceedings of the 5<sup>th</sup> International Conference on Trends in Welding Research: Pine Mountain, GA, USA. June 1–5. P. 541.
- Arbegast, WJ and Allen, CD. (2004) Friction stir welding of complex curvature parts using rapid configurable tooling. Proceedings of the 5<sup>th</sup> International Symposium on Friction Stir Welding: France. 14-16 September. TWI(UK). Retrieved: CD-ROM.
- Ashby, MF; Jones, DRH. (1980)  
*Engineering Materials 1*. Pergamon Press, Oxford.
- ASM International. (1991) *Atlas of time-temperature diagrams for irons and steels*. ASM:USA. Pp 558.
- Bannantine, JA; Comer, JJ; Handrock, JL. (1990) *Fundamentals of metal Fatigue Analysis*. Englewood Cliffs: Prentice:Hall.
- Benavides, S; Li, Y; Murr, LE; Brown D and McClure, JC. (1991) Low-temperature friction stir welding of 2024 aluminum. *Scripta Materialia*. 10 September. 41 (8). Pp. 809-815.
- Bendzsak, GJ; North TH and Smith, CB. (2000) An experimentally validated 3D model of friction stir welding. Proceedings of the 2<sup>nd</sup> Friction Stir Welding Symposium: Gothenburg, Sweden. June 2000. TWI(UK) Retrieved: CD-ROM.
- Benson, PG and Backland, J. (2000) Possibilities with aluminium extrusions joined by friction stir welding. Proceedings of the 4<sup>th</sup> International Forum on Aluminium Ships: New Orleans. 10-11 May. Retrieved: CD-ROM.

- (vi) The study in this thesis can be extended to include the shift in the angle of the resultant force. It would be useful to investigate the possibility of the variation in the angle of the resultant force with plastic flow processes during FS welding and the mechanical properties of FSW. This will finally clarify whether the force footprint monitoring data can be used to indicate optimum FS welds.



- Bevington, J. (1891) Spinning tubes mode of welding the ends of wire, rods, etc and mode of making tubes. US Patent 463134. 13 January.
- Bhadেশia, HKDH. (2003) Joining of commercial aluminium alloys. Proceedings of the International Conference on Aluminium (INCAL '03). Aluminium Association of India: Bangalore. Eds: S. Subramanian and D. H. Sastry. Pp. 195-204.
- Biallas, G; Braun, R; Dalle Donne, C; Staniek, G; Kaysser, WA. (1999) Mechanical properties and corrosion behaviour of friction stir welded 2024-T3 1<sup>st</sup> International Symposium on Friction Stir Welding, Thousand Oaks, California, USA, 14-16 June. TWI(UK). Retrieved: CD-ROM.
- Bird, C. (2003) Ultrasonic phased array inspection for the evaluation of friction stir welds. Proceedings of the 4<sup>th</sup> International Symposium on Friction Stir Welding: Utah, USA. 14-16 May. TWI(UK). Retrieved: CD-ROM.
- Bird, C. (2004). The inspection of Friction Stir welded aluminium plant. Proceedings of the 5<sup>th</sup> International Symposium on Friction Stir Welding: Metz, France. 14 – 16 September. TWI(UK). Retrieved: CD-ROM.
- Blacklund, J; Norlin, A and Anderson, A. (1998) Friction stir welding-weld properties and manufacturing techniques. Proceedings of the 7<sup>th</sup> International Conference on Joints in Aluminium (Inalco). Pp. 184-196
- Blignaut, C. (2004) *Design, development and analysis of the friction stir welding process*. M. Tech dissertation. Faculty of Engineering, Port Elizabeth Technikon.
- Blum, W; Zhu, Q; Merkel, R and Mc Quen, HJ. (1996) Geometric dynamic recrystallization of hot torsion in Al<sub>5</sub>Mg<sub>0.6</sub>Mn. *Materials Science and Engineering A* (205). Pp. 23-30.
- Booth, D and Sinclair, I. (2001) Fatigue of friction stir welded aluminium alloy 2024-T351. Retrieved: [www.southampton.ac.uk/ses/docs/pgconf2001/diccon\\_pgq.pdf](http://www.southampton.ac.uk/ses/docs/pgconf2001/diccon_pgq.pdf). January 2003.
- Bradley, GR. (2000) *Geometry and microstructure of metal inert gas and friction stir welded aluminium alloy 5383-H321*. PhD Thesis. Department of Mechanical and Marine Engineering. University of Plymouth: England.
- Bradley, GR and James, MN. (2000) Residual stresses/strains induced by the metal; inert gas and friction stir welding processes. Retrieved: [http://www.tech.plymouth.ac.uk/sme/UoA30/Weld\\_Microstructure.PDF](http://www.tech.plymouth.ac.uk/sme/UoA30/Weld_Microstructure.PDF)
- Bradley, GR; Hattingh, DG; Yio, TC and James, MN. (2003) Crack paths in friction stir welded 5083-H321 and 5383-H321 aluminium alloys. International Conference on Crack Paths: Parma, Italy. September 2003. Retrieved: CD-ROM.
- Brandes, EA and Brook, GB. (1992) *Smithells Metals Reference Book*. 7<sup>th</sup> Edition. Butterworth-Heinemann: Woburn, Massachusetts.
- Brinckmann, S; Von Strombeck, A; Schilling, C; Dos Santos, JF; Lohwasser D and Koçak, M. (2000) Mechanical and toughness properties of robotic-FSW repair welds in 6061-T6 Aluminum alloys. Proceedings of the 2<sup>nd</sup> International

Symposium on Friction Stir Welding: Sweden. 26-28 June. TWI(UK). Retrieved: CD-ROM.

Brooksbank, ED and Andrews, KW. (1968) *Journal of the Iron and Steel Institute* (206) June. Pp 595-599.

Brooksbank, ED and Andrews KW. (1969) *Journal of the Iron and Steel Institute* (207) June. Pp 474-483

Brooksbank, ED and Andrews KW. (1972) *Journal of the Iron and Steel Institute* (210) April. Pp 246-255.

Bukarov, V. (1997) Development of models controlling arc welding performance and quality. *Welding Journal*. 79(12). Pp. 35-39.

Bussu, G and Irving, PE. (1999) Fatigue performance of friction stir welded 2024-T351 aluminium joints. Proceedings of the 1st International Symposium on Friction Stir Welding: Thousand Oaks, CA, USA. 14-16 June. TWI(UK). Retrieved: CD-ROM.

Bussu, G and Irving, PE. (2003). The role of residual stress and heat affected zone properties on fatigue crack propagation in friction stir welded 2024-T351 aluminium joints. *International Journal of Fatigue*. 25. Pp. 77-88.

Camassa, A; Capitani, V and Lamarre, A. (2001) New development of the ultrasound phased-array and eddy current array technologies for the evaluation of friction stir welds. Proceedings of the 3<sup>rd</sup> International Symposium on Friction Stir Welding: Kobe, Japan. 27-28 September. TWI (UK). Retrieved: CD-ROM.

Chao, YJ and Qi, X. (1998). Thermal and thermo-mechanical modeling of friction stir welding of aluminum alloy - 6061-T6. *Journal of Materials Processing & Manufacturing Science* (USA). 7(2). Pp. 215-233.

Chao, YJ and Qi, X. (1999) Heat transfer and thermo-mechanical analysis of friction stir joining AA 6061-T6 plates. Proceedings of the 1<sup>st</sup> International Symposium on Friction Stir Welding: Thousand Oaks, CA, USA. 14-16 June TWI(UK). Retrieved: CD-ROM.

Chen, C and Kovacevic, R. (2003) Finite element modeling of thermomechanical performance of friction stir welding. Proceedings of the 4<sup>th</sup> International Symposium on Friction Stir Welding: Utah, USA. 14-16 May. TWI(UK).

Chen, ZW and Maginess, R. (2004) Formation of weld zones during friction stir welding of aluminium alloys. Proceedings of the 5<sup>th</sup> International Symposium on Friction Stir Welding: Metz, France. 14 – 16 September. TWI(UK). Retrieved: CD-ROM.

Choueiki, MH and Mount-Campbell, CA. (1999) Training data development with the D-optimality criterion . *IEEE Transactions on Neural networks* 10 (1) 56-s to 63-s. (IEEE Computational Intelligence Society)

Claussen, B; Lorentzen, T and Leffers, T. (1998) Self consistent modelling of plastic deformation of FCC polycrystals and its implications for diffraction measurements of internal stresses. *Acta Materialia*. (46)9. Pp. 3087-3098.

Colegrove, P; Painter, M; Graham, D and Miller, T. (1999) 3 Dimensional flow and thermal modelling of the friction stir welding process. Proceedings of the 1<sup>st</sup> International Symposium on Friction Stir Welding: Thousand Oaks, CA, USA. 14-16 June. TWI(UK). Retrieved: CD-ROM.

Colegrove, P; Painter, M; Graham, D and Miller, T. (2000) Three-dimensional flow and thermal modelling of the friction stir welding process. Proceedings of the 2<sup>nd</sup> FSW Symposium: Gothenburg, Sweden. 26-28 June. TWI(UK). Retrieved: CD-ROM.

Colegrove, PA; Shercliff, HR and Threadgill, PL. (2003) Modelling and development of the TRivex TM friction stir welding tool. Proceedings of the 4<sup>th</sup> International Symposium on Friction Stir Welding Utah, USA. 14-16 May. TWI(UK). Retrieved: CD-ROM.

Colegrove, PA and Shercliff, H. (2003) Experimental and numerical analysis of aluminum alloy 7075-T7351 friction stir welds. *Science and Technology of Welding & Joining*. 8(5). Pp. 360–369.

Colligan, KJ. (1999) Material flow behaviour during friction stir welding of aluminium. Supplement to the *Welding Journal*. American welding society and research council. Pp. 229s-37s. Retrieved: <http://aws.org/wjl>

Colligan, KJ; Ucock, I; McTernan, K; Konkol, PJ and Pickens, JR. (2001). Friction stir welding of thick section 5083-H131 and 2195-T8P4 aluminium plates. Proceedings of the 3<sup>rd</sup> International Symposium on Friction Stir Welding: Kobe, Japan. 27-28 September. TWI(UK). Retrieved: CD-ROM.

Colligan, KJ : Friction stir welding tool for welding variable thickness workpieces (Boeing). United States Patent No 5,718,366.

Colligan, KJ; Xu, J and Pickens, JR. (2003) Welding tool and process parameter effects in friction stir welding of aluminium alloys. *Friction Stir Welding and Processing II*. Edited by : Jata, KV; Mahoney, MW; Lienert, TJ and Mishra, RS. The Minerals, Metals and Materials Society (TMS). Pp. 181-190.

Collins, JA. (1993) *Failure of materials in mechanical design* .2<sup>nd</sup> Edition, John Wiley and Sons, (USA).

Cullity, BD. (1967)  
*X-ray Diffraction*, Addison-Wesley publishers.

Dalle Donne, C and Biallas, G. (1998) Fatigue and fracture performance of friction stir welded 2024-T3 joints. Proceedings: European Conference on Spacecraft Structures, Materials and Mechanical Testing: Braunschweig, Germany. 4-6 November. (ESA SP-428, February 1999). Pp. 309 – 314.

Dalle Donne, C; Biallas, G; Ghidini, T and Raimbeaux, G. (2000) Effect of weld imperfections and residual stresses on the fatigue crack propagation in friction stir welded joints. Proceedings of the 2<sup>nd</sup> International Conference on FSW: Sweden. 26-28 June. TWI(UK). Retrieved: CD-ROM.

Dalle Donne, D. (2001) Investigations on residual stresses in friction stir welds. Proceedings of the 3<sup>rd</sup> International Symposium on Friction Stir Welding: Kobe, Japan. 27-28 September. TWI (UK). TWI(UK). Retrieved: CD-ROM.

Dalle Donne, C and Raimbeaux, G. (2001) Residual stress effects on fatigue crack propagation in friction stir welds International Conference on Fracture ICF 10, 3-7 December 2001, Hawaii, USA, Elsevier.

Dawes, CJ and Thomas, WM. (1996). Friction stir process welds aluminium alloys. *Welding Journal*. 75(3). Pp. 41-45.

Dawes, CJ and Thomas, WM. (1999) Development of improved tool designs for friction stir welding of aluminium. Proceedings of the 1<sup>st</sup> International Symposium on Friction Stir Welding: Thousand Oaks, CA, USA. 14-16 June. TWI(UK). Retrieved: CD-ROM.

Dawes, CJ; Li, Z and Adams, G. (1999) FSW Aluminium Alloy 5083 - Increased welding speed. *TWI CRP Report 684/1999*. August.

Dawes, CJ; Staines, DG and Spurgin, EJR. (1999a) Tool development for friction stir welding of 6mm thick aluminium alloys 7417. 02/99/1056.3 TWI.

Dawes, CJ; Krager, SA and Dickerson, TL. (2000) Strength and Fracture Toughness of Friction Stir Welds in Aluminium alloys. TWI website: ([www.twi.co.uk](http://www.twi.co.uk))

Dawes, CJ. (2000). Friction stir welding of transport structures-phase 2. *TWI GSP Report No. 12020/11/00*. August.

Design of experiments. [http://www.isixsigma.com/dictionary/Design\\_of\\_Experiments-DOE-41.htm](http://www.isixsigma.com/dictionary/Design_of_Experiments-DOE-41.htm) iSixsigma website. Retrieved: June 2004.

Dickerson, PB. (1993) Welding of aluminium alloys. *In ASM Handbook, Volume 6 – Welding, Brazing and Soldering*, Pp 722-739. ASM International, Ohio; 1993. ISBN 0-87170-382-3

Dickerson, TL and Przydatek, J. (2003) Fatigue of friction stir welds in aluminium alloys that contain root flaws. *International Journal of Fatigue*. 25. Pp. 1399-1409.

Dieter, G. (1976) *Mechanical Metallurgy*. Second edition. McGraw Hill: USA.

Dieter, GE. (1989) *Mechanical Metallurgy*. Second edition. McGraw Hill: New York

Dong, P; Lu, F; Hong, JK and Cao, Z. (2001) Coupled thermomechanical analysis of friction stir welding process using simplified models. *Science and Technology of Welding and Joining*. 6(5). Pp. 281-287.

Dye, D; Stone, HJ and Reed, RC. (2001) Intergranular and interphase microstresses. *Current option in Solid State and materials Science*. 5(1). Pp. 31-37.

Easterling, K. (1992) *Introduction to the physical metallurgy of welding*. Butterworth-Heineman: Oxford Press (London).

Ericsson, M and Sandström, R. (2003) Influence of welding speed on the fatigue of friction stir welds, and comparison with MIG and TIG. *International Journal of Fatigue*. 25. Pp. 1379-1387.

Field, DP; Nelson, TW; Hovanski, Y and Jata, KV. (2001) Heterogeneity of Crystallographic Texture. *Friction Stir Welds of Aluminum, Metallurgical and Materials Transactions A*. 32A(11). November. Pp. 2869-2877.

Fisher, RA. (1925) *Statistical Methods for Research Workers*. Polver and Boyd: London.

Fitzpatrick, ME; Hitchings MT and Withers, PJ. (1997) Separation of macroscopic elastic mismatch and thermal expansion misfits stresses in metal matrix composites quenched plates from neutron diffraction measurements. *Acta Materials*. 45 (12). Pp. 4867-4876.

Fitzpatrick, ME and Lodini, A. (2003) *Analysis of residual stress by diffraction using neutron and synchrotron radiation*. Taylor and Francis , new York, USA.

Flores, OV; Kennedy, C; Murr, LE; Brown, D; Pappu, S; Nowak, BM and McClure, JC. (1998) Microstructural issues in a friction stir welded aluminium alloy. *Scripta Materialia*. 38(5). Pp. 703-708.

Friction Stir Weld Geometries. <http://www.twi.co.uk/j32k/unprotected/band1/fswjoint.html> Retrieved : April 2003.

Frigaard, Ø; Grong, Ø and Midling, OT. (1999) Modeling of the heat flow phenomena in friction stir welding of aluminum alloys. Proceedings of the 7<sup>th</sup> International Conference on Joints in Aluminum (INALCO '98). Cambridge:UK. April 15-17. Pp. 208-218.

Frigaard, ØG and Midling, OT. (2001) A Process Model for Friction Stir Welding of Age Hardening Aluminum Alloys. *Metallurgical and Materials Transactions A*. 32(5). May. Pp. 1189-1200.

Gallais, C; Denquin, A; Pic, A; Simar, A; Pardoën, T and Bréchet, Y. (2004) Modelling the relationship between process parameters, microstructural evolutions and mechanical behaviour in friction stir welded 6xxx aluminium alloy. Proceedings of the 5<sup>th</sup> International Symposium on Friction Stir Welding: Metz, France. 14 – 16 September. TWI(UK). Retrieved: CD-ROM.

Gould, JE and Feng, Z. (1998) Heat flow model for friction stir welding of aluminum alloys. *Journal of Material Processing and Manufacturing Science*. 7. Pp. 185-194.

Guerra, M; Schmidt, C; McClure, JC; Murr, LE and Nunes, AC. (2003) Flow patterns during friction stir welding. *Materials Characterization*. 49. Pp. 95–101.

Haagensen, PJ; Midling, OT and Ranes, M. (1995) Fatigue performance of friction stir butt welds in a 6000 series aluminium alloy, *Computer Methods and Experimental Measurements for Surface Treatment Effects II*, Computational Mechanics Publications. Pp. 225-237.

Haagensen, PJ; Midling, OT and Ranes, M. (1996) Fatigue performance of friction stir butt welds in a 6000 series aluminum alloy. *International Journal of Fatigue*. 18(7). October. P. 508.

Hall, EO. (1951) The deformation and ageing of mild steel: III Discussion of results. *Proc. Phys. Soc. London B64*, Pp. 747-753.

Hansen, M. (2003) A cooler weld. *Mechanical Engineering Design*. Retrieved: <http://www.memagazine.org/medes03/coolweld/cwsidebar.html> 5 March 2003.

Harwig, DD.(2000) A wise method for assessing arc welding performance and quality. *Welding Journal*. 79(12). Pp. 35–39.

Hassan, Kh AA; Norman, AF and Prangnell, PB. (2001) The effect of welding conditions on the microstructure and mechanical properties of the nugget zone in AA7010 alloy friction stir welds. *Proceedings of the 3<sup>rd</sup> International Symposium on Friction Stir Welding: Kobe, Japan. 27-28 September. TWI(UK)*. Retrieved: CD-ROM.

Hassan, Kh AA; Wynne, BP and Prangnell, BP. (2003) The simulation of nugget zone grain structures in high strength aluminium alloys friction stir welds by high strain torsion testing. *Proceedings of the 4<sup>th</sup> International Symposium on Friction Stir Welding: Utah, USA. 14-16 May. TWI(UK)*.

Hashimoto, T; Jyogan, S; Nakata, K, Kim YG and Ushio, M. (1999) FSW joints of high strength aluminium alloy. *Proceedings of the 1<sup>st</sup> International Symposium on Friction Stir Welding: Thousand Oaks, CA, USA. 14-16 June TWI(UK)*. Retrieved: CD-ROM.

Hattingh, DG; van Niekerk, TI; Blignault, C ; Kruger, G and James, MN. (2004) Analysis of the FSW force footprint and its relationship with process parameters to optimise weld performance and tool design. *IJW Journal Welding in the World*. 48(1-2). Pp. 50-58.

Hauk, V.(1997)  
*Structural and residual stress analysis by non destructive methods*, Elsevier, Amsterdam, Oxford.

Hayashi, M and Oyama, K. (2001) Mechanical properties of friction stir welded 5083 aluminium alloy at cryogenic temperatures. *Proceedings of the 3<sup>rd</sup> International Symposium on Friction Stir Welding: Kobe, Japan. 27-28 September. TWI(UK)*. Retrieved: CD-ROM.

Heinz, B and Skrotzki, B. (2002) Characterization of a friction stir welded aluminum alloy 6013. *Metallurgical and Materials Transactions B*. 33B(3). June. Pp. 489-498.

Hennebloeche, U; Palm, F and Steiger, H. (2003) The origin of particle oxide traces in friction stir welds. Proceedings of the 4<sup>th</sup> International Symposium on Friction Stir Welding, Utah, USA. 14-16 May. TWI(UK). Retrieved: CD-ROM.

Heston, T. (2002) Taking Off with Friction Stir Welding. *Fabrication and Metalworking Magazine*. [http://www.ndx.com/article.asp?article id=392&channel id=4](http://www.ndx.com/article.asp?article%20id=392&channel%20id=4) Retrieved: 3 January 2004.

Hirano, S; Okamoto,K; Aota,K; Okamura,H; Aono, Y and Odakura, T. (2001) Development of a three dimensional type friction stir welding equipment . 3rd International Symposium on Friction Stir Welding: Kobe, Japan. 27-28 September. TWI(UK). Retrieved: CD-ROM.

Holt, ES and Lang, JL. Programmable friction stir welding process (Rockwell), United States Patent 5,713,507.

Hori, H; Makita, S and Hino, H. (1999) Friction Stir welding of rolling stock for subway. Proceedings of the 1<sup>st</sup> International Symposium on Friction Stir Welding: Kobe, Japan. 27-28 June. TWI(UK). Retrieved: CD-ROM.

Hughes, DJ; James, MN; Hattingh, DG and Webster, PJ. (2004) *Journal of Neutron Research*. 00(0). Pp.1-5.

Humphreys, FJ and Hatherley, M. (2002) *Recrystallization and related annealing phenomena*. Elsevier Science Ltd , Oxford, UK.

Hutchings, MT; Withers, PJ; Holden, TM and Lorentzen, T (2005) *Introduction to the characterization of residual stress by neutron diffraction*. Taylor and Francis, New York, USA.

ISO standard. (2001) Technology Trends Assessment ISO/TTA 3. Polycrystalline materials — Determination of residual stresses by neutron diffraction. Versailles Project on Advanced Materials and Standards National Institute of Standards and Technology. Gaithersburg, Maryland 20899-0001, USA. Ref. No.: ISO/TTA 3:2001(E)

James, MN. (1991) The role of the fracture expert in failure analyses. *Forensic Engineering*. 3(1). Pp. 7-21.

James, M R and Lu ,J. (1996). *Introduction*. 'Handbook of Measurement of Residual Stress'. Edited by Lu J. The Fairmont Press, Inc.

James, MN and Hattingh, DG. (2002). Influence of travel speed on fatigue life of friction stir welds in 5083 aluminium. *Fatigue 2002*. 25(12) Pp. 1389-1398.

James, MN; Hattingh, DG and Bradley, GR. (2003) Weld tool travel speed effects on fatigue life of friction stir welds in 5083 aluminium. *International Journal of Fatigue*. 25. Pp. 1389–1398.

James, M and Mahoney, M. (1999) Proceedings of the 1<sup>st</sup> International Symposium on Friction Stir Welding: Thousand Oaks, CA, USA. June 14–16. TWI(UK). Retrieved: CD-ROM.

James, MN; Hugh, DJ; Hattingh, DG; Bradley, GR; Mill, G and Webster, PJ. (2004) Synchrotron diffraction measurement of residual stresses in friction stir welded 5383-H321 aluminium butt joints and their modification by fatigue cycling. *Fatigue & Fracture of Engineering Materials & Structures* 27(3). March P. 187.

James, MN; Bradley, GR; Lombard, H and Hattingh, DG. (2005) The Relationship between Process Mechanisms and Crack Paths in Friction Stir Welded 5083-H321 and 5383-H321 Aluminium Alloys. *Fatigue and Fracture of Engineering Materials and Structures*. 28. Pp. 662-678.

James, MN (2006) Measurement of residual stresses. Presentation at residual stress seminar. Nelson Mandela Metropolitan University. South Africa

Jata, KV; Sankaran, KK and Ruschau, JJ. (2000) Friction stir welding effects on microstructure and fatigue of aluminum alloy 7050-T7451. *Metallurgical and Materials Transactions A*. 31A(9). September. Pp. 2181-2192.

Jata, KV and Semiatin, SL. (2000) Continuous dynamic recrystallization during friction stir welding of high strength aluminum alloys. *Scripta Materialia*. 43(8). 29 September. Pp. 743-749.

Jayaraman, N; Prevey, P; Mahoney, M; Jata, KV; Mahoney, MW; Mishra, RS; Semiatin, SL; Lienert, T. (2003) Friction Stir Welding and Processing II. *The Minerals, Metals & Materials Society*. P. 259.

John, R ; Jatta, KV and Sadananda, KV. (2003) Residual stresses effects on near-threshold fatigue crack growth in friction stir welds in aerospace alloys. *International Journal of Fatigue*. 25. Pp. 939-948.

Johnson, R. (2000) Force in friction stir welding of aluminium alloys - further studies. TWI bulletin 7417.01/00/1076.3. Retrieved: [http://www.twi.co.uk/j32k/unprotected/band\\_1/offhigh\\_papers.html](http://www.twi.co.uk/j32k/unprotected/band_1/offhigh_papers.html)

Johnson, R. (2001) Forces in Friction Stir Welding of Aluminium Alloys. Proceedings of the 3rd International Symposium on Friction Stir Welding: Kobe, Japan. 27-28 September. TWI(UK). Retrieved: CD-ROM.

Jun-Ming, L and Zhuang-Chun, W. (1997) Grain growth and grain boundary segregation in binary alloys: a Monte-Carlo simulation. *Scripta Materialia*. 37(4). 15 August. Pp. 385-391.

Kaelble, EF. (1967)  
*Handbook of X-rays for diffraction emission, absorption and microscopy*. Mc-Graw Hill, New York , USA.

Kallee, SW; Nicholas, D; Powell, H and Lawrence, L. (1998) Knowledge-based software package for friction stir welding. Proceedings of the 7<sup>th</sup> International Conference on Joints in Aluminium: Cambridge, UK. 15-17 April.



Kallee, SW; Nicholas, D; Powell, H and Lawrence, L. (1998) Knowledge-based software package for friction stir welding. Proceedings of the 7<sup>th</sup> International Conference on Joints in Aluminium: Cambridge, UK. 15-17 April.

Kallee, SW. (2001) Friction stir welding - how to weld aluminium without melting it. *Innovations for New Rail Business*. IMechE: London, 24 May.

Karlsen, M; Tangen, S; Hjelen, J; Frigaard, O and Grong, O. (2001) Characterization of the deformation microstructure in friction stir welded 7075 T6 aluminium alloy using the SEM-EBSD technique. Proceedings of the 3<sup>rd</sup> International Symposium on Friction Stir Welding: Kobe, Japan. 27-28 September. TWI(UK). Retrieved: CD-ROM.

Karlsson, J; Karlsson, B; Larsson, H; Karlsson, L; Svensson, L-E (1998) Microstructure and properties of friction stir welded aluminium alloys. INALCO '98 – Joints in Aluminium, 7<sup>th</sup> International Conference Pre-prints (Volume 2) –Cambridge, UK, 15 April. Pp. 221–230.

Khandkar, MZH; Khan, JA and Reynolds, AP. (2003) Prediction of temperature distribution and thermal history during friction stir welding: input torque based model. *Science and Technology of Welding and Joining*. 8(3). Pp.165-174.

Klopstock, H and Neelands, AR. (1941) An improvement method of joining or welding metals. British Patent specification 572789, October 17.

Klug, HP and Alexander, LE (1974) *X-ray diffraction procedures. for polycrystalline and amorphous materials*, John Wiley and sons, New York, USA,

Kohstall, P. (1999) Safety and Seat development. *Automobiltechnische Zeitschrift* 101(12).

Krishnan, KN. (2001). On the formation of onion rings in friction stir welds. *Materials Science and Engineering A*. 327(2). 30 April. Pp. 246-251.

Kruger, G. (2003) *Intelligent Monitoring and Control systems for a friction stir welding process*. M. Tech dissertation. Faculty of Engineering, Port Elizabeth Technikon.

Kwon, YJ; Saito, N and Shigematsu, I. (2002) Friction stir process as a new manufacturing technique of ultrafine grained aluminum alloy. *Journal of Material Science Letters* 4(21). Pp. 1473-1476.

Kwon, YJ; Shigematsu, I and Saito, N. (2003) Mechanical properties of fine-grained aluminum alloy produced by friction stir process. *Scripta Materiala*. 49. Pp. 785-789.

Larsson, H; Karlsson, L; Svensson, LE. (1998) Characteristics of friction stir welds in AA 5083 and AA 6082 aluminium. *Proceedings of International Conference on Aluminium Alloys* 3(6). Pp. 1471-1476.

Lee, SL and Wu, SE. (1986) Influences of soaking treatments on hot ductility of Al 4.85 Mg alloys containing manganese. *Metallurgical and materials transactions*. 17A(15). Pp. 833-841.

Lee, WB; Yeon, YM and Jung, SB. (2003) The improvement of mechanical properties of friction stir welded A356 Al alloy. *Materials Science and Engineering A*. Pp. 1-6.

Leonard, AJ and Lockyer, SA. (2003) Flaws in friction stir welds. Proceedings of the 4<sup>th</sup> International Symposium on FSW: Utah, USA. 14-16 May. TWI(UK). Retrieved: CD-ROM.

Li, Y; Murr, LE and McClure, JC. (1999) Flow visualization and residual microstructures associated with the friction-stir welding of 2024 aluminum to 6061 aluminum. *Material Science and Engineering A*. (271). Pp. 213-223.

Lienert, TJ. (2002) Presentation at 5<sup>th</sup> International conference on Trends in welding Research, April, Pine Mountain, GA, USA.

Lienert, TJ; Stellweg, WL and Lehman, LR. (2003) Heat inputs, peak temperatures and process efficiencies. Proceedings of the 4<sup>th</sup> International Symposium on FSW: USA. 14-16 May. TWI(UK). Retrieved: CD-ROM.

Lindner, L; Khandkar, Z; Khan, J; Tang, W and Reynolds, AP. (2003) Rationalization of hardness distributions in alloy 7050 friction stir welds based on weld energy, weld power and time temperature history. Proceedings of the 4<sup>th</sup> International Symposium on FSW: USA. 14-16 May. TWI(UK). Retrieved: CD-ROM.

Little, RE. (1975) *Manual and Statistical Planning and Analysis of Fatigue Experiments*, STP 588, ASTM, Philadelphia.

Liu, G; Murr, LE; Niou, CS; McClure, JC and Vega, FR. (1997) Microstructural aspects of the friction stir welding of 6061-T6 aluminium. *Scripta Materialia*. 37(3). 1 August. Pp. 355-361.

Liu, G; Murr, LE; Niou, C-S and McClure, JC. (2001) A process model for friction stir welding of age hardening aluminum alloys. *Metallurgical and Materials Transactions A*.32A(5). May. Pp.1189-1200.

Liu, HJ; Fujii, H; Maeda, M and Nogi, K. (2003) Comparative study on fracture locations of FSW joints for different types of aluminium. Proceedings of the 4<sup>th</sup> International Symposium on FSW: Part City, Utah, USA. 14-16 May. TWI(UK). Retrieved: CD-ROM.

Loftus, Z; Venable, R and Adams, G. (1999) Development and implementation of a load controlled friction stir welder. Proceedings of the 1<sup>st</sup> International Symposium on Friction Stir Welding: Rockwell Science Centre, Thousand Oaks, California. TWI(UK). Retrieved: CD-ROM.

Lomolino, S; Tovob, R and Dos Santosa, J. (2004) On the fatigue behaviour and design curves of friction stir butt-welded Al alloys. *International Journal of Fatigue*. Pp. 1-12.

- Lu, J. (1996) *Handbook of measurements of residual Stresses*. Society for Experimental Mechanics Inc. Prentice–Hall: USA.
- Lumsden, JB; Mahoney, MW; Pollock, G and Rhodes, CG. (1999) Intergranular corrosion following friction stir welding of aluminum alloy 7075-T651. *Corrosion* 55(12), Pp. 1127 - 1135
- Mackwood, AP and Crafer, RC. (2005) Thermal modelling of laser welding and related processes: a literature review. *Optics & Laser Technology*. 37. Pp. 99-115.
- Maddox, SJ. (1991) *Fatigue Strength of Welded Materials*. 2<sup>nd</sup> Edition. Abington Publishing Ltd: Abington.
- Magnusson, L and Källman, L. (2000) Mechanical properties of FSW in tin sheet of aluminium 2024, 6013 and 7475. Proceedings of the 2<sup>nd</sup> International Conference on Friction Stir Welding: Gothenburg, Sweden. 26-28 June. TWI(UK). Retrieved: CD-ROM.
- Mahoney, MW; Rhodes, CG; Flintoff, JG; Spurling, RA and Bingel, WH. (1998) Properties of Friction Stir Welded 7075 T651 Aluminum. *Metallurgical and Materials Transactions A*. 29A(7). July. Pp. 1955-1964.
- Mahoney, MW; Mishra, R and Nelson, T. (2001). High strain rate superplasticity in thick section 7050 aluminium created by friction stir welding processing. Proceedings of the 3rd International Symposium on Friction Stir Welding: Kobe, Japan. 27-28 September. TWI(UK). Retrieved: CD-ROM.
- Marie, F; Allehaux, D and Esmiller-EADS, B. (2004) Development of the bobbin tool technique on various aluminium alloys. Proceedings of the 5<sup>th</sup> International Symposium on Friction Stir Welding: Metz, France. 14-16 September. TWI(UK). Retrieved: CD-ROM.
- Montgomery, DC.(1976)  
*Design and analysis of Experiments*, John Wiley and sons. New York.
- Masubuchi, K. (1980) *Analysis of Welded Structures*. Pergamon Press: Oxford, New York.
- Matsomoto, K and Sasabe, S. (2001). Lap joints of aluminium alloys by friction stir welding. Proceedings of the 3rd International Symposium on Friction Stir Welding: Kobe, Japan. 27-28 September. TWI(UK).
- Mendez, PF. (2000) Conference Proceedings: New trends for the Manufacturing in the Aeronautic Industry (Hegan/Inasmet): San Sebastian, Spain. May 24-25. Pp. 21-38.
- Messler, RW. (1999) *Principles of Welding: Processes, Physics, Chemistry, and Metallurgy*. John Wiley & Sons: New York, USA.
- Midling, OT; Oosterkamp, LD; Bersaas, J. (1998) Friction stir welding aluminium—process and applications. 7<sup>th</sup> International conference INALCO'98, Cambridge, UK April.

Midling, OT and Rørwick G. (1999) Effect of tool shoulder material on heat input during friction stir welding. Proceedings of the 1<sup>st</sup> International Symposium on Friction Stir Welding: Thousand Oaks, CA, USA. 14-16 June. TWI(UK). Retrieved: CD-ROM.

Midling, OT. (2003) High Speed Friction Stir Welding of Aluminium Panels for transport applications. *Materials Science Forum*. Vol 426-432. Pp 2897-2902.

Miller, KJ. (1993) Material science perspective of metal fatigue resistance. *Material Science and Technology*. 9. Pp. 453-462.

Mishra, RA and Ma, ZY. (2005) Friction stir welding and processing. *Materials Science and Engineering R*. 50. Pp. 1-78.

Mortimer, J. (2005) Jaguar. Roadmap rethinks self-piercing technology. Retrieved: <http://www.emeraldinsight.com/Insight/ViewContentServlet?Filename=Published/EmeraldFullTextArticle/Articles/0490320303.html>

Murr, LE; Liu, G; McClure, JC. (1997) Dynamic recrystallization in friction-stir welding of aluminium alloy 1100. *Journal of Materials Science Letters*. 16. Pp. 1801-1803.

Murr, LE; Li, Y; Trillo, EA; Flores, RD and McClure, JC. (1998) Microstructures in friction stir welded metals. *Journal of Materials Processing and Manufacturing Science*. 7. Pp. 145-161.

Nakata, K; Inoki, S; Nagano, Y; Hashimoto, T; Johgan, S and Ushio, M. (2001). Friction stir welding of AZ91D Thixomolded sheet. Proceedings of the 3<sup>rd</sup> International Symposium on Friction Stir Welding: Kobe, Japan. 27-28 September. TWI(UK). Retrieved: CD-ROM.

Navidi, W. (2007)  
*Statistics for Engineers and Scientists*. Mc Graw Hill. New York.

Nelson, TW; Hunsaker, B and Filed, DP. (1999) Local texture characterization of friction stir weld in 1100 aluminium. Proceedings of the 1<sup>st</sup> International Symposium on Friction Stir Welding: Thousand Oaks, CA, USA. 14-16 June. TWI(UK). Retrieved: CD-ROM.

Nicholas, ED and Kallee, SW. (2000) "Friction stir welding-A decade on". TWI Ltd, Granta Park, Cambridge CB1 6AL, United Kingdom, tratto da IIW Asian Pacific International Congress Sydney, 29 October to 2 November

Norman AF; Drazhner V; Prangnell PB. (2000) Effect of welding parameters on the solidification microstructure of autogenous TIG welds in an Al-Cu-Mg-Mn alloy. *Materials Science Engineering A*. 259. Pp. 53-64.

North, TH; Bendzsak, GJ and Smith, CB. (2000) Material properties relevant to 3-D FSW modeling. Proceedings of the 2<sup>nd</sup> FSW Symposium: Gothenburg, Sweden. 26-28 June. TWI(UK). Retrieved: CD-ROM.

Noruk, JS. (1997) Gas metal arc penetration welding development utilizing neuralnets. *Robotic Arc Welding Conference Proceedings*: Orlando, Florida.

Otto, J.W. (1997). On the peak profiles in energy-Dispersive Powder X-ray Diffraction with synchrotron Radiation. *Journal Applied Crystals* 30. Pp. 1008-1015.

Ouyang, JH; Jandric, D and Kovacevic, R. (2002) Visualization of material flow in friction stir welding of the same and dissimilar welds. *Proceedings of the 6<sup>th</sup> International Conference on Trends in Welding research*, Pine Mountain, GA, USA.

Owen, RA. (2002) *Synchrotron Strain Mapping: Aerospace applications*. Dissertation PhD Material Science Centre, Manchester University, Manchester.

Pang, JWL; Holden, TM and Mason, TE. (1998) Insitu generation of intergranular strains in an Al 17050. *Acta Materialia*. 46(5). Pp. 1503.

Pao, PS; Gill, SJ; Feng, CR and Sankaran, KK. (2001) Corrosion-fatigue crack growth in friction stir welded Al 7050. *Scripta Materialia*. 45(5). 12 September. Pp. 605-612.

Pao, PS; Lee, E; Feng, CR; Jones, HN; Moon, DW. (2003) Corrosion Fatigue in FSW Welded Al 2519. Pp. 113-122. *Friction Stir Welding and Processing II*. The Minerals, Metals & Materials Society (TMS): Warrendale, PA, USA. Pp. 113-122. Editors: Jata, KV; Mahoney, MW; Mishra, RS; Semiatin, SL and Lienert, T. (Eds.)

Park, SH. (1996) *Robust design and analysis for quality engineering*. Chapman and Hall: London.

Pedwell, R; Davies, H and Jefferson, A. (1999) Application of friction stir welding to aircraft wing structures. *Proceedings of the 1<sup>st</sup> International Symposium on Friction Stir Welding*: Rockwell Science Centre, Thousand Oaks, California. 14-16 June. TWI(UK). Retrieved: CD-ROM.

Peel, M; Steuwer, A; Preuss, M and Withers, PJ. (2003) Microstructure mechanical properties and residual stresses as a function of welding speed in aluminum AA5083 friction stir welds. *Acta Materials*. 51. Pp 4791-4801.

Peel, M.J. (2005), *The Friction-Stir Welding of Dissimilar Aluminium Alloys*, PhD Thesis, University of Manchester.

Phadke, SM. (1989) *Quality Engineering Using Robust Design*. Prentice Hall: Englewood Cliffs, NJ.

Polmear, IJ. (1995) *Light alloys metallurgy of the light metals*. Arnold.

Prado, RA; Murr, LE; Shindo, DJ and Soto, KF. (2001). Tool wear in the friction stir welding of aluminum alloy 6061+20% Al<sub>2</sub>O<sub>3</sub>: a preliminary study. *Scripta Materialia*. 45(1). 13 July. Pp. 75-80.

Preston, RV; Shercliff, HR; Withers, PJ and Smith, S. (2004) Physically-based constitutive modelling of residual stress development in welding of aluminium alloy 2024. *Acta Materialia*. 52. Pp. 4973–4983.

Przydatek, J. (2000) Friction stir welding with Loyds register. Presented at the Royal Institute of Naval Architects. 24<sup>th</sup> and 25<sup>th</sup> February.

Quintana, MA; Barton, D. and Hsu, LC. (2002) Novel optimization methodology for welding process. *Consumable Integration Half Year Report*. Lincoln Electric Company: Cleveland, Ohio. January.

Record, JH; Convington, JL; Nelson, TW; Sorenson, CD and Webb, BW. (2004) Fundamental characterization of friction stir welding. Proceedings of the 5<sup>th</sup> International Symposium on Friction Stir Welding: France. 14-16 September TWI(UK). Retrieved: CD-ROM.

Reynolds, AP; Seidel, TU and Simonsen M. (1999) Visualization of material flow in an autogenous friction stir weld. Proceedings of the 1<sup>st</sup> International Symposium on Friction Stir Welding: Kobe, Japan. 27-28 June. TWI(UK). Retrieved: CD-ROM.

Reynolds, AP; Posada, M; DeLoach, J; Skinner, MJ; Halpin, J and Lienert, TJ. (2001) FSW of autenitic stainless steel. Proceedings of the 3rd International Symposium on Friction Stir Welding: Kobe, Japan. 27-28 September. TWI(UK). Retrieved: CD-ROM.

Reynolds, AP. (2003) FSW Basics. Proceedings of the 1<sup>st</sup> International workshop on Friction Stir Welding: South Africa. 1-3 April.

Reynolds, AP; Tang, W; Gnaupel-Herold, T and Prask, H. (2003a) Structure properties and residual stresses of 304L stainless steel friction stir welds. *Scripta Materialia*. (48) Pp. 1289-1294(6)

Reynolds, AP; Khandkar, Z; Long, T; Tang, W and Khan, J. (2003b) Utility or relatively simple models for understanding process parameter effects on FSW. *Materials Science Form*. Trans Tech Publication: Switzerland. 426-432. Pp. 2959-2964.

Rhodes, CG; Mahoney, MW; Bingel, WH; Spurling, RA and Bampton, CC. (1997) Effects of friction stir welding on microstructure of 7075 aluminum. *Scripta Materialia*. 36(1). 1 January. Pp. 69-75.

Rhodes, CG; Mahoney, MW; Bingel, WH and Calabrese, M. (2003) Fine grain evolution in friction stir processed 7050 aluminium. *Scripta Materialia*. 48. Pp. 1451-1455.

Ribardo, C. (2000) *Desirability functions for comparing arc welding parameter optimisation methods and for addressing process variability under six sigma assumptions*. PhD dissertation. The Ohio State University: Columbus, Ohio.

Rosen, CD. (1996) Friction stir welding total penetration technique (Rockwell). United States Patent No 5611479.

Ross, P.J. (1991) *Taguchi Techniques for Quality Engineering*. McGraw Hill: New York.

Russel., MJ and Schercliff. (1999) Analytical modelling of microstructure in Friction Stir Welding. Proceedings of the 1<sup>st</sup> International Symposium on Friction Stir Welding: Thousanda Oaks, California, USA. 14-16 June. TWI(UK). Retrieved: CD-ROM.

Russell, M.J. (2002) Development and modeling of friction stir welding ,PhD Thesis, Cambridge University, August.

Sachs, NW and Sachs, PE. (2005) Understanding the surface features of fatigue fractures: how they describe the failure cause and the failure history. *Journal of Failure Analysis and Prevention*. 5.(2). April. Pp 11-15.

Salem, HG; Reynolds, AP and Lyons, JS. (2002) Microstructure and retention of superplasticity of friction stir welded superplastic 2095 sheet. *Scripta Materialia*. 46(5). March. Pp. 337-342.

Santella, M; Grant, G; and Arbegast, W. (2003) Plunge testing to evaluate tool material for friction stir welding of 6061+20wt% Al<sub>2</sub>O<sub>3</sub> composites. Proceedings of the 4<sup>th</sup> International Symposium on Friction Stir Welding: Utah, USA. 14-16 May. TWI(UK). Retrieved: CD-ROM.

Sato, YS; Kokawa, H; Enomoto, M and Jogan, S. (1999a) Microstructural evolution of 6063 aluminum during friction stir welding. *Metallurgical and Materials Transactions A*. 30A(9). September. Pp. 2429-2437.

Sato YS, Kokawa, H Enomoto, M; Jogan, S and Takenori, H. (1999b) Precipitation Sequence in Friction Stir Weld of 6063 Aluminum during Aging. *Metallurgical and Materials Transactions A*. 30A(12). December. Pp. 3125-3130.

Sato, YS; Urata, M; Kokawa, H; Ikeda, K and Enomoto, M. (2001a) Retention of fine grained microstructure of equal channel angular pressed aluminum alloy 1050 by friction stir welding. *Scripta Materialia*. 45(1). 13 July. Pp. 109-114.

Sato, YS; Kokawa, H; Enomoto, M; Jogan, S and Hashimoto, T. (2001b) Distributions of hardness and microstructure in friction stir welding of Al Alloy 6063. Proceedings of the 3<sup>rd</sup> International Symposium on Friction Stir Welding: Kobe, Japan. 27-28 September. TWI(UK). Retrieved: CD-ROM.

Sato, YS; Kokawa, H; Ikeda, K; Enomoto, M; Jogan, S and Hashimoto, T. (2001c) Micro texture in the friction stir weld of an aluminum alloy. *Metallurgical and Materials Transactions A*. 32A(4). April. Pp. 941-948.

Sato, YS; Urata, M and Kokawa, H. (2002) Parameters controlling microstructure and hardness during friction stir welding of precipitation-hardenable aluminum alloy 6063. *Metallurgical and Materials Transactions A*. 33A(3). March. Pp. 625-635.

Sato, YS; Mitsunari, U; Kokawa, H and Ikeda, K. (2003) Hall-petch relationship in friction stir welds of equal channel angular-pressed aluminium alloys. *Materials Science and Engineering A*. Vol. 00. Pp. 1-8.

Sato, YS; Park, SHC; Michiuchi, M and Kokawa, H. (2004) Constitutional liquation during dissimilar friction stir welding of Al and Mg alloys. *Scripta Materialia*. 50. Pp. 1233–1236.

Schmidt, H; Hattel, J and Wert, W. (2004) An analytical model for the heat generation in friction stir welding. *Modelling and Simulation in Material Science and Engineering*. 12(1) Pp. 143-157.

Schmidt, H and Hattel, J. (2005) A local model for the thermomechanical conditions in friction stir welding. *Modeling and Simulation in Material Science and Engineering*. 13. Pp. 77-93.

Seidel, TU and Reynolds, AP. (2001) Visualization of the material flow in AA2195 friction stir welds using a marker insert technique. *Metallurgical and Materials Transactions A*. 32A(11). November. P. 2879-2884.

Shankar, K and Wu, W. (2001) Effect of welding and weld repair on crack propagation behaviour in aluminium alloy 5083 plates. *Materials and Design* (23) Pp. 201 – 208.

Sharma, SR and Mishra, RS. (2005) Unpublished research in Mishra, RA and Ma, ZY. (2005) Friction stir welding and processing. *Materials Science and Engineering R*(50) Pp. 1-78.

Shi, Q; Dickerson, T and Schercliff, HR. (2003) Thermo-mechanical FE modeling of friction stir welding of aluminium 2024 including tool loads. Proceedings of the 4<sup>th</sup> International Symposium on Friction Stir Welding: Utah, USA. 14-16 May. TWI(UK). Retrieved: CD-ROM.

Shinoda, T and Shibata, D. (2000) Friction stir welding phenomena of aluminium alloys. National meetings pre-prints. Japan Welding Society. No.67. Pp. 64-65.

Shinoda, T. (2001) Effect of tool angle on metal flow phenomenon in Friction Stir Welds. Proceedings of the 3<sup>rd</sup> International Symposium on Friction Stir Welding: Kobe, Japan. 27-28 September. TWI(UK). Retrieved: CD-ROM.

Shinoda, T; Tokisue, H; Enomoto, M; Hori, H; Koga, S; Kumagaai, M; Matsumoto, K; Okamura, H and Tsuchiya, K. (2001). Recent trends of research and developments of FSW technology in Japan. Proceedings of the 3<sup>rd</sup> International Symposium on Friction Stir Welding: Kobe, Japan. 27-28 September. TWI(UK). Retrieved: CD-ROM.

Shukla, AK and Baeslack III, WA. (2006) Effect of process conditions on microstructure evolution and mechanical properties of FSW thin sheet 2024-T3, 6<sup>th</sup> International Symposium on Friction Stir Welding: 10 - 13 October Saint-Sauveur, Nr Montreal, Canada.

Smith, CB. (2000) Robotic friction stir welding using a standard industrial robot. Proceedings of the 2<sup>nd</sup> FSW Symposium: Gothenburg, Sweden. 26-28 June. TWI(UK). Retrieved: CD-ROM.



Song, M and Kovacevic, R. (2002) Thermal modeling of friction stir welding in a moving coordinate system and its validation. *International Journal of Machine Tools and Manufacture*. 43. Pp. 605-615.

Stewart, MB; Adams, G.P.; Nunes, A.C.; Romine, P. (1998) A combined experimental and analytical approach to understanding friction stir welding. *Developments in Theoretical and Applied Mechanics, SECTAM XIX*, P. 472

Stewart, W W. (2001) Welding of airframes using friction stir. "Aircraft Technol AirSpace Eur".3(3/4). Pp 64–66.

Steuwer, A; Peel, M and Withers, PJ. (2006) Influence of welding parameters on the residual stresses in AA 5083-AA 6082 dissimilar friction stir welds. 6<sup>th</sup> International Symposium on Friction Stir Welding: 10 - 13 October Sant-Sauveur, Nr Montreal, Canada.

Steuwer, A. (2006) Diffraction techniques for residual stress analysis. Presentation at residual stress seminar. Nelson Mandela Metropolitan University. South Africa

Strangwood, M; Berry, JE; Cleugh, DP; Leonard, AJ; Threadgill, PL. (1999) Characterization of thermo-mechanical effects on microstructural development in friction stir welded age-hardening aluminium – based alloys. *Proceedings of the 1<sup>st</sup> International Symposium on Friction Stir Welding: Thousand Oaks, California, USA. 14-16 June. TWI(UK). Retrieved: CD-ROM.*

Sutton, MA; Reynolds, AP; Wand, DQ and Hubbard, CR. (2002a) A Study of residual stresses and microstructure in 2024-T3 aluminium friction stir welds. *Journal of Engineering Materials and Technology*. April. 124. Pp. 215.

Sutton, MA; Yang, B; Reynolds, AP and Taylor, R. (2002b) Microstructural studies of friction stir welds in 2024-T3 aluminum. *Materials Science and Engineering A*. 323(1-2). 31 January. P. 160-166.

Sutton, MA; Reynolds, AP; Yang, B and Taylor, R. (2003a) Mode I fracture and microstructure for 2024-T3 friction stir welds. *Materials Science and Engineering A*. 354. Pp. 6-16.

Sutton, MA; Reynolds, AP; Yang, B and Taylor, R. (2003b) Mode I/II fracture and microstructure for 2024-T3 friction stir welds. *Engineering Fracture Mechanics*. 70. Pp. 2215-2234.

Svensson, L and Karlson, L. (2000) Microstructure, hardness and fracture in friction stir welded AA 6082. *Proceedings of the 1<sup>st</sup> International Symposium on Friction Stir Welding: Thousand Oaks, CA, USA. 14-16 June. TWI(UK). Retrieved: CD-ROM.*

Taguchi, G. (1996) *Introduction to Quality Engineering*, White Plains, NY, Kraus International Publications.

Tang, W; Guo, X; McClure, JC and Murr, LE. (1998) Heat input and temperature distribution in friction stir welding, *Journal of Material Processing Manufacturing Science*.7. Pp. 163-172.

Tanaka, S and Kumagai, M. (2001) Joining dissimilar alloys between AA5083 and A6N01 by friction stir welding. Proceedings of the 3rd International Symposium on Friction Stir Welding: Kobe, Japan. 27-28 September. TWI(UK). Retrieved: CD-ROM.

Technology Transfer Department. (2001) Friction Stir Welding, Web Page - Techtrans Report, NASA MSFC Space Flight Centre. Retrieved: <http://techtrans.msfc.nasa.gov/pdf/FSW11.20.01.pdf>.

Thomas, WM et al. (1991) Friction Stir Butt Welding. U.S. Patent No.5460317.

Thomas, WM and Andrews, RE. (1991) High Performance tools for FSW. International patent specification PCT/GB99/01128 , 13 April.

Thomas, WM and Nicholas, ED. (1997) Friction stir welding for the transportation industries. *Materials and Design*. 18(4-6). 1 December. Pp. 269-273.

Thomas, WM. (1999) Friction stir welding and related friction process characteristics. Proceedings of the 7<sup>th</sup> International Conference on Joints in Aluminium: Abington, Cambridge, UK. INALCO. April 1998.

Thomas, WM; Threadgill, PL and Nicholas, ED. (1999) The feasibility of friction stir welding steel. *Science and Technology of Welding and Joining*. 4. (6). Pp 365–372. Retrieved: <http://www.twi.co.uk/j32k/protected/band8/spwmtfeb99.htm>.

Thomas, WM and Gittos, MF. (1999) Development of friction stir welding tools for the welding of thick (25 mm) aluminium alloys. TWI paper 7741.04/99/1044.3.

Thomas W M et al. (2000) Tool technology - the heart of FSW'. *Connect*, July/August.

Thomas, WM; Nicholas, ED and Smith, SD. (2001) Friction stir welding-tool developments. Proceedings of the 2001 TMS Annual Meeting Automotive Alloys and Joining Aluminum Symposia. New Orleans, Louisiana, 11-15 February. The Minerals, Metals & Materials Society (TMS). Editors: Das, SK; Kaufman, JG and Lienert, TJ.

Thomas, WM; Nicholas, ED; Watts, ER and Staines, DG. (2002) *Friction based welding technology for aluminium*. TWI Ltd: Cambridge, UK.

Thomas, WM and Dolby, RE. (2002) Friction Stir Welding Developments. Proceedings of the 8<sup>th</sup> International Conference on Aluminium Alloys: Cambridge, UK. 2-5 July. TWI.

Threadgill, PL.(1999) Friction stir welding – the state of the art. *Bulletin*. 678. TWI.

Threadgill, PL and Nunn, ME. (2003) A review of friction stir welding, Part 1: Process review. Research report: TWI 760/2003.

TWI (The Welding Institute) (1999) Friction stir welding – superior weld quality. Retrieved: <http://www.twi.co.uk/bestprac/datashts/fswqual.html>

Ulysse, P. (2002) Three-dimensional modelling of the friction stir welding process. *International Journal of Machine Tools and Manufacture*. 42(14). November. Pp. 1549-1557.

United States of America. NASA, Marshall Space Centre (2001) *Space shuttle technology summary: friction stir welding*. USA: Government printer.

Uzun,H; Dalle Donne,C Argagnotto ,A and Gambaro, TGC. (2005) Friction stir welding of dissimilar Al 6013-T4 To X5CrNi18-10 stainless steel. *Materials and Design*. 26. Pp. 41–46.

Vamas. (2001) Standard test methods for determining residual stresses by neutron diffraction.

Wang, YD; Lin Peng, R and Wang, XL. (2000) Strain measurements of friction stir welded samples ICRS-6. Experimental report. Retrieved: [www.studsvik.uu.se/Publications/AnnualReports/Ar00/reports/459.pdf](http://www.studsvik.uu.se/Publications/AnnualReports/Ar00/reports/459.pdf)

Webster, GA. (2001) Polycrystalline materials – Determination of Residual stresses by Neutron diffraction, ISO/TTA3 Technology trends assessment, Geneva.

Webster, PJ; Oosterkamp, LD; Browne, PA; Hughes, DJ; Kang, WP, Withers, PJ and Vaughan, GBM. (2001) Synchrotron X-ray residual strain scanning of a friction stir weld. *Journal of strain Analysis* . 36(1). Pp 61-70.

Webster, PJ and Kang,WP. (2002) Optimization of data collection and processing for efficient strain scanning. *Journal of Neutron Research* 10(2) Pp 93-110.

Wilson, AJC. (1973) *Journal Applied Crystals* 6. Pp 230-237.

Withers, PJ. (2001a) Residual stress: Definition. *Encyclopaedia of materials: Science and Technology*. Elsevier Science Ltd.

Withers, PJ. (2001b) Residual stresses: measurement by diffraction. *Encyclopaedia of materials: Science and Technology*. Elsevier Science Ltd.

Withers, PJ and Bhadeshia HKDH.(2001) Residual stress I. measurements Techniques. *Material Science and Technology*. (17). Pp 355-365.

Withers, PJ; Preuss, M; Webster, PJ; Highes, DJ and Korsunsky, AM.(2002) Residual strain measurements by synchrotron diffraction. *Materials Science Forum*. (404-407). Pp 1-12.

Withers, PJ. (2004) Depth capabilities of neutron and synchrotron diffraction strain measurement instruments. II. Practical implications *Journal Applied Crystals*. 37. Pp 607-612.

[www.twi.oc.za/j32k/protected/band8/spwmtfeb2001.html](http://www.twi.oc.za/j32k/protected/band8/spwmtfeb2001.html). TWI website. Retrieved: 3 February 2003.

Xu, S and Deng, X. (2002a) Two and three dimensional models for the friction stir welding process. Proceedings of the 4<sup>th</sup> International Symposium on Friction Stir Welding: Utah, USA. 14-16 May. TWI(UK). Retrieved: CD-ROM.

Xu, S and Deng, X. (2002b) A Three-Dimensional Model for the Friction-Stir Welding Process. Proceedings of the 21<sup>st</sup> Southeastern conference on theoretical and applied mechanics (SECTAM XXI). Orlando, Florida, May 19-21. Pp 699-704.

Yan, J; Sutton, MA and Reynolds, AP. (2004) Process-structure-property relationship for nugget and HAZ regions of AA2524-T351 FSW joints. Proceedings of 5<sup>th</sup> the International Symposium of Friction Stir Welding: France. 14-16 September. TWI(UK). Retrieved: CD-ROM.

Yang, HS. (2000) Microstructure development in friction stir welding of aluminium alloys. Proceedings of the 6<sup>th</sup> International Conference on aluminium alloys (ICAA-6): Toyohashi, Japan. 5 – 10 July. Pp. 1483-1488.

Yan-hau, Z; San-bao, L; Lin, W and Fu-xing, Q. (2005) The influence of pin geometry on bonding and mechanical properties in friction stir welding 2014 Al alloy. *Materials Letters*. 59. Pp. 2948-2952.

Ying, Li; Murr, LE and McClure, JC. (1991) Flow visualization and residual microstructures associated with the friction stir welding of 2024 aluminum to 6061 aluminum. *Materials Science and Engineering A*. 271(1-2). 1 November. Pp. 213-223.

Ying Li, L.E; Murr, LE and McClure, JC. (1991) Solid-state flow visualization in the friction stir welding of 2024 Al to 6061 Al. *Scripta Materialia*. 40(9). April. Pp. 1041-1046.

Zeelie, B (2002) Workshop: Statistical Analysis, 4 December 2002, Personal interviews, Lecture Notes: PE Technikon.

## Appendix

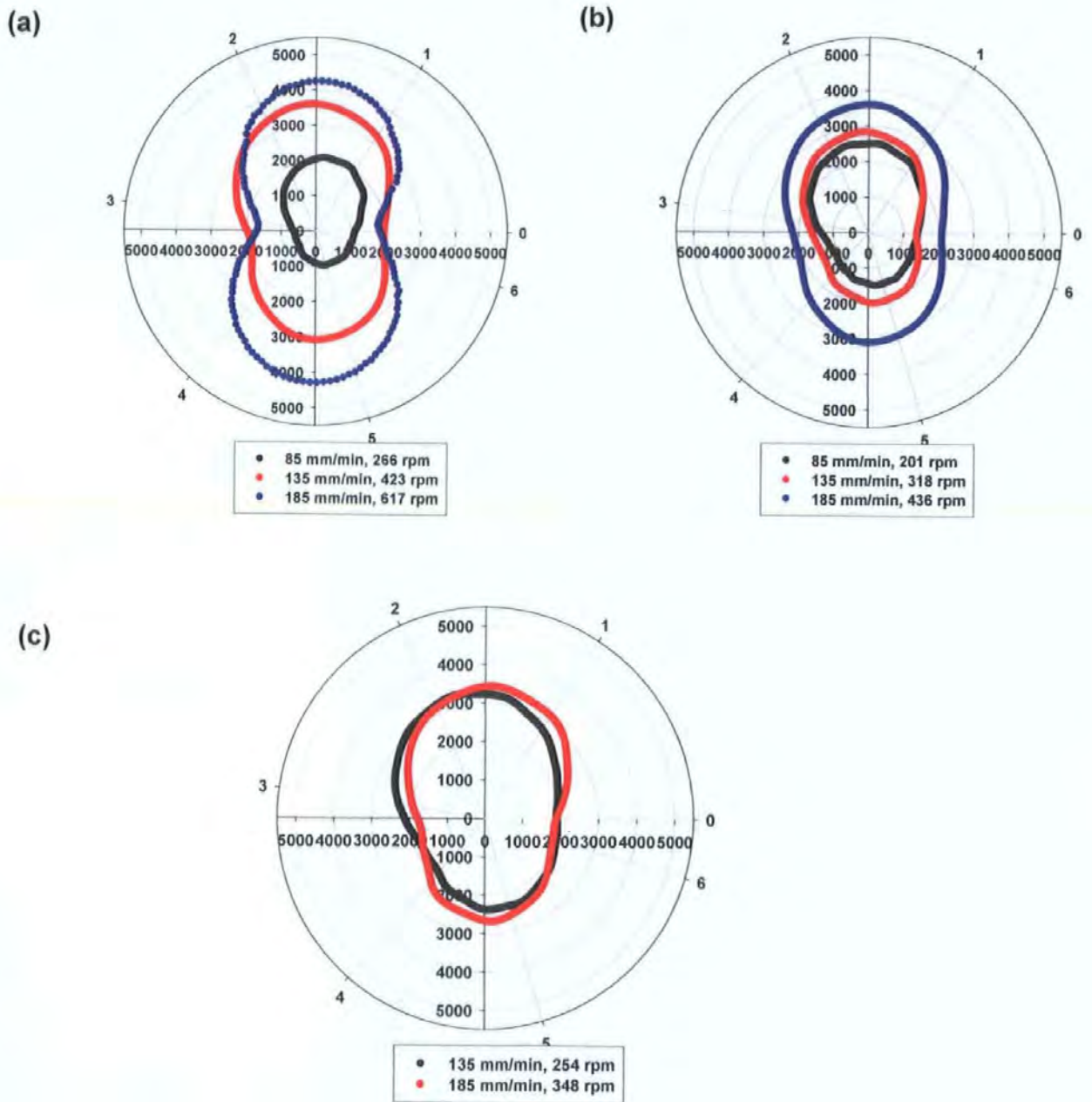


Figure A.1: (a) Resultant polar plot for pitch 0.3.  
(b) Resultant polar plot for pitch 0.4.  
(c) Resultant polar plot for pitch 0.5.

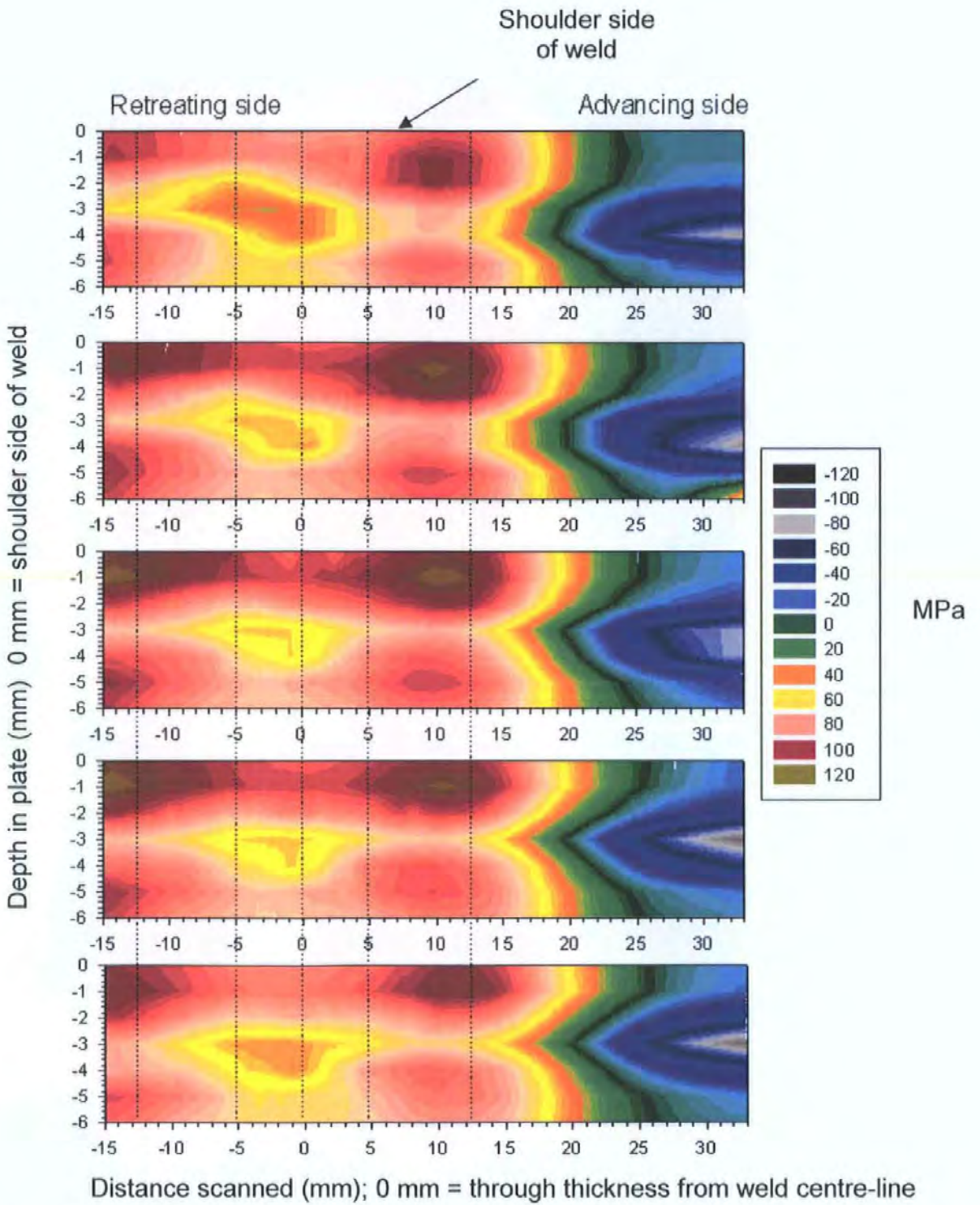


Figure A.2: Longitudinal stress maps of transverse sections of weld 5 (135 mm/min, 254 rpm) at intervals of 15 mm.

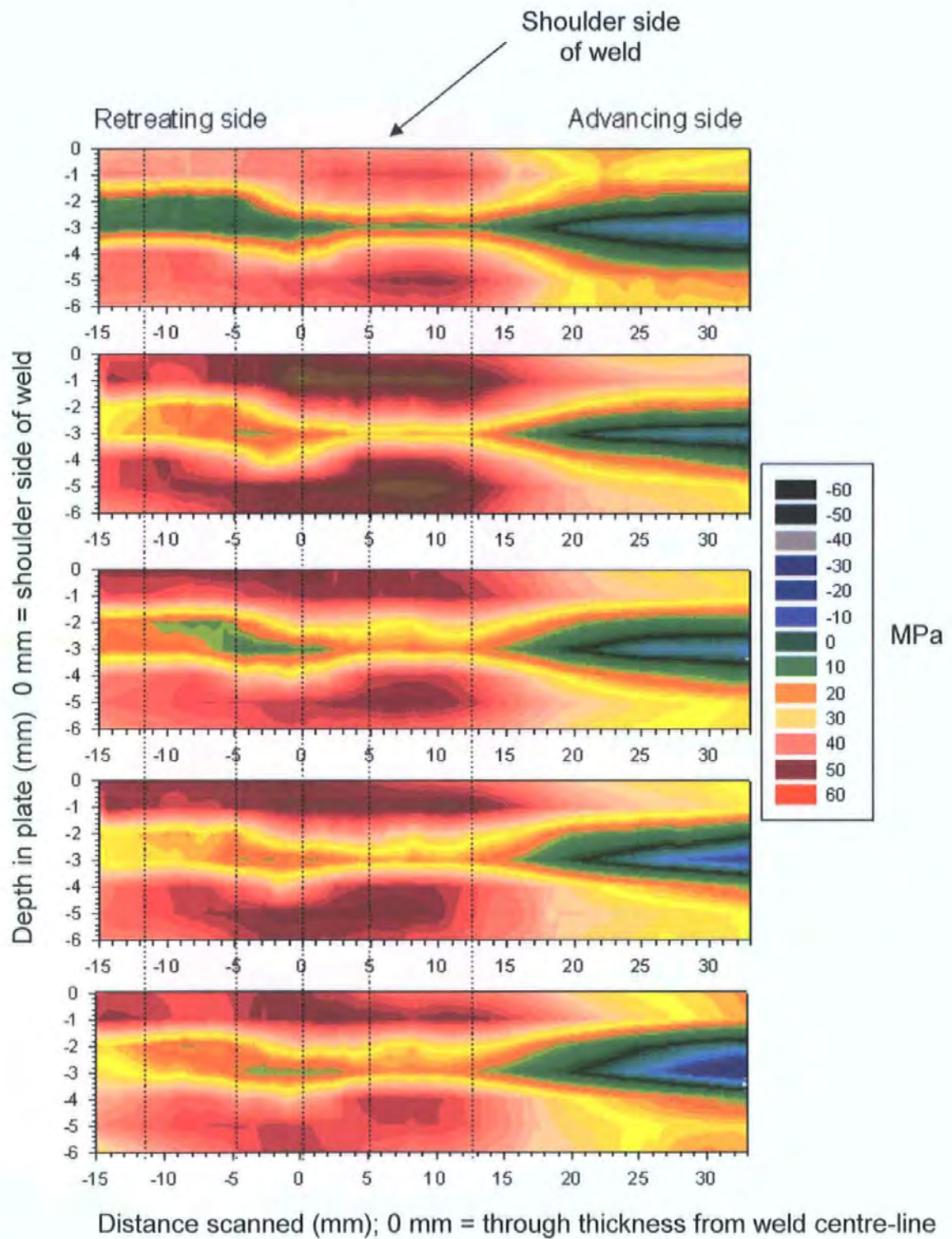


Figure A.3: Transverse stress maps of transverse sections of weld 5 (135 mm/min, 254 rpm) at intervals of 15 mm.

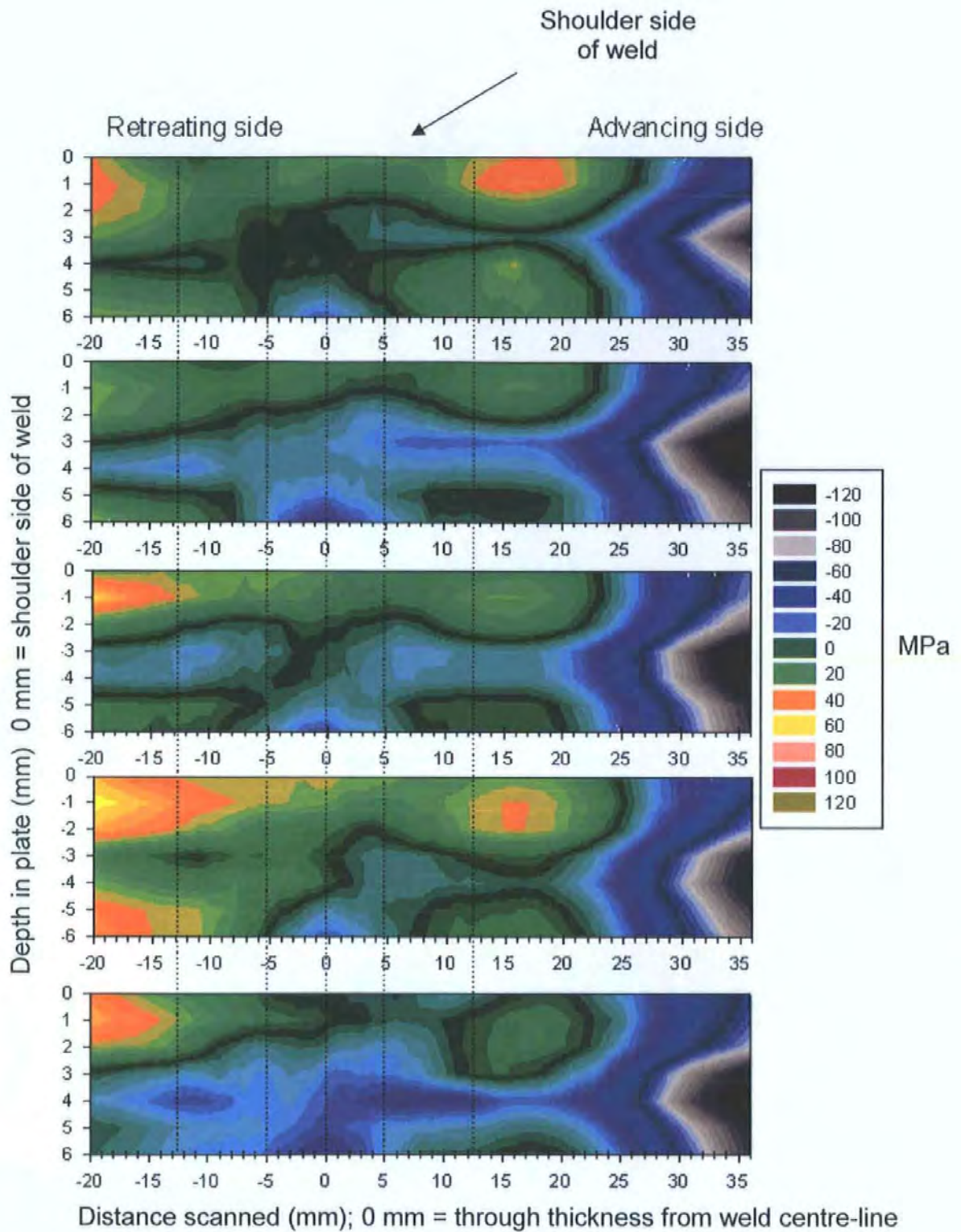


Figure A.4: Longitudinal stress maps of transverse sections of weld 11(135 mm/min, 635 rpm) at intervals of 15 mm.



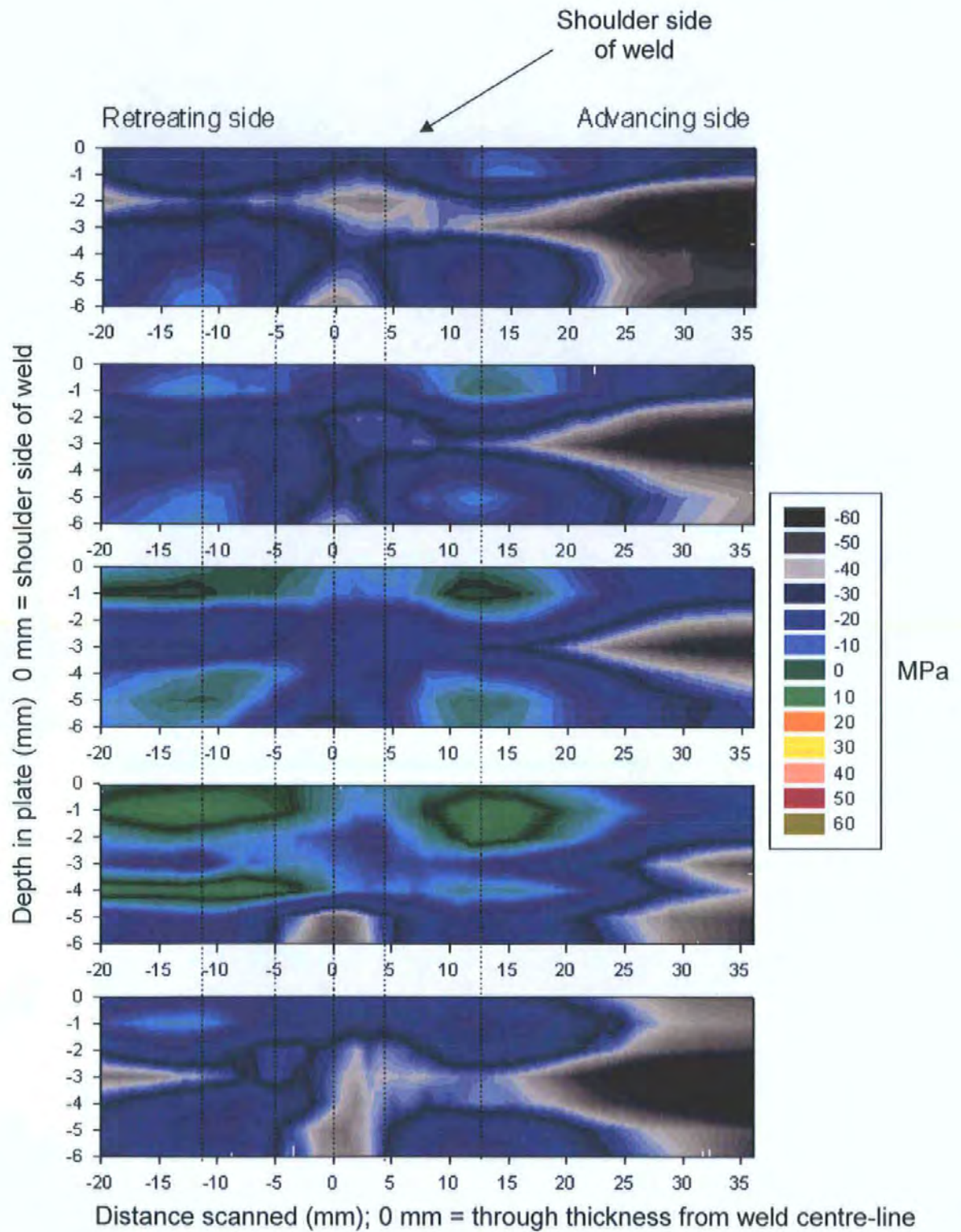


Figure A.5: Transverse stress maps of transverse sections of weld 11 (135 mm/min, 635 rpm) at intervals of 15 mm.

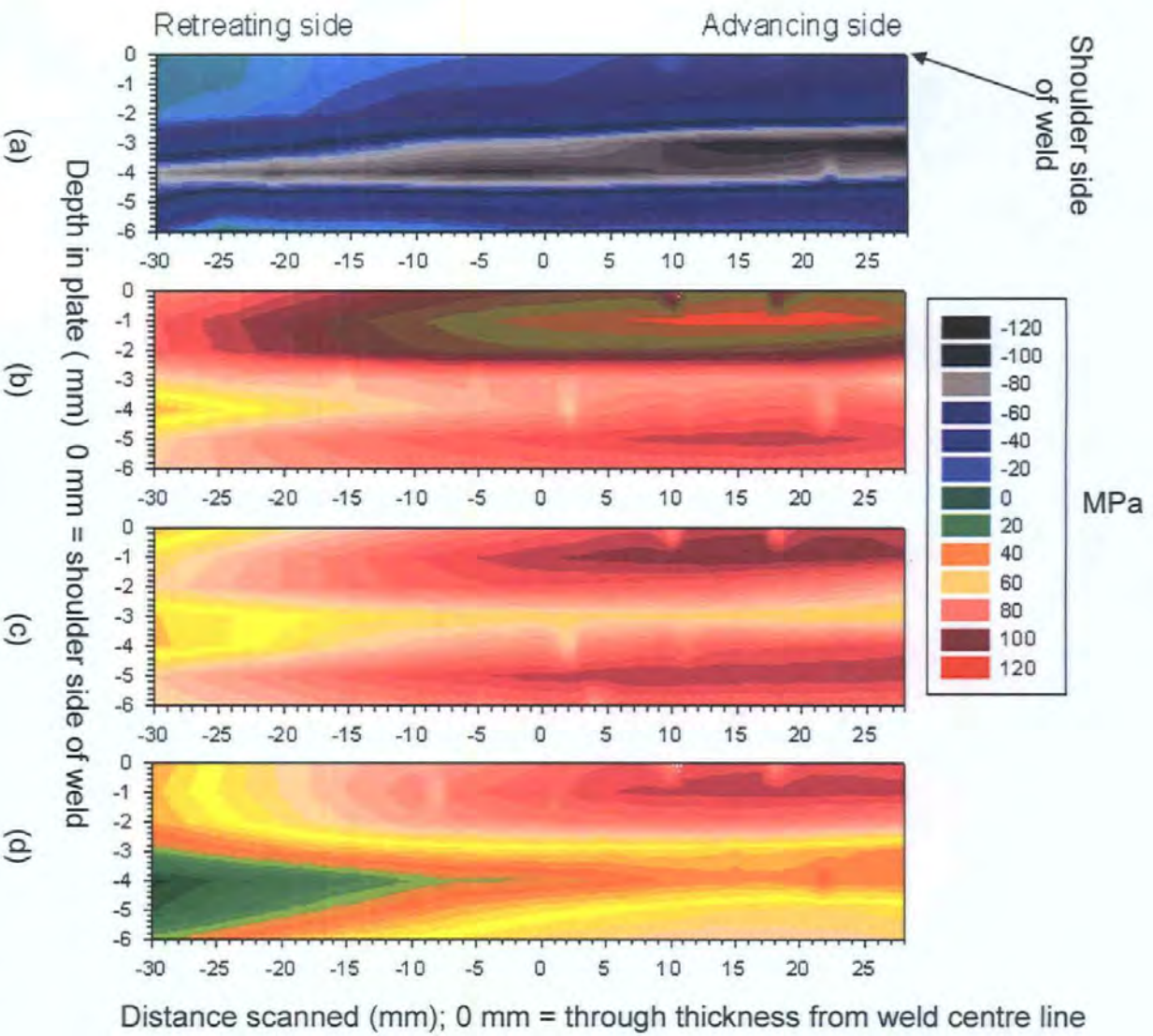


Figure A.6: Longitudinal stress maps of longitudinal sections on the advancing side of weld 5 (135 mm/min, 254 rpm)

(a) 35 mm, in parent plate area.

(b) 10 mm, close to the edge of the shoulder.

(c) 5mm, at edge of the pin.

(d) 0 mm, on weld centre-line.

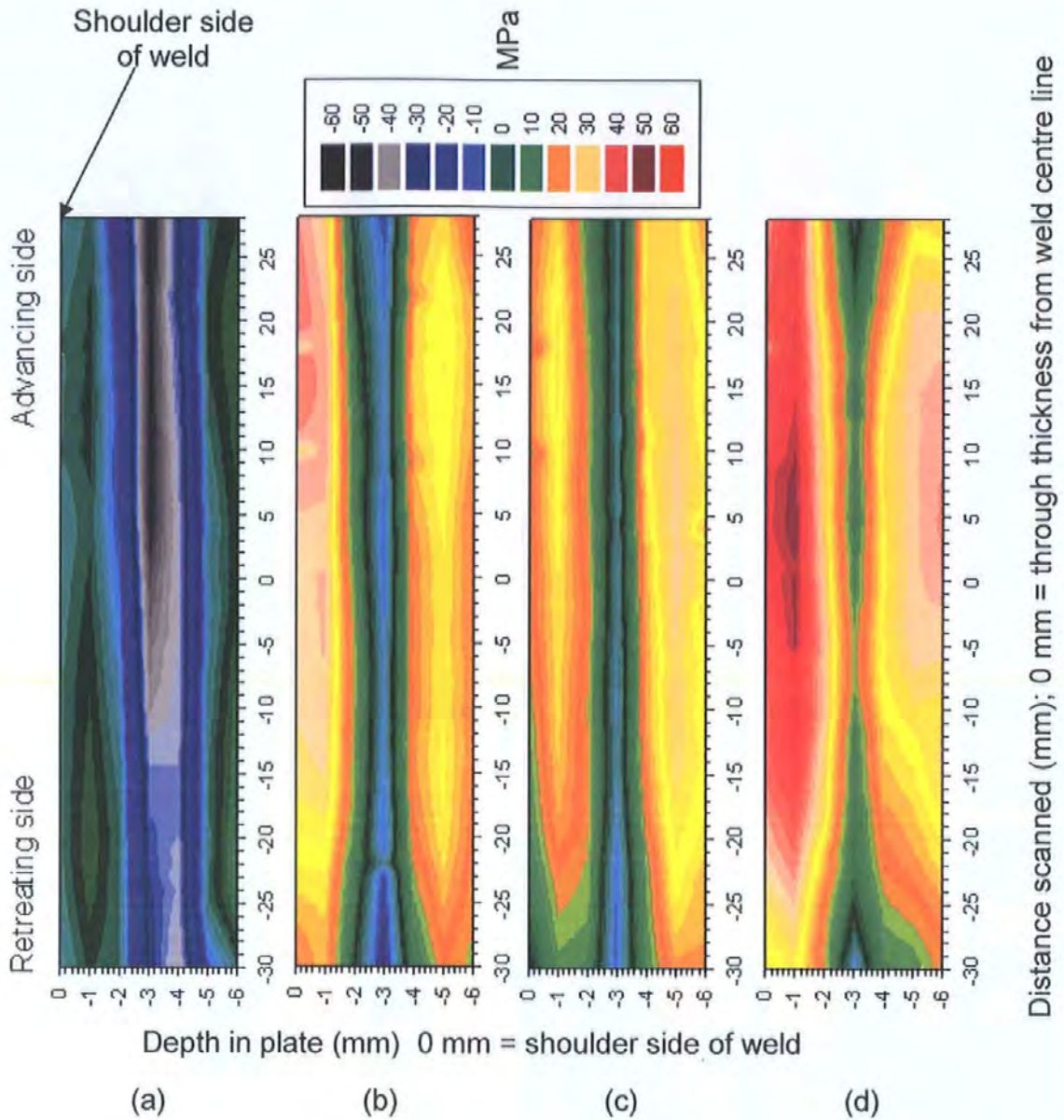


Figure A.7: Transverse stress maps of longitudinal sections on the advancing side of weld 5 (135 mm/min, 254 rpm)  
 (e) 35 mm, in parent plate area.  
 (f) 10 mm, close to the edge of the shoulder.  
 (g) 5mm, at edge of the pin.  
 (h) 0 mm, on weld centre-line.

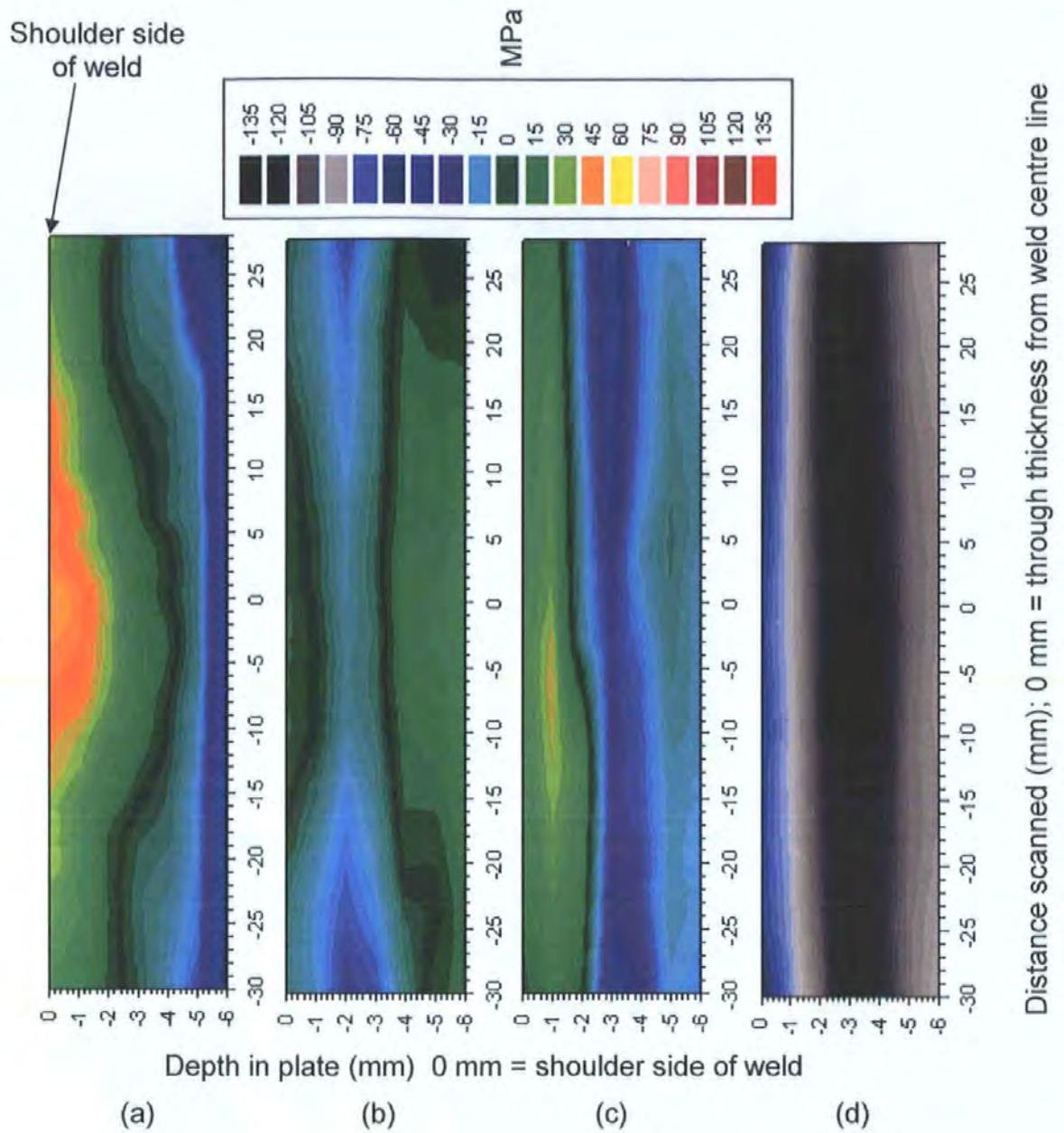


Figure A.8: Longitudinal stress maps of longitudinal sections on the advancing side of weld 11 (135 mm/min, 635 rpm)  
 (a) 0 mm, on weld centre-line.  
 (b) 5mm, at edge of the pin.  
 (c) 10 mm, close to the edge of the shoulder.  
 (d) 35 mm, in parent plate area.

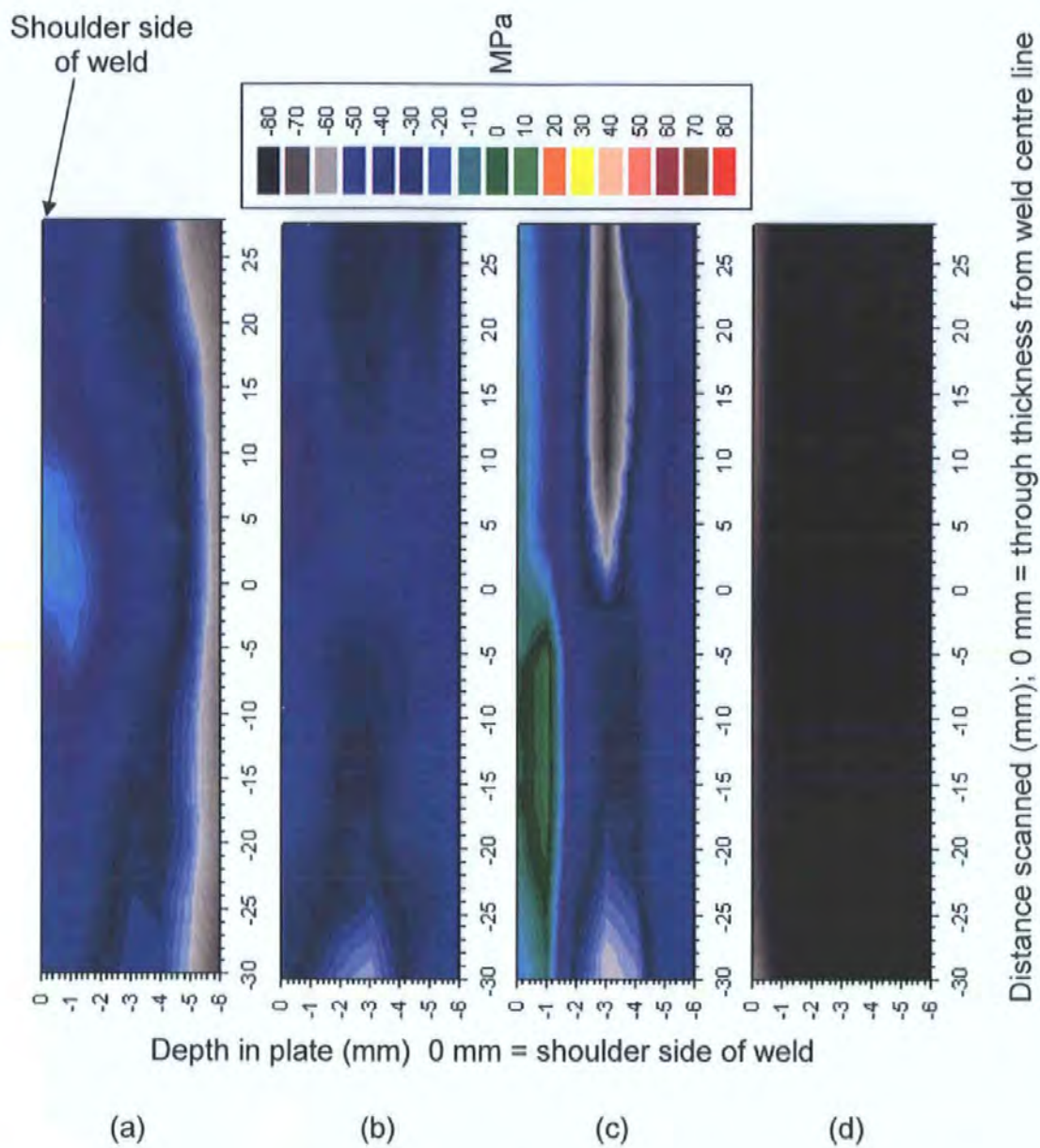


Figure A.9: Transverse stress maps of longitudinal sections on the advancing side of weld 11 (135 mm/min, 635 rpm)  
 (a) 0 mm, on weld centre-line.  
 (b) 5mm, at edge of the pin.  
 (c) 10 mm, close to the edge of the shoulder.  
 (d) 35 mm, in parent plate area.